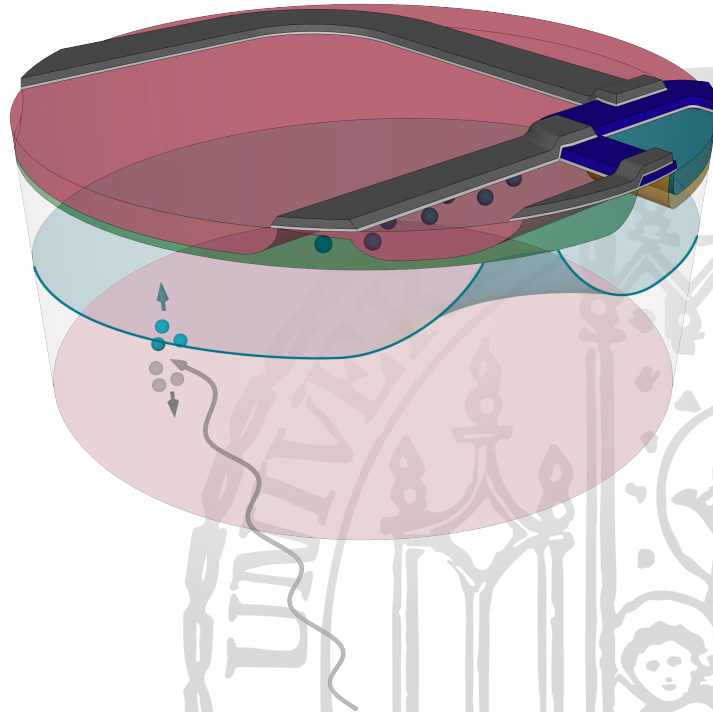

A MEGAHERTZ ACTIVE PIXEL SENSOR FOR X-RAY ASTRONOMY

SPECTROSCOPIC DEPFET ARRAYS WITH INTEGRATED STORAGE



JOHANNES MÜLLER-SEIDLITZ
MÜNCHEN 2019

A MEGAHERTZ ACTIVE PIXEL SENSOR
FOR X-RAY ASTRONOMY

SPECTROSCOPIC DEPFET ARRAYS WITH INTEGRATED STORAGE

DISSERTATION DER FAKULTÄT FÜR PHYSIK
DER LUDWIG-MAXIMILIANS-UNIVERSITÄT MÜNCHEN

VORGELEGT VON
JOHANNES MÜLLER-SEIDLITZ
GEBOREN IN DUISBURG

MÜNCHEN, DEN
03.12.2019

ERSTGUTACHTER: PROF. DR. WERNER BECKER

ZWEITGUTACHTER: PROF. DR. CHRISTIAN KIESLING

DATUM DER MÜNDLICHEN PRÜFUNG: 15.01.2020

Zusammenfassung

Wissenschaftliche Beobachtungen und damit der Zuwachs an Wissen sind durch die verfügbaren Messmethoden und -instrumente limitiert. Um die Genauigkeit wissenschaftlicher Modelle weiter zu verbessern, ist die Entwicklung von Detektoren basierend auf modernsten Technologien unerlässlich. Insbesondere in Raumfahrt-Projekten, die eine umfangreiche Qualifikation aller eingesetzter Teile und Technologien erfordern, ist eine Untersuchung und Verbesserung von Detektorkonzepten nötig, die Jahrzehnte vor deren endgültigem Einsatz beginnen.

Vorgänge in der Umgebung extrem dichter astronomischer Objekte wie Neutronensternen und stellaren schwarzen Löchern finden auf, für astronomische Verhältnisse, kurzen Distanzen und bei extrem hohen effektiven Temperaturen von bis zu 10^7 K^[102] statt. Dies entspricht einer maximalen Emission der thermischen Strahlung bei einigen tausend Elektronenvolt und somit dem Spektralbereich der Röntgenstrahlung. Weitere, im Röntgen-Spektrum sichtbare Merkmale sind Absorptions- und Emissionslinien wie die sehr häufig auftretende Eisen K- α Linie mit einer Ruheenergie von 6.4 keV^[192] oder Bremsstrahlung geladener Teilchen, die in starken Magnetfeldern beschleunigt werden. Um die Eigenschaften solcher kompakter Objekte und ihrer Umgebung, welche auf Zeitskalen im Bereich einiger Mikrosekunden variieren können, weiter zu erforschen, sind schnelle Röntgen-Detektoren erforderlich. Im Vergleich zu CCDs ermöglichen aktive Pixelsensoren kürzere Auslesezyklen und erhöhen damit die erreichbare Zeitauflösung von spektroskopischen Röntgen-Kameras.

Die schnellste Möglichkeit der Auslese ist eine kontinuierliche, für jeden Pixel des Sensors vollständig parallele. Dies reduziert die spektroskopische Leistung eines Detektors signifikant, da Photonen, die während des fast durchgängig stattfindenden Ausleseprozesses eintreffen, mit einer falschen Energie detektiert werden. Dieser Effekt kann umgangen werden, indem ein Speicher für die generierten Ladungsträger in jeden Pixel integriert wird. Eine Umsetzung dieses Konzepts ist der sogenannte Infinipix – ein Pixel bestehend aus zwei verarmten P-Kanal Feldeffekttransistoren (DEPFET). Die Aufgabe der Ladungssammlung und der Auslese wird nach jedem Auslesevorgang zwischen den beiden Sub-Pixeln getauscht. Im Zuge meiner Doktorarbeit wurden erstmals Infinipix Sensoren in der Größenordnung einer Matrix vermessen und dabei drei verschiedene Layout-Varianten verglichen. Es konnte gezeigt werden, dass die untersuchte Umsetzung des Speicher-Konzepts bereits hervorragende spektroskopische Ergebnisse mit einem Rauschen von 2.4 Elektronen und einer Energieauflösung von 123 eV FWHM bei einer Linienenergie von 5.9 keV liefern. Die Dauer des Ausleseprozesses pro Zeile beträgt dabei $5 \mu\text{s}$, was einer Wiederholrate von 6 kHz bei einem quadratischen Sensor mit gut 1000 Pixeln und einer Spalten-parallelen Auslese entspricht.

Die verschiedenen existierenden Layout-Varianten haben die Untersuchung des Einflusses un-

terschiedlicher Design-Parameter auf die spektroskopischen Eigenschaften sowie auf die Leistungsfähigkeit des Speicherkonzepts ermöglicht. Auf diesen Erkenntnissen aufbauend wurden in der vorliegenden Arbeit das Layout optimiert und mit 3D Simulationen getestet. Dabei lag der Fokus auf der Optimierung von Arbeitsfenstern für die Funktionsweise wichtiger Spannungen, um das Speicher-Konzept näher an den Einsatz in zukünftigen Missionen heranzuführen. Mit Messungen und Simulationen konnte auch gezeigt werden, dass das Speicher-Konzept im schnellen Betrieb die erwartete signifikante Verbesserung der spektroskopischen Leistungsfähigkeit gegenüber DEPFET Sensoren ohne Speicher aufweist. Ein optimiertes Infinipix Layout sowie ein erster Infinipix Sensor, der für die vollständig parallele Auslese ausgelegt ist, werden produziert, um die Ergebnisse dieser Arbeit in der Zukunft verifizieren zu können.

Abstract

Scientific observations and thereby the gain of knowledge are limited by the available measurement methods and instruments. To improve the accuracy of scientific models, the development of detectors is an essential activity with the usage of state-of-the-art technology. Especially in space projects with their extensive qualification, the investigation and improvement of concepts have to start decades before the final operation.

Processes around extremely dense celestial objects take place on small scales in hot environments with effective temperatures of up to 10^7 K^[102] that correspond to peak emissions of the thermal radiation of a few thousand electron volts. Further sources for spectral characteristics are absorption and emission features like the very common iron K- α line with a rest energy of 6.4 keV^[192] and bremsstrahlung of charged particles accelerated in the strong magnetic fields. To reveal the nature of such compact celestial bodies and their vicinity that often feature variations on short time scales of a few microseconds, fast X-ray detectors are necessary. Compared to CCDs, active pixel sensors facilitate shorter readout cycles so that they are suitable to increase the time resolution of spectroscopic X-ray imagers.

In the fastest possible readout – the continuous full parallel one – the spectral performance worsens drastically due to photons that hit the detector during the readout process that takes place almost all the time. Such effects can be reduced by implementing a storage for charge carriers generated by an incident photon into each pixel. One approach is the so-called Infinipix, a structure that is composed of two sub-pixels with a depleted p-channel field-effect transistor (DEPFET) each. The charge collection and the readout are interchanged between the sub-pixels after every frame. In the course of my PhD research, three different layout variants are investigated for the first time on matrix scale. It is demonstrated that already the investigated implementation of the concept achieves an excellent spectroscopic performance of 2.4 electrons and 123 eV FWHM at 5.9 keV for a readout time per row of 5 μ s, corresponding to a frame frequency of about 6 kHz even for a kilopixel sensor.

The existing layout variations give the opportunity to study the influence of specific design parameters on the spectroscopic and storage performance and to propose improvements. New layout proposals are investigated by 3D simulations to extend the size of the working windows of operation voltages to further develop a DEPFET with storage to a technology level, adequate to be used in future space missions. Measurements and simulations also indicate the expected improvement, a storage within an active pixel sensor contributes to the spectral performance for high time resolutions. Resulting layout adaptations and a first small sensor in a full parallel readout mode will be fabricated to verify the outcomes of this work in the near future.

Contents

Abstract	III
1 Introduction	1
1.1 Compact Astronomical Objects	4
1.1.1 Spectropolarimetry	8
1.1.2 Quasi-Periodic Oscillations	9
1.1.3 X-Ray Reverberation	9
1.1.4 Pulse Profiles	10
2 Silicon Detectors	13
2.1 Monocrystalline Silicon	13
2.1.1 Energy Levels and Bands	14
2.2 Charge Generation	18
2.2.1 Photoelectric Effect	18
2.2.2 Relaxation	19
2.2.3 Further Photon Interactions	20
2.2.4 Electron Interactions	21
2.2.5 Charge Loss	22
2.2.6 Fano Noise	22
2.3 Doping	23
2.4 Charge Collection	24
2.4.1 PIN Diode	26
2.4.2 Silicon Drift Detector	27
2.4.3 Charge-Coupled Device	28
2.4.4 Active Pixel Sensor	29
3 DEPFET Active Pixel Sensor	31
3.1 DEPFET	32
3.2 Infinipix Principle	34
3.3 Noise	36
3.3.1 White Series Noise	37
3.3.2 Pink Noise	38
3.3.3 Shot Noise	38

4	Measurement Setup and Data Analysis	39
4.1	Califa Test Setup	39
4.2	Electronics	40
4.2.1	Digital Control Unit	41
4.2.2	Steering ASIC	42
4.2.3	Readout ASIC	43
4.2.4	Analogue to Digital Converter	45
4.3	Photon Sources	45
4.3.1	Radioactive Iron-55 Source	45
4.3.2	X-Ray Tube	46
4.3.3	High-Speed LED	46
4.4	Data Analysis	47
4.4.1	Offset and Noise	47
4.4.2	Events	48
4.4.3	Gain	48
4.4.4	Incomplete Clear	49
4.4.5	Results	50
4.4.6	LED Measurements	51
5	Measurements and Evaluation	53
5.1	Readout Principle	53
5.2	Spectral Features	55
5.3	Standard DEPFET	58
5.4	Infinipix	59
5.4.1	Charge Allocation	60
5.4.2	Charge Clearing	63
5.4.3	Layout Variations	65
5.4.4	Window Mode	67
5.4.5	Timing	68
5.4.6	Temperature Dependence	72
5.4.7	Noise	73
5.4.8	Linearity	75
5.5	DEPFETs at High Speed	76
5.6	Review of Results	79
6	Simulations	81
6.1	Device Simulations	81
6.1.1	Bulk Doping	85
6.2	Spatial and Readout Split	86
6.2.1	Charge Generation and Entrance Window	86
6.2.2	Charge Collection and Distribution	88

7 Conclusions and Future Prospects	93
7.1 Future Prospects	94
7.1.1 Technology	94
7.1.2 Layout	96
7.1.3 Inter-Frame Splits	98
7.1.4 Full Parallel Readout	99
References	101
Publications and Manuscripts	117
Associated Publications	117
Further Publications and Manuscripts	118
Figures	121
Tables	123
Appendix	125
Associated Publications	131
Acknowledgements	175

Abbreviations

Al	Aluminium	
ADC	Analogue-to-Digital Converter	41
ADU	Analogue-to-Digital Unit	49
Ag	Silver	
APS	Active Pixel Sensor	11
Ar	Argon	
ASIC	Application-Specific Integrated Circuit	41
Asteroid	Active current Switching TEchnique ReadOut In x-ray spectroscopy with Depfet	43
Athena	Advanced Telescope for High ENergy Astrophysics	2
C	Carbon	
Califa	Calibration Facility	39
CCD	Charge-Coupled Device	2
CMOS	Complementary Metal-Oxide-Semiconductor	97
CTE	Charge Transfer Efficiency	32
Cu	Copper	
DEPFET	DEpleted P-channel Field-Effect Transistor	2
ENC	Equivalent Noise Charge	
eROSITA	extended ROentgen Survey with an Imaging Telescope Array	29
Fe	Iron	45
FWHM	Full Width at Half Maximum	22
HEW	Half Energy Width	4
Ge	Germanium	
LED	Light-Emitting Diode	46
MIXS	Mercury Imaging X-ray Spectrometer	2
Mn	Manganese	45
MOSFET	Metal-Oxide-Semiconductor Field-Effect Transistor	31
MPE	Max Planck institute for Extraterrestrial physics	39
MPG	Max-Planck-Gesellschaft (Max Planck Society)	94
MIP	Minimum Ionizing Particle	47
NICER	Neutron star Interior Composition ExploreR	12
Ni	Nickel	
NIR	Near InfraRed	4
O	Oxygen	
PCB	Printed Circuit Board	40
PCI	Peripheral Component Interconnect	45
PLC	Programmable Logic Controller	40
PSF	Point Spread Function	

PSPC	Position Sensitive Proportional Counter	
QPO	Quasi-Periodic Oscillation	9
RAM	Random-Access Memory	82
ROAn	ROOT Offline Analysis	47
ROSAT	ROentgenSATellit	1
SDD	Silicon Drift Detector	12
Si	Silicon	56
SI	Système International d'unités (International System of Units)	14
S/N	Signal-to-Noise	11
Ti	Titanium	
UV	UltraViolet	10
UVA	UltraViolet A	4
Veritas	VErsatile Readout based on Integrated Trapezoidal Analog Shapers ...	43
WFI	Wide Field Imager	3
Xe	Xenon	
X-IFU	X-ray Integral Field Unit	3
XMM	X-ray Multi Mirror	2

Introduction

The discovery of X-rays by Röntgen (1895)^[167] opened a new approach of investigation to look at and to answer questions that arise in research. Various imaging techniques facilitate the investigation of examination objects in life sciences and in materials analysis. In astronomy, it creates new opportunities to study the universe. Celestial observations in the X-ray range of the electromagnetic spectrum allow for the investigation of high energetic processes and hot environments. Strong magnetic fields of compact objects accelerate charged particles which then trigger characteristic X-ray emission or emit bremsstrahlung. Thermal radiation of gases with temperatures of tens to hundreds of million degrees that are heated in deep gravitational potentials can be studied in the X-ray band because the Planck spectrum peaks at such high energies. It provides the possibility to investigate and understand the large scale structures in the universe and the most dense objects that are conceivable.

Since the atmosphere absorbs most of the electromagnetic radiation on their way to the Earth's surface, it is transparent only for small windows around the visible light and for longer wavelengths from about 10^{-2} to 10^1 m. To investigate the emission in other wavelengths, it is necessary to go to high altitudes or into space to perform astronomical observations. Thereby, contemporary X-ray observatories are based on satellites.

X-ray imaging detectors base on single photon counting. Therefore, a sensor needs to be fast enough to separate individual events depending on the intensity of the source. An early implementation of an imager with low resolution spectroscopic capability was the position sensitive proportional counter (PSPC)^[30] of which two were on board of the ROSAT^[a] telescope.^[202] X-ray photons were absorbed in a thin volume drained with a mixture of gases composed of argon, xenon and methane.^[30] An X-ray photon is absorbed by an atom of the gas via the photoelectric effect (section 2.2.1). The released electron ionises further atoms. The final number of free electrons corresponds to the energy of the incident X-ray photon. The uncertainty in this number is described by the material specific Fano factor (section 2.2.6) and the number of liberated electrons which sets a physical limit for the energy resolution achievable with such a detector concept. The (Fano limited) energy resolution is defined as the full width at the half maximum $\text{FWHM} = 2.355\sqrt{FwE}$ of a Gaussian shaped, measured

^[a]ROentgenSATellit

Table 1.1: The theoretical Fano limit and the development of the energy resolution of different X-ray cameras over the last decades compared to contemporary projects. Since the ROSAT PSPC had a good quantum efficiency only between 0.1 keV and 2 keV, the carbon K- α and the copper L- α emission lines at 0.28 keV and 0.93 keV were typical calibration features.^[30] For the pnCCDs and the DEPFETs, the manganese K- α line at 5.9 keV of an iron-55 source as approximation for the very common iron emission lines is used. The DEPFET array investigated as part of the Athena prototype development consists of 64×64 pixels.

		C K- α	Cu L- α	Mn K- α	Time Resolution
Fano Limit	Ar + 24% Xe	88 eV	162 eV	408 eV	—
	Silicon	26 eV	48 eV	120 eV	—
ROSAT PSPC ^[30]		—	400 eV	—	0.130 ms
XMM-Newton pnCCD ^[185]		—	—	152 eV	73.300 ms
eROSITA pnCCD ^[126]		64 eV	72 eV	141 eV	50.000 ms
Athena WFI ^[127]		—	< 80 eV	< 155 eV	< 5.000 ms
DEPFET Prototypes		49 eV	62 eV	128 eV	0.160 ms
Future DEPFETs*		—	—	< 140 eV	~ 0.001 ms

* All pixels are read out fully parallel. Time resolution is independent from the number of pixels.

emission line with the energy E . For an argon-xenon mixture of about 3:1, the mean energy needed to create a free electron w is $22.1 \text{ eV}/e^-$ and the Fano factor is $F = 0.23$.^[43] Resulting limits for different photon energies are given in Table 1.1. The squares of further noise sources like electronic components in the detector or the readout process itself need to be added to achieve the actual energy resolution $\text{FWHM} = 2.355 \sqrt{FwE + (w\sigma_{\text{noise},e^-})^2}$.

Contemporary X-ray space telescopes like Chandra and XMM^[b]-Newton include, without limitation, CCDs^[c] as very common and well known imaging detectors with spectroscopic capability that are based on silicon as sensor material. Compared to gas atoms, electrons in a semiconductor are only weakly bound. The mean energy needed to create an electron-hole pair is lower $(3.7 \text{ eV}/e^-)$ ^[111] which results in larger electron clouds and, consequently, in a better statistics and an improved achievable energy resolution. The Wide Field Imager^[127,164] of the next generation X-ray observatory Athena^[d]^[142] will make use of DEPFET^[e] active pixel sensors^[98] to overcome negative drawbacks of CCDs like out-of-time events or charge loss during transfer and to speed up the readout and thereby the achievable time resolution. After the MIXS^[f] instrument^[201] on BepiColombo, a mission to planet Mercury scheduled for 2018, it will be the second DEPFET instrument in space. To push the limit of the time resolution to even higher frame rates, active pixel sensors have to be developed that can

^[b]X-ray Multi Mirror

^[c]Charge-Coupled Devices

^[d]Advanced Telescope for High ENergy Astrophysics

^[e]DEpleted P-channel Field-Effect Transistor

^[f]Mercury Imaging X-ray Spectrometer

be read out almost all the time. The aim is to get a reasonable spectroscopic resolution as well as a high throughput even for bright sources while the sensor is permanently sensitive to photons. The devices I investigated in my research were the first spectroscopic DEPFETs with linear gates on matrix scale which allow for smaller charge collection regions (see section 3.1). Their excellent spectroscopic performance and fast timing was a first hint for the results the layouts on the prototype production for the Athena WFI^[g] have delivered.^[198]

The DEPFET as first amplifier in the signal processing chain can be modified to implement additional features like a non-linear amplification to enable high dynamic ranges,^[106] a repetitive non-destructive readout for a readout noise down to single electrons^[215] or a shutter.^[22] To not only blind the pixel in the latter case, a more sophisticated approach is the implementation of a storage into each pixel.^[23] The faster the intended readout of a detector is, the higher is the fraction of readout to exposure time and thereby the relevance of the spatial separation of the charges' collection and their measurement. Otherwise, the spectral performance would drop significantly.

The aim of my PhD research is to study and further develop DEPFET concepts for such high time resolution purposes avoiding a degradation of the measured spectra compared to the physical limit of the sensor. For time resolutions of about one millisecond, the energy resolution of DEPFET prototype detectors with 64×64 pixels is already near the Fano limit (see section 2.2.6). While the theoretical limit at 5.9 keV is (119 ± 2) eV FWHM,^[111] the measured energy resolution for events that do not split over pixel borders is (121 ± 1) eV FWHM which still includes all disturbances by the required electronic components. Since the Fano noise sets a physical lower limit for sensors that base on the photoelectric effect, the energy resolution can only be improved by completely different concepts like the transition edge sensors used for the X-IFU^[h] of Athena.^[10] They are operated based on resistance measurements of superconducting material. The resistance rises if an absorbed X-ray photon increases the sensor's temperature.^[88] While the energy resolution is at about 2.5 eV FWHM for photon energies < 7 keV, the detector has a high complexity due to the low operation temperatures of about 55 mK and the throughput is limited since the sensor needs to settle after it was heated up by an event.^[182] For the observations of objects that require a high count rate and an excellent time resolution, ionisation detectors adapted to these specific needs offer a simpler and therefore more lightweight solution. In my research, I investigated and characterised three existing layout variants of a concept that implements a DEPFET with a pixel-wise storage functionality. These prototype sensors consist of 32×32 pixels and are the first of such storage DEPFETs investigated on matrix scale. The differences in the layout enabled the measurement of different aspects concerning functionality, efficiency and robustness. With these results I developed an adaption of the layout and tested the functionality and improvements with 3D device simulations. In addition, I examined small adaptations in

^[g]Wide Field Imager

^[h]X-ray Integral Field Unit

the technology. Even though a time resolution of 1 μs could not be reached in measurements with the existing devices, I demonstrated the advantage of DEPFET arrays with pixel-wise integrated storages over non-storage DEPFETs using the capability of active pixel sensors to be read out in window mode to increase the time resolution.

The current limitation of the usage of DEPFETs to the high energy range of the electromagnetic spectrum is given by the large area a DEPFET occupies within a pixel. X-ray optics have a relatively large PSF – e.g. 5'' HEW^[i],^[11] corresponding to 290 μm for the 12 m focal length of Athena^{[8][j]} – so that smaller pixels are not reasonable. In addition, electric repulsion in combination with back side illumination leads to a spreading of the charge cloud which is not an issue for single electrons generating radiation in the optical, UVA^[k] and NIR^[l] frequency band. For those applications, the pixels have edge lengths of a few micrometres and could not have been equipped yet with DEPFETs fabricated with the investigated processing technology. With the ongoing development in the production, it may be enabled in the future. But the high time resolution achievable with DEPFET detectors makes them already attractive for other present projects.

1.1 Compact Astronomical Objects

The fusion of metals – in its meaning in astronomy as elements heavier than helium – in the stellar nucleosynthesis lasts as long as the resulting nucleus is more tightly bound as the ones before and energy is emitted in the form of photons and neutrinos. Although ^{62}Ni and ^{58}Fe contain the most tightly bound atomic nuclei,^[59] ^{56}Fe as decay product of ^{56}Ni is much more abundant in the interstellar medium. It is assumed that photodisintegration becomes dominant over alpha particle capturing and prevents the formation of a more significant fraction of ^{62}Ni . All even heavier metals are merged during the explosion of giant stars after the equilibrium between radiation and gravitational pressure collapses due to the decreasing number of photons from fusion processes – or in even more violent events.^[155] As a result, iron is by far the heaviest element among the most abundant ones in the universe.^[109] Thereby, the energy of the characteristic X-ray radiation (see section 2.1.1) is the hardest of these elements.^[137] As the observed photon energy decreases with large distances due to the expansion of the universe as shown in Fig. 1.1, absorption and emission lines of lighter elements are shifted out of the sensitive energy range of the radiation detectors of X-ray telescopes. For those reasons, the iron K lines are a very common feature in X-ray spectra.

^[i]Half Energy Width

^[j]The Chandra X-ray Observatory has a better angular resolution of 0.5''.^[212] However, the used glass-ceramic is more than an order of magnitude heavier than the silicon pore optics^[146] on Athena and therefore not suitable for larger mirrors.

^[k]UltraViolet A

^[l]Near InfraRed

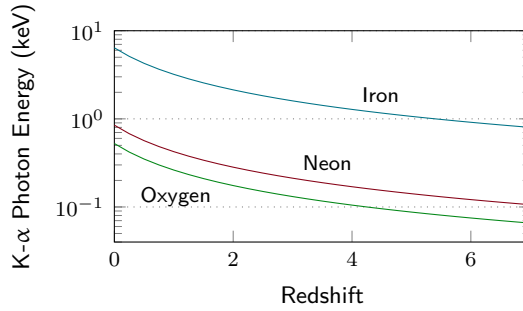


Figure 1.1: Energy of a K- α photon in dependence of the redshift and therefore the distance from its point of origin to the observer. The wave length is shifted to smaller values for increasing distances due to the expansion of the universe which decreases the observed photon energy. For a comparison, the two heaviest more abundant elements neon and oxygen are shown.

Thus, the spectroscopic performance measurements with the samples of this study are mainly performed with a radioactive ^{55}Fe source (see section 4.3.1).

The further evolution of a star at the end of the fusion processes in its core depends on the remaining mass after the star has collapsed and eventually exploded. For remnants with masses lower than the Chandrasekhar limit of about $1.4 M_{\odot}$ ^[m]^[123] – which varies for different compositions of the star^[193] – it becomes a white dwarf. They only emit thermal radiation and get fainter over time as they cool down, becoming black dwarfs.^[65] Their further collapse is stopped by degeneracy pressure of the electrons^[66] which is a consequence of the Pauli exclusion principle.^[154] For larger masses and thereby gravitational forces, the electron degeneracy pressure is overcome and neutrons are formed by electron capture during a core collapse supernova which require masses of at least $8 M_{\odot}$ to $10 M_{\odot}$ of the initial star.^[70] Neutrinos are released during electron capture or by the production of neutrino pairs.^[63] In combination with the high densities around the collapsing stellar core a significant pressure is generated on the very dense inner stellar shells. It is assumed that the neutrino pressure in combination with perturbations which has already existed in the progenitor star triggers the supernova explosion.^[134] In the remaining neutron star the degeneracy pressure of neutrons stabilises the star against the gravitational forces. If the remnant is more massive than $2 M_{\odot}$ to $3 M_{\odot}$, it collapses to a black hole.^[34] A black hole describes an object whose mass is packed within its event horizon^[176] so that nothing can cross this barrier to the outside because of an escape velocity that is larger than the speed of light.

Since most of the massive stars live in multiple star systems,^[50] they still have companions as stellar endpoints. If parts of the companion star cross the Roche limit^[168] – the boundary where the gradient of the gravitational potential of a two body system changes its direction – material streams towards the compact partner. The accreted matter is accelerated and heated by the deep gravitational potentials. Due to the small dimensions of a few kilometres,

^[m] $M_{\odot} = 1.99 \cdot 10^{30}$ kg, ^[203] mass of the Sun

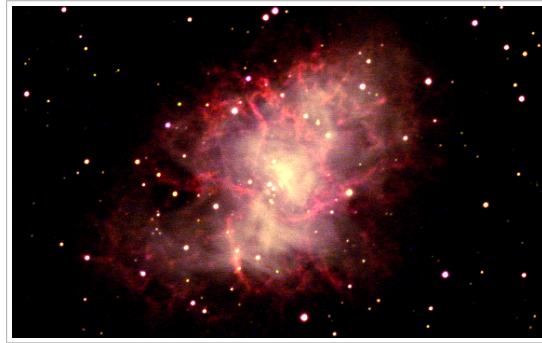


Figure 1.2: Pseudo colour image of the Crab pulsar which is assumed to originate from the supernova SN1054 that was observed by Chinese astronomers.^[122] Whether the nebula surrounding the neutron star is a supernova remnant or has already been existed before is unresolved.^[67] The image was taken in the i- (NIR), r- (red)^[68] and B-band (blue)^[20] with the 40 cm telescope at the Wendelstein Observatory of the Ludwig-Maximilians University Munich.

variations occur on very short time scales. Their compactness in combination with the speed of light c results in variations on a microsecond timescale. For high time resolution purposes, concepts like DEPFETs with storage are needed. Besides the investigation of extremely rapid changes in the spectral features or brightness, the high readout frequency also enables the observation of bright sources with a high throughput. Such bright or fast varying objects are the remnants of stars: white dwarfs, neutron stars and black holes as well as their direct vicinities. Especially the most dense objects in the universe – neutron stars and black holes – and their violent surroundings are of interest in the X-ray regime of the electromagnetic spectrum.

While there is no information flow out of a black hole and observations are limited to the event horizon and its environment, neutron stars themselves can be investigated. Their properties are of interest to deepen the knowledge about stellar endpoints, but also as test laboratories for physics under extreme conditions. Neutron star masses could be determined in the range between $1.17 M_{\odot}$ and $2.0 M_{\odot}$ and radii were measured between 9.9 km and 11.2 km, mostly from neutron stars in binaries.^[221] It results in mean densities that are of the order of the nucleons' density which is up to an order of magnitude above the nuclear density.^[103] Global quantities that can be measured by an external observer like the mass-to-radius relation are described by the equations of state.^[103] Derived from Einstein's equations of general relativity,^[52] the Tolman^[195]-Oppenheimer-Volkov^[148] equations represent the hydrostatic equilibrium.^[103]

$$\frac{dP}{dr} = - \frac{G (m(r) + 4\pi r^3 P/c^2) (\rho + P/c^2)}{r (r - 2Gm(r)/c^2)} \quad (1.1)$$

$$\frac{dm(r)}{dr} = 4\pi \rho r^2 \quad (1.2)$$

· $c = 299\,792\,458 \text{ m s}^{-1}$, speed of light in vacuum

$G^{[n]}$ is the gravitational constant, P the pressure, ρ the mass-energy density and $m(r)$ the mass within the radius r . Even though, exact solutions of the equations exist,^[44] numerical simulations are necessary to obtain realistic descriptions of the P - ρ and mass-to-radius relations.^[103] The initial assumption of a star entirely composed of non-interacting relativistic neutrons^[148,195] is not in consistence with the observed masses – and resulting radii – and rotational periods.^[210] Even though, a large fraction of a neutron star may consist of free nucleons, in particular neutrons, this suggests, that at least the core of the star may be composed of free quarks, mesons – which do not obey the Pauli exclusion principle^[154] as they are bosons – and even stable strange matter (hyperons).^[221] The structure of a neutron star is divided into various shells which are discriminated by their density that sets different conditions for the physics and the involved particles. The outer part is composed of ^{56}Fe nuclei which has built a lattice and an electron gas.^[12] Below densities of 10^9 kg m^{-3} the physics is dominated by the strong magnetic fields of the neutron star and the temperature. Some electrons may be bound to the iron nuclei. It is the surface of the star.^[152] Up to a density of $4.3 \cdot 10^{14} \text{ kg m}^{-3}$, the iron lattice is called outer crust. Above this threshold, the nuclei are enriched by neutrons. This inner crust also contains superfluid neutrons and extends towards a density of $2 \cdot 10^{17} \text{ kg m}^{-3}$. The following outer core is mainly composed of superfluid neutrons as well as electrons and superconducting protons.^[152] The density threshold to the inner core consisting of extraordinary particles is contingent on the exact composition. Depending on the mass-to-radius relation, the resulting gravitational potential defines the size of the different shells. Hypothetical stars that are almost entirely made of quarks or even hyperons are called quarks^[89] or strange stars, respectively. Since the radius depends only weakly on the mass in the transition regime between neutron stars and denser objects, it is difficult to distinguish between the different models on the basis of size measurements considering the measurement errors.^[116]

To set further constrains on the internal structure of a neutron star, the rotational period and its derivatives are investigated. Pulsars are neutron stars with anisotropically emitted radiation formed by their strong magnetic fields. Due to the rotation of the star, the detected signal of those neutron stars appears to be pulsed.^[77,78,149,150] Such signals are known in the radio band since 1968.^[85] Later, they were also discovered in the X-ray regime.^[76] The first pulsed X-ray signal from the group of the very fast spinning millisecond pulsars was discovered in 1993.^[15] Rotational characteristics can be measured most accurately by measuring the radio emission.^[110] Besides the decreasing rotational velocity, also rapid rises in the rotational frequency are detected. Such glitches, like they are observed for the Vela pulsar,^[151] need a shell of superfluid neutrinos to explain the observations.^[116] While the outer solid crust of a neutron star is slowing down, being decelerated by the magnetic field's interaction with the surrounding, the rotational period of the superfluid neutron gas stays constant. If the difference in the rotation velocities between the crust and the core becomes

^[n] $G = 6.674\,08 \cdot 10^{-11} \text{ m}^3 \text{ s}^{-2} \text{ kg}^{-1}$ Gravitational constant^[169]

larger, angular momentum is transferred from the core to the crust.^[151] Since the angular momentum of a superfluid is carried by quantised vortices,^[147] its transfer can only take place in quantised steps which is observed as glitches in the rotational period of the crust. In the future, also the direct measurement of gravitational waves can help to analyse the internal structure of the neutron, quark and strange stars.^[138,166]

The surface of neutron stars and their direct vicinities emit a lot of radiation over the whole electromagnetic spectrum due to an environment at high temperatures which is permeated by strong magnetic fields. The different emission processes and their localisation is summarised by Becker (2009).^[14] Thermal emission of a cooling neutron star can be expected from the whole surface. It is emitted as black-body radiation, but modified as it passes the atmosphere of the neutron star.^[205] A second thermal source may be the polar caps heated by the bombardment caused by particles accelerated along the magnetic field lines towards the neutron star's surface. This pulsed high energy emission may also be generated in the open line region of the magnetosphere near the magnetic poles^[83] or it may be a combination of those.^[218] The magnetic fields also generate a non-thermal component^[35,170] following power-law spectra. If the stellar endpoint is surrounded by a nebula – probably the supernova remnant – the magnetic field of the neutron star can cause synchrotron radiation^[177] by accelerating charged particles.

1.1.1 Spectropolarimetry

The emission from neutron stars can be allocated via its temporal intensity or the distribution over the electromagnetic spectrum. Nevertheless, radiation from unresolved objects will superimpose and may be hardly separated. Another approach to investigate the origin of radiation is the determination and characterisation of a potential polarity of the emitted electromagnetic waves.^[190] Polarimeters were already used to separate the emission from the synchrotron nebular around the crab pulsar and from the neutron star itself using the angular dependence of the Bragg reflection to polarity.^[211] This dependency of the intensity's angular distribution is also used in polarimeters basing on Thomson-scattering.^[143] A concept using DEPFETs with two or more storage regions implemented into the pixels could be used to store separately detected radiation of different polarization. Such a detector is proposed for the European Solar Telescope – a four metre telescope planned to observe the Sun.^[121] Although it is not an X-ray project, one of its instruments could be a polarimeter composed of DEPFETs with four storages in each pixel which are synchronised with a polarising filter, operating at a frequency of the order of 10 kHz. It is much faster than the readout frequency to measure the different fractions of polarisation states independent of temporal intensity variations in the total flux which are caused by external influences like atmospheric turbulences.^[24] Even if the optics of the telescope features a better spatial resolution than the sensor can deliver, the

advantages of multiple internal storages and therefore the switching speed are an argument for using DEPFETs.

1.1.2 Quasi-Periodic Oscillations

At sufficient large distances, accreted material orbits around its central object following the third Keplerian law. ^[100,194]

$$\omega_K = \left(\frac{GM}{r^3} \right)^{1/2} \quad (1.3)$$

The Keplerian angular velocity ω_K depends on the mass M and the distance r to the barycentre of the central object. At the inner boundary of the accretion disk, the rotational period needs to be adjusted to the conditions of the direct vicinity of an accreting white dwarf, neutron star or black hole. In the transition region, kinks and shocks can establish that lead to an anisotropic emission from the accreted material. ^[194] Due to the rotation of the system, they show up as periodic oscillations in the spectrum. Low-frequency QPOs^[o] may also originate from accretion disks in a distorted spacetime twisted up by the spinning central object, ^[87] the so-called Lense–Thirring precession. ^[107] Since the matter is heated up in the gravitational potential to effective temperatures of up to 10^7 K, ^[102] it emits a large fraction of X-ray radiation. A high time resolution in the microsecond regime is a requirement to study such features in the continuous and characteristic X-ray radiation. In Sco X-1, a neutron star in a binary system with a $0.42 M_\odot$ star ^[184] in the constellation Scorpius and the brightest X-ray source on Earth's night sky, QPOs with about 0.8 kHz and 1.1 kHz were found. ^[206] Their investigation required a high time resolution of $16 \mu\text{s}$ using the Rossi X-ray Timing Explorer. ^[29] The high frequency QPOs are expected to originate from the inner edge of the Keplerian orbiting disk while slightly lower QPOs may be overtones of the spin frequency of the neutron star. ^[131] The first investigation of QPOs at a millisecond pulsar with known spin frequency revealed, that all oscillations related to the rotational period of the neutron star are the exact spin frequency and not multiples of it. ^[213] In any case, multiple QPOs appearing in one system seem to be tightly correlated to each other. ^[162] Due to comparable sizes of neutron stars, the high-frequency Keplerian QPOs of pulsars can all be expected to be around 1 kHz. For black hole candidates, high frequency QPOs may be a promising option to study their properties like mass and radius. ^[165]

1.1.3 X-Ray Reverberation

Another option to study the direct environment of neutron stars and black holes is X-ray reverberation. Like for QPOs, accretion is needed. While emission from accretion disks

^[o]Quasi-Periodic Oscillations

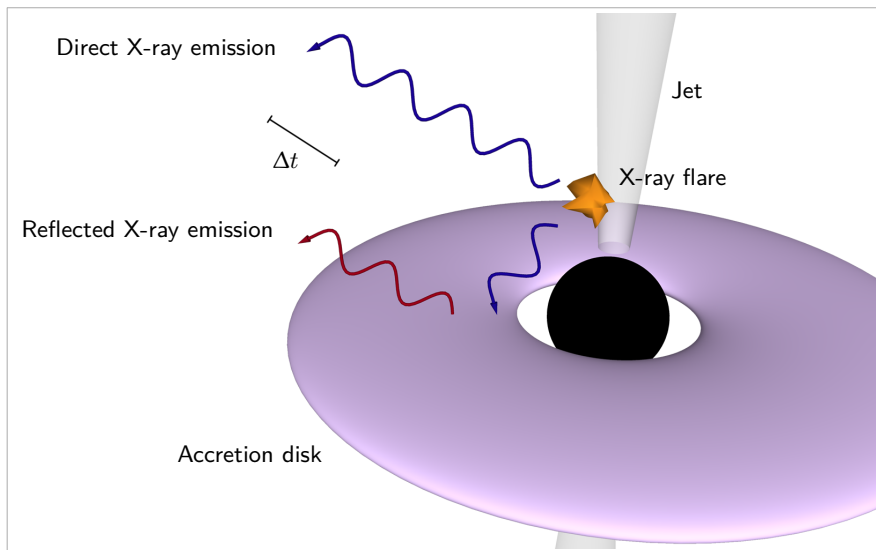


Figure 1.3: Emission from X-ray flares in the corona of a black hole can also be reflected at an accretion disk that may have established around the central compact object. The reflected radiation – shifted in energy and arrival time – provides information on the corona, its temporal evolution and the environmental conditions of the strong gravitational field. ^[204]

around active galactic nuclei peaks in the UV^[p], stellar black holes are featuring emission in their vicinity with energies of a few kiloelectronvolts, the X-ray regime. ^[130] The photons are provided with their high energies via inverse Compton scattering caused by charged particles as part of the corona that are accelerated by strong magnetic fields. ^[188] Such coronae may extend over large areas around a central object or establish a jet. ^[214] Line emission in the surrounding of a central object is broadened by the Doppler^[48] and relativistic effects. Flares in the corona can be reflected by surrounding matter like an accretion disk. The resulting slight differences in the travel distance from the emitter to the observer of direct and reflected radiation (see Fig. 1.3) can be detected as small differences of intensity variations in the arrival times. ^[204] As the reflected light has a longer travelling path through the virulent environment of strong gravity it is influenced differently. By observing both components – the direct emission and the reflection from the accretion disk – the temporal evolution of the corona and strong gravity can be studied. ^[204] As regards black holes, the investigation of their environment is the only possibility to determine their parameters like spin or mass.

1.1.4 Pulse Profiles

Besides the processes in the direct vicinity of black holes and neutron stars, also the emission from a pulsar's surface can be used to study effects caused by strong gravity. The heated polar caps which are penetrated by particles accelerated within the neutron star's magnetic field towards the magnetic poles and the contiguous magnetosphere cause a periodic signal as

^[p]UltraViolet

long as the magnetic axis is not in line with the rotational axis. Since both poles are located on opposite sides of the sphere, they cannot be seen at the same time using a classical approach and neglecting the finite size of the polar regions. While the expanse has to be considered anyway, an additional overlap is being caused by relativistic effects. Gravitational light bending causes radiation emitted at the back side of an object to be visible by the observer. The more compact a neutron star is, the stronger is the light bending. For stellar compactnesses of $m/r > 0.192 M_{\odot}/\text{km}^{[q]}$, radiation from the whole spheric surface will be emitted towards any observer.^[183] Light bending will flatten the light curve of the periodically varying intensity. Therefore, a high time resolution measurement of the emission can be used to study the geometry and general relativity.

Spacecraft Navigation

The known periodic signals from pulsars can also be used to navigate autonomously in space. Contemporary missions in the solar system use small optical telescopes to derive their position relative to solar system bodies and base on radio measurements taken with ground-based telescopes. Once a spacecraft has left the direct vicinity of the Earth, the latter component requires hours of signal transmission in the interplanetary space and worsens with distance to Earth. For future interstellar missions, this concept will fail due to such long signal travel times and its increasing inaccuracy as well as the lack of nearby astronomical bodies. By observing the time resolved emission of pulsars with known signal arrival times in a defined reference system, the position of the spacecraft can be determined on shells around the neutron star measuring the current phase of the pulsed signal arriving at the spacecraft against a reference clock.^[16] Combining at least three pulsars, the possible positions reduce from shells around a pulsar over circles in space to one point with an estimated accuracy of about 5 km.^[16] The accuracy of the determination is a trade-off between the quality of optics, sensor, mass and power consumption as well as observation time and quality of the previously taken light curves.^[18]

One option for the sensor is a DEPFET active pixel array.^[16] Pulsars as point-like sources do not extend over large areas of a spatial resolving sensor. Since their positions are known, the capability of an APS^[r] which can be read out in arbitrary windows that only cover the parts of the sensor that are of interest^[105] enables an option to save power in the signal processing chain with the appropriate electronics. The advantage of a full parallel readout can be used to improve the time resolution of the sensor to about 1 μs for a higher oversampling of the light curves. The faster the readout is, the more a sensor with an internal storage limits the contribution of the detector to the S/N ^[s] compared to one without a storage. However, a

^[q] $0.192 M_{\odot}/\text{km} = 0.284$ for the mass given in units of GM_{\odot}/c^2

^[r]Active Pixel Sensor

^[s]Signal-to-Noise

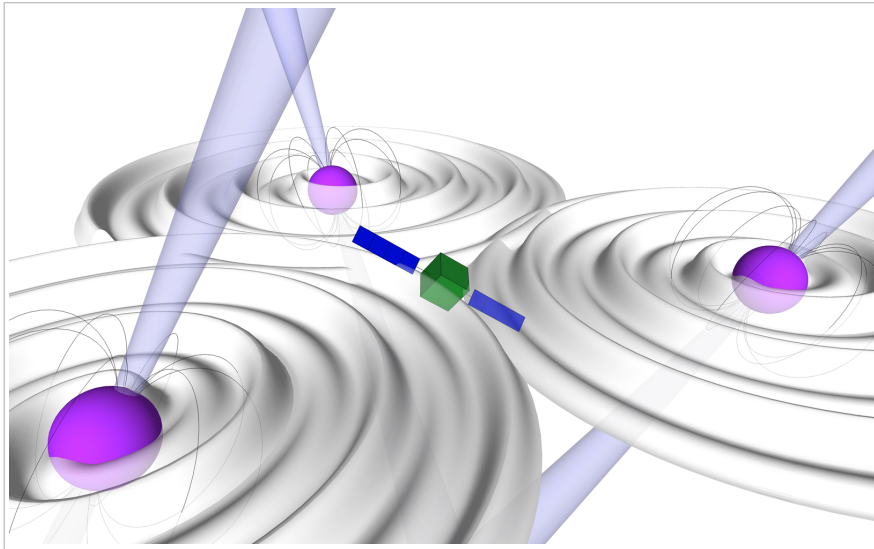


Figure 1.4: The periodic intensity variations in the X-ray emission of pulsars can be used to autonomously navigate in space. The arrival times of the pulses are measured against a reference clock. The differences to the predicted arrival times at a position in space result in a correction of the spacecraft's determined position along the line of sight towards a pulsar.^[18] In an iterative process using multiple pulsars, the location of a spacecraft can be determined down to an accuracy of 5 km.^[16]

high time resolution and therefore readout is needed to accurately determine the temporal position of the neutron stars' X-ray pulse shift, ensured by a sufficiently high oversampling. Isolated millisecond pulsars are the most suitable candidates for an autonomous spacecraft navigation due to their extreme rotational stability of the order of atomic clocks.^[16] The fastest yet known pulsar spins with a frequency of 716 Hz (found in the radio band) and even faster neutron stars may exist,^[84] probably limited to rotational periods of 0.6 ms.^[116] The error in the existing pulse profile data of $> 10^{-3}$ ^[19] results in an accuracy of the available data of about 10^{-6} s. Therefore, a detector with frame rates of the order of some hundred kHz to about one MHz like the sensor concepts analysed and further developed in my research would be desirable.

First navigation tests in space based on pulsars have already been performed by the NICER^[t] mission on board the International Space Station using SDDs^[u]. It resulted in a navigation error below 10 km as soon as the position converged.^[133] The verification of the suitability is also one of the goals for the CubeSat concept CubeX. It is designed as passenger of a primary mission to the Moon.^[187] Its two objectives, X-ray fluorescence of the Moon's surface and X-ray pulsar navigation are covered by two different sensors in one focal plane, again by an SDD for the high time resolution purpose. The spectral, angular and temporal resolution of a DEPFET array with pixel-wise integrated storages in a full parallel readout covers the required performance within one sensor. The feasibility of such sensors will be studied and analysed in my research.

^[t]Neutron star Interior Composition Explorer

^[u]Silicon Drift Detectors

Silicon Detectors

Silicon detectors are used in a wide range of applications for the detection of ionising particles like electromagnetic radiation from near infrared to gamma ray. Although not as pure element, silicon is the second most abundant one in the crust of planet Earth,^[217] well known in semiconductor applications for decades and thereby processible with high purity on industrial scale. In addition, with silicon dioxide there is a good dielectric material available. This chapter gives a brief overview of the necessary physics and the basics of silicon detectors as well as different detector concepts and their characteristics.

The group around Rutherford^[172] discovered in scattering experiments that an atom is composed of an extremely small nucleus in the very centre that is charged and holds most of the atom's mass. Chadwick and Goldhaber^[33] completed the understanding of the atom's building blocks by the discovery of the neutron. Together with the positively charged protons, it builds the nucleus. The number of protons, the atomic number Z , defines the kind of an element. The nucleus of a neutral atom is surrounded by the same number of electrons which have a negative charge and are therefore bound to the nucleus via the Coulomb force.^[42] A first simple atomic model, limited by the measurement accuracy, was introduced by Bohr.^[25] He defined orbits, each consisting of electrons of the same energy. A further developed atomic model assumed shells of electrons. Their location on a shell is described by a probability distribution. These electron shells are numbered alphabetically starting with K for the inner one.

2.1 Monocrystalline Silicon

Silicon has an atomic number Z of 14. The two innermost electron shells are fully populated with two and eight electrons, respectively. The outer third shell of a neutral atom in its ground state consists of the remaining four electrons. The most abundant isotope is ^{28}Si (14 protons plus 14 neutrons) which is produced in the oxygen burning of the stellar nucleosynthesis.^[36]

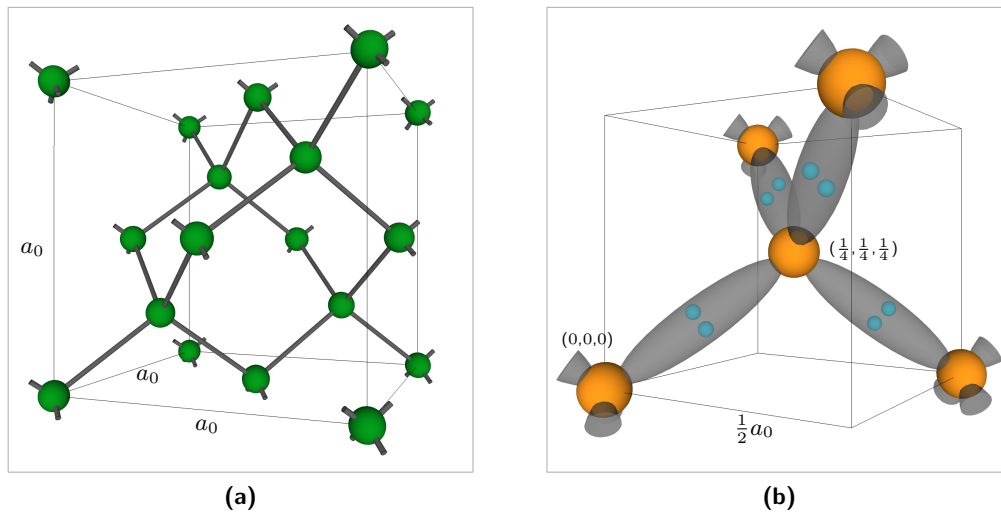


Figure 2.1: (a) Unit cell of the diamond crystal structure to which silicon crystallises (acc. to Shockley (1950, p. 6)^[178]). It consists of eight atoms (green) with four nearest neighbours each. The edge length of the silicon unit cell is $a_0 = 0.5431$ nm at 295.65 K (22.5 °C).^[13] (b) One tetrahedral bonding of which the diamond structure is built. Its edge length is $0.5a_0$. The yellow spheres represent the silicon atoms up to its 2p orbital (see Fig. 2.2b). The four valence electrons of the M shell form the covalent bonds with their neighbouring atoms which are not necessarily the four nearest ones as illustrated here.

Like other tetravalent atoms, elements with four electrons in their outer shell, silicon forms a diamond crystal lattice as shown in Fig. 2.1. The electrons of the outer shell form pairs with the ones of four neighbouring atoms – the so-called covalent bonds. The unit cell of a diamond lattice, the smallest unit that builds the crystal lattice by translations in the three spatial directions by integral multiples of its dimensions, is composed of eight atoms.^[101] Since atoms at the vertexes and faces of the cubic cell are shared with the neighbouring ones, they are counted only partly. The primitive basis has an edge length of 0.5 of the one of the unit cell and consists of two atoms at $0,0,0$ and $\frac{1}{4}, \frac{1}{4}, \frac{1}{4}$ (see Fig. 2.1b). It describes the orientation of the atoms to each other, but does not fulfil the definition of a unit cell.

The dimensions of a unit cell are called lattice constants. In case of the cubic diamond unit cell, there is only one, a_0 , that fully defines the size. It is very precisely measured to $a_0 = 0.5431$ nm at 295.65 K (22.5 °C)^[13] since the usage of ^{28}Si is considered for a redefinition of the SI^[a] unit for the mass.^[40]

2.1.1 Energy Levels and Bands

The atomic model of electron shells already described the location of the electrons via a probability distribution in contrast to the defined orbits introduced by Bohr.^[25] Born^[26] suggested

^[a]Système International d'unités (International System of Units)

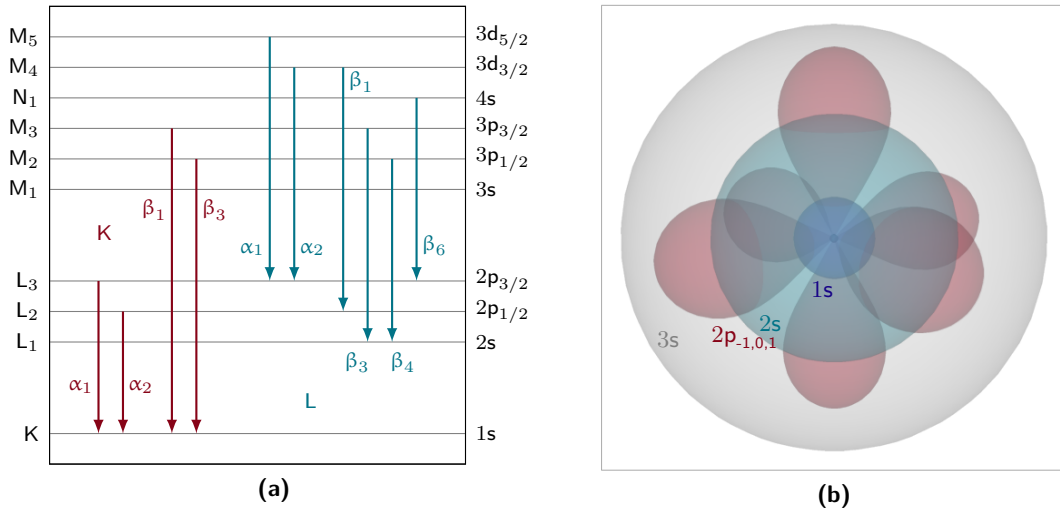


Figure 2.2: (a) Nomenclature for the characteristic radiation. The X-ray notation of the fine structure of the energy levels is noted on the left y-axis. The atomic one on the right is composed of the quantum numbers n , l and j . Spectral lines caused by transitions between the energy levels were named by Siegbahn (1931, p. 309)^[180] which later appeared not to be consistent.^[92] The shown set of transitions is not complete, but limited by the selection rules. (b) Simplified shapes of the atomic orbitals up to $nl = 3s$. They represent the most probable domain where an electron can be measured.^[26]

the square of the absolute value of the quantum mechanical wave function to describe the electrons as probability of presence. The resulting probability distributions are called atomic orbitals (see Fig. 2.2b). The wave function Ψ_{nlm_l} is defined by the quantum numbers n , l , and m_l . The principal quantum number $n \in \mathbb{N}^+$ represents the electron shell which is also associated with $\{K, L, M, \dots\}$. The azimuthal quantum number $l \in \mathbb{N}$ characterises the form of the atomic orbital (see Fig. 2.2b) and describes the sub-shells. Often the azimuthal quantum numbers are written as their historic representations $\{s, p, d, f, g, \dots\}$. Within a magnetic field, the magnetic quantum number $m_l \in \mathbb{Z} = [-l, l]$ becomes important.^[220] The magnetic spin quantum number $m_s = \{-s, -s + 1, \dots, s\}$ is composed of the spin quantum number s which is $\frac{1}{2}$ for electrons. l and s define the total angular momentum quantum number j as

$$j = |l \pm s|. \quad (2.1)$$

A set of quantum numbers fully describes the state of an electron.^[54] As they are fermions, particles that obey the Pauli exclusion principle,^[154] every state can be occupied by only one particle which results in different energy levels for each electron.

Energy that is released if an electron of an excited atom – an atom with vacancies below the most energetic electron – transitions to an energetically lower state, is emitted as electromagnetic radiation. This characteristic X-ray radiation was observed by Barkla^[9] at first and designated with a nomenclature by Siegbahn.^[180] Its first character describes the inner shell the electron transitions to which is indicated by its alphabetic representation starting

· $\mathbb{N} = \{0, 1, 2, \dots\}$, $\mathbb{N}^+ = \{1, 2, 3, \dots\}$

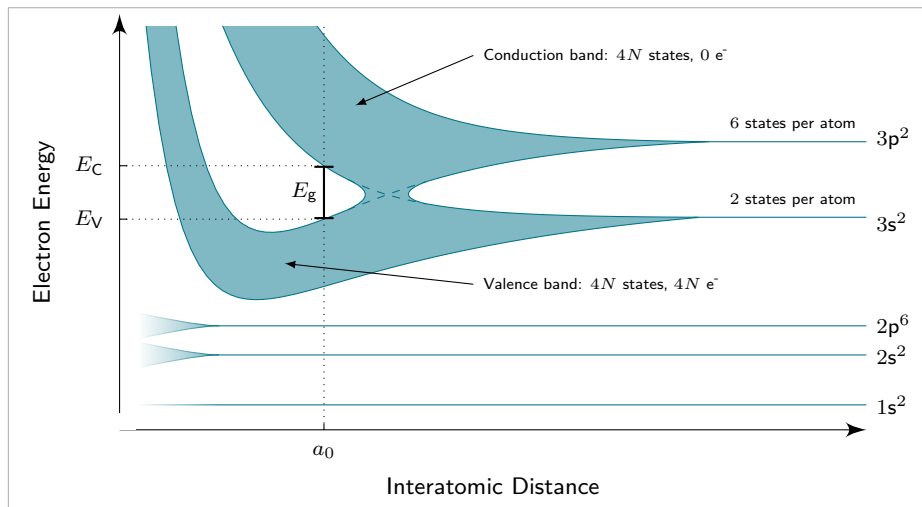


Figure 2.3: Sketch of the electron energy levels of N silicon atoms in dependence of the lattice spacing (acc. to Shockley (1950, p. 133)^[178]). The exponents of the atomic notation on the right show the occupation number for free atoms in their ground state. a_0 is the actual lattice spacing of a silicon crystal (see Fig. 2.1). The highest possible energy state in the valence band is E_V , the lowest in the conduction band E_C . The gap between these two bands is indicated by E_g .

with K and corresponds to the principal quantum number of the final state. The second one, a Greek letter, is not assigned consistently due to overlapping energy bands and incomplete observations of the relative intensity of the lines.^[92] For the innermost shells, it is the number of shells between the initial and the final one, starting with α for one shell. The indices correspond to different sub-shells, also not consistent as shown with a few examples in Fig. 2.2a. Nevertheless, the Siegbahn notation is very common in X-ray spectroscopy and also used in the present study.

Table 2.1: Energies of characteristic X-ray lines that occur in most of the spectra.^[192] In the last column, the sum of unresolved pairs of lines is given. According to Moseley's Law, the energy scales with the atomic number Z squared.^[137]

Element	Line	Energy	
Al	K- α_2	1486.3 eV	1486.6 eV
	K- α_1	1486.7 eV	
Si	K- α_2	1739.4 eV	1739.8 eV
	K- α_1	1740.0 eV	
Mn	K- α_2	5887.6 eV	5895.1 eV
	K- α_1	5898.8 eV	
	K- $\beta_{1,3}$	6490.4 eV	
Fe	K- α_2	6390.8 eV	6399.5 eV
	K- α_1	6403.8 eV	
	K- $\beta_{1,3}$	7058.0 eV	

With the number of electrons as exponent, the sub-shells nl of an isolated neutral silicon atom in its ground state are occupied as follows: $1s^2$, $2s^2$, $2p^6$, $3s^2$, $3p^2$. If the distance between

atoms is decreased, the energy level starts to split due to the Pauli exclusion principle.^[154] For the large number of atoms in a crystal, the resulting amount of energy levels form a range of allowed electron energies, a so-called energy band. The energy levels and bands are sketched in Fig. 2.3 depending on the interatomic distance. For the actual lattice spacing a_0 of silicon, the orbitals of the M shell overlap and form the valence and the conduction band. The indirect band gap for silicon at room temperature (300 K) is $E_g = 1.124 \text{ eV}$ ^[139] which needs an additional momentum transfer between lattice vibrations and the electron in contrast to a transition over a direct band gap. At absolute zero, every state in the valence band is occupied by an electron while the conduction band is empty. With increasing temperature, electrons are transferred to the conduction band by thermal excitation and a semiconductor like silicon becomes more and more conductive. For insulators, the band gap E_g is too large to be surmountable by thermal excitation at a given temperature. If the valence and the conduction band overlap, the system is a conductor with particles always available for charge transport. Such particles are electrons or so-called holes. A hole is a quasi particle that mathematically describes the absence of an electron as a positive charged particle at this place.

Based on the work of Fermi^[58] and Dirac,^[45] the Fermi energy is defined as the energy of the highest occupied state of a system in its ground state which is the upper edge of the valence band E_V for a semiconductor. For N charged particles of the mass m in the volume V , the Fermi energy is defined by^[101]

$$E = \frac{\hbar^2}{2m} \left(\frac{3\pi^2 N}{V} \right)^{2/3}. \quad (2.2)$$

If energy is added to the system, the probability that a state is occupied by an electron is described by the Fermi-Dirac distribution as function of the absolute temperature T .^[101]

$$f(E) = \frac{1}{\exp[(E - \mu_c)/k_B T] + 1} \quad (2.3)$$

An energy level E that is identical to the chemical potential μ_c is termed Fermi level $E_F = \mu_c$. Since the denominator simplifies to $e^0 + 1 = 2$, it describes the energy where half of the states are populated.

$$f(E_F) = \frac{1}{2} \quad (2.4)$$

For semiconductors, the Fermi level is the centre of the band gap. The Fermi-Dirac distribution changes with temperature and the probability of electrons in the conduction band and thereby the number of holes in the valence band changes.

· $\hbar = h/(2\pi)$, reduced Planck constant

· $h = 6.626\,070 \cdot 10^{-34} \text{ J s}$, Planck constant^[81,156]

· $k_B = 1.380\,648 \cdot 10^{-23} \text{ J K}^{-1}$, Boltzmann constant^[69,156]

2.2 Charge Generation

Electromagnetic radiation can be detected by its interaction with charged matter via the electromagnetic force. The final measurement is done via the determination of the number of collected electrons. Besides the generation of free electrons via the photoelectric effect – an umbrella term for slightly different processes that occur in different places within isolated atoms and molecules or a solid – other interactions with a detector material like silicon contribute to the generation of free charge carriers, to their scattering, and to the uncertainty of their number.

2.2.1 Photoelectric Effect

Photoemission

Discovered already before, Einstein (1905)^[51] described the underlying mechanism of the observation that light with a certain energy and above leads to the emission of electrons from metallic surfaces after they are illuminated. The observed behaviour like an electron energy that only scales with the frequency of the light and not with the intensity cannot be explained with the wave propagation of electromagnetic radiation. Assuming that it could be composed of wave packages, the so-called photon which describes the particle nature of electromagnetic radiation, the observations can be qualified and quantified. This wave-particle duality denotes that every quantum – the smallest entity of a physical quantity^[51,156] – has wave and particle properties. The energy E of a photon with the frequency $\nu = c/\lambda$ is

$$E = h \cdot \nu. \quad (2.5)$$

The factor h in the equation was confirmed as the Planck constant later.^[132] Since the electrons of any material, that are supplied with energy by photon interactions which is sufficient to escape the solid, are emitted into the surrounding, it is termed photoemission.

Photoionisation

If a photon has sufficient energy, an electron can be separated from an atom. The resulting charged atom – with a number of electrons differing from the atomic number Z – is termed ion.^[57] Since the binding energies depend on the composition of an atom, there is not only one specific minimum energy valid for all elements.^[136] While the lowest energy for the ionisation of an atom is 3.89 eV for caesium,^[136] photons with an energy of at least 8.15 eV that is transferred to an electron via photoabsorption are necessary in silicon.^[119]

The energies for the ionisation of an isolated atom are higher than the work function which describes the energy that is necessary to remove an electron from the surface of a solid and that is defined by its surface characteristics.

Photoconductivity

The detection of low energetic radiation of a few electron volts in semiconductors is based on the elevation of electrons from the valence to the conduction band. Due to the indirect band gap of $E_g = 1.124 \text{ eV}$ in silicon,^[139] NIR photons with a maximum wavelength of $\lambda = 1.1 \mu\text{m}$ can be detected. The probability of an electron transition and thereby the absorption coefficient α for radiation increases with photon energy^[39] up to and slightly beyond the direct band gap of 3.43 eV ^[80,153] which corresponds to UVA radiation with a wavelength of $\lambda = 361 \text{ nm}$. With an increasing number of electrons in the conduction band, the semiconductor becomes more and more conductive since more charge carriers are available for charge transport.

Photons with higher energies E_{ph} like X-rays generate free charge carriers mainly from inner electron shells, since the cross section – the area in which the photon and an electron interact – is larger for those electrons.^[94] In addition, excess energy is transformed into kinetic energy E_{kin} of the released electron with a binding energy E_{bind} .

$$E_{\text{kin}} = E_{\text{ph}} - E_{\text{bind}} \quad (2.6)$$

Recent discoveries showed that the emission of a photoelectron does not occur instantly, but is delayed in the intra-atomic space depending on its initial angular momentum^[181] and influenced by multi-electron interactions.^[175]

2.2.2 Relaxation

After the ionisation of an atom by the emission of an inner shell electron, the vacancy will be occupied by a more energetic electron which most likely happens over a cascade. The excess energy of such spontaneous processes is emitted as photons.^[53] With quantum mechanical perturbation theory,^[46] it is possible to calculate the lifetime of this exponential radiative decay. In agreement with measurements^[145] it results in times of the order micro- to nanoseconds for outer levels^[61] and down to sub-femtoseconds for inner-shell vacancies.^[49] The emitted photons can be absorbed again by another electron of the same atom (see Fig. 2.4a) which than is emitted. The generated secondary β -radiation is composed of so-called Auger electrons which were described by Meitner (1922)^[128] for the first time. Thereby, the emission of the photoelectron results in the generation of further (fluorescence) photons

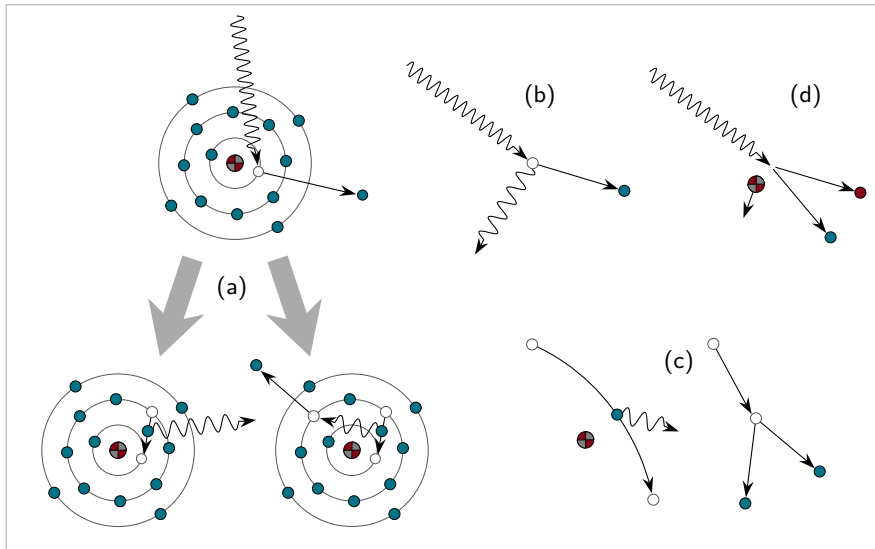


Figure 2.4: Different particle interactions with energy transfer between particles. **(a)** Ionisation of a Si atom by an incident photon. The K, L and M electron shells are indicated. The photon is absorbed completely. The following relaxation process shows two different cases. The emission of an X-ray photon (characteristic radiation) and the creation of an Auger electron. **(b)** Compton scattering of a photon by an electron. **(c)** Coulomb interaction of an electron with an atomic nucleus or another electron. **(d)** Production of an electron-positron pair by a very high energetic photon with momentum transfer to charged particles like an atomic nucleus.

and free electrons already within the atom of the first interaction.

2.2.3 Further Photon Interactions

Besides the way via the dominant photoelectric effect, other interactions of the initial or a secondary photon are possible (cf. Figs. 2.4 and 2.5). For particles that are much smaller than the wavelength of the incident radiation, the photons can be scattered without energy transfer. This so-called Rayleigh scattering only leads to a change in the direction of propagation^[186] and is thereby not important for the generation of free charge carriers.

Of more importance is the incoherent scattering process of an X-ray photon with an electron described by Compton (1923).^[37] Energy is transferred to an electron which leads to the excitation or ionisation of an atom. The transferred energy and thereby the change of the photon's wavelength depends on the scattering angle θ only which means it is independent from the energy of the incident photon.

$$\Delta\lambda = \frac{h}{m_e c} (1 - \cos\theta) \quad (2.7)$$

$h/m_e c$ is the Compton wavelength of an electron with its mass m_e . The interaction is

^[186] $m_e = 9.109\,384 \cdot 10^{-31}$ kg, mass of an electron^[219]

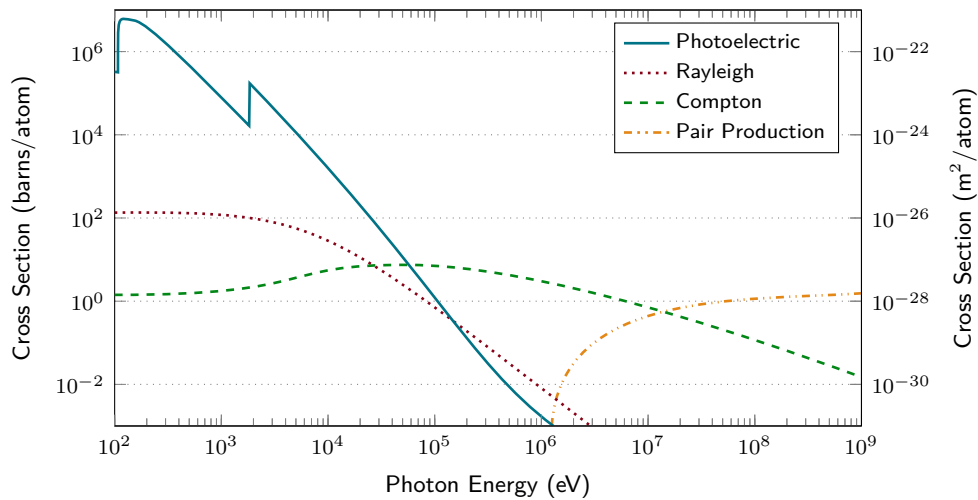


Figure 2.5: Photon-electron cross sections in silicon depending on the photon energy taken from Berghmans et al. (2008).^[17] For the energies of interest in the present work of a few kiloelectronvolts, the photoelectric effect is the dominant interaction.

illustrated in Fig. 2.4b.

Extremely energetic photons can produce pairs of electrons and positrons^[3] in the vicinity of atomic nuclei to which momentum is transferred to. Such positrons, particles with the mass of an electron, but with a positive charge, were predicted already in 1928.^[47] In a cloud chamber, they were observed as paths four years later.^[2] Since the process is based on photons with energies in the megaelectronvolt regime (cf. Fig. 2.5), it does not play a role for X-ray interactions.

2.2.4 Electron Interactions

Free electrons can lose their energy via the Coulomb interaction with other electrons or atomic nuclei as shown in Fig. 2.4c. The energy loss per length depends on the kinetic energy of the electron^[21] that leads to an energy deposition mainly at the end of the electrons' path. The dominant process is the interaction with shell electrons. Parts of the energy of the incident electron are transferred to a shell electron that leads to an excited or ionised atom.

If an electron is decelerated in the Coulomb potential of an atomic nucleus or a shell electron,^[191] it loses energy emitted as bremsstrahlung. If the energy of the emitted photons is big enough, they can contribute to further charge carrier generation in the silicon crystal.

2.2.5 Charge Loss

Charge generated by an incident X-ray photon and subsequent processes near the edge of the sensor can be lost already before it is collected for readout. A fluorescence photon like the one from the Si K- α transition can leave the sensitive area (cf. section 2.4) and is therefore missing in the measured amount of energy. The fast photoelectrons may take the same path before they deposit all of their kinetic energy in the detector. In addition, a few electrons of a charge cloud generated near the sensor edge may be drained to the insensitive part. Furthermore, electron-hole pairs generated close to the surface where the electric field is weak, can recombine.

Photons that are backscattered by Compton scattering and which do not interact before they leave the sensitive area place only the energy that was transferred to the electron within the detector. All these processes lead to a degradation of the spectral performance of the detector. Their influence on the formation of different spectral features is illustrated in section 5.2.

2.2.6 Fano Noise

Although the photoelectric effect is the dominant one for the photon-electron interaction in the energy range of interest and the resulting photoelectron produces mainly electron-hole pairs via the interaction with shell electrons, the cascade of processes initiated by the incident X-ray photon does not result in an exactly reproducible number of charge carriers and energy is transferred from and to lattice vibrations.^[56,90] These quantised vibration modes can be described mathematically as particles, so-called quasiparticles, which are termed phonons. Their mean population density $\langle n \rangle$ is described by the Bose-Einstein statistics^[27]

$$\langle n \rangle (\omega) = \frac{1}{\exp[\hbar\omega/k_{\text{B}}T] - 1}. \quad (2.8)$$

An increasing number of phonons or larger angular frequencies ω lead to a macroscopically higher temperature T . The uncertainty of the number of generated charge carriers causes a broadening of the spectral features and limits the achievable spectral performance. This effect was observed and described at first for ionising radiation in a cloud chamber by Fano (1947).^[56] In silicon the mean electron-hole pair creation energy is $w = 3.71 \text{ eV/e}^-$ at 200 K.^[111] The material specific Fano factor F defines the relative FWHM^[b] of a particle energy E as^[91]

$$\frac{\text{FWHM}}{\mu} = 2\sqrt{2\ln 2}\sqrt{\frac{Fw}{E}} \approx 2.355\sqrt{\frac{Fw}{E}} \quad (2.9)$$

^[b]Full Width at Half Maximum

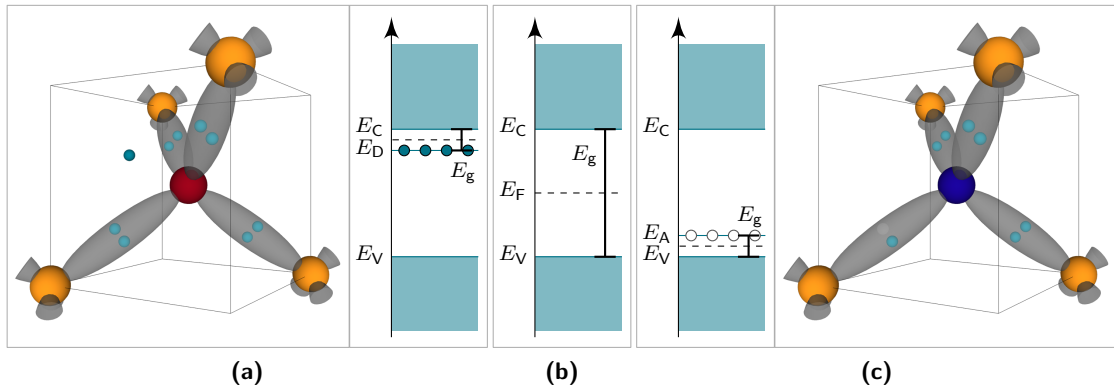


Figure 2.6: (a) n-doping: Part of the tetravalent silicon atoms are replaced by pentavalent elements like arsenic or phosphorus, so-called donor atoms with five electrons in their outer shell. In the crystal lattice, the fifth electron is almost unbound. (b) Energy bands and the band gap of an undoped semiconductor for comparison. (c) p-doping: Trivalent elements like boron or aluminium lead to a vacancy in the covalent bonds. The missing electron is called hole and can be treated like a positively charged particle.^[101]

with $\mu = E$. The Fano factor for silicon is determined as 0.118 ± 0.004 and is constant over a wide temperature range from 110 K to 240 K.^[111]

There are photon detectors that are not limited by the Fano noise. They are operated at extremely low temperatures where the detector material becomes superconductive. It is the state of the absence of an electrical resistance that appears abrupt below a material specific temperature – ~ 0.35 K for highly boron doped silicon.^[32] They base either on a measurement of the change in the kinetic inductance^[41] or of the conductivity around the critical temperature that separates superconductivity and conduction.^[4] The latter so-called transition-edge sensors are also used for the X-IFU, the second instrument on board of Athena.^[10]

2.3 Doping

Pure silicon is an intrinsic semiconductor. By replacing silicon atoms with elements that have more – or less – electrons in their outer shell (valence electrons) than the four needed for the covalent bonds in the diamond crystal lattice of silicon, additional possible energy states are added within the band gap and it is called extrinsic semiconductor. Arsenic and phosphorus with five valence electrons each are so-called donor atoms. The fifth electron is almost unbound and only $E_g = E_C - E_D = 0.049$ eV and 0.044 eV are needed to lift those electrons to the conduction band for an arsenic and phosphorus doping, respectively, compared to the 1.124 eV for the band gap of the intrinsic semiconductor.^[139] The band gap E_g is reduced to only 4% of the indirect one of silicon. A semiconductor with donor

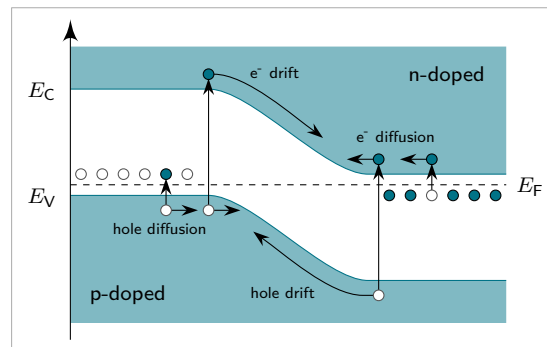


Figure 2.7: The energy band diagram of the transition area between a p-doped and an n-doped region – the p-n junction (acc. to Sze and Ng (2006, p. 80)^[189]) – without an external voltage. The majority carriers recombine at the boundary layer and the neutral crystal becomes charged due to the ionised dopants. The resulting electric field counteracts the diffusion and leads to a depletion zone where there are almost no majority carriers.

atoms as impurities is termed n-doped referring to the negatively charged additional electron. Due to the filled state within the band gap and thereby a shifted Fermi level (see Fig. 2.6a) electrons lifted to the conduction band are the main contributors to the current transport and are called majority carriers. Consequently, holes are the minority carriers. Their assignments are switched in p-doped semiconductors. Atoms with three valence electrons lead to holes in the covalent bonds which are acceptors for electrons (Fig. 2.6c) represented as empty states within the band gap ($E_g = E_A - E_V = 0.045 \text{ eV}$ for boron^[139]). Electrons that leap to that states leave behind holes in the valence band which can contribute to a hole current.

A minus or a plus sign in the exponent indicates a lower or higher dopant concentration like n^+ for a highly doped n-type semiconductor.

2.4 Charge Collection

To enable reasonable lifetimes of free charge carriers in a semiconductor, it is necessary to establish a sensitive area by separating the generated electrons and vacancies spatially via an electric field to avoid recombination. An intrinsic approach is the p-n junction. At this boundary between a p-doped and an n-doped (see section 2.3) region, the majority carriers diffuse to the opposite side due to the density gradient in each majority carrier concentration perpendicular to the boundary layer. The electrons and holes recombine and establish a region almost free of majority carriers around the p-n junction, the depletion zone.^[189]

The minority carriers left behind form an electric field as the majority carriers recombine. The drift in the electric field counteracts the diffusion of the free charges. An equilibrium between drift and diffusion ensues and – besides the thermal generation of charge carriers – the recombination of electrons and holes ceases. The one-dimensional current density J of

electrons or holes perpendicular to the boundary layer becomes 0^[189]

$$J_{e/h} = 0 = q\mu_{e/h} \left(n_{e/h} \mathcal{E} + \frac{k_B T}{q} \frac{dn_{e/h}}{dx} \right) = \mu_{e/h} n_{e/h} \frac{dE_{F,e/h}}{dx} \quad (2.10)$$

with the mobility $\mu_{e/h}$ (cf. eq. (2.20)), the number of charge carriers $n_{e/h}$, the electric field \mathcal{E} and the elementary charge q .

$$J = 0 \propto \frac{dE_F}{dx} \quad (2.11)$$

is fulfilled only for a Fermi level E_F that is constant over the depletion zone. The valence and conduction band (cf. Fig. 2.6) bend as shown in Fig. 2.7.

Assuming an abrupt transition at the p-n junction, constant donor and acceptor concentrations N_D and N_A as well as that all impurity atoms are ionised, the surface charge density of positive and negative charges is given by^[189]

$$N_A W_{Dp} = N_D W_{Dn} \quad (2.12)$$

for a fully depleted zone with the size $W_D = W_{Dp} + W_{Dn}$. W_{Dp} and W_{Dn} are the sizes of the depletion zone on the p- and the n-doped side.

By integrating the one-dimensional Poisson equation of the electric field with the charge density $\rho = -qN$ and the electrostatic potential Φ

$$\frac{d^2\Phi}{dx^2} = -\frac{\rho}{\epsilon_s} \quad (2.13)$$

over x twice for each side of the junction from 0 to W_{Dp} or W_{Dn} with the permittivity of the semiconductor ϵ_s , the width of the depletion zone W_D can be expressed as^[189]

$$W_D = W_{Dp} + W_{Dn} = \sqrt{\frac{2\epsilon_s}{q} \frac{N_A + N_D}{N_A N_D} \Phi_{bi}} \quad (2.14)$$

with the use of eq. (2.12). For large differences between the impurity atom concentrations of both sides of the junction $N_1 \gg N_2$, it simplifies to

$$W_D = \sqrt{\frac{2\epsilon_s}{q N_2} \Phi_{bi}}. \quad (2.15)$$

The built-in potential difference in the p-n junction Φ_{bi} is given as^[189]

$$\Phi_{bi} = \Phi_p + |\Phi_n| \approx \frac{k_B T}{q} \ln \left(\frac{N_D N_A}{n_i^2} \right) \quad (2.16)$$

· $q = 1.602176 \cdot 10^{-19} \text{ C}$,^[135] elementary charge

· $\epsilon_s = \epsilon_r \epsilon_0$ permittivity of a semiconductor with the relative permittivity ϵ_r of the material

· $\epsilon_0 = 8.854188 \cdot 10^{-12} \text{ F m}^{-1}$,^[135] vacuum permittivity, electric constant

with the intrinsic charge carrier density n_i of the semiconductor which depends on the energy gap E_g and the temperature T . For typical values N_D and N_A for DEPFETs, the built-in widths of the depletion zone are given in Table 2.2 for a temperature of 300 K and 200 K.

Table 2.2: Widths of the depletion zone W_D for typical doping levels at different temperatures.

Temperature	N_D (cm ⁻³)	N_A (cm ⁻³)	n_i^2 (cm ⁻⁶)	ϵ_s	Φ_{bi} (V)	W_D (μm)
200 K	$1 \cdot 10^{12}$	$5 \cdot 10^{18}$	$3.8 \cdot 10^{19}$	11.54	0.82	32
300 K			$1.4 \cdot 10^{10}$	11.68	0.66	29

Charge carriers generated by incident radiation inside the depletion zone, the sensitive area, are separated by the electrostatic potential. Their drift through the depletion zone can be measured as a current between the p- and the n-side.

2.4.1 PIN Diode

The fraction of intensity \mathcal{I} that is not absorbed after the distance x is defined by the Lambert–Beer law

$$\frac{\mathcal{I}(x)}{\mathcal{I}_0} = e^{-x/\epsilon}. \quad (2.17)$$

The absorption length ϵ can be calculated from the photoelectric cross section σ_{ph} .

$$\epsilon = \frac{1}{N\sigma_{ph}} \quad (2.18)$$

With eight atoms per unit cell (cf. section 2.1), the atomic number density for silicon is $N_{Si} = 8/a_0^3 = 4.99 \cdot 10^{28} \text{ m}^{-3}$. Photons with energies of some keV are absorbed mainly within a few tens of micrometre (cf. σ_{ph} in Fig. 2.5). Therefore, the extension of the depletion zone is necessary to increase the probability of the photon detection to an adequate value. The potential barrier and the size of a depletion zone can be extended or reduced by the application of an external voltage U ^[113]

$$W_D \approx \sqrt{\frac{2\epsilon_s}{qN_D} (\Phi_{bi} - U)} \quad (2.19)$$

or by large differences in the impurity atom densities on both sides of the junction (cf. eq. (2.14) and eq. (2.15)). The maximum quantum efficiency is obtained by the extension of the depletion zone over the whole silicon device. To enable the operation of a detector with a reasonable external voltage, an almost undoped region is integrated between the p- and n-side of the p-n junction. One implementation of such a PIN diode^[c] is a slightly n-doped piece of silicon (the silicon bulk) and highly n- and p-doped implants on opposite sides. A

^[c]The I in PIN stands for the (almost) intrinsic semiconductor between the p- and the n-doped parts.

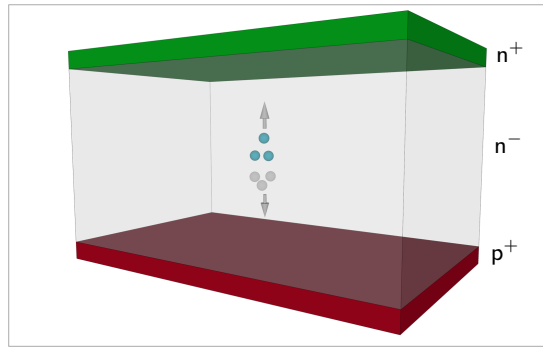


Figure 2.8: PIN diode composed of an n^+ and a p^+ implantation on the opposite sides of a slightly n-doped silicon bulk. The intrinsic layer (cf. section 2.3) between the the p- and the n-contact allows for larger depletion zones compared to the one that can be established at a p-n junction with similar impurity atom densities on both sides of the junction.

depletion zone establishes at the p^+-n^- junction and can be extended by an external voltage $U < 0$ (reverse voltage) applied at the p-side.

As an ancillary effect, the mobility of the charge carriers increases for lower impurity atom densities. The mobility $\mu_{e/h}$ for electrons or holes is a factor in the relation between an electric field \mathcal{E} and the drift velocity v_d .

$$v_d = \mu_{e/h} \mathcal{E} \quad (2.20)$$

The mobility is influenced by interactions with phonons whose number depends on the temperature (cf. eq. (2.8)), defects in the crystal lattice and ionised impurity atoms. A lower doping increases the mobility due to the reduction of Coulomb interactions and leads to higher drift velocities.

2.4.2 Silicon Drift Detector

The capacity of the n^+ contact scales with its size. A larger capacity leads to a higher noise contribution during readout (cf. section 3.3). Since a small readout node is desirable and the size of the n^+ implant in a PIN diode scales with its dimensions, these two quantities should be decoupled. One implementation is realised with the sideward depletion suggested by Gatti and Rehak (1984).^[72] Two PIN diodes are connected to each other at their n-sides. The extensive n^+ -implantations are replaced by a small one at the edge of the sensitive area. The principle is illustrated in Fig. 2.9. The depletion of the device is realised from both of its sides which further reduces the necessary voltages. Depending on the size of the sensor, the p^+ implantations have to be split to ensure an electric field perpendicular to the depletion field so that the electrons drift towards the anode at the side. These drift rings are supplied with an increasing negative voltage with distance to the n^+ contact and are necessary only

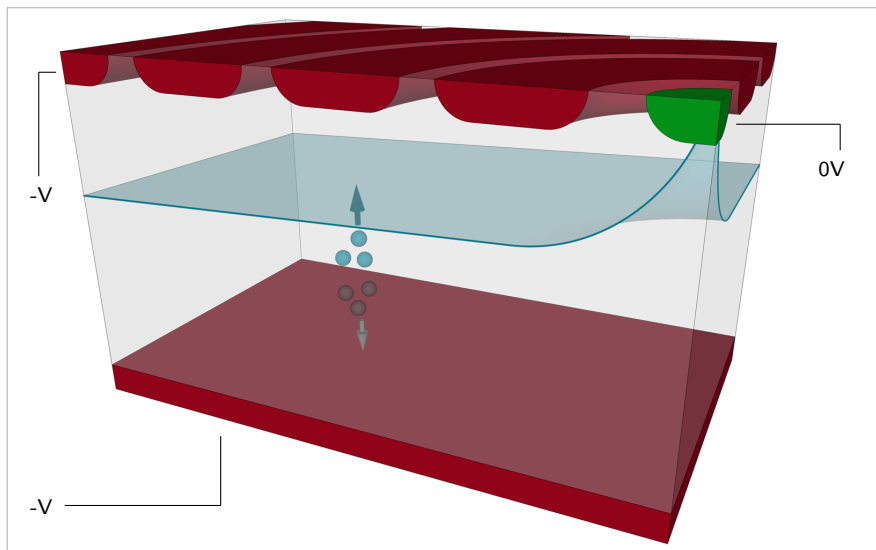


Figure 2.9: Sideways depleted silicon device as proposed by Gatti and Rehak (1984).^[72] Two PIN diodes are 'merged' at their n-sides. The n^+ implantation is moved to the surface. The depletion is realised from the front and the back side via the application of negative voltages at the front and the back while the n-contact (green) as potential minimum for the electrons is at about 0V. The turquoise surface represents the potential minimum in z-direction which can be shifted within the bulk via the applied front and back side voltages. To ensure a drift parallel to the surface, the p^+ implants are structured. With a voltage gradient becoming more and more positive towards the n^+ contact, all electrons drift to this anode.

on one side of the silicon bulk.^[99] These SDDs enable large sensors without the disadvantage of increasing readout node capacities.

2.4.3 Charge-Coupled Device

If a better spatial resolution is required, the front-side of the sensor can be structured into smaller pixels. A very common approach is the CCD invented by Boyle and Smith (1970).^[28] Each pixel consists typically of three electrodes. During the charge collection, one of them is biased in a way that a potential minimum in the pixel is formed. To transfer the collected charge of each pixel to the readout node that is located at the side of the sensor, a second electrode is set to the same voltage. The charges reallocate in the broader potential minimum formed by two neighbouring electrodes. The third electrode serves as a barrier between the pixels. The first electrode is now set to the voltage of the third one and all charge carriers move under the second electrode. By repeating this principle, the charge carriers are shifted from electrode to electrode within the pixels and over the pixel borders. To move the charge cloud from one to the adjacent pixel, six changes in the voltage configuration at the electrodes are necessary. There are CCDs with readout nodes at every pixel row^[185] or only a few for the whole sensor.^[86] For the latter, an additional shift of the charges at the border of the sensor perpendicular to the one inside the pixels is needed and the readout

time is increased significantly. CCDs are used in a wide range of radiation detectors from the infrared to the X-ray regime. For high photon energies, the electrodes can be implemented on a sideways depleted device to have sufficient sensitive volume. These CCDs are used on board of XMM-Newton^[185] as well as in the upcoming survey telescope eROSITA^[d]^[161] and are called pnCCDs.

2.4.4 Active Pixel Sensor

Due to the charge transfer through the sensor, CCDs suffer from disadvantages. The distance for the transfer scales with the pixel size which is, therefore, not indefinitely scalable. The malfunction of one pixel can influence a complete detector row if charge carriers are trapped or generated at defects in the crystal structure. In addition, bright sources contaminate all pixel in the column parallel to the readout direction since the pixels are not blinded during the charge transfer. Such detections are called out-of-time events. To get a sufficient two-dimensional spatial resolution, the exposure time has to be much longer than the charge transfer through the whole sensor. To speed up the latter, some CCDs feature a blinded frame storage region to decouple the readout speed from the charge transfer. Such effects were overcome with the invention of active pixel sensors in 1985.^[120] A readout node is implemented into each pixel. This also enables the implementation of further functionality into a pixel like a non-destructive readout. The amplification of the detection at this early stage improves the S/N and by using a built-in potential minimum, the pixel can be switched off completely during charge collection to save power compared to the electrodes of a CCD. APSs replaced CCDs in commercial applications like digital and cell phone cameras and feature pixel sizes down to $1 \times 1 \mu\text{m}^2$.^[108] An implementation of an APS for the usage in X-ray astronomy is the DEPFET which will be introduced in the next chapter. The significantly increased number of readout nodes with all its contacts that need to be attached to steering and readout lines, enforces a more complex wiring and electronics (see chapter 4). Depending on the readout mode, APSs cause different problems – compared to CCDs – as described in section 5.1. On top of that, a readout node inside the pixel also allows for the integration of functionality directly into the pixel. This opens up the possibility to address further issues that occur in applications which have to handle large intensity variations, a high throughput for bright sources, ultra low noise for small signals or an excellent time resolution.

^[d]extended ROentgen Survey with an Imaging Telescope Array

DEPFET Active Pixel Sensor

DEPFETs are one option to implement an active pixel sensor. The key idea is the amplification of the collected signal charges within the pixel and a readout that does not destruct the measured electrons. It allows for the implementation of further features like a shutter, a storage, or non-linear characteristics for a high dynamic range. The direct readout that does not need any charge transfer to the border of the sensor makes shorter frame times feasible compared to other imaging sensors.

The signal amplification and readout – the determination of the number of collected charges – is based on transistors. A transistor consists of three parts. The current between two of them – the source and the drain which act as source and sink for charge carriers – is controlled by the third one – the gate. Besides others, the MOSFET^[a] is one implementation of a transistor. Its functionality was demonstrated in 1960.^[95] A field-effect transistor (FET) is a transistor where only one type of charge carriers (electrons or holes) is involved. The gate of a MOSFET is composed of a metallic (M) contact insulated via an oxide (O) from the semiconductor (S) where the source and the drain regions are implemented. The name MOSFET is still in use although the conducting metal layer of the gate is usually replaced by poly-silicon. For a p-channel transistor, source and drain are implemented as p-doped regions in the slightly n-doped silicon wafer. At the edges of the implants, the p-n junction (section 2.4) establishes a depletion zone. A negative voltage at the gate contact repels the majority carriers (electrons) from the surface and forms a conductive channel between source and drain. The necessary minimum voltage between gate and source to establish an unintermittent channel is the threshold voltage U_{th} . In the formed channel the number of minority carriers is larger than the number of majority carriers. In semiconductors in general and in the transistor in particular, this state is called inversion (Fig. 3.1).

The relation between the change in the gate-source voltage U_{GS} and the deviation of the transistor current I_{DS} is called transconductance g_m .

$$g_m = \frac{\partial I_{DS}}{\partial U_{GS}} \quad (3.1)$$

^[a]Metal–Oxide–Semiconductor Field-Effect Transistor

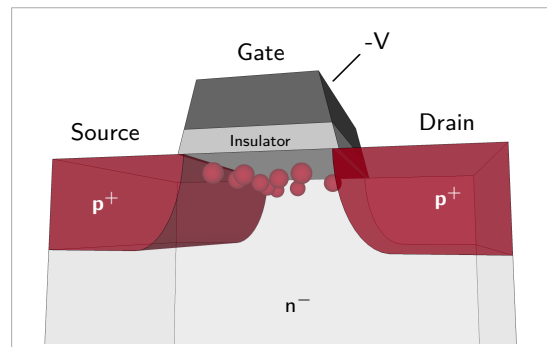


Figure 3.1: Transistor in inversion. The negative voltage at the gate contact repels the electrons of the donor atoms in the n-doped substrate under the oxide (insulator) and forms a conductive channel between source and drain that allows for a hole current between the two regions.

The transconductance can also be expressed with the potential difference between source and drain U_{DS} or the current between the two regions I_{DS} , the capacity per unit area of the gate oxide $C_{ox} = \epsilon_{ox}\epsilon_0/d_{ox}$ as well as the width W and the length L of the gate.^[113]

$$g_m = -\frac{W}{L}\mu_h C_{ox} U_{DS} = \sqrt{-2\frac{W}{L}\mu_h C_{ox} I_{DS}} \quad (3.2)$$

3.1 DEPFET

The DEPFET is a p-channel MOSFET (PMOS) integrated on an fully depleted silicon bulk invented by Kemmer and Lutz (1987).^[98] Compared to a simple MOSFET described above there are some further adaptations. A shallow p-implant under the gate with its dopant maximum a few tens of nanometre below the Si-SiO₂ interface shifts the threshold voltage U_{th} to more positive values and the conductive channel deeper into the device.^[200] It prevents charge carriers from interaction with defects at the Si-SiO₂ interface. Such buried channels that were two orders of magnitude deeper in the silicon bulk, have already been used for CCDs to improve the CTE^[b].^[209] To form the DEPFET, a shallow deep n-implant is realised below the complete transistor structure. In the source and the drain regions this implant is partially compensated by the p-implants. This leads to the formation of a positive potential minimum for electrons below the external gate of the transistor (see Fig. 3.2). The electrostatic field generated by the electrons collected in the local minimum needs to be compensated by positive charges – holes – in the environment. Such so-called mirror charges arrange primarily in the transistor channel. These holes contribute to the charge drift in the transistor and therefore its conductivity. Since the collected electrons influence the properties of the transistor channel in a similar way as the MOSFET gate, it is called internal gate while

^[b]Charge Transfer Efficiency

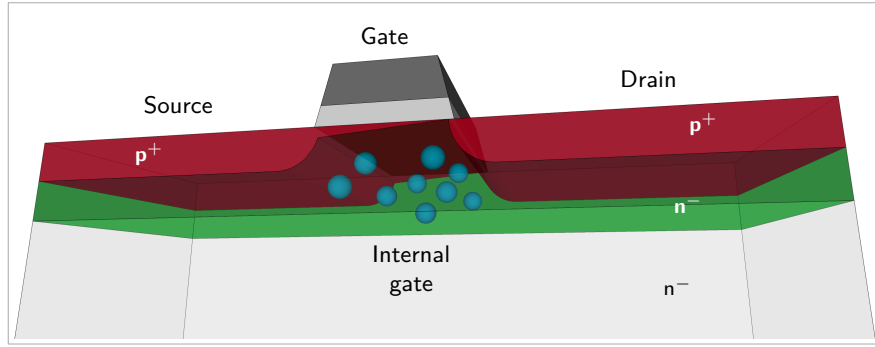


Figure 3.2: Cross section through a DEPFET. The baseline for the charge collecting internal gate is a high energy arsenic or phosphorus implant (green). The large dose boron implant (red) that is shot after the second poly-silicon layer (dark grey) forms the drain, the source and, by omission, the internal gate that is located under the transistor gate. The electrons in the internal gate influence the conductivity of the transistor channel through mirror charges and are thereby measurable without destruction.

the gate is often termed external gate for a unique nomenclature. In the first order, the corresponding transconductance of the internal gate is given by^[113]

$$g_q = \frac{\partial I_{DS}}{\partial Q_{sig}} \propto -\frac{1}{L^2} \mu_h U_{DS} = \sqrt{-\frac{2\mu_h}{WL^3 C_{ox}} I_{DS}} \quad (3.3)$$

where Q_{sig} is the collected signal charge. Since not all mirror charges are located within the transistor channel, the two sides of eq. (3.3) are only proportional to each other. The constant of proportionality is the fraction of collected electrons that generate a mirror charge in the conductive channel.

To be able to remove the collected electrons from the internal gate, n-channel transistors are situated at each gate. While the internal gate serves as source, the n^+ implant is the drain. To minimise potential charge loss to this clear region during the charge collection, it is protected by a deep p-implant.

The baseline layout which is used on board of BepiColombo and that was the fallback option for the WFI of Athena is the so-called Cut Gate design as shown in Fig. 3.3a. The drain region in the centre is surrounded by a circular gate. The area around the gate is occupied by the source and, depending on the size of a pixel, one or more drift structures. On one side the external gate is truncated and the clear transistor is connected. Taking into account that misalignments in the manufacturing process may occur, the two poly-silicon layer that form the clear gate and the external gate overlap. The Cut Gate layout is minimised to essential parts that are necessary for a DEPFET, but has also some disadvantages. The contact hole and the corresponding steering line for the drain confine the minimum gate width while the contact hole for the gate limits its length. The maximum path that an electron has to drift through the internal gate to reach the clear transistor is roughly half the circumference of the gate. The lower limit for the gate width also sets a minimum for this maximal clear distance.

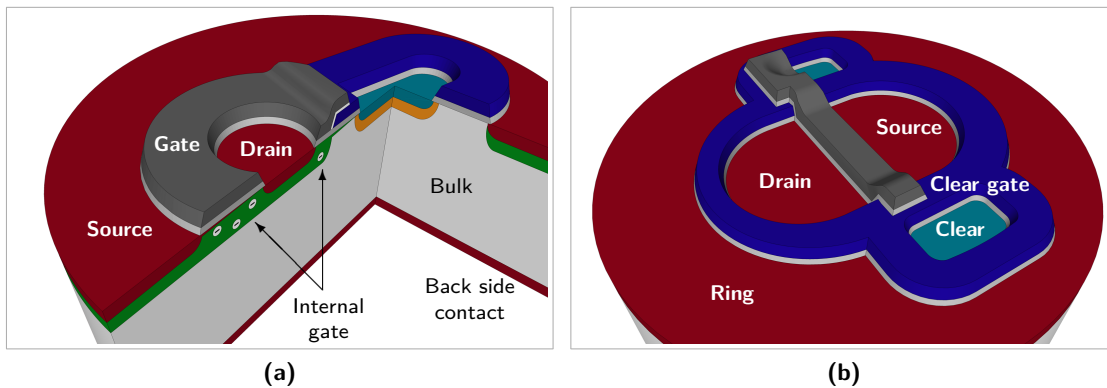


Figure 3.3: A model of (a) a Cut Gate, the former baseline layout of a DEPFET for X-ray spectroscopy, and (b) a Linear Gate as it is planned for the Athena WFI. The electrons generated by an incident X-ray photon in the fully depleted silicon bulk are collected in the internal gate. By measuring the hole current between the drain and the source or the source voltage for a fixed current, the number of electrons in the internal gate can be determined. The collected charges can be removed through the clear transistor.

Since the electrostatic potential drops exponentially with the distance, this lower limit in the Cut Gate design is one of the biggest issues that affects the completeness of the clear process and thereby the spectroscopic performance due to the readout scheme presented in section 5.1.

The limitation of such a circular gate structure can be omitted by changing to a linear gate shape with two clear regions, each on one side of the DEPFET gate. Besides a larger clear area, further poly-silicon spacers are needed to separate source, drain and the drift rings. The layout for the steering lines and contacts becomes more challenging since external gate, clear gate and clear are aligned in one direction perpendicular to the source–drain orientation. Nevertheless, the large pixels of the Athena WFI set by the performance of the Athena optics allow for larger structures. In addition, by changing to shared contacts between the pixels, it is possible to build the tiniest DEPFETs currently available on the basis of linear gates (see section 7.1.2).^[112]

3.2 Infinipix Principle

The driver for the development of pixel concepts with an internal storage like the Infinipix is the issue of so-called energy misfits. They occur during the signal determination by the readout electronics and decrease the spectral performance of the detector. The events that are affected are the ones whose charge cloud arrives at least partly in the internal gate during the readout of the pixel. The conductance of the transistor changes during the measurement and distorts the result. The concerned period is given by the convolution of the temporal

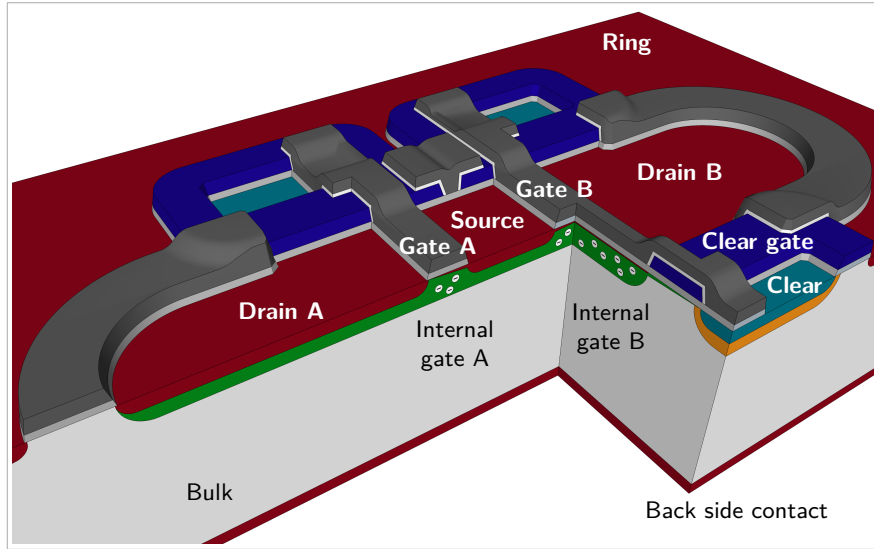


Figure 3.4: A model of the Infinipix. The charges are collected either in internal gate A or in internal gate B. Besides their function in the readout transistor, the two drains also act as switcher for the different tasks of the sub-pixel. Alternating, they are used for charge collection in and readout of the pixel. The shared source is the readout node. For the baseline measurement, the collected charges are removed from the internal gates via the clear transistors.

spread of the charge cloud t_{cloud} with the signal integration time t_{int} . The fraction of such events compared to all that occur during the total photon exposure time of one frame t_{exp} is

$$n_{\text{misfit}} = \frac{t_{\text{int}} + t_{\text{cloud}}}{t_{\text{exp}}} \quad (3.4)$$

for equally distributed events.

To avoid energy misfits, the readout node could be blinded. It is the direct drift to the clear region during the readout process. But since a large n_{misfit} also implies a large number of discarded events, which is not an option for the low photon rates in astronomy, the charges have to be stored for the next readout cycle. One option for such a storage is the implementation of two DEPFETs into each pixel. One is read out while the other one collects the charges generated by incident photons.^[163] After one readout of the complete sensor, the assignment of the two sub-pixels is interchanged. While the read-out one accumulates incoming electrons, the potentially collected charges in the other sub-pixel are determined. The two DEPFETs share their source as shown in Fig. 3.4. The change in the sub-pixel assignment is done via the drain voltages. The sub-pixel in readout state has a more negative drain with respect to the other one and its internal gate is thereby less attractive. Charges generated in the biggest part of the sensor will end in the internal gate of the collecting sub-pixel. For back side illuminated devices of sufficient thickness, most of the X-ray photons will be absorbed far away from the sensor surface and the probability of electrons ending up the wrong internal gate is vanishingly small. The electrostatic potential in an Infinipix pixel is shown in Fig. 3.5.

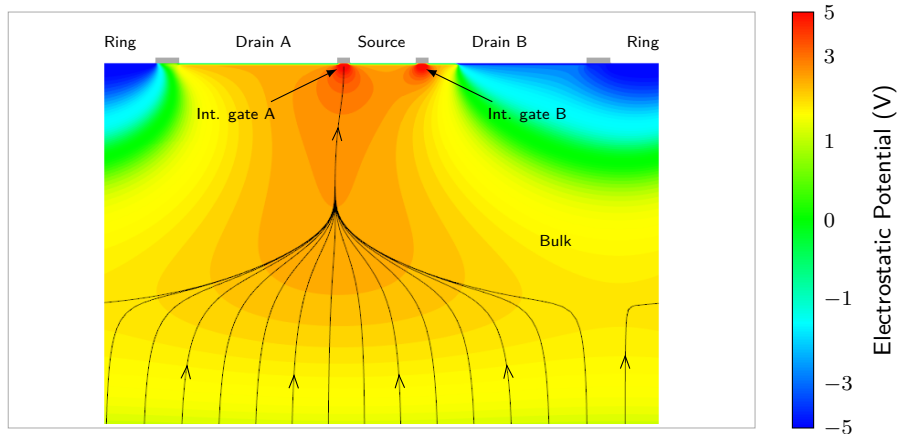


Figure 3.5: 2D simulation of the electrostatic potential in an Infinipix pixel. The streamlines show the gradient of the potential to which charges generated deep in the silicon bulk are exposed. The actual pixel borders differ slightly from the middle of two pixels in the layout and are shifted with the charge collection changing to the other sub-pixel.

Even though this concept does not produce energy misfits, a charge cloud can still be split between two consecutive frames. It is limited by the switching time of the drain voltages t_{drs} and its convolution with the temporal spread of the charge cloud.

$$n_{split} = \frac{t_{cloud} + t_{drs}}{t_{exp}} \quad (3.5)$$

Normally, t_{int} is about two orders of magnitude larger than t_{drs} which results in a fraction of one order of magnitude between n_{misfit} and n_{split} and reduces the number of mismeasured events for DEPFETs with storage. In addition, inter-frame split events can be recombined while the energy misfits described above cannot be detected in the data and contribute to the spectrum like events affected by charge loss.

The basic principle and functionality was already demonstrated by Bähr et al. (2014)^[23] with a single pixel device. But since there are no boundary effects of neighbouring pixels for isolated ones and small windows in their operation voltages do not influence fluctuations as they appear between thousands of different pixels, the further investigation and development is done with Infinipix arrays.

3.3 Noise

Noise – the fluctuation of a signal by disturbances over a wide range of frequencies – is the main contributor to measuring inaccuracies. Besides the Fano noise explained in section 2.2.6, an incomplete clear process adds an uncertainty to the result. Since the number of electrons potentially left in the internal gate varies each time the sensor is read out and reset, the

determined signal fluctuates by the same amount. The readout scheme that causes this readout noise is depicted in more detail in section 5.1.

Noise as current fluctuation was discovered by Schottky (1918).^[174] It is quantified as equivalent noise charge (ENC), the amount of charge that would cause the same deviation when put on a capacity.^[140] The noise is composed of distinct parts that scale differently with the total capacity C_{tot} of the detector and the signal integration time of the readout electronics τ .^[74]

$$\text{ENC}^2 = \frac{a_1}{\tau} C_{\text{tot}}^2 A_1 + 2\pi a_2 C_{\text{tot}}^2 A_2 + a_3 \tau A_3 \quad (3.6)$$

a_1 , a_2 and a_3 are the noise sources while A_n are the shape factors of the function used to filter the different noise contributions white series noise, pink noise and shot noise.

3.3.1 White Series Noise

The thermal motion of charge carriers in the conduction band of a conductor or a semiconductor causes a noise contribution in electronic components. Investigated by Johnson (1928)^[93] and described by Nyquist (1928),^[144] the thermal noise of a conductor only scales with its resistance R and the temperature T .

$$\frac{d\overline{U_n^2}}{df} = 4k_B T R \quad (3.7)$$

$\overline{U_n^2}$ is the mean of the squared deviation of the measured voltage.^[113] Since the spectral density of the thermal noise is constant over the frequency f , it is called white noise referring to the resulting colour of electromagnetic radiation that is uniformly distributed over the whole visible frequency spectrum.

The resistance of the conductive channel of a MOSFET is $1/g_m$ (cf. eq. (3.1)). The noise defined as standard deviation – which is the square root of the mean of the squared deviation – is

$$a_1 = \sqrt{\frac{4k_B T}{g_m}} \quad (3.8)$$

for thermal sources. According to eq. (3.6), the white series noise is lower for smaller capacities and can be reduced by applying longer filtering times. Nevertheless, the weaker dependence to all these parameters due to the square root makes the white series noise the dominant contribution at the applied operation conditions of less than 220 K and at a few microseconds per readout.^[141,158]

3.3.2 Pink Noise

Defects in the crystal lattice generate energy states in the band gap. These states can easily be filled by charge carriers which are released again with some delay.^[96] The temporarily trapped charges can induce mirror charges into the transistor channel which change its conductivity.^[113] In MOSFETs, such traps are located mainly in the gate oxide and at the interface to the silicon bulk. The superposition of trapped and released charge carriers in all defects results in a noise spectrum

$$\frac{d\overline{U_n^2}}{df} \propto \frac{1}{f^a} \quad (3.9)$$

with $a \approx 1$.^[97] The frequency dependence of this $1/f$ noise is the reason for the naming of pink noise since reddish colours would dominate in a visible electromagnetic spectrum. While the white series noise can be reduced by extended integration times, pink noise adds a constant contribution to the noise in a DEPFET. a_2 cannot be calculated analytically and has to be measured for every sensor design separately.

3.3.3 Shot Noise

Shot noise (white parallel noise) appears in the whole sensitive area of the sensor – the depletion zone. The finite quantity of the electron charge q causes quantised steps in the current that crosses a boundary^[174] like a reverse biased p-n junction or PIN diode. It only scales with the current I .^[113]

$$\frac{d\overline{I_n^2}}{df} = a_3 = 2Iq \quad (3.10)$$

Traps in reverse biased diodes like the sideways depleted DEPFET devices can add additional states in the band gap that allow for an easier generation of free charge carriers by double excitation.^[179] This leakage current and, thereby, the shot noise increases exponentially with temperature. Therefore, it dominates the noise at positive temperatures, but can almost be omitted by cooling (see Fig. 5.14).

In case of high electric fields, charge carriers can gain sufficient energy to create further electron-hole pairs.^[189] This so-called impact ionisation increases the current by the provision of additional charge carriers. They can contribute to the electron-hole pair creation as well which can end in an avalanche breakdown – an exponential increase in the number of charge carriers.^[124] The raised current leads to an even higher shot noise. Therefore, peaks in the electrostatic potential within the sensor have to be avoided. Leakage current during the signal integration adds a Poisson distributed noise component that leads to an increasing (shot) noise for longer integration times.

Measurement Setup and Data Analysis

A reliably designed and known setup is the basis for the very sensitive low noise measurements that can be performed with the DEPFET devices. Ground loops and external coupling have to be avoided if possible since the measured results are influenced by a combination of the noise of the investigated devices and all required electronic components necessary for the steering and the readout of the DEPFETs. A stable and fast data analysis is essential to be able to investigate all the tiny effects that contribute to a spectrum in a reproducible way.

4.1 Califa Test Setup

The reduction of thermal noise by cooling requires a setup that protects the detector from ice buildup. It can be achieved by drying the air inside the setup or by using a vacuum chamber.^[208] Since the latter is also necessary to reduce the absorption of X-rays on their way to the sensor, it is the method of choice for the measurements presented in this thesis and beyond.

Califa^[a] is a vacuum chamber with an integrated X-ray tube (see section 4.3.2) built at the MPE^[b]. It has a separated pre-vacuum and high vacuum system provided by one pre-vacuum and three high vacuum pumps which evacuate three separable parts of the facility to about 10^{-6} mbar to 10^{-7} mbar. It enables to ventilate the measurement chamber in order to change the different investigated detectors without venting the rear part of the facility with the X-ray tube and the delicate filters (see Fig. 4.1). The filters are used to suppress the emitted infrared and visual light as well as continuum radiation for low energies that consists of bremsstrahlung generated in the X-ray tube. Otherwise, it would dominate the low energy tail of the observed lines and analysis of the spectroscopic performance of the investigated samples would become more difficult.

^[a]Calibration Facility

^[b]Max Planck institute for Extraterrestrial physics

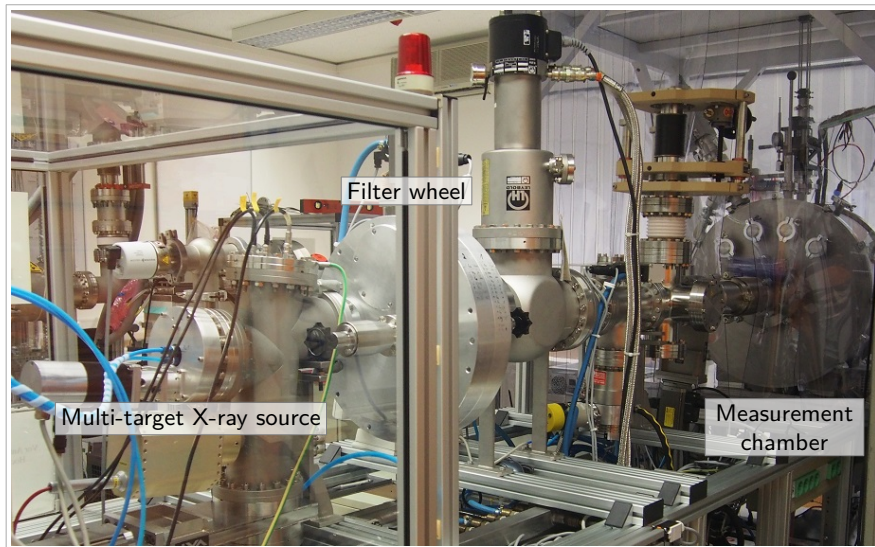


Figure 4.1: Calibration facility (*Califa*) that was used for the measurements on the DEPFET prototype arrays with integrated storage.

The whole facility is monitored and can be steered by a PLC^[c]. It is connected to the vacuum gauges, a wheel with various targets in the X-ray tube, the three turbo pumps and the valves that separate the different parts of the facility and its connection to the outside. The latter can be used to ventilate the facility or parts of it with the connected nitrogen supply. Pure nitrogen is used to reduce the contamination within the vacuum chamber that would emerge from pollutants – mainly water molecules – in the surrounding air.

The facility is equipped with two coolers. One is a cryocooler that serves as a cold trap to enhance the vacuum in the beam line. The second cooler makes use of the Stirling cycle. It is flange-mounted to the measurement chamber and used to cool the detector to reduce the influence of leakage current and, thereby, shot noise in the sensor and to protect the electronics from overheating since convection is almost not present in the evacuated facility. With the room temperature as the limiting factor on the warm side of the cooler and thermal loss at the various interfaces between cooler and the detector, temperatures of about 190 K are feasible on the sensor.

4.2 Electronics

Besides the vacuum chamber with the integrated photon sources, an electronic setup is needed to steer and read out the detectors under investigation. The core of the measurement system is a PCB^[d] mounted directly outside at the measurement chamber (oPCB,

^[c]Programmable Logic Controller

^[d]Printed Circuit Board

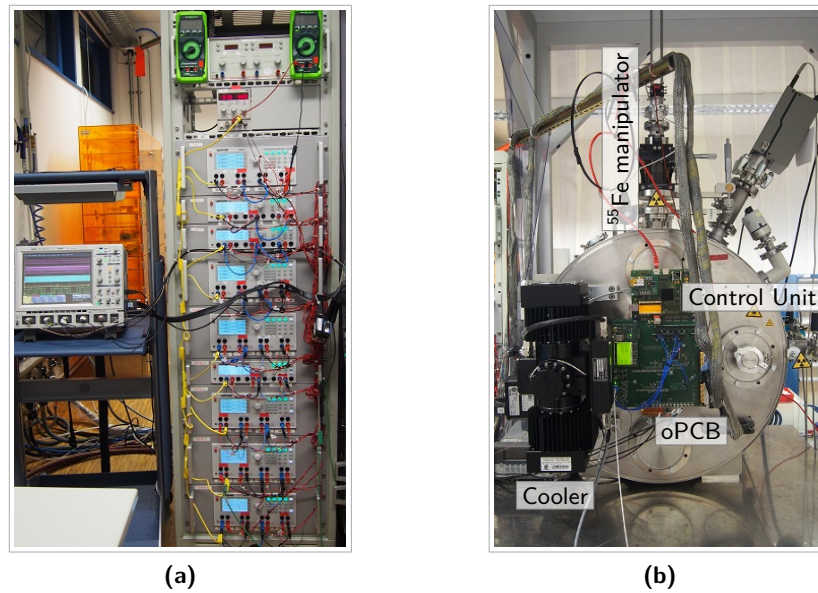


Figure 4.2: (a) The power supplies and an oscilloscope for the monitoring of the DEPFET operation. (b) The measurement chamber with the support electronics, the digital control unit on its top and a Stirling cooler on the left side.

see Figs. 4.2b and 4.5) which underwent a continuous development in all the setups used for active pixel sensor measurements by the MPE in the last decade.^[129] It forwards the voltages and currents from the power supplies assembled in a power tower (Fig. 4.2a). Over flexible PCB leads and a flange, they are distributed to the DEPFET sensor and the ASICs^[e] mounted on a ceramics carrier board that make up the detector. This ceramics carrier board is plugged onto a second PCB (iPCB, Fig. 4.5). The PCBs are equipped with electronic components that protect the delicate electronic parts of the detector. In addition, the outgoing signal lines are provided with buffer amplifiers. They adjust the differing impedances of the readout ASIC and the ADC^[f], the dissimilar operating ranges, and help to drive the long signal lines from the inside of the vacuum chamber to the outside where the ADC is located.

4.2.1 Digital Control Unit

The oPCB is connected to a programmable control unit that generates the digital signals for the operation of the ASICs. It is implemented on a PCB, the so-called xBoard (cf. Treis et al. (2004)^[199]). The whole xBoard and thereby the digital signals from the control unit are electrically decoupled from the oPCB via opto-isolators. They are part of the electric decoupling shown in Fig. 4.5 that is implemented to avoid undesired ground loops

^[e]Application-Specific Integrated Circuits

^[f]Analogue-to-Digital Converter

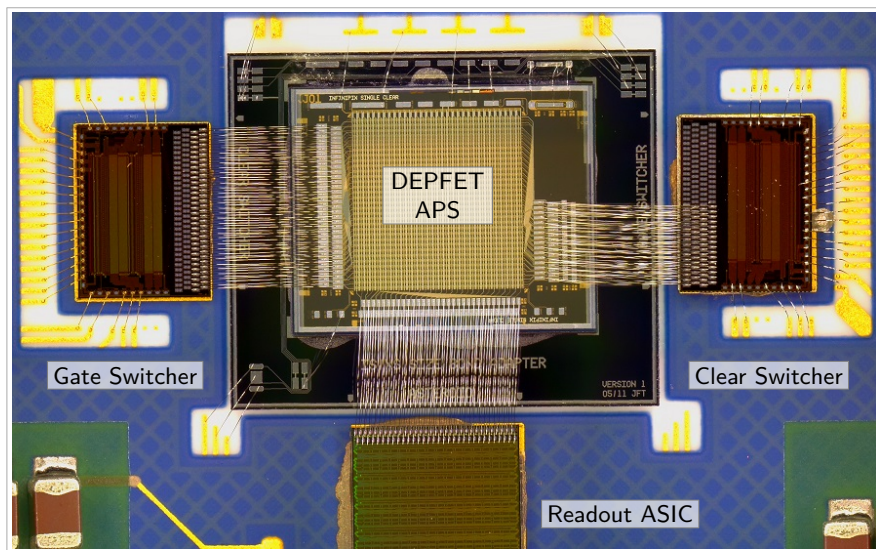


Figure 4.3: The sensor and the bonded ASICs. Two switcher ASICs steer the row-wise switched voltages for gate (on the left), clear gate and clear (on the right). The readout ASIC is connected to the source of the Infinipix in a column-wise way.

which would increase the noise contribution to the electric setup. The digital control unit is able to interpret a few basic commands. A 'halt' multiplies the rows to which it is applied by integral multiples of the control unit's clock length. Further functionality are 'jumps' within the control sequence and iterable internal registers that both allow for more complex sequences without their lengths being significantly increased. A more detailed description and an excerpt of a sequence are given in Appendix B.

4.2.2 Steering ASIC

The steering of the different voltages necessary to operate a DEPFET is done via a switcher ASIC. The 'Switcher S' that is used for the measurements in the present work, features 64 output channels with two different outputs each that are switchable independently.^[62] The high and low levels of the two outputs of each channel are defined via global external voltages. The standard voltage of each of the two outputs is globally set via a polarity bit for all 64 channels. Over a shift register, the individual channels can be selected and activated. The actual voltage switching of an output node is done via global enable bits. They ensure that the two outputs of each channel can be addressed separately. The combination of the global enable bits and the activated channels allows for individual patterns that define the temporal behaviour of the sensor.

The 'Switcher S' is used to steer the gate, the clear gate and the clear regions of the DEPFET. Since the switcher ASIC only features two separate output voltages, a second one is necessary on the opposite side of the sensor as shown in Fig. 4.3. It is rotated by 180°.

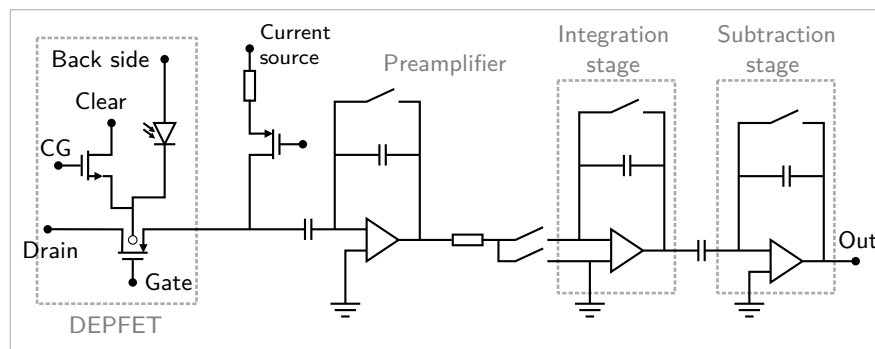


Figure 4.4: Schematics of the Asteroid acc. to Porro et al. (2010)^[158] and an equivalent circuit diagram of a DEPFET.

To enable a synchronised operation of both switchers, the shift register can be operated in both directions.

The drain voltages of the two sub-pixels are global contacts which do not need a row-wise selection. Therefore, they are not steered by a switcher ASIC, but via a separate PCB (Fig. 4.6a) that can be mounted on the iPCB. It comprises two drivers that switch the two global drain voltage levels on demand to either the high or the low level, which are provided by external power supplies. The voltage levels are switched within 10 ns. A fast operation is fundamental for the functionality of the Infinipix principle at high speeds since it is one factor that limits the performance (see eq. (3.5)).

4.2.3 Readout ASIC

There are two different readout modes that are suitable to determine the charge collected in the internal gate of the DEPFET – the drain current and the source follower readout. In the drain current readout, the current through the transistor channel between external and internal gate is measured directly by a readout ASIC connected to the drain region. For that purpose, the Veritas^[g] ASIC was developed for X-ray imaging and spectroscopy.^[159] With the Veritas 2,^[160] the first successful measurements on spectroscopic DEPFETs were performed in 2016.^[196] Without an ASIC available for spectroscopy in drain current readout, all previous samples were investigated in the second readout mode, the so-called source follower. It is the measurement of the source potential while the external gate and drain voltage as well as the transistor current are at fixed values. A change in the transistor channel conductivity then leads to a variation of the source potential. The constant transistor channel current is supplied by a current source in the readout ASIC. While the Veritas is capable to read out DEPFETs in both modes, the ASIC available in the past was the Asteroid^[h], permitting

^[g] Versatile Readout based on Integrated Trapezoidal Analog Shapers

^[h] Active current Switching TEchnique ReadOut In x-ray spectroscopy with Depfet

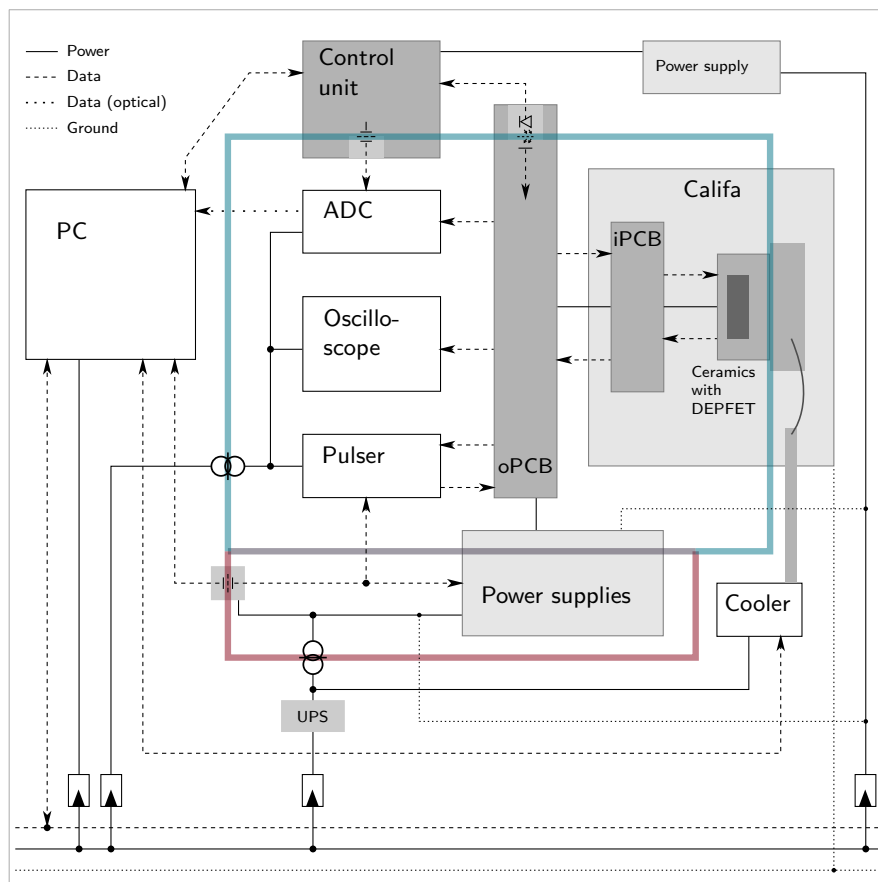


Figure 4.5: Block diagram of the setup at Califa. The turquoise line skirts the (except for one point) electrically insulated subsystem of the PCBs, the DEPFET and the readout part. The red line marks the one of the power supplies which are protected from a power failure by an uninterruptible power source (UPS).

source follower operation only.^[158] A schematic is shown in Fig. 4.4. The source potential is amplified by the preamplifier and converted into a current. The signal filter is built out of the integration and the subtraction stage. With switchable resistors, the amplification of the signal can be reduced by a factor of two, three or four. The actual signal determination the Asteroid is designed for, is depicted in section 5.1. In addition to the absence of a suitable readout ASIC in the past, the Infinipix can be read out only in the source follower mode with the present hardware. With the functional principle of the Infinipix with the switched drain voltages and a Veritas that needs a fixed drain potential, a drain current readout of the Infinipix is not possible without implementing further functionalities into the detector and setup.

4.2.4 Analogue to Digital Converter

The differential output signal of the Asteroid that is buffered on the PCBs at the vacuum chamber is connected to an ADC. It converts the analogue signal to digital data which are transferred via a fibre optic cable and stored on a measuring computer. The ADC is triggered by the digital control unit to synchronise it with the operation of the detector and thereby the data put out of the Asteroid. The board with the ADC that is mounted into a PCI^[i] rack was developed at the MPE in the past to ensure a low noise operation. The ADC has a sampling rate of 80 MHz which also limits the positioning of the sampling point in this setup to steps with a size of 12.5 ns. It has a dynamic range of 2.03 V with a resolution of 14 bit.

In addition to the actual measurement, the output of the Asteroid as well as all the digital signals can be monitored with an oscilloscope by connecting it to the provided plugs on the oPCB. By losing the capability to read out the DEPFET with the ASIC, a direct access to the source node can also be used to analyse the temporal behaviour of the potential of the readout node of the DEPFET with an oscilloscope. For that purpose, the readout ASIC provides switches directly at the input stage of every channel to send a test signal through the readout chain or to connect directly to the DEPFET by skipping the ASIC.

4.3 Photon Sources

To investigate the spectroscopic and timing performance of a photodetector, various photon sources are integrated in the setup. Depending on the purpose of a measurement, different sources were used that are based on radioactive decay, characteristic radiation and recombination in semiconductors.

4.3.1 Radioactive Iron-55 Source

⁵⁵Fe decays with a half-life of 2.737 years via electron capture to the stable isotope ⁵⁵Mn.^[7] The vacant state on an inner shell is then filled by an electron from an outer shell and the energy difference is emitted by a photon which can produce characteristic X-ray radiation (compare relaxation in Fig. 2.4a). The transition that is most likely is the Mn^[j] K- α line with an energy of 5895 eV (see Fig. 2.2a, Table 2.1). It is close to the energy of the important Fe^[k] K- α line at 6399 eV.^[192] The activity of the radioactive source degraded during the

^[i]Peripheral Component Interconnect

^[j]Manganese

^[k]Iron

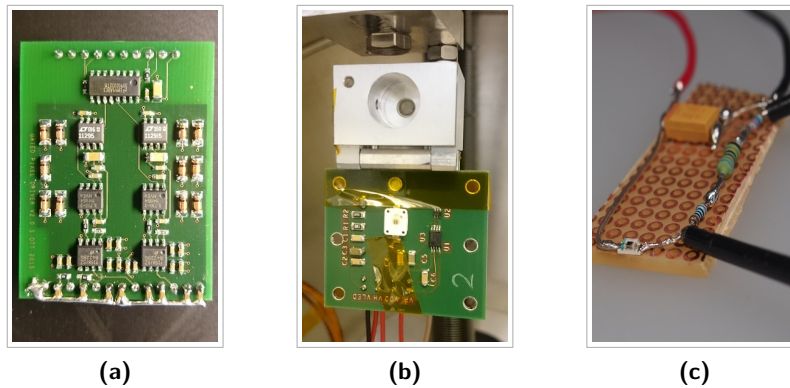


Figure 4.6: (a) Drain switching unit that is necessary to make the setup capable for the operation of Infineon DEPFET arrays. (b) Radioactive Iron-55 Source and the infra-red LED on its driver board.^[82] (c) Photodiode for the measurement of the timing performance of the infra-red LED.

measurement period from 300 MBq to 200 MBq. Potentially generated Auger electrons are stopped by a beryllium window in front of the actual radioactive source.

4.3.2 X-Ray Tube

In an X-ray tube thermally generated electrons are emitted from a cathode and accelerated by an electric field defined by potential differences of several kilovolts. The electrons are focused to a target wheel by a Wehnelt cylinder. Inside the selected target, the electrons are decelerated via Coulomb interaction with shell electrons or the atomic nuclei and bremsstrahlung is emitted. Furthermore, the atoms of the target material can be ionised by the fast electrons. The characteristic radiation (cf. section 2.1.1) emitted during the relaxation of the atom is the second contribution to the generated spectrum. Since these lines are the desired features, the bremsstrahlung continuum above the line energy is suppressed with filters located in the beam line of Califa (Fig. 4.1).

4.3.3 High-Speed LED

The ^{55}Fe source and the X-ray tube supply the setup with X-ray photons of the desired energy to test the spectral performance of a detector. But the X-ray events occur randomly and, therefore, they are not suitable to test the timing behaviour of the investigated devices. The easiest approach for a photon source that satisfies these needs is a triggerable LED^[1]. The NIR LED (860 nm) with its driver that is placed directly at the ^{55}Fe source in the measurement chamber is shown in Fig. 4.6b and is based on the design presented by

^[1]Light-Emitting Diode

Halbritter et al. (2014).^[82] To enable a high-speed operation, two key features are implemented. The turning-on and turning-off is supported by a capacity and an inductivity. In addition, the LED is not controlled by an external voltage, but by a driver that switches the gate of a transistor at the cathode side of the LED. It is controlled by an external pulser which is connected to the digital signals provided by the control unit. With a photodiode (Fig. 4.6c), LED pulses with a minimum length of about 20 ns at 10 % of the peak height were determined.

4.4 Data Analysis

To identify the detector characteristics like the noise and the spectroscopic performance as result of the determined emission line properties, an analysis of the obtained data is necessary. Since the computational power of the measuring computer is limited, it is done after the measurement – offline. The raw data with X-ray photons taken at Califa were analysed with ROAn^[m],^[104] a modular step-based offline analysis tool based on ROOT.^[31] ROAn was developed specifically for the analysis of DEPFET data. Since the two sub-pixels in an Infinipix have different properties, frames with data from the sub-pixel A and the ones from B have to be analysed separately. To avoid large adaptations in ROAn, two consecutive frames were combined to one with twice the size. The only issue to consider was the suppression of event recombination at the edges of the two sub-frames which are also located in the centre of that super-frame. For clarity, the frames of the two sub-pixels are always shown in two separate maps in this work.

4.4.1 Offset and Noise

The offset is composed of two parts. Different characteristics of all the pixels in an APS cause displacements between the read-out mean values. In addition, the whole signals are shifted on purpose to avoid values that are out of range of the ADC due to fluctuations caused by the sensor noise. The offset and the noise are determined from dark frames – frames without illumination by a photon source – taken under the same conditions as the associated photon frames – frames that potentially contain events. Examinations in the past showed that a number of 200 frames is sufficient to get reliable results for these quantities. Frames with pixels over a definable threshold are skipped to omit the influence of MIPs^[n] on the data. Such cosmic ray events place a large amount of energy in the detector and would increase the determined values for offset and noise. The offset is a map with the pixel-wise mean of the remaining dark frames. Before the noise is calculated, the so-called common mode noise

^[m]ROOT Offline Analysis

^[n]Minimum Ionizing Particles

is subtracted. Common mode noise is a disturbance in the setup that influences all data from one row in the same way since the readout is performed column-parallel. By subtracting the median row-wisely, the common mode noise is cancelled out even from photon frames. The noise map is the pixel-wise determined standard deviation

$$\sigma = \sqrt{\frac{1}{N-1} \left[\sum_i x_i^2 - \frac{1}{N} \left(\sum_i x_i \right)^2 \right]} \quad (4.1)$$

for the common mode corrected values x_i from N dark frames.

4.4.2 Events

After the offset is subtracted from every frame and the common mode is determined and subtracted for every row of every frame, the event recognition starts. In a first step, all signals that are larger or equal to the primary threshold, usually five times the noise of the pixel, are detected. Since the probability of an event that splits over more than one pixel is higher than a noise excess in an adjacent pixel, all signals with a size of the threefold noise and larger, the secondary threshold, are assumed to be part of the event. All neighbouring pixels with detected signals are combined to split events. To avoid the consideration of multiple events, only specific split events are marked as valid patterns (see Fig. 4.7). Other and larger patterns are most likely to be composed of more than one event and, therefore, omitted since they would appear as one event with a too large measured energy in the spectrum. Events that are composed of charge clouds from multiple photons which form valid patterns, contaminate the spectrum as so-called undetected pile-up.

The thresholds for the signal detection are a trade-off between the risk to lose an actual signal and the adding of a noise excess which may also result in an invalid pattern. The primary and secondary threshold of five σ and three σ are the standard for DEPFET measurements and are used for comparability also in this thesis. For the flight operation of Athena, a global threshold of four sigma is also conceivable for simplification and needs to be investigated in the future.

4.4.3 Gain

The pixel-wise gain is the total amplification of the whole readout chain from the internal gate of the DEPFET to the ADC. In the source follower mode, it contains the DEPFET transconductances g_q and g_m (see chapter 3) as well as the amplification in the Asteroid and by the buffer amplifiers on the PCBs. Its inverse is used to convert the values determined

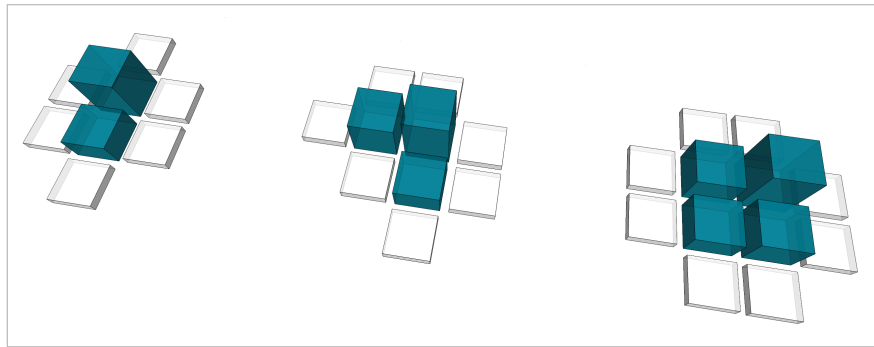


Figure 4.7: Besides a single event that has no signal in the adjacent pixels, the shown patterns and their rotations in units of quadrants are accepted as valid events. Other or larger patterns are most likely to be composed of multiple events and, therefore, skipped to reduce the influence of pile-up events to a spectrum.

by the ADC measured in ADU^[o] back to the number of collected electrons. Since the gain varies with the operational conditions, it is determined for every measurement that is done in the development phase. For that purpose, the events in ADU marked as valid patterns are put into pixel-wise histograms and the position of the investigated emission line is fitted. In case of the mainly used ⁵⁵Mn spectrum, the fit considers both the K- α and K- β lines to improve the accuracy since the relation between their positions and their intensities is known and can be fixed in the fit. The result divided by the actual line energy (see Table 2.1) converted to the expected number of electrons with the factor w (cf. section 2.2.6) gives the gain map.

4.4.4 Incomplete Clear

One of the main issues of spectroscopic DEPFETs in the past was an incomplete clear process. The readout scheme described in section 5.1 results in a reduced signal at the output of the Asteroid if electrons are left in the internal gate after the clear process. To investigate the influence of such effects on the spectral performance, ROAn^[104] was equipped with tools that characterise the signal in the frames following an event in a pixel. It is assumed that local potential pockets formed in the internal gate during the manufacturing process prevent electrons from a drift to the clear region if the internal gate is filled with a charge carriers. After a first clear process, they diffuse out of the potential pocket during the exposure time of the next frames and can be removed by one of the next clear cycles. The incompleteness of the clear process is described by three constants. The first is the maximum amount of electrons that the potential pockets at an internal gate can store. The second one describes the filling of the pockets as a fraction of the total number of electrons in the internal gate while the third is the time constant of the diffusion process. The determined constants are used to quantify the clear behaviour and not to recombine the original signal. The goal is to

^[o]Analogue-to-Digital Unit

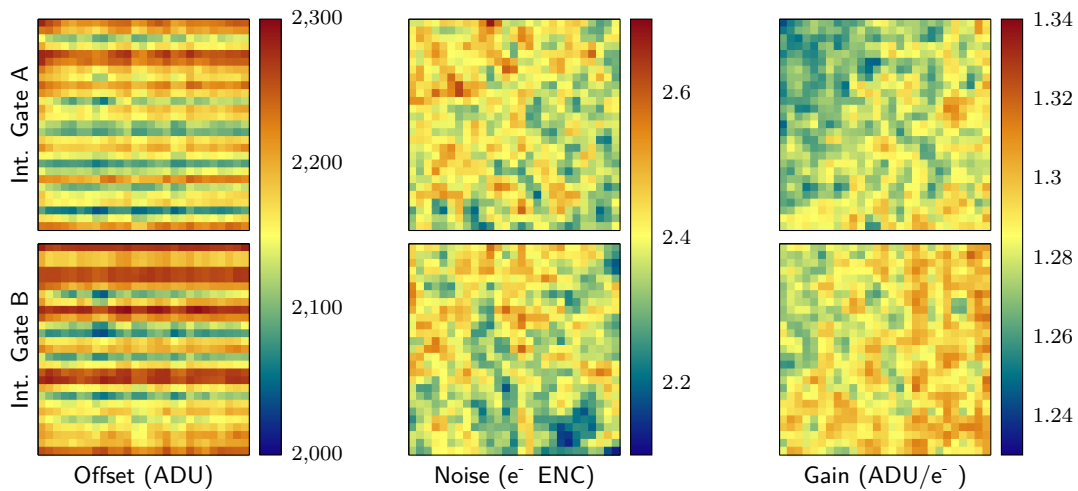


Figure 4.8: Offset, noise and gain map as they are generated by ROAn.

optimise the clear process in the DEPFET and to avoid a software approach.

4.4.5 Results

Most of the results presented in this thesis are the outcome of ROAn, but are further processed with Python^[222,223] scripts developed to extend the offline analysis – also to address specific issues concerning the Infinipix devices. The main disadvantages of ROAn are a missing inter-frame split recombination and absent error information in the output. Since ROAn stores all data in trees, lists of a special format provided by ROOT, they can be used to recalculate and fit the desired information including an appropriate error analysis.

Noise

The noise calculated as pixel-wise standard deviation of 200 dark frames is stored in a map with the size of the investigated sensor as shown in Fig. 4.8 in the centre. The noise of a detector is the mean of the noise values of all pixels. Its error is determined as the standard deviation of that spatially distributed set of results. Due to the thousands of pixels, the overall noise value is a very stable parameter with a small error and, therefore, also suitable for the investigation of tiny effects.

Energy Resolution

One of the most important quantities for the characterisation of the spectral performance of a detector is its energy resolution. It is the minimum energy difference between the position of two lines so that they are still discriminable from each other. This energy equals roughly the full size of the measured emission line with a Gaussian shape at the half of its total height, the so-called full width at half maximum (FWHM). It is determined by a Gaussian fit to the measured line and the relation

$$\text{FWHM} = 2\sqrt{2 \ln 2} \sigma \approx 2.355 \sigma \quad (4.2)$$

Due to charge loss effects that influence the low energy edge of the investigated line (cf. sections 2.2.5 and 5.2) to which the fit is very sensible, the result has to be utilised very carefully. To reduce the error in the fit, a constant offset is taken into account for energies below μ , the expected value of the emission line.

Peak-to-Valley Ratio

Even if it is not significant as absolute value, the peak-to-valley ratio is a first indication for the quality of a spectrum and thereby the performance of the detector. It is the ratio between the total height of an investigated emission line and the background generated at the entrance window of the detector and by the readout scheme (see section 5.2). A worse functionality of the charge suppression at the read-out sub-pixel of an Infinipix also causes charge loss at the collecting internal gate. The split charge cloud adds two entries to the sensor generated background and worsens the peak-to-valley ratio. Therefore, this parameter is a good indication for the quality of a DEPFET with storage. To avoid the contamination by other emission lines from materials near the beam line, the interval between 0.9 keV and 1.1 keV is chosen to calculate the valley by its mean. The peak height is taken from the fit performed to determine the energy resolution.

4.4.6 LED Measurements

The measurements taken with an LED as photon source to study the temporal behaviour of the Infinipix are composed of frames that are illuminated globally. Therefore, the analysis has to differ for these data. The data do not contain spatially separated events, but intensities that cover the whole or large areas of the sensor. A set of Python scripts was developed to extract the desired data. An offset map is determined in the same way from dark frames as for all other measurements. A common mode correction would cancel the whole signal

and is, therefore, omitted. The influence of the common mode and other noise contributions is reduced by taking a few thousand frames under the same timing conditions which is the advantage of a reproducible signal from a triggerable photon source. The signal is determined by the offset subtracted mean of such a set of frames. Due to the column parallel readout the data can be averaged over a whole row or even the whole sensor to further reduce the noise influence depending on the investigated parameter that is of interest in the specific measurement.

Measurements and Evaluation

For the further sensor development of a DEPFET layout with integrated storage, three layout variants of the Infinipix existing as 32×32 pixel arrays were investigated. The comparison of the different designs is based on spectroscopic measurements. The devices were analysed to verify the functionality of the concept and to unveil opportunities for improvement. The different results of the spectroscopic performance measurements are also compared to a non-storage DEPFET. The most critical outcomes were verified with a second device of the same type from a different wafer. A few details and the timing properties of the Infinipix devices were determined with LED measurements additionally.

5.1 Readout Principle

To realise low noise measurements, the electronic noise contributions (see section 3.3) have to be reduced to a minimum. While the pink noise can be lowered by an appropriately shaped filter function in the readout ASIC,^[75] the shot noise reduces with shorter signal integration times τ .^[141] On the contrary, the white series noise can be reduced with a sufficiently long integration time. Both, the shot noise and the white series noise decrease with lower temperatures. To enable a sensible operation, it is absolutely necessary to reduce the thermal generation of electrons, the so-called leakage current that scales exponentially with temperature. It is proportional to the shot noise, the dominant contribution at room temperature. At the investigated temperatures below 220 K and readout speeds of a few microseconds or less, the white series noise dominates.^[141,158] The trapezoidal weighting function as shown in Fig. 5.1a is as good as a triangular shaping with respect to white series noise while the shot noise increases with the length of the flat top.^[71] Considering the time limitations given by the sensor and the complexity of a pink noise shaper, the trapezoidal weighting function is the optimum available and implemented in the Asteroid.^[158]

After a DEPFET is switched on by the application of a lower voltage at the gate to open the transistor channel, the readout ASIC needs some settling time to achieve a stable state. In the

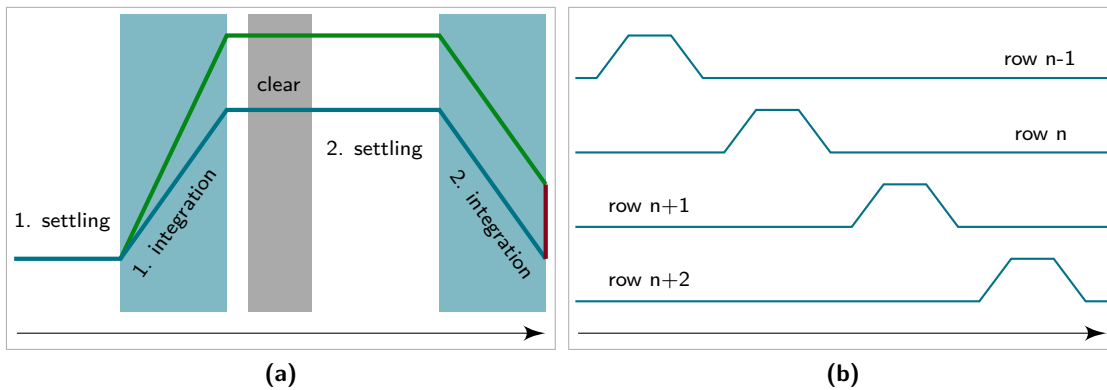


Figure 5.1: (a) Readout scheme of a DEPFET by using correlated double sampling. The readout node has to settle after a pixel is turned on and after the clear process took place. The first integration samples a potential signal and the baseline. After the internal gate is emptied, the baseline is subtracted by the second integration. The green and the blue lines show the difference between a readout process with and without collected electrons in the internal gate. The resulting measured signal is indicated by the red bar. (b) Readout of different rows in the rolling shutter mode. The more rows a sensor has the smaller is the fraction of readout to exposure time in a continuous readout operation.

source follower mode, also the source node of the DEPFET and the connected aluminium readout line that contributes to a parasitic capacitance of the sensor have to settle for a proper measurement. With the first integration, the influence of potentially collected charge carriers on the transistor channel and the baseline signal of the DEPFET are determined. The internal gate is depleted via the clear transistor afterwards. In the source follower mode, a second settling is needed for the source node that follows the modified configuration in the transistor during and after the clear process. A second measurement determines the baseline signal of the DEPFET with an empty internal gate. The difference of the two values that result from the signal integrations is determined by the subtraction stage (see Fig. 4.4) in the Asteroid^[158] and is the actual value of interest that is proportional to the number of potentially collected electrons since the clear process of the previous readout.

The resulting difference is much smaller than the absolute value of one signal integration by the readout ASIC. The further signal processing chain in the Asteroid and up to the ADC is designed for these small signals, which does not allow for measurements with only one integration with the existing setup. Depending on the scientific question, this so-called correlated double sampling is not necessary. In particle physics or at free electron X-ray lasers, only a Boolean value that indicates whether there was a detection or not or a rough intensity measurement may be of interest. By skipping the second integration, the readout time and thus the time resolution can be optimised.

The DEPFETs used for MIXS and Athena are read out in the rolling shutter mode. It is a row-wise, column parallel readout. The number of readout lines is reduced to the number of columns of the detector. External gate, clear and clear gate have to be steerable for each row independently. The rolling shutter mode leads to a slight offset of the time interval

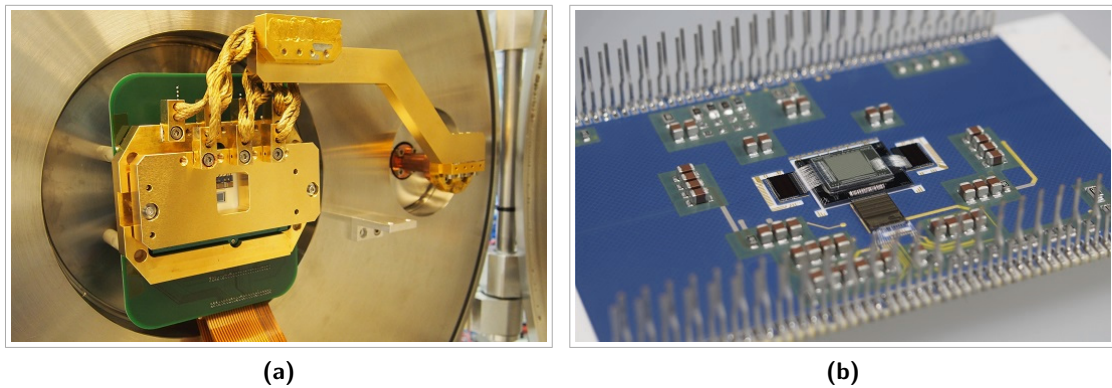


Figure 5.2: (a) A sample mounted within the gilded copper cooling mask inside the vacuum chamber of Califa. (b) Ceramics carrier board with mounted sensor and the ASICs.

and thus the measurable arrival times of the photons detected in different rows. A more sophisticated analysis is required for time-sensitive observations, but in principle, it enables a time resolution of the processing time of one detector row for extensive or defocused objects.

Energy misfits (see section 3.2) that are not detectable by a subsequent analysis occur during the first integration. Charge clouds of incident photons that reach the internal gate of the DEPFET at the end of the clear process or during the second settling or integration contribute with a value to the spectrum that is below the noise peak as long as there is no significant pile-up with other events. Therefore, they can be detected and removed easily. Since the charge carriers of such events stay in the internal gate, they are measurable in the next readout cycle and do not worsen the throughput. A DEPFET with storage does not only avoid energy misfits, but also has a global shutter that synchronises the time intervals of all pixels even in the rolling shutter readout. It is the global charge transfer from a collection area to the readout node or the global switching of the drain voltages in the Infinipix concept. The existing samples are all routed to be operated in the rolling shutter readout mode.

The measurement accuracy of the correlated double sampling is very sensitive to the clear process. If the charge carriers are removed incompletely, the determined signal is reduced by the amount of charge that stays in the internal gate and causes reset noise. Therefore, an almost complete clear process is essential and sets limits to the layout and technology usable to fabricate DEPFETs.

5.2 Spectral Features

Most of the measurements done with the samples in this work are spectroscopic ones. The spectra are dominated by the emission lines of the X-ray photon sources, i.e. the $K\text{-}\alpha_1$, $K\text{-}\alpha_2$,

K- β_1 and K- β_3 lines (see Table 2.1) which are distinguishable only as one K- α and one K- β line due to the Fano limited energy resolution of the detector. Besides the photon energy, the number of electrons in the internal gate is based on the mean electron-hole pair creation energy w of 3.70 eV/e⁻ and 3.71 eV/e⁻ [111] for the typical measuring environments at 220 K and 200 K respectively. The uncertainty in the number of electrons – the noise – is dominated by the Fano noise (see section 2.2.6) that results in a limit of (119 ± 2) eV FWHM for the Mn K- α line.

A shoulder at the low energetic side of the emission lines is usually caused by charge loss. It may occur either at the entrance window, during the charge collection in the pixel, by an incomplete clear process or, in case of the Infinipix, a collection of parts of the charge carriers in the shielded sub-pixel. In spectra generated by the X-ray tube as shown in Fig. 5.3, the large low-energy tail is part of the bremsstrahlung continuum that is suppressed for higher energies than the emission line by filters in the beam line.

If a fluorescence photon of the detector material – silicon – leaves the sensitive area, it is missing in the determined amount of energy. It causes a so-called escape peak that appears below the original energy of the incident photon. The difference of the two spectral features is the energy of the fluorescence photon. In general, it is the Si^[a] K- α line energy. In addition, fluorescence photons from outside the sensitive area of the sensor can be absorbed and add additional peaks. They are from materials that are located near the beam line. Measurements with the ⁵⁵Fe source show traces of aluminium and silver which, therefore, have to be used in the mounting of the radioactive source.

Besides the peak features caused by photons entering and leaving the sensitive area, a charge loss of electrons near the entrance window of the sensor is also possible. Since electrons are not absorbed, but lose their energy by generating electron hole pairs along their path of movement, the lost energy can take any value between 0 and the energy of the electron. The sum of many such events is a uniformly distributed contribution to the spectrum between the peak of the incident photon and the energy of this photon minus the electron energy. To describe this contribution to the valley between the noise and the event peak – the so-called flat shelf – three cases must be differentiated. Besides the photoelectron, the creation of an Auger electron is the dominant process for light elements like silicon. [171] It has the energy of a characteristic X-ray minus the binding energy of the ejected electron. Both electrons can leave the sensor and any energy between nearly the one of the incident photon and 0 can be lost. It adds an offset to almost the whole valley. In the second case, the fluorescence photon or the Auger electron has completely absorbed in the sensitive area while the photoelectron leaves the sensor. Since the energy of the characteristic X-ray is detected, charge loss contributes to a further offset only above this energy. The resulting step in the offset is clearly visible in Fig. 5.3. In spectra generated with the ⁵⁵Fe source, the step itself is overlaid

^[a]Silicon

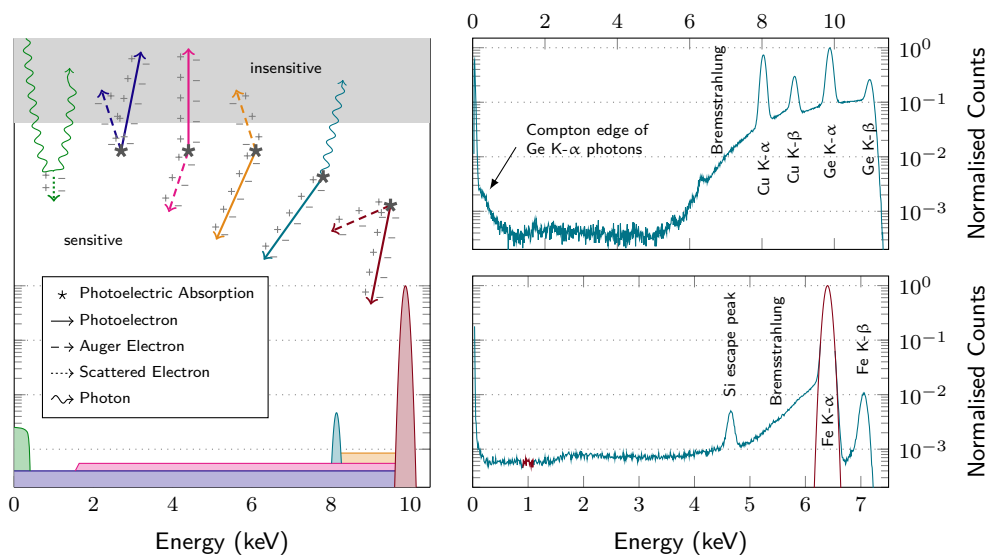


Figure 5.3: A typical spectrum with the most important features normalised to the iron K- α peak is shown in the lower right. Besides the K- β line, also the silicon escape peak is visible. The so-called flat shelf is caused by charge loss at the entrance window.^[79] The different contributions are sketched on the left. Colour coded – Compton scattering, three variants of electron charge loss, an escape photon as well as a completely detected event with their influence on the spectrum are shown from the left to the right. A star symbolises the photoelectric interaction of the incident photon. Tails on the low energy side of a peak can be caused by charge loss in the DEPFET or during the readout. In the shown measurements with the X-ray tube, the power spectrum of bremsstrahlung which is blocked by filters for higher energies dominates the region around the signal peaks. The edge of the noise peak is visible near 0 keV – together with an offset from Compton scattering for Ge. An incomplete clear would be also visible as tail at the high energy side of the noise peak.

by the aluminium emission line. However, the difference in the offset can still be detected in spectra that are not dominated by energy misfits or other effects like an incomplete clear (cf. Fig. 5.12). In the third case, only an Auger electron contributes to the charge loss. It adds an offset to the interval directly below the emission line peak with the size of the Auger electron energy. In this regime, the silicon escape peaks and potential charge losses or the bremsstrahlung contribution dominate the spectrum and its detection is even more delicate. Besides the energy misfits of non-storage DEPFETs and inter-frame split events, this offset with its two steps caused by charge loss at the entrance window also contributes to the level of the valley. Another feature is caused by an energy deposition via Compton scattering with the photon leaving the sensor afterwards. A photon that is backscattered by an angle of 180° transfers the maximal energy to an electron. It sets the maximum energy for the Compton continuum which is the Compton edge. For Mn K- α photons, it is 132.9 eV and can hardly be seen near the noise peak. But it increases to 377 eV for 10 keV photons which is in the order of the germanium K- α emission line which can be produced at Califa.

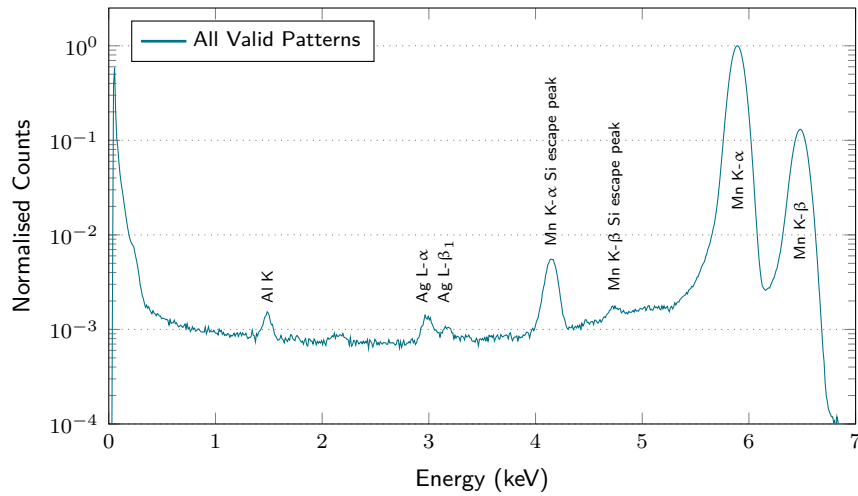


Figure 5.4: Spectrum of all valid events normalised to the ^{55}Mn K- α peak, obtained with a Cut Gate device. For a signal integration time of $1.90\ \mu\text{s}$ and a processing time per row of $6.1\ \mu\text{s}$, a mean noise of $2.76\ e^-$ ENC and an energy resolution of $140.5\ \text{eV}$ FWHM ($130.4\ \text{eV}$ FWHM for single events) at $5.9\ \text{keV}$ incident photon energy can be obtained.

5.3 Standard DEPFET

To classify the results measured with the Infinipix devices, a non-storage DEPFET was used for comparison. The baseline for spectroscopic DEPFET imaging sensors in X-ray astronomy was the circular Cut Gate structure as described in section 3.1. The DEPFET array used consists of 64×64 pixels with a pixel size of $75 \times 75\ \mu\text{m}^2$. The comparison of this and an Infinipix DEPFET array was done with a readout ASIC integration time of $1.90\ \mu\text{s}$ for each integration. In combination with a settling time of $0.70\ \mu\text{s}$ each and a clear of $0.85\ \mu\text{s}$, the total row time is $6.10\ \mu\text{s}$. That leads to a total frame time of $390.40\ \mu\text{s}$ for the 64 rows in the rolling shutter operation.

The integration time of $1.90\ \mu\text{s}$ is the result of an optimum timing for a total processing time of $5\ \mu\text{s}$ per row with an Infinipix and is used for comparability also for the Cut Gate device. The integration time is the dominant factor for the spectral performance in this timing regime assuming sufficiently long settling and clear times given. Since the layout limits the minimal gate length which also defines the maximum distance to the clear transistor, a Cut Gate requires a relatively long clear time. With a maximum distance to the clear gate of $20.8\ \mu\text{m}$, a clear time of about $800\ \text{ns}$ is necessary. But due to potential pockets in the internal gate caused by inhomogenities in the implantation edges, an average of 3.14 electrons – which is 0.2% of the Mn K- α signal – stays in the internal gate. Since the value varies for each pixel, it further broadens the measured peak of the Mn emission line. The resulting energy resolution for the investigated device is $140.5\ \text{eV}$ FWHM ($130.4\ \text{eV}$ FWHM for single events) which is affected by a mean noise of $2.76\ e^-$ ENC per pixel.

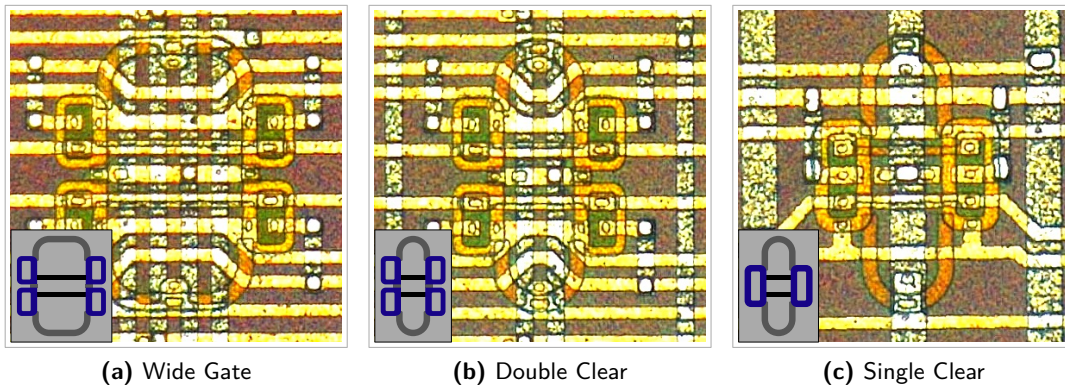


Figure 5.5: Top view of the layout variants. The basic structure is indicated by the drawings in the lower left. The *Clear Gate* which surrounds the *Clear* is presented in dark blue, the *External Gate* in black. The *Drain* and the surrounding *Ring* are separated by the poly-silicon layer in dark grey. The *Source* is in the centre. All other structures visible on the images are the aluminium lines for the power supply, the steering and the readout of the pixel as well as the contact holes to connect them to each other and to the different parts of the sensor.

5.4 Infinipix

Samples with pixels in the Infinipix layout exist in three variants on matrix scale. To use the same electronic components as for the 64×64 pixel non-storage prototypes (two steering and one readout ASIC), the number of pixels for the Infinipix devices was reduced to 32×32 , but with a pixel size of $150 \times 150 \mu\text{m}^2$. Only half of the channels of the Asteroid are used due to the shared readout node, but the steering ASIC is used with up to the same amount of channels since each pixel has two sub-pixels. For one variant, the number of clear channels is bisected. It is the standard variant of the three existing devices. The shared source node is edged by two parallel linear gates. The two other sides are connected to two clear transistors which can remove charge carriers from the internal gates that are formed below the external gates in the silicon bulk. To separate the two drain regions from the surrounding ring structure, additional poly-silicon structures form a transistor which is switched off permanently. An image of one pixel of this so-called Single Clear Infinipix is shown with an outline of the poly-silicon structure in Fig. 5.5c. The clear process should be possible only at a DEPFET switched on. That allows for the selection of the internal gate to clear, while the same clear transistor is also connected to the other sub-pixel. In case the collecting sub-pixel is not properly protected against the clear pulse, a second layout variant exists with the same dimensions, but clear transistors for each sub-pixel separately. It is the Infinipix Double Clear in Fig. 5.5b. A third layout variant with wider gates and, therefore, wider drain regions – the Infinipix Wide Gate (Fig. 5.5a) – was fabricated to ensure a working Infinipix in case different parts of the DEPFET located close together would influence each other excessively.

Before the 32×32 pixel arrays were mounted on the ceramics carrier board, they had been

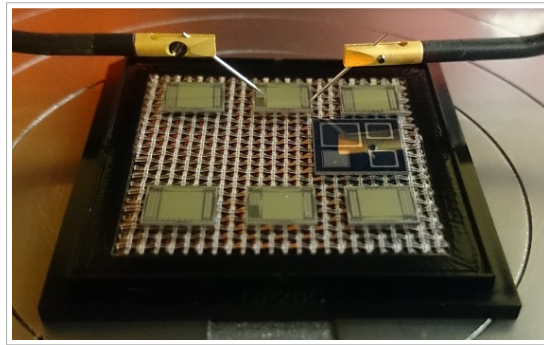


Figure 5.6: The functional test of six samples with two probes. The devices were spot-checked for electrical shorts that may occur between contact holes, poly-silicon and metal layers as well as inside the transistors.

spot-checked for electrical shorts to verify the quality of the wafer processing. The yield was unclear since the production had been finished just shortly before with the dicing of the wafers. The diode characteristics between the global contacts of the guard ring around the whole sensor, the ring in each pixel as well as the two drain regions and the substrate were tested to verify their principal functionality without the investigation of further details. In addition, in every tenth row the switchable contacts – gate and clear gate – were tested for electrical shorts among each other. None of the six samples – three layout variants from two wafers – showed any defects. That was also confirmed with the five samples mounted on a ceramics carrier board. Only one out of the 10 240 sub-pixels of the five DEPFET arrays was conspicuous. That is less than 0.1 ‰ of the tested DEPFETs.

The three investigated layout variants were taken from the same wafer – termed #W1 in this work – for reasons of comparability. To verify the outcome of these measurements and to further investigate the performance of the Single Clear and Double Clear Infinipix, these two layouts were also tested with DEPFET arrays from a second wafer, #W2. The actual naming on the wafer production is presented in Appendix A.

5.4.1 Charge Allocation

The silicon bulk is sideways depleted by the back side contact voltage and the drain and ring voltages on the front side. A set of minimum voltages is needed to fully deplete the sensor. In addition, the potential minimum in z-direction (cf. Fig. 2.9) has to be established relatively deep in the silicon bulk to avoid charge losses. That is, for the Infinipix, also the drift of charge carriers into the shielded internal gate. To ensure a deep position of the potential minimum plane, the ring and drain voltages have to follow a more negative back side voltage. However, the maximum absolute drain voltage is limited by a nascent impact ionisation at the boundary between gate and drain. The increasing noise limits the applicable voltages at the drain regions with respect to the energy resolution.

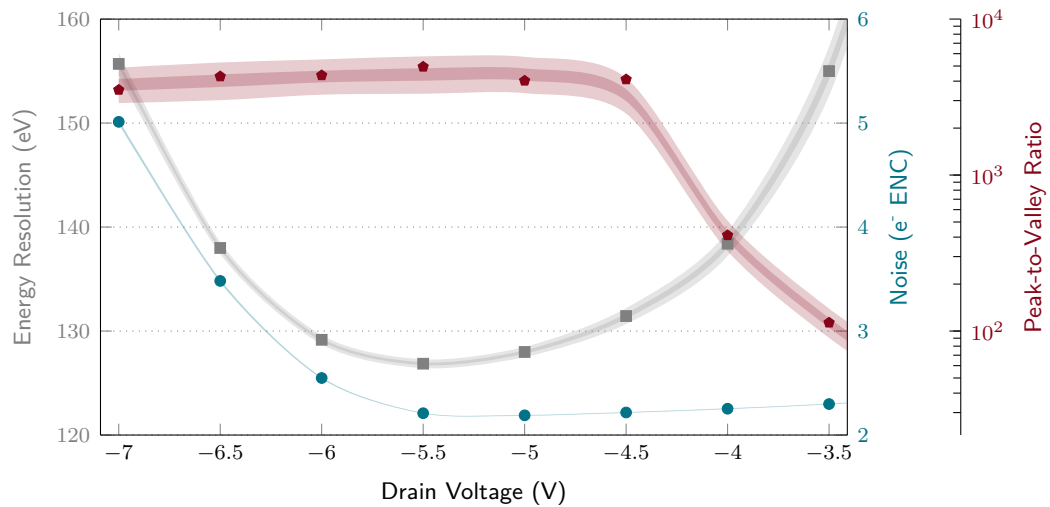


Figure 5.7: Noise and Peak-to-valley dependence for different drain voltages. The increasing noise for voltages at the drain region below -5.5 V and a dysfunctionality of the Infinipix principle above -4.5 V appears to be a worse performance in the energy resolution which is presented for all valid events here. The error bands represent the one and three sigma error of the measured values.

The result of these two effects is shown in Fig. 5.7. For a fixed back side contact voltage, the drain voltage was varied. A minimum of -4.5 V at the drain regions is needed to shield the internal gate that is read out. Otherwise, charge carriers can be lost into the wrong internal gate which decreases the energy resolution. With more negative drain voltages, the impact ionisation increases the noise which worsens the energy resolution as well. These two effects limit the operational window of the drain voltage depending on the requirements for the spectral performance.

Inhomogeneities

The necessary voltages to fully deplete the silicon bulk depend on the intrinsic doping of the wafer and, thus, its resistivity. The resistivity varies over distance to the wafer centre with nearly 20%,^[207] but also shows strong local variations.^[117] Among others, they are visible in the different depletion voltages necessary to detect a signal in a DEPFET pixel. Differences of up to 30% were measured within one sensor. It further limits the margin for the voltages that contribute to the sensor depletion. Due to the necessary depth of the electric field minimum in the sensor, the restrictions in the drain voltages also limit the applicable back side contact voltage. If the local bulk resistivity variations are larger than the available operational window of the back side contact voltage, the sensor is not operable as a whole. Such an example is shown in Fig. 5.8. The two sensors from #W1 were illuminated with the NIR LED and the back side contact voltage was varied. The colours represent the amount of signal that is collected in the internal gates. If the voltage is too positive, the sensor is not fully depleted. At the transition to the depletion of a pixel, charge is lost to the other

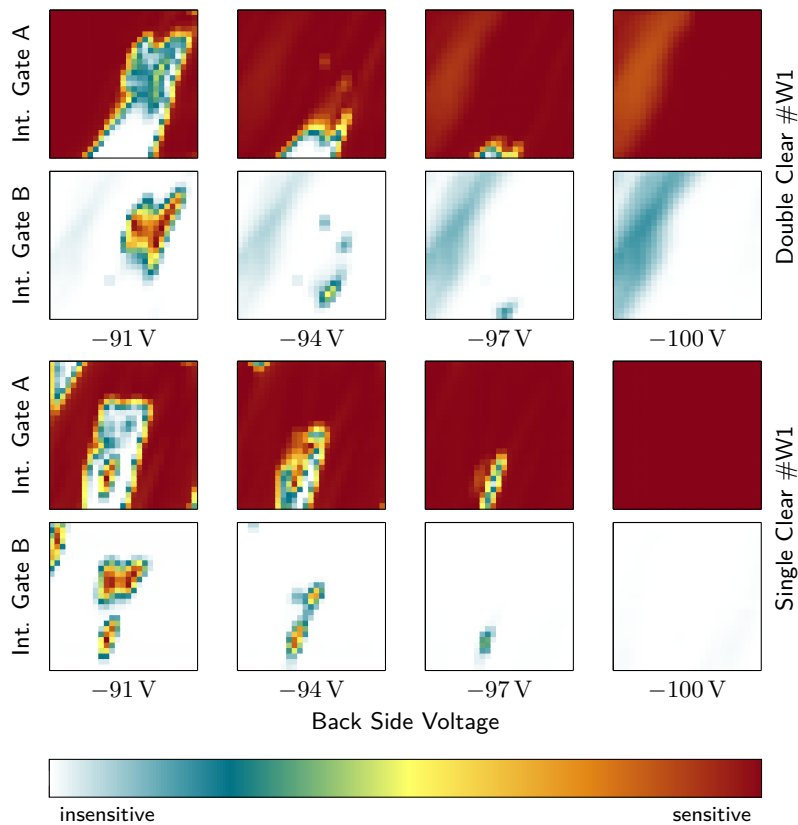


Figure 5.8: Charge loss from internal gate A to internal gate B for different back side voltages. The Double Clear from #W1 is not operable for one set of voltages since large areas of the sensor already lose charge to the other internal gate if all pixels are depleted.

internal gate. For the Single Clear #W1, the completely depleted sensor does not show any charge loss between the sub-pixels. The back side contact voltage necessary to also deplete the pixels with the lowest resistivity leads to charge loss in the over-depleted parts of the Double Clear #W2. A signal in the shielded internal gate (B) is visible already at -91 V.

Since the two samples from #W1 presented in Fig. 5.8 consist of different layouts, the influence of the pixel design and local resistivity variations in the devices have to be discerned and quantified. Two regions with 3×3 pixels which are depleted at the earliest and at the latest were selected in both layout variants from the two investigated wafers. Illuminated again with the NIR LED for different back side contact voltages, the turn-on displacement of the two pixel groups represents the bulk doping variations. The size of the plateau (see Fig. 5.9) is the operation voltage window defined by the layout of the Infinipix. These are the voltages which are sufficient to deplete the sensor, but positive enough not to lose a significant fraction of the charge carriers to the shielded sub-pixel. The Double Clear has an operation voltage window at the back side contact of about 15 V which is 40% larger for the Single Clear layout. Nevertheless, the strong bulk doping variations in Double Clear #W1 lead to differences in the depletion voltage of up to 23 V. Even for a Single Clear device it would result in an inoperable detector. An additional advantage of the Single Clear layout is

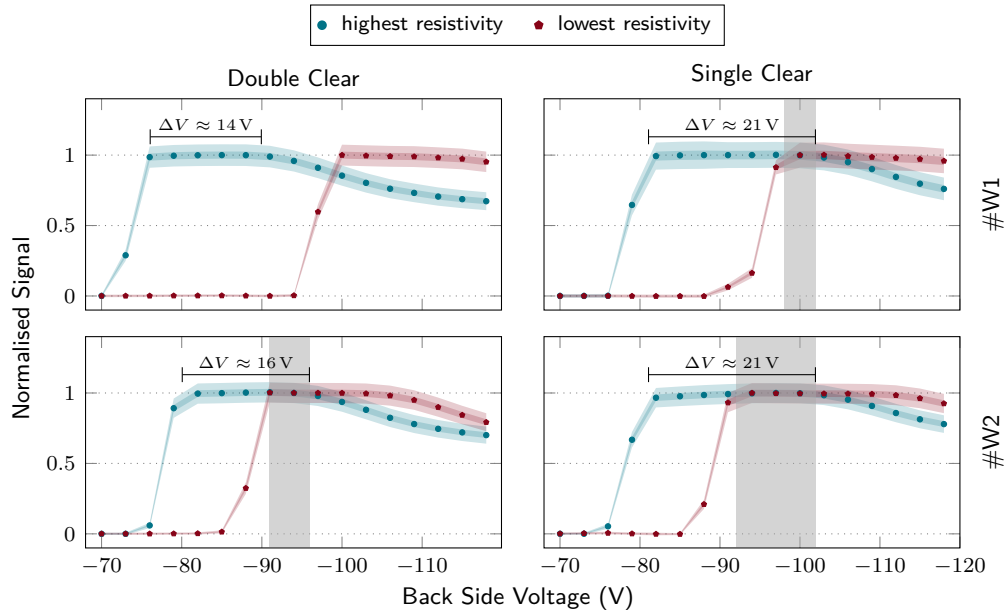


Figure 5.9: The operational window of the back side contact voltage is limited by two factors which are compared for four samples. Silicon bulk doping variations lead to a difference in the required minimum voltage for depletion for different areas of the sensors.^[117] The blue curves show the normalised mean signal for nine pixels that are fully depleted at first while the back side voltage is ramped up. In contrast, the red curves represent nine pixels which need the most negative back side contact. In addition, the layout defines different ranges in which the pixels are depleted, but do not suffer from charge loss to the other internal gate of the pixel. If this range is small and the bulk doping variations are high, like for Double Clear #W1, an operation of the whole sensor with the same voltages is not possible. The resulting operational window is marked by the grey bar.

the smaller clear region area (see section 5.4.3).

5.4.2 Charge Clearing

An efficient charge clearing process is essential for the spectral and timing performance of the DEPFET in an imager with spectral capabilities. The necessary clear time influences the noise performance of the filter function. An increasing flat top of the trapezoidal filter function raises the influence of the shot and pink noise (see section 5.1) and, moreover, limits the overall readout speed. In addition, an incomplete clear process appears as charge loss in the resulting signal produced by the correlated double sampling and worsens the spectral performance significantly.

Operation voltages

The operation voltages of the clear transistors are limited by various states that are not desired. The clear transistor has to remove the electrons from the internal gate after the

readout ASIC performed the first signal integration, but should not be attractive for charge carriers for the rest of the time. Appropriate voltages have to be applied for the on- and the off-state. If the transistor is switched off and the clear region is not coupled to the internal gate, it can still be attractive for electrons of the charge clouds drifting through the sensor. For that reason, the clear region has to be set to a sufficiently negative voltage while it is turned off. On the other hand, it has to be positive enough. Otherwise, it would serve as a source for electrons that would be drained to the internal gate. This so-called back injection also depends on the clear gate voltage which needs an adequate negative value to close the transistor.

A voltage at the clear gate that is too negative causes an inversion layer in the n-doped substrate under the clear gate and forms additional paths for a hole current between source and drain of the DEPFET. Since this conduction takes place alongside the influence of the internal gate, a measured result is distorted under such conditions. The clear gate may hold even the whole current which is, therefore, completely decoupled from the internal gate. This inversion in the clear transistor, charge loss to the clear region and the back injection form a two-dimensional, triangular operation voltages window.^[197] However, its size of several volts in both directions is sufficiently large not to cause any restrictions in the operation of a DEPFET.

Since the two sub-pixels of the Infinipix Single Clear have shared clear regions, the applicable voltages are further confined. The clear pulse has to remove the charge carriers from the shielded internal gate, but should not influence the number of electrons in the collecting sub-pixel. The two voltages at the clear transistor, clear and clear gate, have to be reduced in the way that the gate voltage of the switched off DEPFET causes a potential in the internal gate that is still more attractive than the clear structure. As a result, the clear region has an operation voltage window of several volts while the clear gate is limited to a few hundred millivolts. It is the voltage necessary to switch on the clear transistor during the clear process without removing electrons from the collecting internal gate which then would be drained into the clear and appear as charge loss in the measurement. A degradation of the spectral performance of several electronvolts or more would be the consequence.

Time and Completeness

The required time for an almost complete clear process depends on the maximum distance the electrons have to drift to the clear region. While the Cut Gate is limited to a minimum gate width of about $42\ \mu\text{m}$ – which is twice the maximum clear distance – the linear gates of the Infinipix exist with gate widths of nearly $32\ \mu\text{m}$ and $62\ \mu\text{m}$. The devices showed a huge difference in their clear performance. While the internal gate of the Infinipix Double Clear – the device with the narrowest gate – can be depleted completely with a clear pulse of less

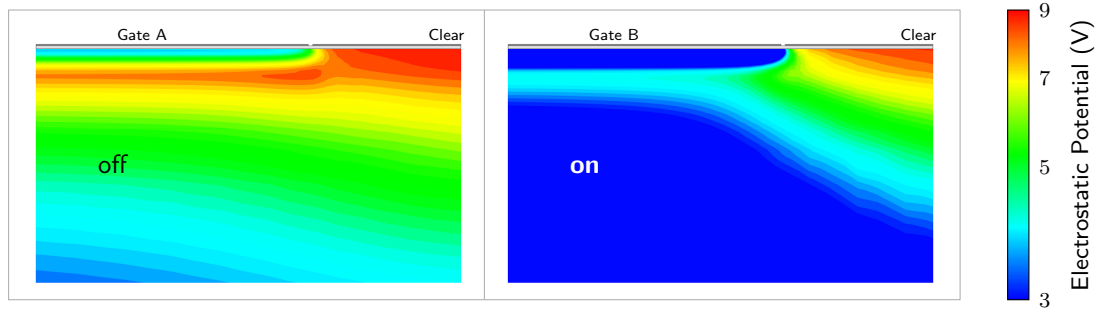


Figure 5.10: The electrostatic potential at the border of the internal gates and the clear gate. A 2D cut of a 3D simulation during a clear pulse in an Infinipix with shared clear is shown. The gate on the left side contains electrons and is switched off. The collected charge carriers stay in the internal gate due to the remaining potential barrier, even though they are pulled towards the clear gate. On the right side, all electrons would drift into the clear region.

than 70 ns, it requires almost 1 μ s or even more to remove the charge carriers from broader internal gates as good as it is possible within one clear cycle (see Fig. 5.11a). Electrons that are retained in potential pockets only diffuse slowly into the emptied internal gate and can be removed by clear pulses of the next readout cycles. This incomplete clear causes a degradation of the spectral performance at the order of 10 eV for the Cut Gate and the Infinipix Wide Gate. It was the main limitation of the spectroscopic DEPFETs in the past. With the narrow linear gate devices, the incomplete clear is overcome.

Besides charge loss into the clear during the off-state of the clear transistor which has to be avoided by appropriate voltages, electrons can drift from neighbouring rows directly to the clear of the active row during the clear pulse of the readout process. In case of an Infinipix, also the charge carriers in the same pixel are affected which actually should be collected in the sensitive sub-pixel. To investigate the quantity of the charge loss, the clear pulse of one detector row was sampled with LED pulses. The missing signal in the neighbouring rows of the homogeneously illuminated sensor could then be determined. As shown in Fig. 5.11b, the direct sub-pixel loses almost 25 % of the charge carriers. They are not electrons already collected in the internal gate, but those of charge clouds arriving at the DEPFET while the clear has been switched on. The next two rows in both directions are affected significantly, too. For the frame cycles which could be realised in measurements in this work, the effect of the charge loss on the spectral performance is negligible. But for the goal of a full parallel readout device with a clear time of approximately 10 % of the total frame time, the clear region has to be shielded more efficiently against electrons moving through the bulk.

5.4.3 Layout Variations

The two narrow gate Infinipix layouts show small differences in the back side contact operation voltage window as shown above. However, the Wide Gate features a much larger

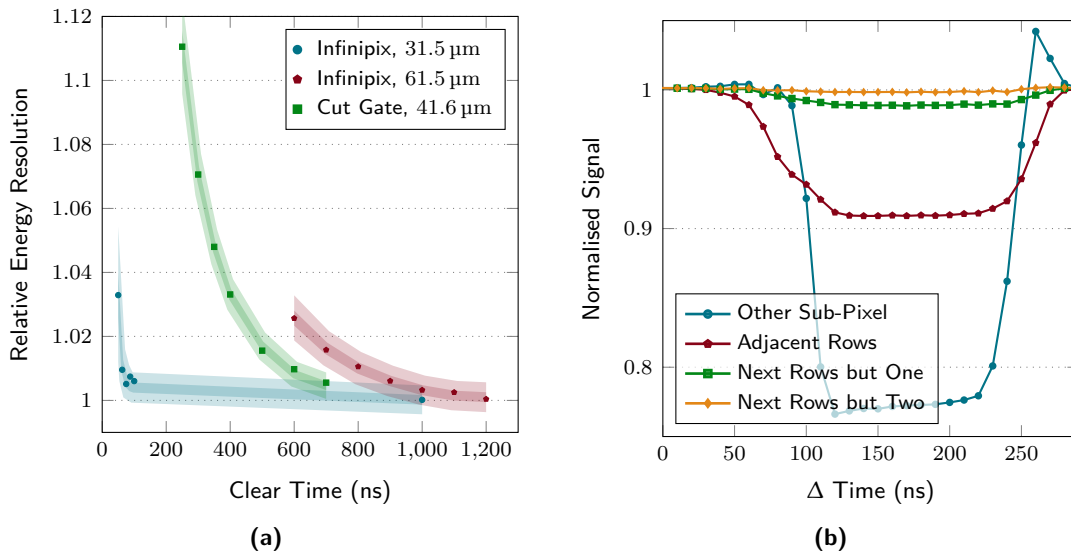


Figure 5.11: (a) The necessary clear time for three different gate widths. With increasing maximum distance to the clear transistor, the clear pulse needs to be longer to obtain the achievable energy resolution. (b) Charge loss during the clear process of one sub-pixel. The sensor was illuminated with the infra-red LED and its pulse has been shifted over the clear. Charge that should be collected in the other sub-pixel and in neighbouring rows is lost only if it arrives during the clear. There is no significant loss of electrons that are already collected in an internal gate.

robustness against bulk doping variations. But its overall worse performance caused by the incomplete clear behaviour might just create a wrong impression. The good performance the narrow gate devices can be operated at with a smaller operation voltage window could never be reached. With measurements, it is not possible to clearly disentangle both effects. A first hint that larger drain regions lead to a better suppression of charges being collected in the read-out sub-pixel is given by the Infinipix Single Clear that showed the best spectral performance. Compared to the Double Clear, the overall smaller clear area less constrains the drain regions. The potential differences in the two sub-pixels, therefore, will form in a more pronounced way. A smaller total clear area also reduces the risk of charge loss directly to the clear region and should always be selected as long as a good clear performance is guaranteed.

In the source follower readout mode, the source voltage is defined by the current to other regions of the sensor. It is the back side, the clear and, predominantly, the drain of the DEPFET. The current between the source and the drain and thereby the source potential is adjusted by the gate voltage in the transistor's on-state. In addition, the double clear layouts need a polysilicon separator to disconnect the source and the ring potential. It is a further p-channel MOSFET whose gate is on the source's potential in the current design. Since the ring voltage had a significant influence on the source potential, this transistor appears not to be completely switched off and features a parasitic current to the source. It adds a further complexity to the set of voltages which is avoided in the Single Clear layout.

The three layout variants from wafer #W1 were compared to each other with a relaxed timing of $6.1\ \mu\text{s}$ for the readout of one row. It is composed of $1.0\ \mu\text{s}$ for each settling and the clear pulse and $1.5\ \mu\text{s}$ per signal integration. The remaining $100\ \text{ns}$ are used for a delay between clear gate and clear to ensure that no electrons are back injected to the internal gate and for necessary steps in the control sequence to steer the ASICs. For a high flexibility at the early stage of the measurements and to avoid cross talk effects, the analogue signal is multiplexed to the ADC before the readout of the next row starts. Therefore, the processing time per row is $12.25\ \mu\text{s}$. Typical voltages are listed in Appendix C. The resulting performance is presented in Table 5.1. The difference in the spectral performance of the narrow gate and the Wide Gate variants is caused mainly by the incomplete clear. The worse noise performance due to the larger gate contributes with $3\ \text{eV}$ to the degradation of the spectrum for single events at the Mn K- α line. In case of the Cut Gate, it is only $0.5\ \text{eV}$.

Table 5.1: Noise and spectral performance of the three Infinipix layout variants compared to a Cut Gate. All devices were operated at a relatively slow readout to ensure a good clear behaviour and settled source nodes. The overall processing time per detector row was $12.25\ \mu\text{s}$. The Infinipix devices are all from #W1. Therefore, the results for the Double Clear are only from a small window of the sensor. The energy resolution is given as FWHM.

	Wide Gate	Double Clear	Single Clear	Cut Gate
Noise	$4.6\ \text{e}^-$ ENC	$3.5\ \text{e}^-$ ENC	$3.3\ \text{e}^-$ ENC	$3.6\ \text{e}^-$ ENC
Energy resolution @ 5.9 keV for single events	147 eV 137 eV	136 eV* 128 eV*	134 eV 127 eV	142 eV 132 eV
Peak-to-valley ratio	4000	4200*	4900	1000

* Only a small window ($\sim 20\%$) of the sensor

5.4.4 Window Mode

To investigate the performance of the Double Clear from #W1 without the limitation given by the bulk doping variations, the window mode was operated for the first time at a DEPFET array. This operation mode is one of the advantages of an active pixel sensor. For the sensor itself, no adaptations need to be done. Columns can easily be skipped with the skip bits of the readout ASIC. More challenging is the steering of the sensor rows. The sequence to operate the Switcher ASIC must not only activate the rows of the selected window, but has to ensure also a regular clearing of the remaining transistors of the sensor. If too much electrons are accumulated over time, the increasing number of mirror charges under the external gate can create a conductive channel without the application of an appropriate voltage at the MOS gate.

Windows of 16 rows and 13 columns – about 20% of the sensor – were selected. This can also be done with software and the rejection of the rest of the data after the measurement of the full sensor. It was used to verify the functionality of the actual window mode. As expected,

there is no significant difference visible in the data. All skipped pixels in the read-out rows are cleared during the readout of the window. In principle, the necessary clear process of all other rows can be done at once. As shown in Fig. 5.10, the transistor has to be switched on for a successful clearing of the internal gate. The drain-source current I_{DS} supplied by the readout ASIC is split over all transistors while the gate and drain level defined by external power supplies stay the same. As a consequence of the reduced current per transistor, the source voltage becomes more negative. It may reduce the gate-to-source voltage U_{GS} which then exceeds the threshold voltage U_{th} that is necessary to switch on the transistors. The potential of the internal gate would be dominated by the external gate voltage and not by the transistor channel potential.^[215] Since the gate voltage is more positive than the channel potential of a transistor in the on-state that is located between the source and the drain potential, the internal gate becomes more attractive and the clear pulse is less effective. The phenomenon was not studied in detail, but six rows could be cleared together ($I_{DS} > 16 \mu\text{A}$) while ten rows at the same time ($I_{DS} = 10 \mu\text{A}$) led to spilling internal gates that switched on the transistors all the time. It makes a readout of other pixels in the same column impossible. One may increase the drain-source current in general or adapt the gate voltage, but it is optimised for the readout and not for a full parallel clear process of all transistor rows not read out. With the current setup, no additional states than the two for the switched off and switched on single transistor per column are possible.

Besides a case in the laboratory with a detector that is operable with one set of voltages only on sub-sensor size, the window mode can be used to shorten the overall frame time. The higher readout frequency enables a higher throughput of this part of the sensor and facilitates a better time resolution. It makes an active pixel sensor more flexible since the throughput and the time resolution can be adapted to the properties of the observed object. In addition, it enables first tests for a high-speed operation as it will be provided by a full parallel readout device.

5.4.5 Timing

The Single Clear #W2 has the largest operation voltage window regarding the back side contact (see Fig. 5.9) and shows the best performance of all investigated Infinipix devices. It is, therefore, chosen for a more detailed investigation of the timing and noise characteristics. If a transistor is switched on in the source follower readout mode, the source node has to settle since the sources of all pixels in a column were on the level of the previously read-out pixel. If the first integration starts before the source has settled, this almost reproducible offset per pixel leads to a higher offset spread over the sensor. It limits the dynamic range for the actual signal measurement and leads to a higher noise for short settling times. The noise broadens the measured emission lines and adds features to the spectrum at low energies. They are

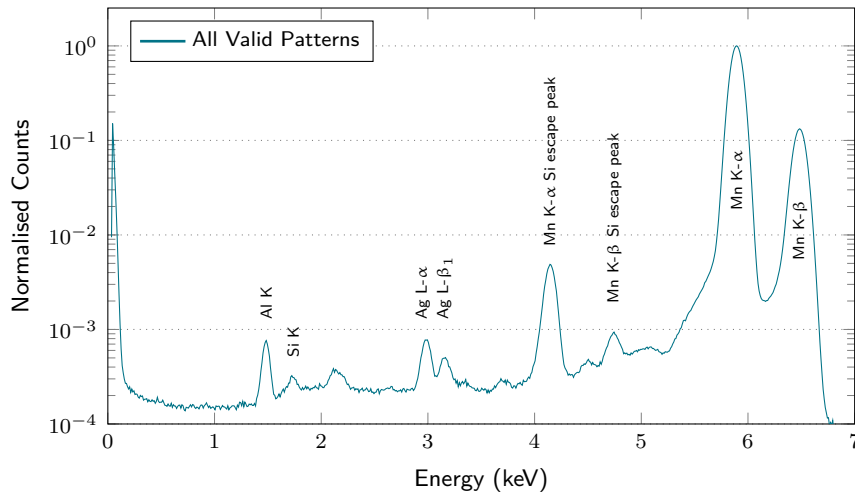


Figure 5.12: Spectrum of all valid events normalised to the ^{55}Mn K- α peak with good statistics and an optimised timing. The total processing time per row of $5.0\ \mu\text{s}$ contains an integration time of $1.9\ \mu\text{s}$. It features an energy resolution of $(127.40 \pm 0.07)\ \text{eV}$ FWHM for all valid events (single events: $(123.61 \pm 0.07)\ \text{eV}$ FWHM) and a noise of $(2.333 \pm 0.004)\ e^-$ ENC. The applied voltages are listed in Appendix C.

caused by a crosstalk from an event in the previous row. The source transitions differently and since it is not settled completely, the resulting offset differs and generates a fake peak. Therefore, almost settled source nodes are the requirement for a good spectral performance also at low energies of a few hundred electronvolts. A second settling is necessary after the clear process. The positive clear voltages pull the source voltage to a more positive value. Since this is the same for all pixels, an incomplete second settling does not reduce the dynamic range, but can still worsen the noise performance.

The settlings as well as the clear need a sufficient time to achieve a good performance. However, the signal integration time influences the various noise contributions differently. While longer integration times reduce the white series noise, the shot noise will be increased. In addition, every extension in the readout process increases the overall frame time as long as there was no additional exposure time that can be reduced. The longer the total exposure time is, the more thermally generated electrons are collected. Therefore, the optimal signal integration time is determined by a more detailed noise analysis that is presented in section 5.4.7.

The timing optimisation led to a readout per row of $5.0\ \mu\text{s}$. Each of the two settlings was set to $500\ \text{ns}$ with a clear pulse width of $150\ \text{ns}$. The remaining time is used for the signal integration which is $1.9\ \mu\text{s}$ per integration. With this final settings, a long measurement was done to obtain good statistics to verify the quality of the results of all previous measurements. It turned out that the amount of data was sufficient. But good statistics allows for a more detailed view on tiny effects and the analysis of the performance of single pixels. The optimisation process of the applied timing results in a significantly increased perfor-

mance. The noise is reduced to $(2.333 \pm 0.004) e^-$ ENC. It leads to an energy resolution of $(127.40 \pm 0.07) eV$ FWHM with a peak-to-valley ratio of 6900 ± 500 for all valid events and of $(123.61 \pm 0.07) eV$ FWHM for single events at 5.895 keV. The standard procedure to determine the energy resolution is a simple Gaussian fit to the emission line of interest. The standard deviation of that normal distributed peak is then converted to the FWHM using eq. (4.2). Due to good statistics, it is also possible to determine small residuals that still worsen the spectral features even for a sensor with such a good performance. For that purpose, a more complex fit function was introduced. Besides the Gaussian function, an exponential part plus a constant offset is added to the low energy side of the emission line to account for charge losses. A second exponential term on the high energy tail considers the pile-up of real events with noise excess. In addition, both peaks, the K- α and K- β emission lines of manganese, were fitted since their tails influence each other due to their close vicinity. The energy resolution of all valid events is determined as $(126.70 \pm 0.02) eV$ FWHM. It means that charge loss and noise pile-up cause a degradation by 0.7 eV and are negligible. The theoretical energy resolution at 5.9 keV considering Fano noise $[(50.8 \pm 0.5) eV]$ and the noise determined in the dark frames (12.4 eV) is $(123 \pm 1) eV$ FWHM.

With the theoretical mean number of electrons for a Mn K- α event

$$N_{e^-} = \frac{E}{w} = \frac{5895.1 eV}{3.71 eV/e^-} \approx 1589 e^- \quad (5.1)$$

at 200 K and the measured signal at the ADC, the overall amplification of the detector and the electronics system in the described configuration and an Asteroid gain reduced by a factor of two, it is determined as $4.76 \text{ ADU}/e^-$. Considering the range and the resolution of the ADC, it is $0.59 \text{ mV}/e^-$. Measuring all other components separately, the gain of the sensor can be quantified. The Asteroid amplification at its half gain combined with a signal integration time of $1.9 \mu\text{s}$ is 220.4. The electronics between the readout ASIC and the ADC has an amplification of 0.595. A Mn K- α event results in a voltage variation at the source of $\partial U_{GS} = 7.14 \text{ mV}$. The sensor gain \mathcal{G} then is

$$\mathcal{G} = \frac{g_q}{g_m} = \frac{\partial U_{GS}}{\partial Q_{\text{sig}}} = \frac{7.14 \text{ mV}}{1589 e^-} = 4.5 \frac{\mu\text{V}}{e^-}. \quad (5.2)$$

For a drain-source current I_{DS} of $100 \mu\text{A}$, g_m is roughly $0.11 \text{ mA}/\text{V}$ according to eq. (3.2). It results in a g_q of $0.5 \text{ nA}/e^-$.

A spectrum with high statistics also allows for the investigation of weaker emission lines. The ones around 3 keV could be clearly identified as the Ag-L lines. In that energy regime, also Ar-K lines are present in theory. They were also considered as the origin of the determined feature in previous measurements with less statistics. [23]

Drain switching

The faster the readout, the more important becomes the time the global drain switching takes. Due to the finite size of the charge cloud, the limiting factor is not just the switching time of the drain regions. It is the convolution of this switching time and the temporal arrival of the charge carriers at the Infinipix DEPFET. Since this parameter cannot be determined separately, it has to be extracted from a few measurements taken with the NIR LED (cf. section 4.3.3). Its pulse was temporally shifted over the switching process in the sensor and the fraction of signal that is collected in one or the other sub-pixel was determined. Since the signal from the LED is composed of many NIR photons, it has an intrinsic temporal spread even before any interaction in the sensor has taken place. To determine the timing performance of the LED, it was investigated with a photodiode (see Fig. 4.6c). Since also the photodiode has a finite time resolution, it was surveyed with a picosecond laser whose pulse is three orders of magnitude shorter than the times of interest and, therefore, can be treated as infinitesimal short. The photodiode broadens the pulse to a peak with a standard deviation σ of 0.55 ns. For a measured LED peak width of 7.37 ns, it results in the actual width of $\sigma_{\text{LED}} = 7.35$ ns. The switching process can be described by an error function which is the convolution of a Gaussian function with the Heaviside step function. This Gaussian function describing the switching process and the one defining the charge cloud size, form the convolution that is measured as charge distribution in the internal gates of the two sub-pixels. The intrinsic spread σ_{LED} of the charge cloud can be subtracted out of the result while the further spread during the movement through the sensor cannot be determined and is still included in the result. The measured switching time is $\sigma = 13.19$ ns which results in a drain switching time of $\sigma_{\text{Dr}} = 10.95$ ns including the charge cloud broadening in the sensor. It is a switching time of 28 ns from 10 % to 90 % of the voltage level. The time in which on average more than 0.1 ‰ of the signal – which is less than one electron of a Mn K- α peak – is collected in the other sub-pixel, is 85 ns.

The actual switching time of the drains can be estimated by measuring the temporal behaviour of the voltage level at the steering lines to the sensor. They are directly connected to the drain regions without any further resistor besides the resistance of the steering lines. The σ_{Dr} obtained from this measurement is 8.1 ns. It results in an affected time of 63 ns in which more than 0.1 ‰ of the signal, on average, would end in the other sub-pixel. As expected, it indicates that the charge cloud generated by the LED pulse is further broadened while it moves through the sensor. With the determined numbers, it has a σ of 10.4 ns as it arrives at the DEPFET. It also shows that the temporal charge cloud size and the switching time of the drain regions are at the same order of magnitude.

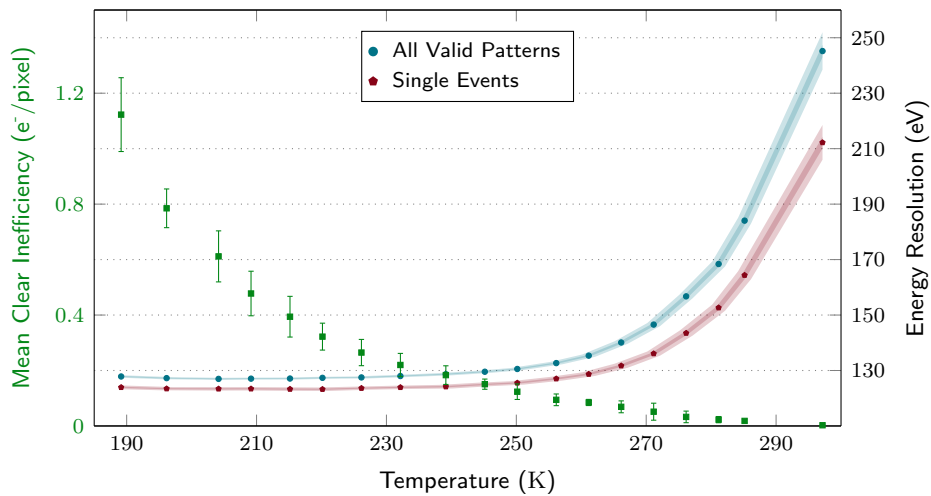


Figure 5.13: Measured energy resolution of single and all valid events for different temperatures. At low temperatures, the clear process becomes more inefficient which counteracts a further improving energy resolution.

5.4.6 Temperature Dependence

To investigate the stability of the spectroscopic performance against temperature variations, measurements over a range of more than 100 K were taken. The voltages at the detector and the current through the DEPFET were kept constantly over all measurements. With increasing temperature, the leakage current in the sensor raises exponentially.^[216] Since the shot noise scales with the current, the overall noise performance decreases for higher temperatures and worsens the energy resolution of the detector. Nevertheless, the spectral performance is almost constant over a range of 60 K. While the sweep goes up to room temperature, the lower limit is set by the Stirling cooler. It also depends on the environmental conditions since the Stirling is cooled by fans and radiators on its warm side. The minimum set temperature at the Stirling cooler achievable in the laboratory is at about 70 K. The difference of 120 K is lost over the thermal resistance of the copper cooling chain and interfaces with a poor heat conduction. In addition, the detector is heated by its link to the iPCB via 110 metallic pins for the voltage supply as well as the steering and readout signals. Besides the dominant effect of the leakage current noise, also thermal noise increases with temperature. It is almost not visible in the trend of the energy resolution since the clear process becomes more incomplete with decreasing temperature. It has a complementary effect on the energy resolution. The higher inefficiency in the clear process is caused by a slower diffusion at lower temperatures^[60] that is necessary to empty potential pockets in the internal gate. The uncertainty in the clear process is the reset noise which increases with the incompleteness of the clear.

5.4.7 Noise

The readout noise of the detector is determined with dark frames – frames taken without any photon source. The direct investigation of the noise instead of its influence on the energy resolution has the advantage that it is almost free of reset noise and charge loss effects. In addition, there is no superposition with the Fano noise of a charge cloud that worsens the spectral performance the most. In the absence of reset noise, the noise deviation for temperature variations are limited to thermally generated charge carriers – the white series noise – and shot noise caused by leakage current. The white series noise is proportional to the square root of the absolute temperature (cf. eq. (3.8)) while the leakage current and, thereby, the shot noise increases exponentially with temperature. This exponential term was separated from the other noise components by a fit which is plotted in the lower left of Fig. 5.14. It shows clearly that under typical measurement conditions between 200 K and 220 K, there is almost no leakage current while it dominates the noise performance above 270 K. The necessity to cool the sensor is demonstrated. A further reduction of the temperature below 220 K reduces the remaining noise components only slightly. In addition, below 200 K, the energy resolution seems to worsen again (Fig. 5.13) – caused by reset noise of an increasing incompleteness of the clear process.

The readout noise can be investigated by varying the integration time τ . The individual noise contributions are affected differently by a changing integration time (cf. eq. (3.6)). The pink noise is independent of τ and constant as long as the ratio between integration time and the length of the flat top is constant.^[74,157] For a constant flat top, a longer integration time also reduces the pink noise since its form converges against the more optimal triangular form. The main contributor at short integration times and temperatures below 250 K is the white series noise. It scales with τ^{-1} and describes the measured noise shown in the upper left of Fig. 5.14. The shot noise generated in the transistor channel scales with τ . At the measured integration times and applied temperatures, it is not visible. Longer integration times were not feasible at the setup in use since the overall detector gain scales with τ . It shifts the peak generated by the incident photons out of the dynamic range. Even though the noise itself is determined from dark frames, the event peak with the known theoretical energy and, therefore, the number of generated electrons is needed to calibrate the results from the noise calculations. To neglect further noise contributions, the total frame time was fixed to 448 μs for all measurements. Otherwise, thermally generated charge carriers are accumulated in the internal gate. This linear effect is shown in the upper right of Fig. 5.14. The superposition of the two effects – an integration time variation without further exposure time – results in an optimum processing time per row between 5 μs and 9 μs .

The necessary voltages at the drain regions for the functional principle of the *Infinipix* have already caused a nascent impact ionisation at the boundary between gate and drain (sec-

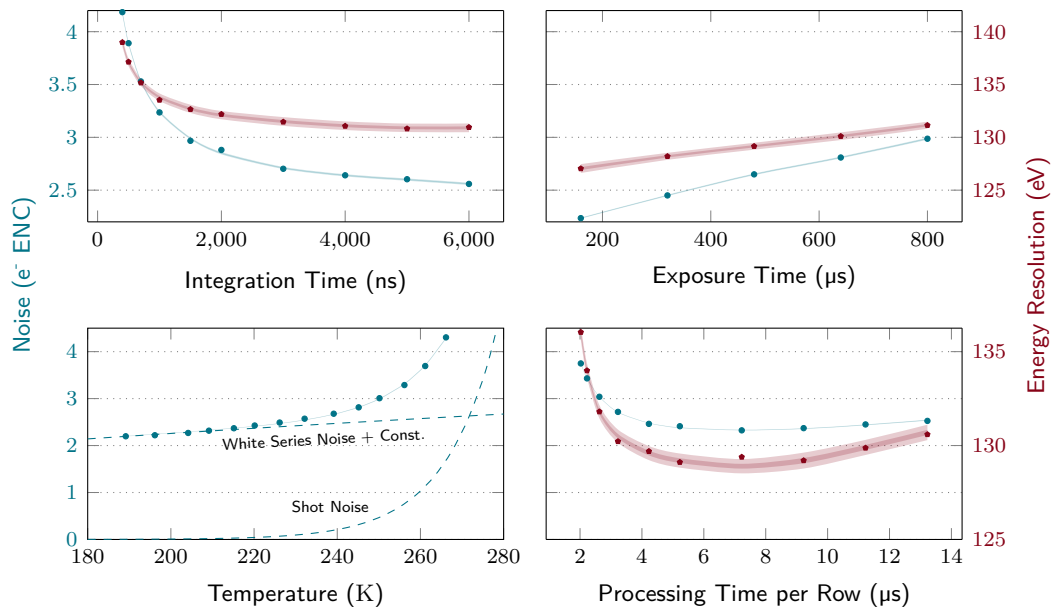


Figure 5.14: Contribution of the noise with varied timing and temperature parameters. On the upper left, the exposure time of $448\ \mu\text{s}$ is kept constantly while the integration time is varied. In the plot in the upper right, the readout time per row of $5\ \mu\text{s}$ and, thereby, the total readout time of $160\ \mu\text{s}$ is constant with varying exposure times enabled by a hold in the readout sequence. The summed noise effects from these two plots are a combination of the reduced readout noise and the collection of thermally generated charge carriers due to longer exposure times as a consequence of the extended readout. The result shown in the lower right is an optimal timing for the sensor of about $5\ \mu\text{s}$ to $9\ \mu\text{s}$ per row. In the lower left, the increasing contribution due to thermal noise including shot noise due to raising leakage current is shown. The dashed lines are the fitted contributions of the white series noise together with the pink noise and the shot noise which scales with the exponentially increasing leakage current. All measurements with fixed temperature were taken at $220\ \text{K}$.

tion 5.4.1). It increases the overall noise by more than 10% compared to lower drain voltages. With future technology improvements (see section 7.1.1), this unnecessary noise contribution is expected to be avoided and enables values of about $2\ e^- \text{ ENC}$ for a readout processing time per row of $5\ \mu\text{s}$.

Because the dominating white series noise scales with the width of the gate W and the gain \mathcal{G} is improved by shrinking W , the overall noise performance increases with decreasing gate widths. It is an additional advantage of the linear gate that allows for the reduction of the gate width compared to the Cut Gate layout. A noise of $2\ e^- \text{ ENC}$ contributes to a Mn K- α line broadening only with $1.3\ \text{eV}$ for single events at FWHM. The reduction of the noise by small gates and sufficiently long signal integration times is therefore the key to a nearly Fano noise limited spectroscopic performance. Furthermore, narrower gates enable shorter clear times which allow for a longer signal integration for a given timing requirement.

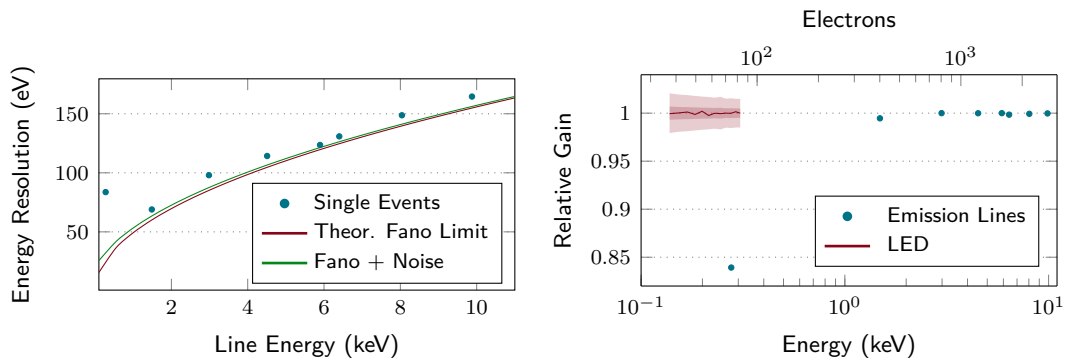


Figure 5.15: Spectra of different emission lines are compared to the theoretical Fano limit and the Fano limit combined with a noise of $2.3 e^-$ ENC on the left. The gain dependence for different energies of incident photons is shown on the right. The errors of the determined values are smaller than the plotted points representing the data. Measurements with LED pulses show that it is not a linearity problem of the DEPFET, but charge losses at the entrance window. The intensity of the LED was calibrated with a ^{55}Mn measurement under the same conditions.

5.4.8 Linearity

Low energetic emission lines like carbon at 277 eV or strongly redshifted spectral features from distant celestial objects require a good energy resolution also at low energies of a few hundred electronvolts. With the X-ray tube of Califa, the atoms of several targets were excited and the emitted characteristic radiation was measured. The determined energy resolutions for different emission line energies follow the the curve of the theoretical Fano limit, but show a strong deviation for low energies (see Fig. 5.15 and Table 5.2). The penetration depth of less energetic X-ray photons is lower. This increases the probability that a part of the energy is deposited outside the sensitive area of the sensor^[173] and adds a further statistical fluctuation to the final charge cloud. Nevertheless, the determined energy resolution of the carbon line above 80 eV FWHM is much higher than expected. With pnCCDs, an energy resolution below 50 eV FWHM could be achieved.^[125] The DEPFETs for MIXS comprise an energy resolution of about 60 eV FWHM.^[118] A detailed study of the entrance window of the sensor would go beyond the scope of this thesis. But the technology of the production run which contained the present Infinipix arrays was not optimised for spectroscopic measurements. It needs to be investigated in the future with devices from the Athena prototype and pre-flight production to certainly exclude a principal disadvantage of the Infinipix layout. A first indication that the degradation of the spectral performance at low photon energies is caused by charge loss at the entrance window are the clearly visible step-like features in the flat shelf originating from Auger and photoelectrons leaving the sensitive volume (cf. Fig. 5.3). The effect would be orders of magnitude lower for a perfectly sharp entrance window. Also the pnCCDs from eROSITA show a weaker flat shelf and its steps can hardly be seen due to a more optimal entrance window.^[79]

The decreasing gain for low energetic X-ray photons is caused by charge losses at the entrance

Table 5.2: The energy resolution expressed as FWHM for different emission lines compared to the theoretical Fano limit. In addition, the theoretical limit for a Fano noise plus the determined dark frame noise of the detector is given. To reduce charge loss effects and the influence of changing pattern statistics due to the charge clouds size, the energy resolutions are given for single events of the α emission lines.

Emission Line	Energy ^[192]	Fano Limit	Fano + DF Noise	Energy Resolution
C-K	277 eV	(25.9 ± 0.3) eV	(33.0 ± 0.2) eV	(83.7 ± 0.4) eV
Al-K	1486.6 eV	(60.1 ± 0.5) eV	(63.4 ± 0.5) eV	(69.0 ± 0.2) eV
Ag-L	2983.7 eV	(85.1 ± 0.8) eV	(87.5 ± 0.7) eV	(98.0 ± 0.4) eV
Ti-K	4508.8 eV	(104.6 ± 0.9) eV	(106.6 ± 0.9) eV	(114.3 ± 0.2) eV
Mn-K	5895.1 eV	(119 ± 1) eV	(121 ± 1) eV	(123.6 ± 0.2) eV
Fe-K	6399.5 eV	(125 ± 1) eV	(126 ± 1) eV	(130.9 ± 0.2) eV
Cu-K	8041.0 eV	(140 ± 2) eV	(141 ± 2) eV	(148.7 ± 0.5) eV
Ge-K	9875.9 eV	(155 ± 2) eV	(156 ± 2) eV	(164.6 ± 0.6) eV

window, too.^[118] The mean charge loss due to smaller penetration depths for lower photon energies appears as a change in the gain. The linearity scan was repeated with the NIR LED at low energies. To ensure a linear behaviour of the LED, the intensity was varied by the number of pulses within one frame and not by an adaption of the supply voltages or the pulse length. Since the intensity of a monochromatic light source and not the energy of single photons with different energies is determined, entrance window effects can be excluded (see Fig. 5.15). First results from the LED also showed a decreasing gain at low energies. In a more detailed analysis, they were determined as transient response from the LED driver circuit. To omit these charging effects in the LED circuit which distort the actual result, the distance of the LED pulses was kept constantly and the exposure time was extended to add more LED pulses and, thereby, intensity to a frame. Therefore, a separate offset calibration of every measurement is necessary to determine the dark current. Further effects by a heating of the operated LED in the vacuum chamber could be neglected by observing the intensity during a measurement. Below 100 eV, there are still deviations visible. But since they do not show clear trends in different measurements, a still unknown behaviour of the LED cannot be excluded. Furthermore, the analysis of the dark current did not show any non-linearity. Since it adds $2.47 e^-/ms$ to the internal gate of one pixel, the linearity is verified down to sub-electron accuracy because no deviation is visible even for frame times of a few hundred microseconds.

5.5 DEPFETs at High Speed

A significant degradation of the spectral performance only occurs at high frame rates. Thereby, the invention of a DEPFET with storage is useful only for sensors dedicated for high time resolutions or the reduction of pile-up caused by bright celestial sources. The effect is too small for the additional effort otherwise. The size of the sensor in a full frame readout

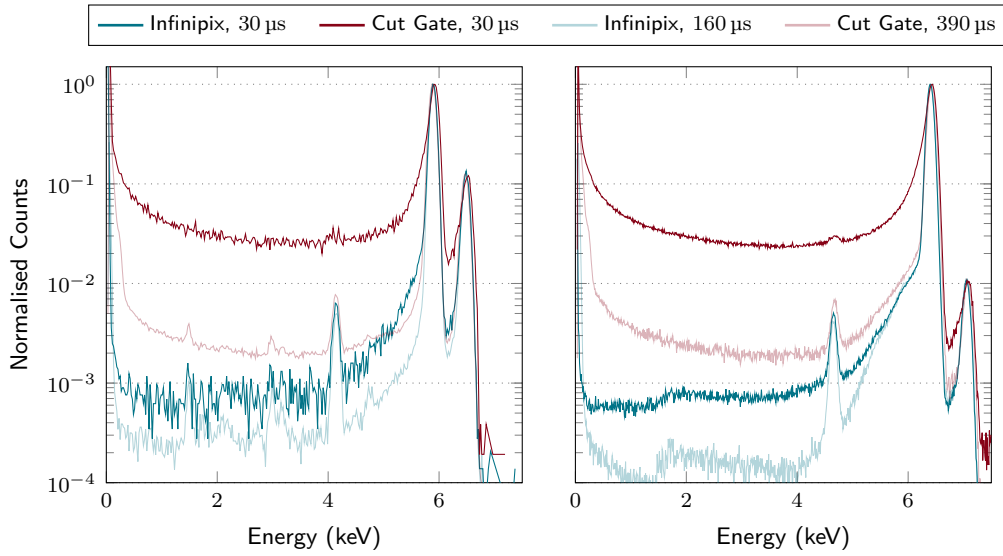


Figure 5.16: Spectra of single and double events normalised to the K- α peak for an ^{55}Fe source (left) and a Fe target using an X-ray tube with higher intensities for better statistics. The intense lines show the spectral responses for a readout with a frame time of $30\ \mu\text{s}$. To achieve this fast timing, only three rows are read out. All other detector rows are cleared only. The weak lines show the normal continuous rolling shutter operation of the full sensor for comparison.

with a continuous rolling shutter limits the achievable time resolution. Since no full parallel readout device has existed for measurements yet, the present samples were investigated in the window mode. The smallest useful window consists of three rows. The middle row is evaluated while the neighbouring rows are needed to identify split events. Due to the column parallel readout, the number of columns does not limit the achievable time resolution as long as there is sufficient time to transfer the analogue signals from the readout ASIC to the ADC. Besides the three rows read out, the internal gates of all others have to be emptied regularly to prevent a turning-on of the pixels in these rows. Since the Cut Gate needs a relatively long clear time, it limits the maximum speed in the comparison to an Infinipix. Using $5\ \mu\text{s}$ readout processing per row, an overall time resolution of $30\ \mu\text{s}$ can be achieved. The resulting spectra are shown in Fig. 5.16 for ^{55}Mn emission lines from an ^{55}Fe source and for Fe emission lines from the X-ray tube at Califa to improve the statistics. They only consist of single events and doubles, which split within the row in the centre. The measurements at high speed in the window mode are compared to standard full frame read-out data to show the influence of the energy misfits on the spectrum. The data from the Infinipix are also degraded since the fraction of inter-frame splits increases. Inter-frame splits can in principle be recombined which has not yet been implemented in the analysis tools.

A further influence on the spectrum is the pixel size. With smaller pixels, the probability of parts of the charge cloud collected in neighbouring pixels which are not detected since they are below the threshold increases. While the Infinipix devices feature a pixel size of $150 \times 150\ \mu\text{m}^2$, the Cut Gate only cover a quarter of that area per pixel. It broadens the

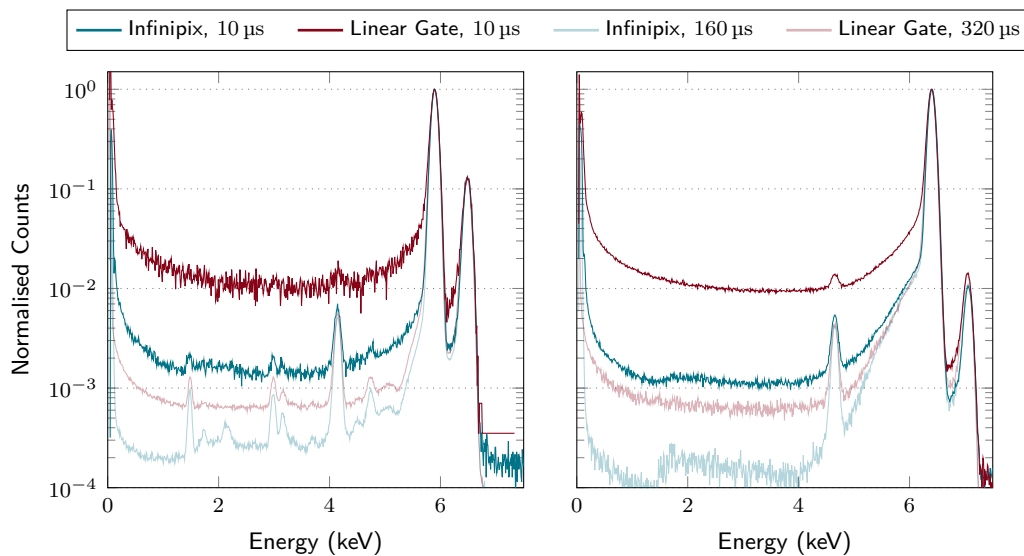


Figure 5.17: Spectrum of single and double events normalised to the K- α peak for an ^{55}Fe source (on the left) and a Fe target using an X-ray tube as shown in Fig. 5.16, but for a Linear Gate from the Athena prototype production. The shorter clear times of the narrower gates allow for shorter frame cycles of $10\ \mu\text{s}$ which was also the fastest readout realised with the Infinipix.

noise peak at $0\ \text{keV}$ clearly visible for the Cut Gate sample. With the availability of linear gate devices without storage for the Athena prototyping phase, it is possible to compare two layouts with almost the same pixel size ($130 \times 130\ \mu\text{m}^2$ for the Athena Linear Gate devices) and comparable timing performance. The readout processing time of the three rows was reduced to $2.5\ \mu\text{s}$ per row. The fast clear of the narrow linear gates also enables a fast clear of the remaining rows. A time resolution of $10\ \mu\text{s}$ was realised. The result is shown in Fig. 5.17 and Table 5.3.

Table 5.3: The energy resolution FWHM_E and the peak-to-valley ratio for all single events as well as doubles that split within the evaluated row of the read-out window. Since other events do not exist in the $10\ \mu\text{s}$ measurements, they are also skipped in the full frame results for a better comparison. The numbers correspond to the spectra shown in Fig. 5.17.

		^{55}Fe Source 5895.1 eV		X-Ray Tube, Iron Target 6399.5 eV	
		FWHM_E (eV)	Peak/Valley	FWHM_E (eV)	Peak/Valley
Linear Gate	Full Frame	131.4	1400	138.6	1300
	Window	144.4	70	149.0	70
Infinipix	Full Frame	125.6	5400	134.8	9600
	Window	131.2	700	138.9	800

A difference in the spectral performance is still clearly visible even though it is smaller than for the comparison with a Cut Gate which suffers from its small pixels of the existing devices. The benefit of a DEPFET with storage will increase with full parallel readout devices and an inter-frame split recombination. Especially weak spectral features at the low energetic side of a dominant emission line can be detected more easily with a DEPFET with storage. If

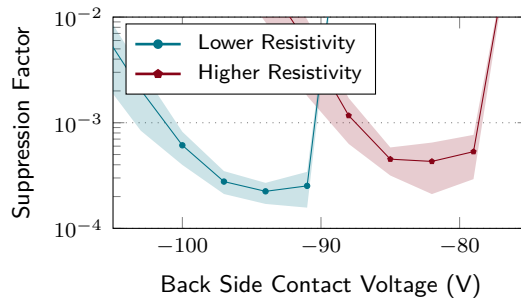


Figure 5.18: The suppression factor for different regions of the Double Clear #W1. Due to the large resistivity variations in the wafer, the necessary back side contact voltage to completely deplete the bulk is different. But it shows that a lower resistivity leads to a better shielding of the internal gate.

the degradation of the spectral performance is too strong or the feature is too weak, such details can vanish in the detector background completely.

5.6 Review of Results

The successful implementation of a DEPFET with storage was already demonstrated on single pixel basis by Bähr et al. (2014).^[23] With the measurements performed in the scope of this thesis, also their operation on matrix scale was verified. Even more, with an energy resolution of (123.61 ± 0.07) eV FWHM for single events from the Mn K- α emission line at 5.895 keV, a better spectral performance than ever before with an array of DEPFETs at such timing conditions (160 μ s per frame, 5 μ s per row) was achieved. Only the new Athena Linear Gates show a comparable, slightly better energy resolution, but suffer from a larger detector background due to energy misfits. The noise performance of Infinipix devices is at (2.333 ± 0.004) e⁻ ENC at the same readout speed at 220 K.

With the three Infinipix layout variants existing as APS arrays, the influence of the layout on the different performance parameters could be determined. It is a starting point for the further optimisation of the layout. The width of the DEPFET gate and, therefore, the maximum distance inside the internal gate to a clear region is the most important key for an excellent spectroscopic performance at the current status of development. On the other hand, large drain regions lead to a higher robustness of a design against bulk doping variations with respect to the shielding of the read-out internal gate of an Infinipix. This intrinsic properties of the wafer material cannot be influenced. Therefore, it is important to have a reliable layout which provides a robust performance. The differences of the three investigated layout variants are summarised in Table 5.4.

Since the gate width and the size of the drain regions are connected to each other in the present layouts, a decoupling of the two dimensions is necessary as far as it possible. In

Table 5.4: The existing and investigated Infinipix layout variants show different advantages and disadvantages. The most important are summarised in this table. They also serve as starting point for a further layout optimisation.

Layout	Advantages	Disadvantages
Wide Gate	<ul style="list-style-type: none"> – Most robust against bulk doping variations – Large clear operation window 	<ul style="list-style-type: none"> – Slow and incomplete clear
Double Clear	<ul style="list-style-type: none"> – Excellent spectroscopic performance – Fast and complete clear – Large clear operation window 	<ul style="list-style-type: none"> – Most sensitive to bulk doping variations
Single Clear	<ul style="list-style-type: none"> – Excellent spectroscopic performance – Fast clear – Saving of steering lines – Simplest layout 	<ul style="list-style-type: none"> – Sensitive to bulk doping variations – Small clear operation window

addition, the omitting of a ring-source transistor reduces the complexity and seems to be feasible. The operation windows of the clear voltages are reduced for a shared clear region, but show no limitation in the successful operation of such a Single Clear Infinipix. In addition, smaller clear region areas and more negative clear voltages decrease the risk of charge loss directly to a clear region during the charge collection. A significant charge loss is visible in the row which is read out (25% in the collecting sub-pixel) and in the adjacent rows. The faster the readout is, the larger is the fraction of clear time to exposure time. In case of a full parallel readout with a processing and, thereby, frame time of 1 μs , the clear will be in the on-state at about 10% of the time. A good shielding of the clear region is, therefore, mandatory.

The large bulk doping variations of the Single Clear #W1 which made an operation of the whole sensor with one set of voltages impossible, opens the possibility to investigate an option for a technology adaption. Lower dopant concentrations lead to a higher resistivity of the semiconductor which requires lower voltages for a full depletion of the bulk. By the investigation of this depletion voltage, the resistivity can be determined. It shows that areas of the sensor with a lower resistivity show a better charge suppression at the internal gates (see Fig. 5.18). Differences in the energy resolution could not be determined. However, the selection of a suitable wafer material can increase the performance of an Infinipix. The effect can also be investigated with simulations easily in addition to layout variations. It may further help to improve the shielding of the clear region.

Simulations

Not all effects can be addressed by measurements. Either because it is not possible to measure the quantity separated from other influences or because a measurement is not possible with the present samples. Simulations help to understand the measurement results and – due to the long manufacturing process of up to two years – to speed up the layout development by testing new ideas. In addition, quantities like the pixel size that also influence the spectral performance can be investigated separately while all other conditions are kept constantly. It allows for the exploration of features and devices that have not yet been fabricated and whether it is worth to produce them.

6.1 Device Simulations

As it turned out in the measurements, the area of the drains is the key parameter for the size of the operational window of the back side voltage and, in turn, for the robustness of the functionality of the Infinipix. For the existing layouts that were all investigated, the size of the drain regions scales with the gate width. Since the distance from the centre of the internal gate to a clear region – the maximum clear distance – is connected to the gate width, the clear behaviour limits the extension of that measure. To combine these contrary effects, the layout has to be adapted differently than only by the gate width. Concepts to realise narrow gates with large drain regions are investigated with 3D simulations with Synopsys TCAD.^[224,225] Existing Infinipix DEPFET layouts were simulated by Aschauer et al. (2014)^[5] already before. The analytical doping profiles are adapted to the actual fabrication parameters which were applied during the production at the semiconductor laboratory of the Max Planck Society. To quantify the impact of a layout to the robustness against varying operation voltages, the movement of charge carriers induced near the back side of the sensor was simulated. The fraction of charge collected in the shielded internal gate for different voltages at the back side contact of a pixel then indicates the operation voltage window with regard to the suppression factor.

To reduce computation time, only one pixel was included in the 3D simulations. Furthermore,

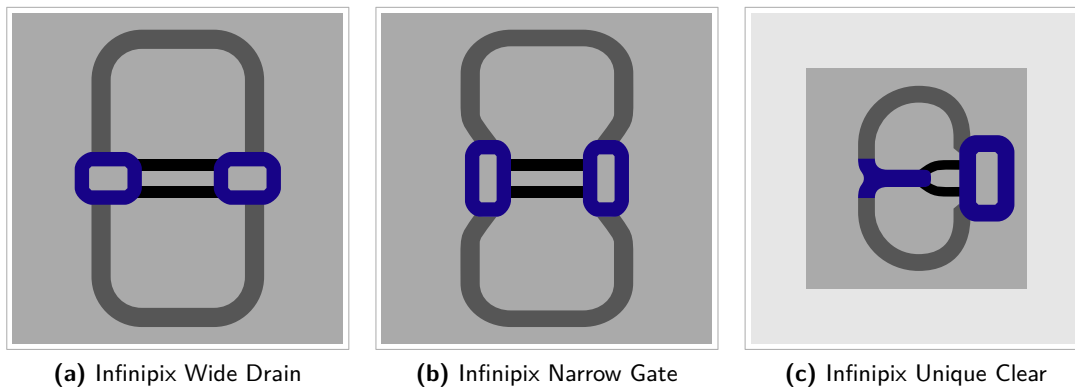


Figure 6.1: Based on the findings from the measurements, new layouts were investigated by simulations for a DEP-FET with integrated storage. The main approach is the maximisation of the drain regions for a more robust suppression factor while the gates need to be narrow enough for an efficient clear process. The Infinipix Wide Drain and Infinipix Narrow Gate were simulated with a pixel size of $150\ \mu\text{m}$ while the Infinipix Unique Clear has been designed on an $100\ \mu\text{m}$ pixel due to its compact layout. The measures are listed in Appendix D.

symmetries in the pixels were used. In most cases, only the half of a pixel was integrated in the simulation tools. Nevertheless, to achieve reliable results, up to about one million grid nodes were necessary. Since the Poisson equation has to be solved for every node at every time step, it results in computation times of several days for a simulation from the generation of the grid to the final results with generated and collected charge carriers with the available computation infrastructure. These are 1 TB of RAM^[a] and 64 processor cores with clock rates of 2.2 GHz, each containing two hardware threads. Up to 20 threads were used for a simulation. The simulated layouts are composed out of simple geometric forms and modelled as close as possible to the actual pixel design of the existing devices. With ranges for the node density for different parts of the sensor, the grid is calculated and optimised by the Structure Editor.^[225] It has to be verified by the input parameters that there is a sufficient number of grid nodes at critical points like gradients in the doping concentration, at round layout structures and in the region of the sideward drift in the silicon bulk. In addition, strong changes in the node density have to be avoided to ensure smooth transitions in the grid structure. Irregularities in the grid may produce potential minima that capture charge carriers and distort the result.

The simulations were all computed with a device temperature of 200 K to reflect the conditions in the measurements. To enable Sentaurus Device^[224] to find a converging solution, all voltages are set to 0 at first. After this first step converged to a steady state, the voltages are adapted to ensure a fully depleted sensor and an empty internal gate. The clear region serves as the n^+ node for the sideways depleted device and all electrons that populate the sensor are collected there. In a third step, the sensor is transitioned to the normal state of operation with one collecting and one shielded internal gate. At $30\ \mu\text{m}$ behind the back side

^[a]Random-Access Memory

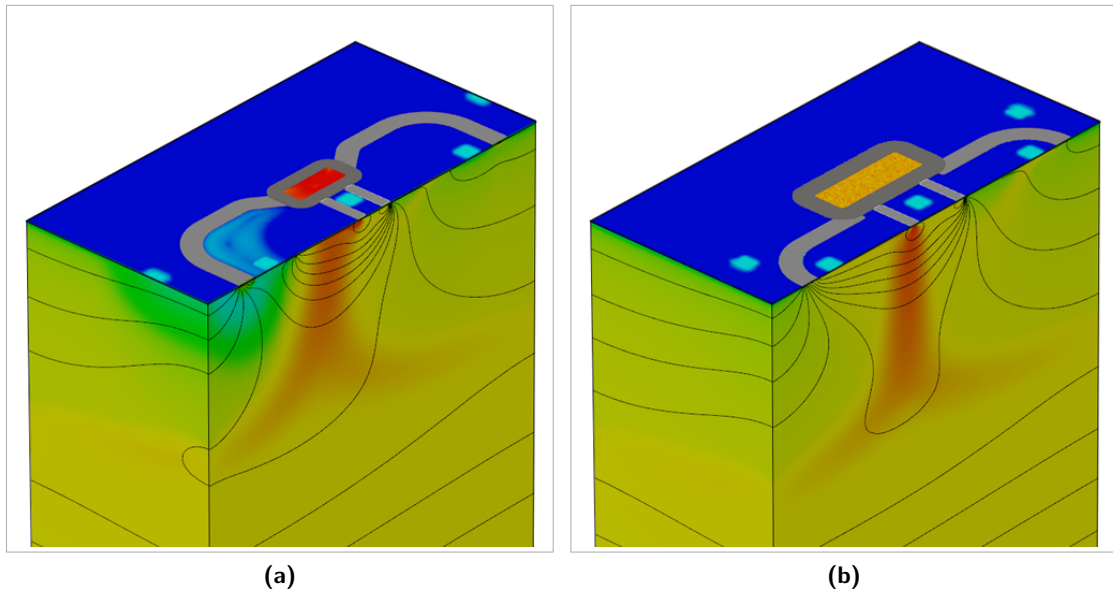


Figure 6.2: The charge collection into the internal gate is influenced by the shape of the drain. If it straitens towards the gate, the charges drift under the drain and only directly below the surface into the internal gate. The electron current density illustrates the paths of the electrons in **(a)** an Infinipix Narrow Gate layout and **(b)** an Infinipix Single Clear for comparison.

of the sensor, charge carriers are generated in the whole x-y plane. Due to the applied voltages, they drift in z-direction towards the surface. In the potential minimum in z-direction, the sideward drift starts and the electrons are collected below the more positive drain in the depth before their drift towards the surface increases again up to the internal gate of the collecting electron. Such a potential condition with streamlines indicating the way of a test charge is shown in Fig. 3.5. Normalised by the maximum charge that was in the bulk, the amount collected in the volumes of the internal gates is investigated. It can be determined directly while the results from the measurements are influenced by an incomplete clear and other effects in the readout.

To decouple the size of the drain and the width of the linear gate, a few different geometries were tested by simulations. The three most promising are shown in Fig. 6.1. In the scope of the layout variations, it was also verified that a reduced distance between the internal gates increases the the charge separation between the two sub-pixels. For that reason, the size of the clear is significantly reduced for all variants. The most intuitive variant adapting the existing Infinipix layouts may be the Infinipix Narrow Gate. The size of the drain regions and the width of the (internal) gate are decoupled by a converging drain. The disadvantage is a more positive potential at the wider drain region which causes the electrons to be collected in the depth below the drain and not under the internal gate. Only shortly before they reach the surface, they drift into the internal gate. While it improves the suppression at the shielded internal gate, the probability for defects in the crystal lattice increases near the surface which may lead to charge loss due to trapped charge carriers. The final approach of

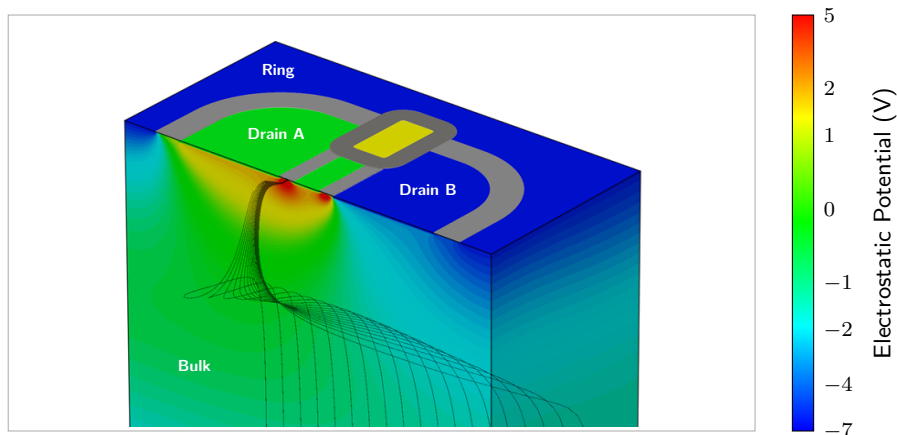


Figure 6.3: The electrostatic potential of an Infinipix Wide Drain is shown. Streamlines represent the charge collection for electrons that are generated near the back side. In the region of sideward depletion, they move under the drain of the collecting sub-pixel. Near the front side, they finally drift into the internal gate. By extending the full drain width to the gate as close as possible, this path near the front side is minimised for this kind of layout (cf. Infinipix Narrow Gate, Fig. 6.2).

electrons at the internal gate of an Infinipix Narrow Gate and an Infinipix Single Clear from the existing layout variants is shown in Fig. 6.2 for illustration and comparison. They feature the electron current at the end of the charge collection process in the simulated half pixels.

To bring the full drain width closer to the internal gate, the clear regions are rotated by 90° . The drain is extended over the width of the gate almost to the outer edge of the clear regions. The drain width only straitens in the small region between the clear gates. It also reduces the distance which charge has to drift near the surface. It is the best compromise between almost decoupled gate and drain widths, and the omission of charge drift near the surface. This approach was then also used to enlarge the drain regions of the Quadropix to optimise the charge collection.^[24] A crucial point is the connection of the internal gate to the clear. To reduce the narrowing of the drain region, the gate is slightly set off from the clear region. During the clear process, the electrons need to take an angled path under the internal gate. In addition, the nearby drain – which is on a negative potential during the readout – constrains the channel for the electrons. But in the simulations, a complete depletion of the internal gate over the clear region was still achieved. The performance of this Infinipix Wide Drain will be investigated with measurements in the future. Its layout was proposed as a test structure on the Athena pre-flight production whose fabrication was started at the semiconductor laboratory of the Max Planck Society at the time of this thesis. The electrostatic potential and the charge collection in a simulated Infinipix Wide Drain are shown in Fig. 6.3. Due to the reduced source area compared to the Infinipix Wide Gate, the drain regions are further enlarged. The improvement in the charge suppression as absolute value and also its effect on the operation voltage at the back side contact is presented in Fig. 6.4. Since the size of the drain regions also changes the configuration at the front side for the sideward depletion of the device, the back side contact voltage needs to be adapted

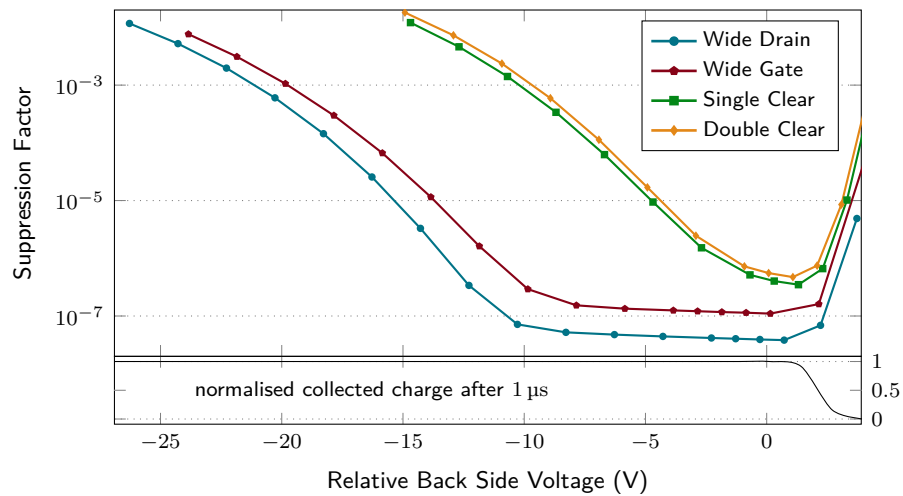


Figure 6.4: Simulated suppression factors of the three existing Infinipix variants which were all measured and the simulated Wide Drain layout. Since the size of the drain regions influences not only the operational window of the back side voltage, but also the necessary value to deplete the bulk, the data curves are shifted to the voltage of a complete charge collection after $1 \mu\text{s}$. The relative back side voltage then represents the operational window.

to some extent for every layout. For an easier comparison, all data are given with their back side voltage relative to the depletion voltage.

The last layout variant – the Infinipix Unique Clear – is the attempt of a true separation of the gate width and the size of the drain regions. The clear at one side of the gates is dropped. The redundant space then is used to assemble the drain regions around the gates. The gate width is reduced to ensure an efficient clear process even though the internal gate is depleted only from one side. A smaller gate also reduces the noise due to an improved gain of the DEPFET and leads to less volume that may be the source for noise contributions. In addition, smaller clear regions decrease the probability for charge loss into it. In the simulations, the larger fraction of the pixel area covered by the drain regions and the reduced distance between the gates showed an improved charge suppression at the shielded internal gate compared to the existing devices. Also the clear pulse depleted the internal gate efficiently. The concept provides an option in case the clear process in the Infinipix Wide Drain suffers from the spatial offset between the internal gate and the clear or the constrained channel under the clear gate.

6.1.1 Bulk Doping

As already discernible in the measurements obtained with the Double Clear #W1, the resistivity of the wafer material is another starting point to optimise the back side contact operation voltage window (see Fig. 5.18). To test for this suspicion, the bulk doping concentration was varied in the device simulations up to a factor of ten – from $9 \cdot 10^{11} \text{ cm}^{-3}$

to $9 \cdot 10^{12} \text{ cm}^{-3}$. It showed that the absolute operation voltage window increases over the whole resistivity range. The relative operation voltage window – the operation voltage window normalised to the voltage applied at the back side contact – decreases. But at least at this order of magnitude, the selection of wafer material with a lower resistivity would increase the robustness of the functional principal of an Infinipix. With slightly higher doping concentrations, the conductivity is increased and the electrostatic potential flattens. The resulting decreased electric field reduces the probability that electrons are accelerated into the clear or the insensitive internal gate.

6.2 Spatial and Readout Split

To be able to show the advantages of a concept with storage compared to a DEPFET which suffers from energy misfits during the readout process, a simulation was set up in Python^[222,223] using the Monte Carlo method. It is based on basic assumptions of the electric potential and the charge drift in the detector to investigate the charge spread over space and time. The influence of the charge distribution over the pixels and of the readout sequence on the spectroscopic performance was studied by simulations for DEPFETs with and without a storage. The code is based on statistical evaluations and does not calculate accurately the movement of charge carriers in a semiconductor as it is done by tools like Geant4.^[1] By reducing the generated spectra to a few basic assumptions, it is demonstrated that – besides the entrance window – the main contribution to the background generated by the sensor itself can be explained with the pixel size and the applied readout.

6.2.1 Charge Generation and Entrance Window

The input parameters for the charge deposited in the sensitive volume of the sensor is provided by a list of photon energies with their abundances and the attenuation length in silicon. In addition, a probability for a fluorescence photon to leave the sensitive volume can be given. The photon energy then is selected randomly, considering their relative frequencies. Focusing on silicon as detector material, binding energies of the electrons as well as the energies and attenuation lengths of photons released during transitions inside the silicon atoms and the probability of an Auger electron are hard-coded. The actual penetration depth is generated as an exponentially distributed random number using the the attenuation length as input parameter for the probability distribution. The generated photoelectron and a potential Auger electron are then further spatially distributed generating additional random numbers for their direction of movement. The angle relative to the incident photon – whose angle of incidence is assumed to be perpendicular to the sensor surface – is uniformly distributed for an Auger electron, but shows a dipolar behaviour for the photoelectron in the first approximation.^[38]

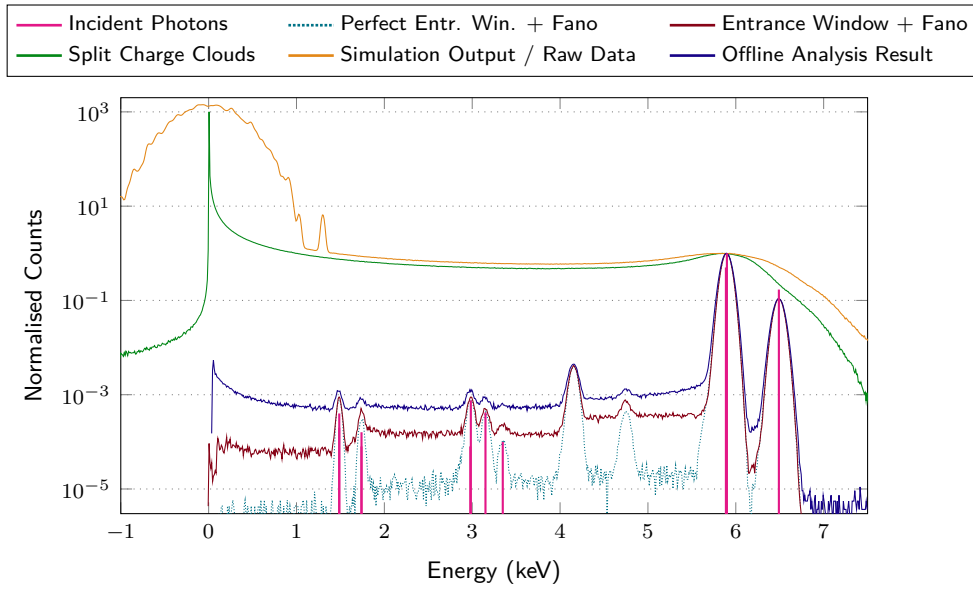


Figure 6.5: Different steps of the simulation of the spatial distribution of charge carriers and readout effects normalised to the Mn $K\text{-}\alpha_{(1)}$ peak. The energies of the incident photons as input parameter (pink peaks) are redistributed with respect to charge loss at the entrance window or escaping fluorescence photons and broadened by Fano noise (red). A perfect entrance window is shown for comparison (blue dots). The charge clouds are distributed over the pixels and a readout is applied for a non-storage DEPFET that also leads to negative energy misfits (green). After offset and noise – including the common mode – are added, the resulting data (yellow) can be analysed with the standard offline analysis also used for the measurements. Its output is shown in purple.

Fast electrons lose their kinetic energy along their path by the generation of electron-hole pairs. The total distance D_{\max} of the Auger and the photoelectron with a kinetic energy E_{kin} can be estimated by the formula given by Fitting (1974).^[64]

$$D_{\max} = 90 \frac{E_{\text{kin}}^{0.3}}{\rho^{0.8}} \quad (6.1)$$

ρ is the density of the detector material. Assuming a constant charge loss over the whole distance,^[64] the fraction of energy deposited inside and outside the sensor – in case the electron leaves the sensitive volume – can be calculated. It is the first contribution to a sensor generated background. Taking into account that the entrance window is not a hard transition, a region can also be defined where only parts of the deposited energy are lost. It simulates a more realistic, not perfect entrance window. In addition to the charge loss caused by electrons, also fluorescence photons can leave the sensor and all their energy is subtracted from that of the incident event. In a last step, the remaining energy is blurred by applying a normal distributed offset representing the energy dependent Fano noise. The effects on the spectrum from the Dirac delta distributions of the incident photon energies to the Fano noise and entrance window effects are shown in Fig. 6.5.

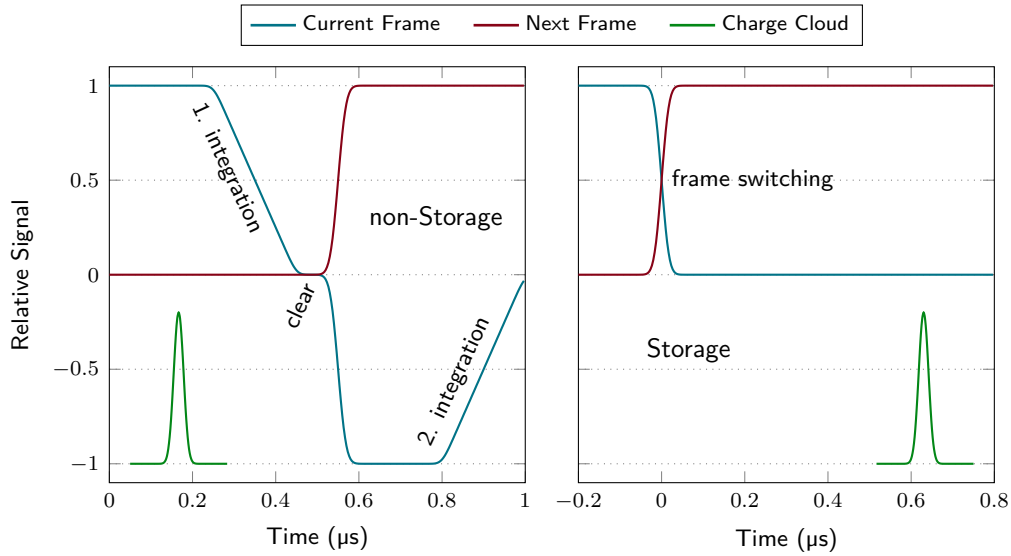


Figure 6.6: A charge cloud (green) convoluted with the readout of a non-storage DEPFET and a storage DEPFET. The relative signal in a pixel for the current and the next frame is shown as it is weighted depending on the arrival time. Energy misfits of a non-storage DEPFET appear during the first integration – the linear decrease of the turquoise line from 1 to 0. The charge cloud is shown for demonstration – the position and its height is given in arbitrary units.

6.2.2 Charge Collection and Distribution

Besides the actual penetration depth of the incident X-ray photon, also its location in the sensor plane and the arrival time are generated using Monte Carlo methods. For this x , y and t coordinates, uniformly distributed random variables are used. They are distributed in the interval $[0, 1)$ and can be redistributed later according to the desired sensor geometry and applied timing. The pixel size, the number of pixels – quadric pixels and sensors are assumed – can be defined. The further development of the charge cloud depends on the time it takes to reach the front side of the sensor. A simple two dimensional electric field is applied to calculate the drift times. The solution of the one-dimensional Poisson equation (eq. (2.13)) is a parabola^[72] that describes the one dimensional electrostatic potential in z direction with the boundary conditions defined by the applied voltages at the front and the back side, U_F and U_B .

$$\Phi(z) = -\frac{qN_D}{2\epsilon_s}z^2 + \left(\frac{qN_Dd_s}{2\epsilon_s} + \frac{U_B - U_F}{d_s}\right)z + U_F \quad (6.2)$$

The thickness of the sensor is d_s . To obtain a sideward drift at the potential minimum in z , the front side voltage U_F is implemented as a radial dependent function. With the electron mobility as further input parameter, the velocity a test particle is accelerated to in the electrostatic potential, can be calculated. The time it needs from the interaction position of the incident X-ray photon to the point at which a significant sideward drift towards the pixel centre starts is used to calculate the charge cloud expansion.^[73] Parts of the charge

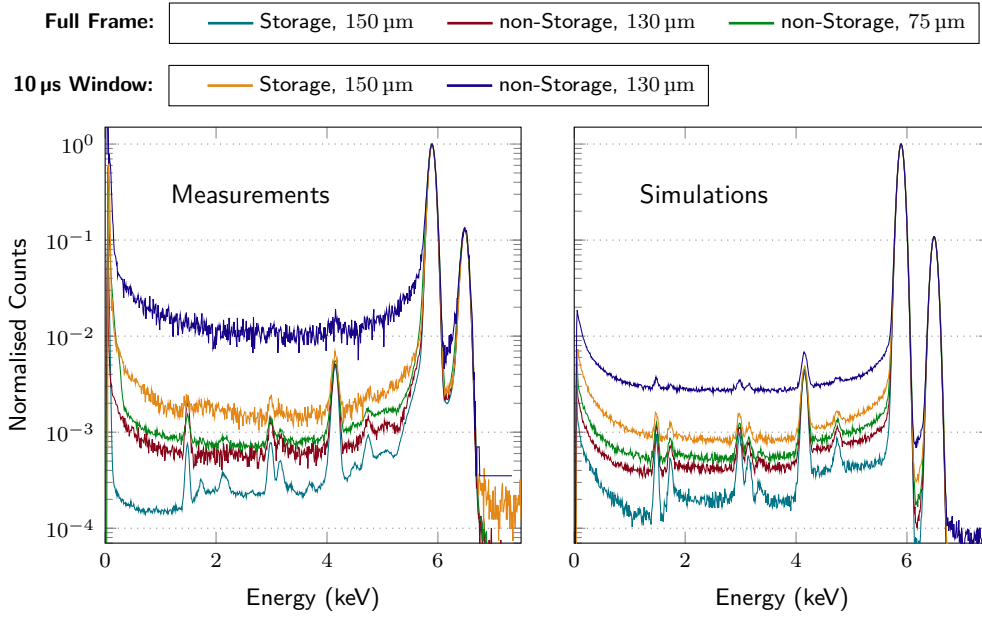


Figure 6.7: On the left, measurements with existing devices at a readout speed of $5 \mu\text{s}$ per row and $10 \mu\text{s}$ frame are shown. The simulations on the right consider only charge loss at the entrance window, the charge distribution over the pixels of different sizes and the different readout effects of storage and non-storage devices. The DEPFET is assumed to be perfect. Therefore, charge loss or an incomplete clear in the DEPFET as visible in the measurements is not included. As input, only characteristic radiation from manganese, silver, aluminium and silicon is used, while the measurements show some further emission lines from heavier elements. The difference between the non-storage and the storage DEPFETs is underestimated by the simulations as clearly visible for the short frame rates.

cloud that cross pixel borders are assigned to those pixels. Split events are formed. For the sideward drift towards the potential minimum in z at the pixel centre, a linear potential and, therefore, constant electric field and velocity is assumed. The missing distance towards the surface is modelled with an exponential function. The total charge collection time results in a charge cloud spread^[73] that is converted to a spread in time. Although a Gaussian distribution is only a rough approximation,^[55] it is used to describe the charge cloud which is then convoluted with the readout scheme of the desired sensor type. It is demonstrated in Fig. 6.6 for a non-storage and a storage DEPFET.

At the end, offset and noise – common mode separately – can be added by defining the expectation value and standard deviation of their Gaussian shaped distribution. Since these numbers can be obtained from actual measurements, all other steps of the calculation of the charge cloud splitting over the pixels and in time can be verified. The output of the simulation is stored in the format that is also used for the measurements taken in the laboratory and can be analysed with the same offline analysis.^[104] Measurements from three different sensors were taken for comparison. As shown in Fig. 6.7, the sensor background is not only caused by the energy misfits – as expected – but also by the pixel size. Since no charge loss in the DEPFET is considered in the simulations, the charge loss to adjacent pixels below the noise threshold degrades the spectrum, too. The higher background in the measurements

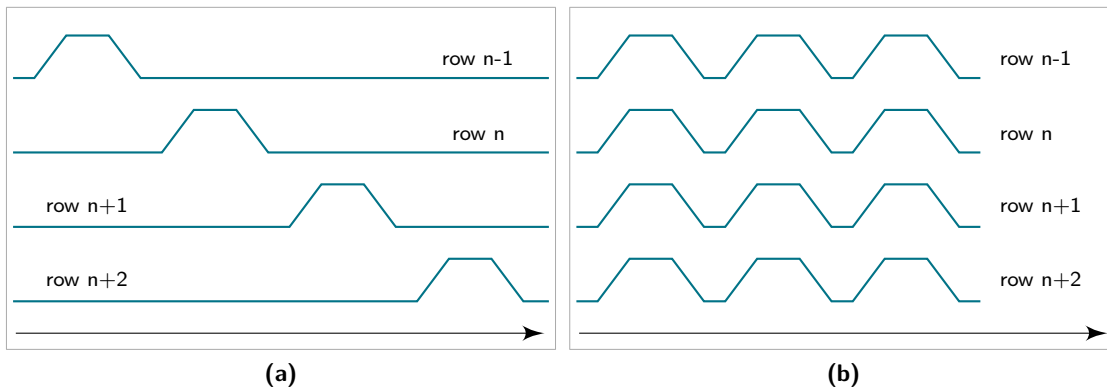


Figure 6.8: (a) Readout of different rows in the rolling shutter mode as presented in section 4.2. (b) Full parallel continuous readout. Each pixel has to be connected to a separate readout channel and is turned on all the time. Since it is the fastest possible readout, a DEPFET with storage is essential to omit energy misfits which would appear most of the time otherwise.

compared to the simulations originates from the assumption of a perfect DEPFET. Charge loss – also visible at the manganese peaks – is not present in the simulations. Nevertheless, with the Python scripts, it is possible to generate spectra that cannot be obtained by measurements with the existing devices. Furthermore, all parameters can be kept constantly while only one feature, like the storage, is changed to investigate their influence on a spectrum. As a further test, the fast window mode measurements were simulated. A comparison to the measured spectra demonstrates, that the energy misfits generated by a non-storage DEPFET are underestimated. That may originate from a charge cloud that has a larger temporal spread than assumed in the simulation.

The change from the rolling shutter operation of the present samples to a full parallel readout is one case that can be simulated and not yet measured. The different readout schemes are depicted in Fig. 6.8. The exposure time t_{exp} shrinks to the length of the readout cycle of one pixel. It increases n_{misfit} to about 30%. Nevertheless, also the voltage at the drain contacts of the Infinipix have to be switched after each of the short exposure times. Due to the finite switching time of the drain regions and the finite size of the charge cloud, the probability of an inter-frame splitting of an event, n_{split} , increases at the same order of magnitude. It can be expected, that the differences in the spectra are small. But while energy misfits during the first integration cannot be recognised or corrected, split events between two consecutive frames can be recombined. It is the same as the recombination of split charge clouds between multiple pixels of the same frame, but in a further dimension. Since an appropriate inter-frame split recombination has not yet been available in the analysis tools and its implementation in the complex event recognition would go beyond the scope of this thesis, it can be simulated by assuming an infinitesimal charge cloud arriving at the front side. Although there will be a degradation during the recombination of the events like it is visible in a worse energy resolution for multiples compared to single events, the advantage

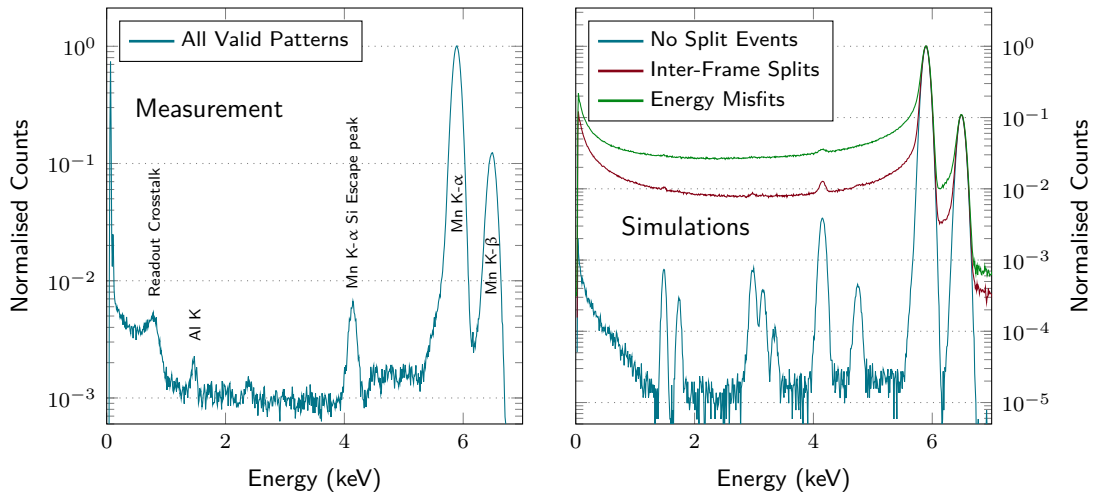


Figure 6.9: A spectrum of all valid events normalised to the ^{55}Mn K- α peak for a measurement with $1\ \mu\text{s}$ per row taken with a linear gate device from the Athena prototype production is shown. Crosstalk visible below 1 keV is a result of a not completely settled source node. It vanishes if the drain current readout is used for such a measurement. On the right, simulations of a non-storage DEPFET (green) and a storage DEPFET with (red) and without inter-frame splits (turquoise) are presented. All three cases are simulated for a pixel size of $130\ \mu\text{m}$.

of an implemented storage can be shown.

The linear gates enable a shorter clear time and, due to smaller capacitances, reduced settling times. Since the gate dimensions of the Athena prototypes are even smaller, a further increased readout speed is possible. Preserving a still good spectral performance, a readout time of $1\ \mu\text{s}$ per row resulted in a noise of $3.5\ e^-$ ENC and an energy resolution of about 150 eV FWHM at 5.9 keV. The spectrum is shown on the left in Fig. 6.9. Due to a relatively short settling of the source node of 250 ns, crosstalk effects are visible below 1 keV. Not yet fully understood, they seem to be the result of an interaction between the source potential and the readout ASIC. If the drain current readout is used which does not need a settling process at the sensor, the low energetic features can be omitted. It is not shown since the drain current readout has not yet been possible with the Infinipix and the present readout ASIC (see section 4.2.3).

Applying the same timing conditions as in the $1\ \mu\text{s}$ -measurement, but for a full parallel readout with this non-storage DEPFET, the resulting simulated spectrum worsens drastically. It leads to a very high sensor-generated background between the event and the noise peak. From the comparison shown in Fig. 6.7 one can assume that it will be even worse for a real measurement. Emission lines with low intensities are almost not visible. The storage DEPFET creates a slightly smaller sensor background. Weaker emission lines are more pronounced. Omitting inter-frame split events as a first approximation for a recombination in the feature, the spectral quality increases drastically. For these simulations, a perfect entrance window was set which allows for such weak contributions to the valley. But measurements

with pnCCDs show^[79] that an extremely low flat shelf is possible. The last uncertainty is the quality of a potential inter-frame split recombination which needs to be implemented in the future to finally verify the advantages of DEPFETs with storage as soon as they are available as full parallel readout devices.

Conclusions and Future Prospects

First instruments for space science are and will be equipped with DEPFETs, a concept for an active pixel sensor, improving the time resolution and omitting the disadvantages of CCDs like out-of-time events and potential charge loss during the transfer towards the readout node. However, a DEPFET delivers false energy information if the charge cloud generated by an incident photon approaches during the readout. In case of a full parallel readout, about 30 % of all events would be affected. The implementation of a storage that separates the charge collection and the readout spatially can solve this problem. One solution for this approach is the so-called Infinipix DEPFET.

The DEPFET active pixel sensors that I investigated and which are composed of 32×32 pixels of the Infinipix type are the first linear gate DEPFETs on matrix scale tested for spectroscopic purposes. Including the storage functionality, my measurements show a very promising performance with better results than achieved by previous DEPFET productions. In contrast to the Cut Gate design, shorter and narrower gates are feasible which has been limited by the necessary steering lines and vias before. As a result of the smaller gate dimensions, the capacity of the internal gate is reduced and the gain is increased which leads to a better noise performance and a more complete clear process. In addition, the processing time per row can be increased significantly. The Infinipix DEPFET exists in three layout variants which I investigated to determine potential weak spots that need to be optimised. A detailed table of the differences is presented in section 5.6. The main outcome of my measurements is the requirement of large drain regions for a robust functionality of the Infinipix principle. At the present layout, the size of the drain regions is coupled to the width of the DEPFET gate. Since the gate width also scales with the maximum distance in the internal gate to the clear region, narrow gates are needed to perform an efficient clear process of the collected charge carriers with respect to completeness and timing. With the present Infinipix devices with narrow gates I obtained an energy resolution of (123.61 ± 0.07) eV FWHM for single events ((127.40 ± 0.07) eV FWHM for all valid events) at the Mn K- α emission line energy of 5.895 keV, operated at a readout speed of 5 μ s per row. The noise performance at 220 K is at (2.333 ± 0.004) e⁻ ENC. The lower limit achievable in theory for the energy resolution with this noise component is 121.2 eV FWHM for events appearing in only one pixel.

The decoupling of the size of the drain region and the gate width in the layout of the Infinipix was addressed by simulations. I tested different layouts (see Fig. 6.1). They all showed an improved robustness against intrinsic bulk doping variations that limit the operation voltage at the back side contact. I proposed the most simple layout adaption for fabrication. It is shown in more detail in section 7.1.2. The disadvantages like a worse clear performance seem to be negligible according to the results of my simulations.

With a further simulation based on Monte Carlo methods I implemented in Python scripts, the influence of the entrance window, the pixel size and the readout scheme on the background generated by the sensor itself was investigated. I could show that in a first approximation, the obtained spectral features can be reduced to these three effects. In addition, an outlook on the future full-parallel readout was possible. Assuming an optimised entrance window and a functioning inter-frame split recombination in the offline analysis tools, the difference in the sensor background between a non-storage and a storage DEPFET is up to the order of three magnitudes. It allows for the investigation of weak spectral features even in the combination with a high time resolution.

7.1 Future Prospects

Nevertheless, to be prepared for future missions, the layout and technology has to be improved to get a reliable device that features a storage inside every pixel. The drain and the back side contact voltages are limited to very small operational windows which is a risk for larger sensors and limits already the functionality of the present samples. If the local bulk doping fluctuations and thereby the resistivity variations are too high, a detector is not operable with a reasonable spectroscopic performance. Already one out of five devices I investigated showed an inoperability due to a combination of high resistivity variations and the limited operational windows of the prototype devices. Improvements in technology and layout which were already implemented in the Athena prototype production or simulated to be applied in the next productions, will enhance the reliability of DEPFETs with storage.

7.1.1 Technology

Although the technology development – meaning the implantations into the silicon bulk as well as the layer dimensions on top of the wafer – is mainly done at the MPG^[a] semiconductor laboratory,^[114] measurements are needed for the validation and the results yield information for the further optimisation. The limited operational window on the drain regions of the

^[a]Max-Planck-Gesellschaft (Max Planck Society)

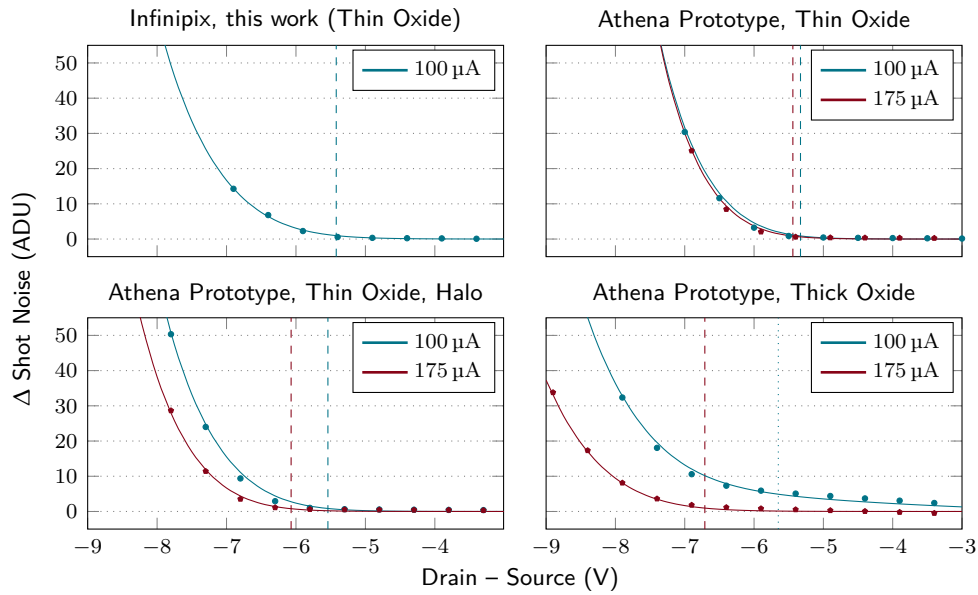


Figure 7.1: Shot noise due to impact ionisation as a function of the drain-source voltage difference for technology variants of the Athena prototype production compared to the one of the Infinipix measured for this study. For the thick oxide and the halo implant, the operational window for the drain voltage can be extended by the application of a higher transistor current.^[197] For lower currents, the thick oxide technology suffers from short channel effects. The vertical lines mark the voltage for which the overall noise is increased by 10%. For the 'thick oxide, 100 μA ', the linear term is neglected.

Infinipix due to a nascent impact ionisation at the boundary between gate and drain can be extended by variations of the technology. Thicker oxides or an additional p implant reduce the peaks in the electrostatic potential at the boundary. The effect of a reduced noise and an increased operational window was already measured for the Athena prototype devices (Fig. 7.1). Since Infinipix arrays were manufactured on that wafers, the extended operational window and its effect on the reliability of the devices can be studied in the near future.

Another issue that has to be solved by changing technology parameters is the significant charge loss around the cleared sub-pixel. With higher readout frequencies a good shielding of the clear regions becomes even more necessary. For a megahertz full parallel readout about 10% to 20% of the time is affected. For the other sub-pixel of the read-out pixel, it would lead to a charge loss of about 4%. An increased dopant concentration of the p implant under the clear improves the shielding which was already done in the Athena prototype production and reduces the charge loss by one order of magnitude (Fig. 7.2). I confirmed expected dependencies, the signal charge suppression at the shielded internal gate shows for higher bulk dopant concentrations and thereby lower bulk resistivities, with measurements and simulations. By choosing wafer material with a lower resistivity, a better functionality of a DEPFET with storage can be achieved easily.

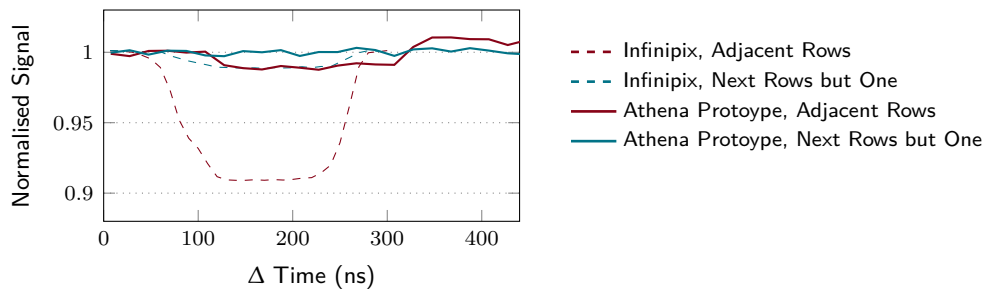


Figure 7.2: The charge loss during the clear process in the rows adjoining the read-out one is significantly reduced for Athena prototype sensors compared to previous productions. By increasing the dopant concentration in the p implant under the clear, the shielding against the bulk is improved.

7.1.2 Layout

The two different gate widths of $30\ \mu\text{m}$ and $60\ \mu\text{m}$ of the Infinipix prototype devices showed a contrary behaviour. While the charge is not completely removable from the $60\ \mu\text{m}$ wide gates within one readout cycle, the resulting larger drains lead to a more robust storage functionality. Retaining the good performance and avoiding the implementation of disadvantages like potential pockets for charges that should be collected inside the internal gate, I tested layouts with simulations to extend the robustness against bulk doping variations. A necessary larger operational window of the back side contact voltage is achievable by combining large drains with narrow gates. The resulting layout adaptations may worsen the clear performance which seem to be negligible according to simulations. To be able to test the changes, the Wide Drain layout will be manufactured as 32×32 pixels device on the pre-flight production for Athena.

Besides the implementation of a storage by using two or more fully functional sub-pixels, another option is a separated storage region in each pixel. Before each readout, the collected charge is transferred from the storage regions to the internal gates while charge arriving during the readout is collected in the storage.^[5,115] This concept is simpler and saves steering lines, which reduces the complexity of the layout and the necessary steering electronics. Nevertheless, present implementations of this principal are not functional and have to be improved in the future.

Pixel Size

The pixel size of a detector is adapted to the performance of the optics of a telescope and the scientific needs of the experiment. Therefore, a detector that is functional for a large range of pixel sizes is desirable. Compared to CCDs which are not indefinitely scalable due to the direct connection to the transfer channel length, a DEPFET that is read out inside the pixel can easily be scaled up by adding additional drift rings. It results in a SDD (cf.

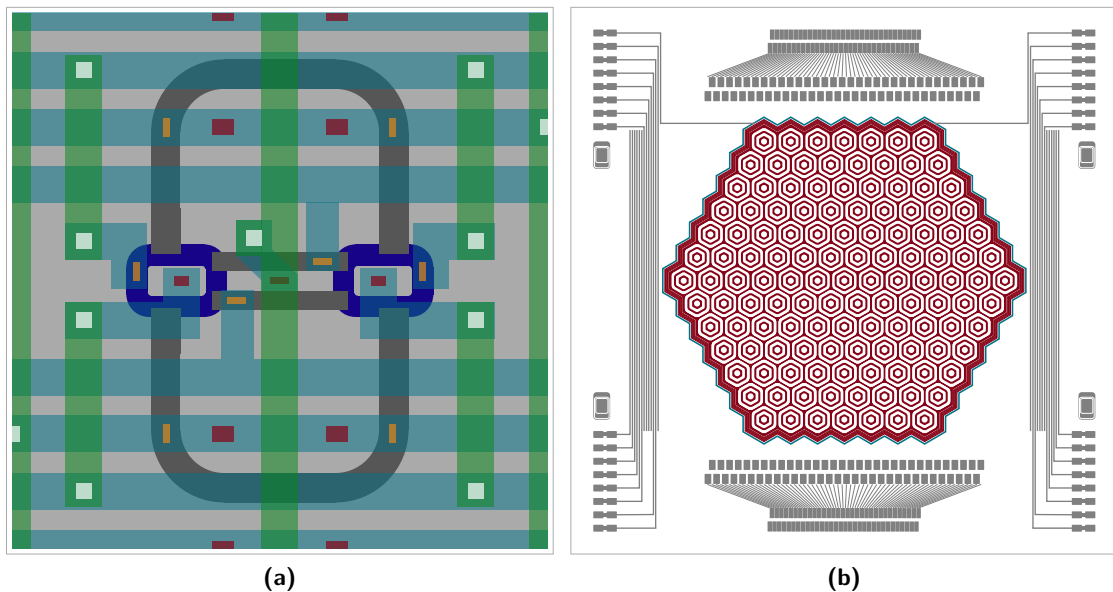


Figure 7.3: (a) The layout of the Infinipix Wide Drain with the aluminium steering and readout lines in green and turquoise as well as (b) the assembly of the 127 pixels of a first device designed for a full parallel readout as they are implemented by P. Lechner at the MPG semiconductor laboratory on the pre-flight production for Athena.

section 2.4.2) with a DEPFET as readout node.

Smaller pixel sizes are limited to the minimum size an Infinipix – or a DEPFET in general – needs. To further reduce this size, neighbouring pixels can share drain, source or clear regions like it is already done for Belle II^[112] and GRE^T.^[24] Considering a successful further development in the wafer processing at the semiconductor laboratory of the MPG, I evaluated pixels down to 12 μm edge length in simulations without losing the storage functionality as shown in Fig. 7.4. The layout is based on the Quadropix design used in the prototyping for GRE^T.^[24] A further reduction of the feature size is in preparation at the semiconductor laboratory of the MPG and will also be available if an adaption of the DEPFET to the CMOS^[b] technology is successful. First results of the latter approach are presented by Aschauer et al. (2017).^[6] Due to the shared drain regions, the electrons tend to drift under the pixel border before they are split between the individual pixels. To reduce the effect, I omitted the n implant, that also forms the internal gate, at the pixel borders. A more negative intrinsic potential is formed. To influence the paths of the electrons, the sideward drift region has to be shifted towards the surface. While it leads to a worse suppression at the shielded internal gate, the shown advantage of a reduced sub-pixel distance can compensate the effect.

^[b]Complementary Metal-Oxide-Semiconductor

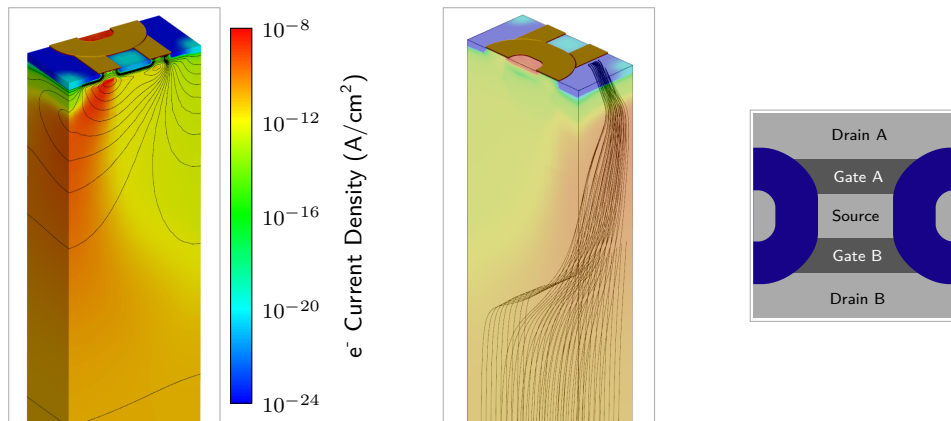


Figure 7.4: The half of a simulated 12 μm pixel. On the left side, the electric field in the silicon bulk is indicated by the edges of the equipotential surfaces as black lines. The colours show the e^- current density after most of the charge is collected within the internal gate. Like the streamlines in the centre, it represents the way of electrons generated near the back side. The layout is shown on the right while the measures are listed in Appendix D. The two drain regions and the clear are shared with the neighbouring pixels.

7.1.3 Inter-Frame Splits

The limiting factor for DEPFETs with storage with respect to the time resolution is the spatial and thereby temporal spread of the charge cloud as it arrives at the readout node. At the moment, it dominates the achievable effective switching time of the Infinipix which would be the same for a DEPFET with a separated storage region. Since the size of the charge cloud is defined by the charge collection time due to electric repulsion and diffusion which is mainly extended during the sideward drift in the silicon bulk, a subsequent solution is the recombination of events that split over consecutive frames. By extending the pattern recognition from neighbouring pixels to adjoining frames which has not yet been implemented in the analysis software, the number of adjacent pixels raises by a factor of 3.25 (see Fig. 7.5a) which also increases the pattern pile-up. In addition, the electrical setup and the measuring computer used to take the data were not powerful enough to store the data from every frame.

The gain in the accuracy of the photon energy determination considering the inter-frame splits may be used up by pile-up events for bright sources and the throughput of the detector reduces. During the switching process while charge is collected in both sub-pixels at the same time, the signal shows no significant charge loss as shown in Fig. 7.5b. For an almost complete split event recombination, an efficient data acquisition is mandatory. Missing frames would lead to a leakage of split partners which makes the inter-frame split recognition impossible for such events and results in charge loss in the results.

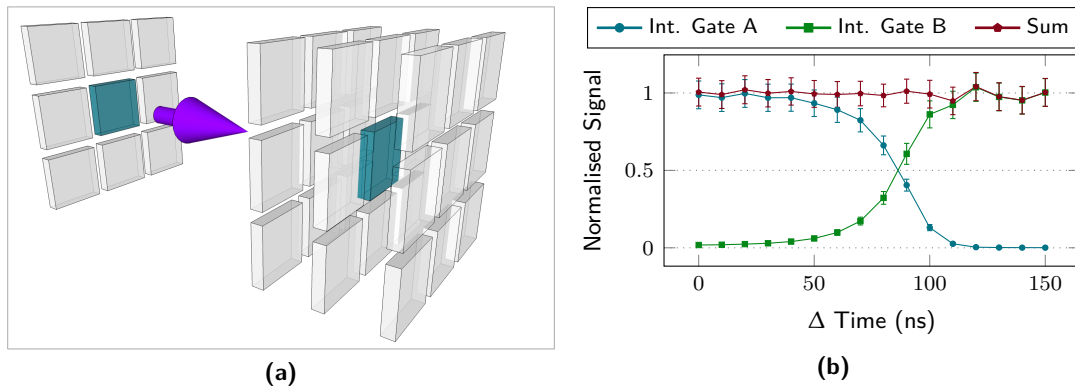


Figure 7.5: Pattern recognition also regarding events that split over consecutive frames increases the pile-up due to a larger number of pixels that have to be considered as shown in (a). The turquoise pixel represents the one with the highest signal of a recognised event while the grey ones are considered for split events for the present routine on the left and inter-frame split recombination on the right. (b) The summed signal from the two sub-pixels illuminated by an LED during the switching of the drain voltages shows no significant charge loss so that a recombination of inter-frame splits should deliver a proper result.

7.1.4 Full Parallel Readout

The goal of all these developments was and is the fabrication of a detector which can be read out completely in a parallel way. Since the functionality of the Infinipix was shown with measurements on matrix scale and the advantage of a DEPFET with storage compared to one without was demonstrated with measurements and simulations, a first full parallel readout prototype with 127 pixels will be added to the pre-flight production for Athena. With good results of fast measurements taken with the Athena prototypes, a spectroscopic imager with a time resolution of the order of one micro-second appears to be feasible in the near future.

References

- [1] S. Agostinelli, et al. Geant4—a simulation toolkit. *Nucl. Instr. Meth. Phys. Res. A*, 506(3): 250 – 303, 2003. doi:10.1016/S0168-9002(03)01368-8. [↑86]
- [2] C. D. Anderson. Energies of Cosmic-Ray Particles. *Phys. Rev.*, 41:405–421, 1932. doi:10.1103/PhysRev.41.405. [↑21]
- [3] C. D. Anderson. The Positive Electron. *Phys. Rev.*, 43:491–494, 1933. doi:10.1103/PhysRev.43.491. [↑21]
- [4] D. H. Andrews, et al. Attenuated Superconductors I. For Measuring Infra-Red Radiation. *Review of Scientific Instruments*, 13(7):281–292, 1942. doi:10.1063/1.1770037. [↑23]
- [5] S. Aschauer, et al. Prospects and limitations of DEPFET active pixel sensors as high speed spectroscopic x-ray imager for the ATHENA wide field imager. In *Proc. of SPIE*, volume 9144, pages 9144 – 9144 – 8, 2014. doi:10.1117/12.2056398. [↑81,↑96]
- [6] S. Aschauer, et al. First results on DEPFET Active Pixel Sensors fabricated in a CMOS foundry—a promising approach for new detector development and scientific instrumentation. *Journal of Instrumentation*, 12(11):P11013, 2017. doi:10.1088/1748-0221/12/11/P11013. [↑97]
- [7] G. Audi, et al. The Nubase evaluation of nuclear and decay properties. *Nuclear Physics A*, 729(1):3 – 128, 2003. doi:10.1016/j.nuclphysa.2003.11.001. The 2003 NUBASE and Atomic Mass Evaluations. [↑45]
- [8] M. Ayre, et al. ATHENA: system studies and optics accommodation. In *Proc. of SPIE*, volume 9905, 2016. doi:10.1117/12.2234275. [↑4]
- [9] C. G. Barkla. Phenomena of X-Ray Transmission. *Proc. Cambridge Phil. Soc.*, 15:257, 1909. [↑15]
- [10] D. Barret, et al. The Athena X-ray Integral Field Unit (X-IFU). In *Proc. of SPIE*, pages 9905 – 41, 2016. doi:10.1117/12.2232432. [↑3,↑23]
- [11] M. Bavdaz, et al. The ATHENA optics development. In *Proc. of SPIE*, volume 9905, 2016. doi:10.1117/12.2233037. [↑4]
- [12] G. Baym and C. Pethick. Neutron Stars. *Annual Review of Nuclear Science*, 25(1), 1975. doi:10.1146/annurev.ns.25.120175.000331. [↑7]
- [13] P. Becker, et al. Confirmation of the INRiM and PTB Determinations of the Si Lattice Parameter. *IEEE Transactions on Instrumentation and Measurement*, 56(2):230–234, 2007. doi:10.1109/TIM.2007.890618. [↑14]

- [14] W. Becker. *X-Ray Emission from Pulsars and Neutron Stars*, chapter 6, pages 91–140. Springer Berlin Heidelberg, Berlin, Heidelberg, 2009. doi:10.1007/978-3-540-76965-1_6. [↑8]
- [15] W. Becker and J. Trümper. Detection of pulsed X-rays from the binary millisecond pulsar J0437 – 4715. *Nature*, 365:528 – 530, 1993. doi:10.1038/365528a0. [↑7]
- [16] W. Becker, et al. Autonomous Spacecraft Navigation With Pulsars. *Acta Futura*, 7:11–28, 2013. doi:10.2420/AF07.2013.11. [↑11,↑12]
- [17] F. Berghmans, et al. *An Introduction to Radiation Effects on Optical Components and Fiber Optic Sensors*, pages 127–165. Springer Netherlands, 2008. doi:10.1007/978-1-4020-6952-9_6. [↑21]
- [18] M. G. Bernhardt, et al. Autonomous spacecraft navigation based on pulsar timing information. In *2011 2nd International Conference on Space Technology*, pages 1–4, 2011. doi:10.1109/ICSpT.2011.6064649. [↑11,↑12]
- [19] M. G. Bernhardt, et al. Timing X-ray Pulsars with Application to Spacecraft Navigation. In *Proc. of Science*, volume 108 - High Time Resolution Astrophysics, 2011. doi:10.22323/1.108.0050. [↑12]
- [20] M. S. Bessell. UBVRI passbands. *Publications of the Astronomical Society of the Pacific*, 102:1181–1199, 1990. doi:10.1086/132749. [↑6]
- [21] H. A. Bethe. Bremsformel für Elektronen relativistischer Geschwindigkeiten. *Zeitschrift für Physik*, 76:293, 1932. [↑21]
- [22] A. Bähr, et al. Spectral performance of DEPFET and gateable DEPFET macropixel devices. *Journal of Instrumentation*, 9(03):P03018, 2014. doi:10.1088/1748-0221/9/03/P03018. [↑3]
- [23] A. Bähr, et al. Development of DEPFET active pixel sensors to improve the spectroscopic response for high time resolution applications. In *Proc. of SPIE*, volume 9144, 2014. doi:10.1117/12.2055411. [↑3,↑36,↑70,↑79]
- [24] A. Bähr, et al. Advanced DePFET concepts: Quadropix. In *Nucl. Instr. Meth. Phys. Res. A*, 2017. doi:10.1016/j.nima.2017.10.048. [↑8,↑84,↑97]
- [25] N. Bohr. On the Constitution of Atoms and Molecules. *Philosophical Magazine*, 26, 1913. [↑13,↑14]
- [26] M. Born. Zur Quantenmechanik der Stoßvorgänge. *Zeitschrift für Physik A Hadrons and Nuclei*, 37(12):863–867, 1926. doi:10.1007/bf01397477. [↑14,↑15]
- [27] Bose. Plancks Gesetz und Lichtquantenhypothese. *Zeitschrift für Physik*, 26(1):178–181, 1924. doi:10.1007/BF01327326. [↑22]
- [28] W. S. Boyle and G. E. Smith. Charge coupled semiconductor devices. *The Bell System Technical Journal*, 49(4):587–593, 1970. doi:10.1002/j.1538-7305.1970.tb01790.x. [↑28]
- [29] H. V. Bradt, et al. The X-ray timing explorer. *Advances in Space Research*, 11(8), 1991. doi:10.1016/0273-1177(91)90176-K. [↑9]

- [30] U. G. Briel and E. Pfeffermann. The position sensitive proportional counter (PSPC) of the Rosat telescope. *Nucl. Instr. Meth. Phys. Res. A*, 242(3):376 – 381, 1986. doi:10.1016/0168-9002(86)90433-X. [↑1,↑2]
- [31] R. Brun and F. Rademakers. ROOT — An object oriented data analysis framework. *Nucl. Instr. Meth. Phys. Res. A*, 389(1):81 – 86, 1997. doi:10.1016/S0168-9002(97)00048-X. New Computing Techniques in Physics Research V. [↑47]
- [32] E. Bustarret, et al. Superconductivity in doped cubic silicon. *Nature*, 444:465–468, 2006. doi:10.1038/nature05340. [↑23]
- [33] J. Chadwick and M. Goldhaber. The Nuclear Photoelectric Effect. *Proceedings of the Royal Society of London A: Mathematical, Physical and Engineering Sciences*, 151(873):479–493, 1935. doi:10.1098/rspa.1935.0162. [↑13]
- [34] N. Chamel, et al. On the Maximum Mass of Neutron Stars. *International Journal of Modern Physics E*, 22, 2013. doi:10.1142/S021830131330018X. [↑5]
- [35] K. S. Cheng, et al. Energetic radiation from rapidly spinning pulsars. I - Outer magnetosphere gaps. II - VELA and Crab. *The Astrophysical Journal*, 300, 1986. doi:10.1086/163829. [↑8]
- [36] D. Clayton. *Principles of Stellar Evolution and Nucleosynthesis*. University of Chicago Press, 1968. ISBN 9780226109534. [↑13]
- [37] A. H. Compton. A Quantum Theory of the Scattering of X-rays by Light Elements. *Phys. Rev.*, 21:483–502, 1923. doi:10.1103/PhysRev.21.483. [↑20]
- [38] J. W. Cooper. Photoelectron-angular-distribution parameters for rare-gas subshells. *Phys. Rev. A*, 47:1841–1851, Mar 1993. doi:10.1103/PhysRevA.47.1841. [↑86]
- [39] W. C. Dash and R. Newman. Intrinsic Optical Absorption in Single-Crystal Germanium and Silicon at 77°K and 300°K. *Phys. Rev.*, 99:1151–1155, 1955. doi:10.1103/PhysRev.99.1151. [↑19]
- [40] R. Davis. The SI unit of mass. *Metrologia*, 40(6):299, 2003. doi:10.1088/0026-1394/40/6/001. [↑14]
- [41] P. K. Day, et al. A broadband superconducting detector suitable for use in large arrays. *Nature*, 425:817–821, 2003. doi:10.1038/nature02037. [↑23]
- [42] C. A. de Coulomb. Premier Mémoire sur l'Électricité et le Magnétisme. *Histoire de l'Académie Royale des Sciences*, pages 569–577, 1785. [↑13]
- [43] E. P. De Lima, et al. Fano factors of rare gases and their mixtures. *Nuclear Instruments and Methods in Physics Research*, 192(2):575 – 581, 1982. doi:10.1016/0029-554X(82)90875-8. [↑2]
- [44] M. S. R. Delgaty and K. Lake. Physical acceptability of isolated, static, spherically symmetric, perfect fluid solutions of Einstein's equations. *Computer Physics Communications*, 115(2), 1998. doi:https://doi.org/10.1016/S0010-4655(98)00130-1. [↑7]

- [45] P. A. M. Dirac. On the Theory of Quantum Mechanics. *Proceedings of the Royal Society of London A: Mathematical, Physical and Engineering Sciences*, 112(762):661–677, 1926. doi:10.1098/rspa.1926.0133. [↑17]
- [46] P. A. M. Dirac. The Quantum Theory of the Emission and Absorption of Radiation. *Proceedings of the Royal Society of London A: Mathematical, Physical and Engineering Sciences*, 114(767):243–265, 1927. doi:10.1098/rspa.1927.0039. [↑19]
- [47] P. A. M. Dirac. The Quantum Theory of the Electron. *Proceedings of the Royal Society of London A: Mathematical, Physical and Engineering Sciences*, 117(778):610–624, 1928. doi:10.1098/rspa.1928.0023. [↑21]
- [48] C. Doppler. *Ueber das farbige Licht der Doppelsterne*. Verlag der Königl. Böhm. Gesellschaft der Wissenschaften, 1903. [↑10]
- [49] M. Drescher, et al. *Time-Resolved Inner Shell Spectroscopy with Sub-fs EUV Pulses*, pages 475–481. Springer New York, 2004. doi:10.1007/978-0-387-34756-1_60. [↑19]
- [50] G. Duchêne and A. Kraus. Stellar Multiplicity. *Annual Review of Astronomy and Astrophysics*, 51(1):269–310, 2013. doi:10.1146/annurev-astro-081710-102602. [↑5]
- [51] A. Einstein. Über einen die Erzeugung und Verwandlung des Lichtes betreffenden heuristischen Gesichtspunkt. *Annalen der Physik*, 322(6):132–148, 1905. doi:10.1002/andp.19053220607. [↑18]
- [52] A. Einstein. Die Feldgleichungen der Gravitation. *Sitzungsberichte der Königlich Preußischen Akademie der Wissenschaften (Berlin)*, Seite 844–847., 1915. [↑6]
- [53] A. Einstein. Zur Quantentheorie der Strahlung. *Physikalische Gesellschaft Zürich*, 18:47–62, 1916. [↑19]
- [54] R. Eisberg and R. Resnick. *Quantum Physics of Atoms, Molecules, Solids, Nuclei, and Particles*. John Wiley & Sons, 2nd edition, 1985. [↑15]
- [55] M. Esposito, et al. Geant4-based simulations of charge collection in CMOS Active Pixel Sensors. *Journal of Instrumentation*, 12(03):P03028, 2017. doi:10.1088/1748-0221/12/03/P03028. [↑89]
- [56] U. Fano. Ionization Yield of Radiations. II. The Fluctuations of the Number of Ions. *Phys. Rev.*, 72:26–29, 1947. doi:10.1103/PhysRev.72.26. [↑22]
- [57] M. Faraday. VI. Experimental researches in electricity.—Sixth series. *Philosophical Transactions of the Royal Society of London*, 124:77–122, 1834. doi:10.1098/rstl.1834.0008. [↑18]
- [58] E. Fermi. Zur Quantelung des idealen einatomigen Gases. *Zeitschrift für Physik*, 36(11): 902–912, 1926. doi:10.1007/BF01400221. [↑17]
- [59] M. P. Fewell. The atomic nuclide with the highest mean binding energy. *American Journal of Physics*, 63:653–658, 1995. doi:10.1119/1.17828. [↑4]

- [60] A. Fick. Ueber Diffusion. *Annalen der Physik*, 170(1):59–86, 1855. doi:10.1002/andp.18551700105. [↑72]
- [61] C. F. Fischer. Breit-Pauli lifetimes and transition probabilities for Si I. *Phys. Rev. A*, 71: 042506, 2005. doi:10.1103/PhysRevA.71.042506. [↑19]
- [62] P. Fischer, et al. Readout concepts for DEPFET pixel arrays. *Nucl. Instr. Meth. Phys. Res. A*, 512(1):318 – 325, 2003. doi:10.1016/S0168-9002(03)01909-0. [↑42]
- [63] T. Fischer, et al. Neutrino-pair emission from nuclear de-excitation in core-collapse supernova simulations. *Physical Review C*, 88, 2013. doi:10.1103/PhysRevC.88.065804. [↑5]
- [64] H.-J. Fitting. Transmission, energy distribution, and SE excitation of fast electrons in thin solid films. *physica status solidi (a)*, 26(2):525–535, 1974. doi:10.1002/pssa.2210260216. [↑87]
- [65] G. Fontaine, et al. The Potential of White Dwarf Cosmochronology. *Publications of the Astronomical Society of the Pacific*, 113(782):409, 2001. doi:10.1086/319535. [↑5]
- [66] R. H. Fowler. On dense matter. *Monthly Notices of the Royal Astronomical Society*, 87: 114–122, 1926. doi:10.1093/mnras/87.2.114. [↑5]
- [67] D. A. Frail, et al. Does the Crab Have a Shell? *The Astrophysical Journal Letters*, 454(2), 1995. doi:10.1086/309794. [↑6]
- [68] M. Fukugita, et al. The Sloan Digital Sky Survey Photometric System. *Astronomical Journal*, 111:1748, 1996. doi:10.1086/117915. [↑6]
- [69] C. Gaiser, et al. Final determination of the Boltzmann constant by dielectric-constant gas thermometry. *Metrologia*, 54(3):280, 2017. doi:10.1088/1681-7575/aa62e3. [↑17]
- [70] E. García-Berro. The Formation and Evolution of ONe White Dwarfs: Prospects for Accretion Induced Collapse. In R. Di Stefano, et al., editors, *Binary Paths to Type Ia Supernovae Explosions*, volume 281 of *IAU Symposium*, pages 52–59, 2013. doi:10.1017/S1743921312014688. [↑5]
- [71] E. Gatti and P. F. Manfredi. Processing the signals from solid-state detectors in elementary-particle physics. *La Rivista del Nuovo Cimento (1978-1999)*, 9(1):1–146, 1986. doi:10.1007/BF02822156. [↑53]
- [72] E. Gatti and P. Rehak. Semiconductor drift chamber — An application of a novel charge transport scheme. *Nucl. Instr. Meth. Phys. Res.*, 225(3):608 – 614, 1984. doi:10.1016/0167-5087(84)90113-3. [↑27,↑28,↑88]
- [73] E. Gatti, et al. Dynamics of electrons in drift detectors. *Nucl. Instr. Meth. Phys. Res. A*, 253 (3):393 – 399, 1987. doi:10.1016/0168-9002(87)90522-5. [↑88,↑89]
- [74] E. Gatti, et al. Suboptimal filtering of 1/f-noise in detector charge measurements. *Nucl. Instr. Meth. Phys. Res. A*, 297(3):467 – 478, 1990. doi:10.1016/0168-9002(90)91331-5. [↑37,↑73]

- [75] E. Gatti, et al. Optimum filters for detector charge measurements in presence of 1f noise. *Nucl. Instr. Meth. Phys. Res. A*, 287(3):513 – 520, 1990. doi:10.1016/0168-9002(90)91571-R. [↑53]
- [76] R. Giacconi, et al. Discovery of Periodic X-Ray Pulsations in Centaurus X-3 from UHURU. *The Astrophysical Journal*, 167:L67, 1971. doi:10.1086/180762. [↑7]
- [77] T. Gold. Rotating Neutron Stars as the Origin of the Pulsating Radio Sources. *Nature*, 218, 1968. doi:10.1038/218731a0. [↑7]
- [78] T. Gold. Rotating Neutron Stars and the Nature of Pulsars. *Nature*, 221, 1969. doi:10.1038/221025a0. [↑7]
- [79] S. Granato, et al. Characterization of eROSITA PNCCDs. *IEEE Transactions on Nuclear Science*, 60(4):3150–3157, 2013. doi:10.1109/TNS.2013.2269907. [↑57,↑75,↑92]
- [80] M. A. Green. Self-consistent optical parameters of intrinsic silicon at 300K including temperature coefficients. *Solar Energy Materials and Solar Cells*, 92(11):1305 – 1310, 2008. doi:10.1016/j.solmat.2008.06.009. [↑19]
- [81] D. Haddad, et al. Invited Article: A precise instrument to determine the Planck constant, and the future kilogram. *Review of Scientific Instruments*, 87(6):061301, 2016. doi:10.1063/1.4953825. [↑17]
- [82] H. Halbritter, et al. High-Speed LED Driver for ns-Pulse Switching of High-Current LEDs. *IEEE Photonics Technology Letters*, 26(18):1871–1873, 2014. doi:10.1109/LPT.2014.2336732. [↑46,↑47]
- [83] A. K. Harding. *High-energy Emission from the Polar Cap and Slot Gap*, chapter 19, pages 521–542. Springer Berlin Heidelberg, 2009. doi:10.1007/978-3-540-76965-1_19. [↑8]
- [84] J. W. T. Hessels, et al. A Radio Pulsar Spinning at 716 Hz. *Science*, 311(5769):1901–1904, 2006. doi:10.1126/science.1123430. [↑12]
- [85] A. Hewish, et al. Observation of a Rapidly Pulsating Radio Source. *Nature*, 1968. doi:10.1038/217709a0. [↑7]
- [86] A. D. Holland, et al. MOS CCDs for the European Photon Imaging Camera. In *Proc. of SPIE*, volume 2006, pages 2006 – 2006 – 9, 1993. doi:10.1117/12.162820. [↑28]
- [87] A. Ingram, et al. A quasi-periodic modulation of the iron line centroid energy in the black hole binary H1743–322. *Monthly Notices of the Royal Astronomical Society*, 461(2), 2016. doi:10.1093/mnras/stw1245. [↑9]
- [88] K. D. Irwin, et al. X-ray detection using a superconducting transition-edge sensor microcalorimeter with electrothermal feedback. *Applied Physics Letters*, 69(13), 1996. doi:10.1063/1.117630. [↑3]
- [89] D. D. Ivanenko and D. F. Kurdgelaidze. Hypothesis concerning quark stars. *Astrophysics*, 1 (4), 1965. doi:10.1007/BF01042830. [↑7]

- [90] J. Janesick, et al. Fano-Noise-Limited CCDs. In *Proc. of SPIE*, volume 0982, pages 0982 – 0982 – 26, 1988. doi:10.1117/12.948704. [↑22]
- [91] J. R. Janesick. *Scientific Charge-coupled Devices*, volume PM83 of *Press Monograph Series*. SPIE, Bellingham, WA, 2001. ISBN 9780819436986. [↑22]
- [92] R. Jenkins, et al. Nomenclature, symbols, units and their usage in spectrochemical analysis - VIII. Nomenclature system for X-ray spectroscopy. *Pure Appl. Chem.*, 63(5):735–746, 1991. doi:10.1351/pac199163050735. [↑15,↑16]
- [93] J. B. Johnson. Thermal Agitation of Electricity in Conductors. *Phys. Rev.*, 32:97–109, 1928. doi:10.1103/PhysRev.32.97. [↑37]
- [94] J. S. Kaastra, et al. Thermal Radiation Processes. *Space Science Reviews*, 134(1):155–190, 2008. ISSN 1572-9672. doi:10.1007/s11214-008-9310-y. [↑19]
- [95] D. Kahng and M. M. Atalla. Silicon-Silicon Dioxide Field Induced Surface Devices. *IRE-AIEE Solid-state Device Res. Conf.*, 1960. [↑31]
- [96] K. Kandiah, et al. The characteristics of noise due to individual defects in JFETs. In *Sixth International Conference on Noise in Physical Systems: Proceedings of a Conference Held at the National Bureau of Standards, Gaithersburg, MD*, 1981. [↑38]
- [97] K. Kandiah, et al. A physical model for random telegraph signal currents in semiconductor devices. *Journal of Applied Physics*, 66(2):937–948, 1989. doi:10.1063/1.343523. [↑38]
- [98] J. Kemmer and G. Lutz. New detector concepts. *Nucl. Instr. Meth. Phys. Res. A*, 253: 365–377, 1987. doi:10.1016/0168-9002(87)90518-3. [↑2,↑32]
- [99] J. Kemmer, et al. Low capacity drift diode. *Nucl. Instr. Meth. Phys. Res. A*, 253(3):378 – 381, 1987. doi:10.1016/0168-9002(87)90519-5. [↑28]
- [100] J. Kepler, et al. *Virtutem quam Planetam movet in circulum, attenuari cum discessu a fonte.*, chapter XXXII, pages 165–167. G. Voegelinus, 1609. doi:10.5479/sil.126675.39088002685477. [↑9]
- [101] C. Kittel. *Introduction to Solid State Physics*. Wiley, 8th edition, 2004. ISBN 9780471415268. [↑14,↑17,↑23]
- [102] J.-P. Lasota. *Black Hole Accretion Discs*, chapter 1, pages 1–60. Springer Berlin Heidelberg, Berlin, Heidelberg, 2016. ISBN 978-3-662-52859-4. doi:10.1007/978-3-662-52859-4_1. [↑1,↑III,↑9]
- [103] J. M. Lattimer and M. Prakash. The Physics of Neutron Stars. *Science*, 304(5670), 2004. doi:10.1126/science.1090720. [↑6,↑7]
- [104] T. Lauf and R. Andritschke. ROOT based Offline and Online Analysis (ROAn): An analysis framework for X-ray detector data. *Nucl. Instr. Meth. Phys. Res. A*, 762:142 – 148, 2014. doi:10.1016/j.nima.2014.05.065. [↑47,↑49,↑89]
- [105] P. Lechner, et al. The low energy detector of Simbol-X. In *Proc. of SPIE*, volume 7021, 2008. doi:10.1117/12.788702. [↑11]

- [106] P. Lechner, et al. DEPFET active pixel sensor with non-linear amplification. In *2011 IEEE Nuclear Science Symposium Conference Record*, pages 563–568, 2011. doi:10.1109/NSSMIC.2011.6154112. [↑3]
- [107] J. Lense and H. Thirring. Über den Einfluß der Eigenrotation der Zentralkörper auf die Bewegung der Planeten und Monde nach der Einsteinschen Gravitationstheorie. *Physikalische Zeitschrift*, 19, 1918. [↑9]
- [108] K.-F. Lin, et al. Controlling electromagnetic wave through dual heights micro-lens array of a CMOS image sensor. *Optics Communications*, 367(Supplement C):254 – 258, 2016. doi:10.1016/j.optcom.2016.01.047. [↑29]
- [109] K. Lodders. Solar System Abundances and Condensation Temperatures of the Elements. *The Astrophysical Journal*, 591:1220–1247, 2003. doi:10.1086/375492. [↑4]
- [110] D. R. Lorimer. *Radio Pulsar Statistics*, chapter 1, pages 1–17. Springer Berlin Heidelberg, Berlin, Heidelberg, 2009. doi:10.1007/978-3-540-76965-1_1. [↑7]
- [111] B. G. Lowe and R. A. Sareen. A measurement of the electron–hole pair creation energy and the Fano factor in silicon for 5.9 keV X-rays and their temperature dependence in the range 80–270 K. *Nucl. Instr. Meth. Phys. Res. A*, 576(2–3):367 – 370, 2007. doi:10.1016/j.nima.2007.03.020. [↑2,↑3,↑22,↑23,↑56]
- [112] F. Lütticke. The Belle II DEPFET pixel detector. *Journal of Instrumentation*, 8(02):C02006, 2013. doi:10.1088/1748-0221/8/02/C02006. [↑34,↑97]
- [113] G. Lutz. *Semiconductor Radiation Detectors*. Springer, 1st edition, 1999. [↑26,↑32,↑33,↑37,↑38]
- [114] G. Lutz. DEPFET development at the MPI semiconductor laboratory. *Nucl. Instr. Meth. Phys. Res. A*, 549(1):103 – 111, 2005. doi:10.1016/j.nima.2005.04.034. [↑94]
- [115] G. Lutz, et al. The DEPFET detector-amplifier structure for spectroscopic imaging in astronomy and for experiments at free electron lasers. *Nucl. Instr. Meth. Phys. Res. A*, 845: 122 – 127, 2017. doi:10.1016/j.nima.2016.04.049. Proceedings of the Vienna Conference on Instrumentation 2016. [↑96]
- [116] J. Madsen. Bulk viscosity of strange quark matter, damping of quark star vibration, and the maximum rotation rate of pulsars. *Phys. Rev. D*, 46, 1992. doi:10.1103/PhysRevD.46.3290. [↑7,↑12]
- [117] P. Majewski, et al. DEPFET Macropixel Detectors for MIXS: Integration and Qualification of the Flight Detectors. *IEEE Transactions on Nuclear Science*, 59(5, 3):2479–2486, 2012. doi:10.1109/TNS.2012.2211616. [↑61,↑63]
- [118] P. Majewski, et al. Calibration measurements on the DEPFET Detectors for the MIXS instrument on BepiColombo. *Experimental Astronomy*, 37:525–538, 2014. doi:10.1007/s10686-014-9374-5. [↑75,↑76]
- [119] W. C. Martin and R. Zalubas. Energy Levels of Silicon, Si I through Si XIV. *Journal of Physical and Chemical Reference Data*, 12(2):323–380, 1983. doi:10.1063/1.555685. [↑18]

- [120] K. Matsumoto, et al. A New MOS Phototransistor Operating in a Non-Destructive Readout Mode. *Japanese Journal of Applied Physics*, 24(5A):L323, 1985. doi:10.1143/JJAP.24.L323. [↑29]
- [121] S. A. Matthews, et al. The European Solar Telescope (EST). In *Proc. of SPIE*, volume 9908, 2016. doi:10.1117/12.2234145. [↑8]
- [122] N. U. Mayall. The Crab Nebula, a Probable Supernova. *Leaflet of the Astronomical Society of the Pacific*, 3:145, 1939. [↑6]
- [123] P. A. Mazzali, et al. A Common Explosion Mechanism for Type Ia Supernovae. *Science*, 315(5813):825–828, 2007. doi:10.1126/science.1136259. [↑5]
- [124] K. G. McKay. Avalanche Breakdown in Silicon. *Phys. Rev.*, 94:877–884, 1954. doi:10.1103/PhysRev.94.877. [↑38]
- [125] N. Meidinger, et al. First measurements with DUO/ROSITA pnCCDs. In *Proc. of SPIE*, volume 5898, 2005. doi:10.1117/12.614827. [↑75]
- [126] N. Meidinger, et al. Report on the eROSITA camera system. In *Proc. of SPIE*, volume 9144, 2014. doi:10.1117/12.2055703. [↑2]
- [127] N. Meidinger, et al. The Wide Field Imager instrument for Athena. In *Proc. of SPIE*, volume 10397, 2017. doi:10.1117/12.2271844. [↑2]
- [128] L. Meitner. Über die Entstehung der β -Strahl-Spektren radioaktiver Substanzen. *Zeitschrift für Physik*, 9(1):131–144, 1922. doi:10.1007/BF01326962. [↑19]
- [129] A. Meuris, et al. Development and characterization of new 256×256 pixel DEPFET detectors for X-ray astronomy. In *IEEE Nuclear Science Symposium Medical Imaging Conference*, pages 38–42, 2010. doi:10.1109/NSSMIC.2010.5873713. [↑41]
- [130] J. M. Miller. Relativistic X-Ray Lines from the Inner Accretion Disks Around Black Holes. *Annual Review of Astronomy and Astrophysics*, 45(1), 2007. doi:10.1146/annurev.astro.45.051806.110555. [↑10]
- [131] M. C. Miller, et al. Sonic-Point Model of Kilohertz Quasi-periodic Brightness Oscillations in Low-Mass X-Ray Binaries. *The Astrophysical Journal*, 508(2), 1998. doi:10.1086/306408. [↑9]
- [132] R. A. Millikan. A Direct Photoelectric Determination of Planck's " h ". *Phys. Rev.*, 7:355–388, 1916. doi:10.1103/PhysRev.7.355. [↑18]
- [133] J. W. Mitchell, et al. Sextant X-Ray Pulsar Navigation Demonstration: Initial On-Orbit Results. In *41st Annual AAS Guidance and Control Conference*, 2018. [↑12]
- [134] B. Müller, et al. Supernova simulations from a 3D progenitor model – Impact of perturbations and evolution of explosion properties. *Monthly Notices of the Royal Astronomical Society*, 472(1):491–513, 2017. doi:10.1093/mnras/stx1962. [↑5]
- [135] P. J. Mohr, et al. CODATA recommended values of the fundamental physical constants: 2006. *Rev. Mod. Phys.*, 80:633–730, 2008. doi:10.1103/RevModPhys.80.633. [↑25]

- [136] C. E. Moore. Ionization Potentials and Ionization Limits Derived from the Analysis of Optical Spectra. U.S. National Bureau of Standards, 1970. [[↑18](#)]
- [137] H. G. J. Moseley. XCIII. The high-frequency spectra of the elements. *Philosophical Magazine*, 26(156):1024–1034, 1913. doi:10.1080/14786441308635052. [[↑4](#),[↑16](#)]
- [138] E. R. Most, et al. New Constraints on Radii and Tidal Deformabilities of Neutron Stars from GW170817. *Phys. Rev. Lett.*, 120, 2018. doi:10.1103/PhysRevLett.120.261103. [[↑8](#)]
- [139] R. Muller, et al. *Device Electronics for Integrated Circuits*. Wiley, 2003. ISBN 9780471428770. [[↑17](#),[↑19](#),[↑23](#),[↑24](#)]
- [140] H. Murakami. On the Equivalent Noise Charge (ENC) of a CR-(RC)ⁿ prefilter into a gated integrator system including the 1f noise source. *Nucl. Instr. Meth. Phys. Res. A*, 234(1):132 – 141, 1985. doi:10.1016/0168-9002(85)90818-6. [[↑37](#)]
- [141] M. Nakhostin. *Signal Processing for Radiation Detectors*. Wiley, 2017. ISBN 9781119410157. Fig. 4.27. [[↑37](#),[↑53](#)]
- [142] K. Nandra, et al. The Hot and Energetic Universe - A White paper presenting the science theme motivating the Athena+ mission, 2013. [[↑2](#)]
- [143] R. Novick. Stellar and solar X-ray polarimetry. *Space Science Reviews*, 18(3), 1975. doi:10.1007/BF00212912. [[↑8](#)]
- [144] H. Nyquist. Thermal Agitation of Electric Charge in Conductors. *Phys. Rev.*, 32:110–113, Jul 1928. doi:10.1103/PhysRev.32.110. [[↑37](#)]
- [145] T. R. O'Brian and J. E. Lawler. Radiative lifetimes in Si i from laser-induced fluorescence in the visible, ultraviolet, and vacuum ultraviolet. *Phys. Rev. A*, 44:7134–7143, 1991. doi:10.1103/PhysRevA.44.7134. [[↑19](#)]
- [146] S. L. O'Dell, et al. High-resolution x-ray telescopes. In *Proc. of SPIE*, volume 7803, 2010. doi:10.1117/12.862315. [[↑4](#)]
- [147] L. Onsager. Statistical hydrodynamics. *Il Nuovo Cimento (1943-1954)*, 6(2), 1949. doi:10.1007/BF02780991. [[↑8](#)]
- [148] J. R. Oppenheimer and G. M. Volkoff. On Massive Neutron Cores. *Phys. Rev.*, 55:374–381, 1939. doi:10.1103/PhysRev.55.374. [[↑6](#),[↑7](#)]
- [149] F. Pacini. Energy Emission from a Neutron Star. *Nature*, 216, 1967. doi:10.1038/216567a0. [[↑7](#)]
- [150] F. Pacini. Rotating Neutron Stars, Pulsars and Supernova Remnants. *Nature*, 219, 1968. doi:10.1038/219145a0. [[↑7](#)]
- [151] J. Palfreyman, et al. Alteration of the magnetosphere of the Vela pulsar during a glitch. *Nature*, 556(7700), 2018. doi:10.1038/s41586-018-0001-x. [[↑7](#),[↑8](#)]
- [152] V. R. Pandharipande, et al. Neutron star structure: theory, observation, and speculation. *The Astrophysical Journal*, 208, 1976. doi:10.1086/154637. [[↑7](#)]

- [153] I. S. Pankratov, et al. A study of direct optical transitions in silicon single crystals based on transmission spectra. *Technical Physics Letters*, 38(7):597–599, 2012. doi:10.1134/S1063785012070097. [↑19]
- [154] W. Pauli. Über den Zusammenhang des Abschlusses der Elektronengruppen im Atom mit der Komplexstruktur der Spektren. *Zeitschrift für Physik*, 31(1):765–783, 1925. doi:10.1007/BF02980631. [↑5,↑7,↑15,↑17]
- [155] E. Pian, et al. Spectroscopic identification of r-process nucleosynthesis in a double neutron-star merger. *Nature*, 2017. doi:10.1038/nature24298. [↑4]
- [156] M. Planck. Ueber das Gesetz der Energieverteilung im Normalspectrum. *Annalen der Physik*, 309(3):553–563, 1901. doi:10.1002/andp.19013090310. [↑17,↑18]
- [157] M. Porro, et al. Theoretical comparison between two different filtering techniques suitable for the VLSI spectroscopic amplifier ROTOR. *Nucl. Instr. Meth. Phys. Res. A*, 512(1):179 – 190, 2003. doi:10.1016/S0168-9002(03)01892-8. [↑73]
- [158] M. Porro, et al. ASTEROID: A 64 channel ASIC for source follower readout of DEPFET arrays for X-ray astronomy. *Nucl. Instr. Meth. Phys. Res. A*, 617(1):351 – 357, 2010. doi:10.1016/j.nima.2009.10.040. 11th Pisa Meeting on Advanced Detectors. [↑37,↑43,↑44,↑53,↑54]
- [159] M. Porro, et al. VERITAS: A 128-Channel ASIC for the Readout of pnCCDs and DEPFET Arrays for X-Ray Imaging, Spectroscopy and XFEL Applications. *IEEE Transactions on Nuclear Science*, 60(1):446–455, 2013. doi:10.1109/TNS.2012.2228410. [↑43]
- [160] M. Porro, et al. VERITAS 2.0 a multi-channel readout ASIC suitable for the DEPFET arrays of the WFI for Athena. In *Proc. of SPIE*, volume 9144, 2014. doi:10.1117/12.2056097. [↑43]
- [161] P. Predehl, et al. eROSITA on SRG. In *Proc. of SPIE*, volume 7732, 2010. doi:10.1117/12.856577. [↑29]
- [162] D. Psaltis, et al. Correlations in Quasi-periodic Oscillation and Noise Frequencies among Neutron Star and Black Hole X-Ray Binaries. *The Astrophysical Journal*, 520(1), 1999. doi:10.1086/307436. [↑9]
- [163] R. Richter, J. Treis, F. Schopper, and A. Baehr. Detektoranordnung und entsprechendes Betriebsverfahren. Patent, November 2015. DE 201410006648. [↑35]
- [164] A. Rau, et al. The Wide Field Imager (WFI) for Athena+, 2013. [↑2]
- [165] L. Rezzolla, et al. A new simple model for high-frequency quasi-periodic oscillations in black hole candidates. *Monthly Notices of the Royal Astronomical Society*, 344(3), 2003. doi:10.1046/j.1365-8711.2003.07018.x. [↑9]
- [166] L. Rezzolla, et al. Using Gravitational-wave Observations and Quasi-universal Relations to Constrain the Maximum Mass of Neutron Stars. *The Astrophysical Journal Letters*, 852(2), 2018. doi:10.3847/2041-8213/aaa401. [↑8]
- [167] W. C. Röntgen. Ueber eine neue Art von Strahlen, 1895. Aus den Sitzungsberichten der Würzburger Physik.-medic. Gesellschaft. [↑1]

- [168] É. Roche. La figure d'une masse fluide soumise à l'attraction d'un point éloigné. *Acad. des sciences de Montpellier*, 1849. [↑5]
- [169] C. Rothleitner and S. Schlamminger. Invited Review Article: Measurements of the Newtonian constant of gravitation, G. *Review of Scientific Instruments*, 88(11), 2017. doi:10.1063/1.4994619. [↑7]
- [170] M. A. Ruderman and P. G. Sutherland. Theory of pulsars - Polar caps, sparks, and coherent microwave radiation. *The Astrophysical Journal*, 196, 1975. doi:10.1086/153393. [↑8]
- [171] P. Russo. *Handbook of X-ray Imaging: Physics and Technology*. Series in Medical Physics and Biomedical Engineering. CRC Press, 2017. ISBN 9781498741552. Fig. 1.11. [↑56]
- [172] E. Rutherford. The scattering of alpha and beta particles by matter and the structure of the atom. *Phil. Mag.*, 21:669–688, 1911. doi:10.1080/14786440508637080. [↑13]
- [173] F. Scholze and M. Procop. Modelling the response function of energy dispersive X-ray spectrometers with silicon detectors. *X-Ray Spectrometry*, 38(4):312–321, 2009. doi:10.1002/xrs.1165. [↑75]
- [174] W. Schottky. Über spontane Stromschwankungen in verschiedenen Elektrizitätsleitern. *Annalen der Physik*, 362(23):541–567, 1918. doi:10.1002/andp.19183622304. [↑37,↑38]
- [175] M. Schultze, et al. Delay in Photoemission. *Science*, 328(5986):1658–1662, 2010. doi:10.1126/science.1189401. [↑19]
- [176] K. Schwarzschild. Über das Gravitationsfeld eines Massenpunktes nach der Einsteinschen Theorie. *Sitzungsberichte der Deutschen Akademie der Wissenschaften zu Berlin, Klasse für Mathematik, Physik, und Technik*, page 189, 1916. [↑5]
- [177] J. Schwinger. On the Classical Radiation of Accelerated Electrons. *Phys. Rev.*, 75, 1949. doi:10.1103/PhysRev.75.1912. [↑8]
- [178] W. Shockley. *Electrons and Holes in Semiconductors: With Applications to Transistor Electronics*. Bell Telephone Laboratories series. Robert E. Krieger, 1950. [↑14,↑16]
- [179] W. Shockley and W. T. Read. Statistics of the Recombinations of Holes and Electrons. *Phys. Rev.*, 87:835–842, 1952. doi:10.1103/PhysRev.87.835. [↑38]
- [180] M. Siegbahn. *Spektroskopie der Röntgenstrahlen*. Springer Berlin Heidelberg, 1931. doi:10.1007/978-3-642-50783-0. [↑15]
- [181] F. Siek, et al. Angular momentum–induced delays in solid-state photoemission enhanced by intra-atomic interactions. *Science*, 357(6357):1274–1277, 2017. doi:10.1126/science.aam9598. [↑19]
- [182] S. J. Smith, et al. Transition-edge sensor pixel parameter design of the microcalorimeter array for the x-ray integral field unit on Athena. In *Proc. of SPIE*, volume 9905, 2016. doi:10.1117/12.2231749. [↑3]
- [183] H. Sotani and U. Miyamoto. Pulse profiles of highly compact pulsars in general relativity. *Phys. Rev. D*, 98, 2018. doi:10.1103/PhysRevD.98.044017. [↑11]

- [184] D. Steeghs and J. Casares. The Mass Donor of Scorpius X-1 Revealed. *The Astrophysical Journal*, 568(1), 2002. doi:10.1086/339224. [↑9]
- [185] L. Strüder, et al. The European Photon Imaging Camera on XMM-Newton: The pn-CCD camera. *Astronomy and Astrophysics*, 365:L18–L26, 2001. doi:10.1051/0004-6361:20000066. [↑2,↑28,↑29]
- [186] J. W. Strutt. XV. On the light from the sky, its polarization and colour. *Philosophical Magazine*, 41(271):107–120, 1871. doi:10.1080/14786447108640452. [↑20]
- [187] J. Stupl, et al. CubeX: A compact X-Ray Telescope Enables both X-Ray Fluorescence Imaging Spectroscopy and Pulsar Timing Based Navigation. In *32nd Annual AIAA/USU Conference on Small Satellites*, 2018. [↑12]
- [188] R. A. Sunyaev and J. Trümper. Hard X-ray spectrum of Cyg X-1. *Nature*, 279, 1979. doi:10.1038/279506a0. [↑10]
- [189] S. M. Sze and K. K. Ng. *Physics of Semiconductor Devices*. Wiley, 2006. ISBN 9780470068304. [↑24,↑25,↑38]
- [190] R. Taverna, et al. Polarization of neutron star surface emission: a systematic analysis. *Monthly Notices of the Royal Astronomical Society*, 454(3), 2015. doi:10.1093/mnras/stv2168. [↑8]
- [191] F. Tessier and I. Kawrakow. Calculation of the electron—electron bremsstrahlung cross-section in the field of atomic electrons. *Nucl. Instr. Meth. Phys. Res. B*, 266(4):625 – 634, 2008. doi:10.1016/j.nimb.2007.11.063. [↑21]
- [192] A. Thompson, et al. X-ray Data Booklet. Lawrence Berkeley National Laboratory, 2009. [↑1,↑III,↑16,↑45,↑76]
- [193] F. X. Timmes, et al. The Neutron Star and Black Hole Initial Mass Function. *The Astrophysical Journal*, 457:834, 1996. doi:10.1086/176778. [↑5]
- [194] L. Titarchuk, et al. Mechanisms for High-Frequency Quasi-periodic Oscillations in Neutron Star and Black Hole Binaries. *The Astrophysical Journal*, 499(1), 1998. doi:10.1086/305642. [↑9]
- [195] R. C. Tolman. Static Solutions of Einstein’s Field Equations for Spheres of Fluid. *Phys. Rev.*, 55:364–373, 1939. doi:10.1103/PhysRev.55.364. [↑6,↑7]
- [196] W. Treberspurg, et al. Studies of prototype DEPFET sensors for the wide field imager of Athena. In *Proc. of SPIE*, page 99052C, 2016. doi:10.1117/12.2235407. [↑43]
- [197] W. Treberspurg, et al. Measurement results of different options for spectroscopic X-ray DEPFET sensors. *Journal of Instrumentation*, 13(09), 2018. doi:10.1088/1748-0221/13/09/P09014. [↑64,↑95]
- [198] W. Treberspurg, et al. Studies of prototype DEPFET sensors for the Wide Field Imager of Athena. In *Proc. of SPIE*, volume 10397, 2017. doi:10.1117/12.2274032. [↑3]

- [199] J. Treis, et al. First results of DEPFET-based active-pixel-sensor prototypes for the XEUS wide-field imager. In *Proc. of SPIE*, volume 5501, pages 89–100, 2004. doi:10.1117/12.551536. [↑41]
- [200] J. Treis, et al. DEPMOSFET active pixel sensor prototypes for the XEUS wide field imager. *IEEE Transactions on Nuclear Science*, 52(4):1083–1091, 2005. doi:10.1109/TNS.2005.852673. [↑32]
- [201] J. Treis, et al. MIXS on BepiColombo and its DEPFET based focal plane instrumentation. *Nucl. Instr. Meth. Phys. Res. A*, 624(2):540 – 547, 2010. doi:10.1016/j.nima.2010.03.173. New Developments in Radiation Detectors. [↑2]
- [202] J. Trümper. Der Röntgensatellit ROSAT. *Physikalische Blätter*, 46(5):137–143, 1990. doi:10.1002/phbl.19900460502. [↑1]
- [203] S. Urban and P. K. Seidelmann. *Explanatory Supplement to the Astronomical Almanac*. University Science Books, 2012. ISBN 9781891389856. [↑5]
- [204] P. Uttley, et al. X-ray reverberation around accreting black holes. *The Astronomy and Astrophysics Review*, 22(1), 2014. doi:10.1007/s00159-014-0072-0. [↑10]
- [205] M. van Adelsberg, et al. Radiation from Condensed Surface of Magnetic Neutron Stars. *The Astrophysical Journal*, 628(2), 2005. doi:10.1086/430871. [↑8]
- [206] M. van der Klis, et al. Discovery of Submillisecond Quasi-periodic Oscillations in the X-Ray Flux of Scorpius X-1. *The Astrophysical Journal Letters*, 469(1), 1996. doi:10.1086/310251. [↑9]
- [207] W. von Ammon and H. Herzer. The production and availability of high resistivity silicon for detector application. *Nucl. Instr. Meth. Phys. Res. A*, 226(1):94 – 102, 1984. doi:10.1016/0168-9002(84)90174-8. [↑61]
- [208] W. Wagner, et al. New Equations for the Sublimation Pressure and Melting Pressure of H₂O Ice Ih. *Journal of Physical and Chemical Reference Data*, 40(4):043103, 2011. doi:10.1063/1.3657937. [↑39]
- [209] R. H. Walden, et al. The Buried Channel Charge Coupled Device. *Bell System Technical Journal*, 51(7):1635–1640, 1972. doi:10.1002/j.1538-7305.1972.tb02674.x. [↑32]
- [210] F. Weber, et al. *Neutron Star Interiors and the Equation of State of Superdense Matter*, chapter 10, pages 213–245. Springer Berlin Heidelberg, Berlin, Heidelberg, 2009. doi:10.1007/978-3-540-76965-1_0. [↑7]
- [211] M. C. Weisskopf, et al. A precision measurement of the X-ray polarization of the Crab Nebula without pulsar contamination. *The Astrophysical Journal Letters*, 220, 1978. doi:10.1086/182648. [↑8]
- [212] M. C. Weisskopf, et al. Chandra X-ray Observatory (CXO): overview. In *Proc. of SPIE*, volume 4012, 2000. doi:10.1117/12.391545. [↑4]
- [213] R. Wijnands, et al. Quasi-periodic X-ray brightness fluctuations in an accreting millisecond pulsar. *Nature*, 424, 2003. doi:10.1038/nature01754. [↑9]

- [214] D. R. Wilkins, et al. Towards modelling X-ray reverberation in AGN: piecing together the extended corona. *Monthly Notices of the Royal Astronomical Society*, 458(1), 2016. doi:10.1093/mnras/stw276. [↑10]
- [215] S. Wölfel, et al. A Novel Way of Single Optical Photon Detection: Beating the 1/f Noise Limit With Ultra High Resolution DEPFET-RNDR Devices. *IEEE Transactions on Nuclear Science*, 54(4):1311–1318, 2007. doi:10.1109/TNS.2007.901225. [↑3,↑68]
- [216] D. Wolpert and P. Ampadu. *Temperature Effects in Semiconductors*, chapter 2, pages 15–33. Springer New York, New York, NY, 2012. doi:10.1007/978-1-4614-0748-5_2. [↑72]
- [217] A. A. Yaroshevsky. Abundances of chemical elements in the Earth's crust. *Geochemistry International*, 44(1):48–55, 2006. doi:10.1134/S001670290601006X. [↑13]
- [218] S. Yuki and S. Shibata. A Particle Simulation for the Pulsar Magnetosphere: Relationship of Polar Cap, Slot Gap, and Outer Gap. *Publications of the Astronomical Society of Japan*, 64(3), 2012. doi:10.1093/pasj/64.3.43. [↑8]
- [219] J. Zatorski, et al. Extraction of the electron mass from g -factor measurements on light hydrogenlike ions. *Phys. Rev. A*, 96:012502, 2017. doi:10.1103/PhysRevA.96.012502. [↑20]
- [220] P. Zeeman. The Effect of Magnetisation on the Nature of Light Emitted by a Substance. *Nature*, 55:347, 1897. doi:10.1086/140355. [↑15]
- [221] F. Özel and P. Freire. Masses, Radii, and the Equation of State of Neutron Stars. *Annual Review of Astronomy and Astrophysics*, 54(1), 2016. doi:10.1146/annurev-astro-081915-023322. [↑6,↑7]
- [222] Python. Python Software Foundation, Delaware, United States, version 2.7.6. URL <https://www.python.org>. [↑50,↑86]
- [223] NumPy. NumPy Community, version 1.8.2. URL <https://www.numpy.org>. [↑50,↑86]
- [224] Sentaurus Device. Synopsys, Inc., Mountain View, California, United States, version J-2014.09. URL <https://www.synopsys.com>. [↑81,↑82]
- [225] Structure Editor. Synopsys, Inc., Mountain View, California, United States, version J-2014.09. URL <https://www.synopsys.com>. [↑81,↑82]

Publications and Manuscripts

Associated Publications

- [I] **J. Müller-Seidlitz**, R. Andritschke, A. Bähr, N. Meidinger, S. Ott, R. H. Richter, W. Treberspurg, and J. Treis
Spectroscopic Performance of DEPFET active Pixel Sensor Prototypes suitable for the high count rate Athena WFI Detector
Published in *Proceedings of SPIE*,^[c] Volume 9905, 2016, Edinburgh
doi: 10.1117/12.2235408
- [II] **J. Müller-Seidlitz**, R. Andritschke, A. Baehr, N. Meidinger, R. H. Richter, W. Treberspurg, and J. Treis
Performance Study of Spectroscopic DEPFET Arrays with a Pixel-wise Storage Functionality
Published in *Journal of Instrumentation*, Volume 13 (11), 2018
doi: 10.1088/1748-0221/13/11/P11018
- [III] **J. Müller-Seidlitz**, P. Lechner, N. Meidinger, and W. Treberspurg
Spectroscopic DEPFETs at High Frame Rates using Window Mode
Published in *Journal of Instrumentation*, Volume 13 (12), 2018
doi: 10.1088/1748-0221/13/12/P12021
- [IV] **J. Müller-Seidlitz**, A. Baehr, N. Meidinger, and W. Treberspurg
Recent improvements on high-speed DEPFET detectors for X-ray astronomy
Published in *Proceedings of SPIE*, Volume 10709, 2018, Austin (TX)
doi: 10.1117/12.2313203

These publications are attached to the end of the Appendix.

^[c]Society of Photo-optical Instrumentation Engineers

Further Publications and Manuscripts

- [V] J. Fensch, S. Mieske, **J. Müller-Seidlitz**, M. Hilker
The colour-magnitude relation of globular clusters in Centaurus and Hydra.
Constraints on star cluster self-enrichment with a link to massive Milky Way globular clusters
Published in *Astronomy & Astrophysics*, Volume 567, 2014
doi: 10.1051/0004-6361/201423971
- [VI] W. Treberspurg, R. Andritschke, A. Bähr, D. Bianchi, A. Koch, N. Meidinger, **J. Müller-Seidlitz**, S. Ott, and M. Porro
Studies of prototype DEPFET sensors for the wide field imager of Athena
Published in *Proceedings of SPIE*, Volume 9905, 2016
doi: 10.1117/12.2235407
- [VII] S. Ott, R. Andritschke, A. Bähr, N. Meidinger, **J. Müller-Seidlitz**, M. Plattner, W. Stechele, and W. Treberspurg
Modeling of DEPFET based X-ray Detectors for Athena's Wide Field Imager
Published in *IEEE NSS/MIC/RTSD*, 2016
doi: 10.1109/NSSMIC.2016.8069665
- [VIII] N. Meidinger, M. Barbera, V. Emberger, M. Fürmetz, M. Manhart, **J. Müller-Seidlitz**, K. Nandra, M. Plattner, A. Rau, and W. Treberspurg
The Wide Field Imager instrument for Athena
Published in *Proceedings of SPIE*, Volume 10397, 2017
doi: 10.1117/12.2271844
- [IX] W. Treberspurg, R. Andritschke, A. Bähr, A. Behrens, G. Hauser, P. Lechner, N. Meidinger, **J. Müller-Seidlitz**, and J. Treis
Studies of prototype DEPFET sensors for the Wide Field Imager of Athena
Published in *Proceedings of SPIE*, Volume 10397, 2017
doi: 10.1117/12.2274032
- [X] W. Treberspurg, R. Andritschke, A. Behrens, M. Bonholzer, V. Emberger, G. Hauser, N. Meidinger, and **J. Müller-Seidlitz**
Energy response of Athena WFI prototype detectors
Published in *Proceedings of SPIE*, Volume 10699, 2018
doi: 10.1117/12.2313195

- [XI] M. Bonholzer, A. Behrens, V. Emberger, S. Herrmann, N. Meidinger, **J. Müller-Seidlitz**, and W. Treberspurg
First tests of large prototype DEPFET detectors for ATHENA's wide field imager
Published in *Proceedings of SPIE*, Volume 10699, 2018
doi: 10.1117/12.2311318
- [XII] W. Treberspurg, R. Andritschke, G. Hauser, P. Lechner, N. Meidinger, **J. Müller-Seidlitz**, J. Ninkovic, F. Schopper
Measurement results of different options for spectroscopic X-ray DEPFET sensors
Published in *Journal of Instrumentation*, Volume 13 (09), 2018
doi: 10.1088/1748-0221/13/09/P09014
- [XIII] W. Treberspurg, N. Meidinger, **J. Müller-Seidlitz**, S. Herrmann
Achievable noise performance of spectroscopic prototype DEPFET detectors
Published in *Journal of Instrumentation*, Volume 13 (12), 2018
doi: 10.1088/1748-0221/13/12/P12001
- [XIV] W. Treberspurg, G. Hauser, N. Meidinger, **J. Müller-Seidlitz**, S. Ott
Achievable time resolution of spectroscopic prototype DEPFET detectors
Published in *Journal of Instrumentation*, Volume 14 (03), 2019
doi: 10.1088/1748-0221/14/03/P03019
- [XV] W. Treberspurg, R. Andritschke, A. Bähr, A. Behrens, G. Hauser, P. Lechner, N. Meidinger, **J. Müller-Seidlitz**, R. H. Richter, J. Treis
Layout options of spectroscopic X-ray DEPFETs
Published in *Journal of Instrumentation*, Volume 14 (08), 2019
doi: 10.1088/1748-0221/14/08/P08008
- [XVI] W. Treberspurg, R. Andritschke, A. Behrens, M. Bonholzer, V. Emberger, G. Hauser, P. Lechner, N. Meidinger, **J. Müller-Seidlitz**
Characterization of a 256×256 pixel DEPFET detector for the WFI of Athena
Published in *Nucl. Instr. Meth. Phys. Res. A*, Page 162555, 2019
doi: 10.1016/j.nima.2019.162555
- [XVII] M. Bonholzer, R. Andritschke, V. Emberger, N. Meidinger, **J. Müller-Seidlitz**, W. Treberspurg
Electrical characterization of prototype DEPFET detectors for Athena's Wide Field Imager
Published in *Proceedings of SPIE*, Volume 11118, 2019
doi: 10.1117/12.2528403

- [XVIII] N. Meidinger, S. Albrecht, M. Bonholzer, **J. Müller-Seidlitz**, K. Nandra, S. Ott, M. Plattner, W. Treberspurg
Status of the Wide Field Imager Instrument for Athena
Published in *Proceedings of SPIE*, Volume 11118, 2019
doi: 10.1117/12.2528109
- [XIX] **J. Müller-Seidlitz**, M. Bonholzer, V. Emberger, P. Lechner, N. Meidinger, W. Treberspurg
First Results from Flight-like Sensors for Athena's Wide Field Imager
In preparation for *IEEE Transactions on Nuclear Science*

List of Figures

1.1	Redshift of K- α -lines	5
1.2	Crab Nebula	6
1.3	X-Ray Reverberation	10
1.4	X-Ray Pulsar Navigation	12
2.1	Silicon Crystal Lattice	14
2.2	Characteristic X-rays	15
2.3	Energy Levels in Silicon Crystals	16
2.4	Particle Interactions with Energy Transfer	20
2.5	Photon-Electron Cross Sections	21
2.6	Doping	23
2.7	p-n Junction	24
2.8	PIN Diode	27
2.9	Sideward Depletion	28
3.1	Transistor in Inversion	32
3.2	2D DEPFET	33
3.3	3D DEPFET Models	34
3.4	3D Infinipix Model	35
3.5	Charge Collection in an Infinipix	36
4.1	Califa	40
4.2	Power and Electronics	41
4.3	Sensor and ASICs	42
4.4	Asteroid Schematics	43
4.5	Block Diagram of the Setup at Califa	44
4.6	Drain Switch, Photon Sources and Photodiode	46
4.7	Valid Multiple Patterns	49
4.8	Offset, Noise and Gain Map	50
5.1	Readout Scheme of a DEPFET	54
5.2	Cooling Mask and Ceramics with Sensor and ASICs	55
5.3	Simple Spectrum	57
5.4	Spectrum of a non-Storage DEPFET	58
5.5	Top View of the Layout Variants	59
5.6	Functional Test	60

5.7	Noise and Peak-to-Valley Drain Voltage Dependences	61
5.8	Charge Loss between Internal Gates	62
5.9	Back Side Voltage Operational Window	63
5.10	Internal Gate Potential during Clear Pulse	65
5.11	Clear Performance	66
5.12	Spectrum of All Valid Events	69
5.13	Temperature Dependence of the Energy Resolution	72
5.14	Noise contributions	74
5.15	Energy Variations	75
5.16	Infinipix vs. non-Storage DEPFET with 30 μ s Readout	77
5.17	Infinipix vs. non-Storage DEPFET with 10 μ s Readout	78
5.18	Suppression Factor Resistivity Dependence	79
6.1	Simulated Layouts	82
6.2	Charge Collection Infinipix Narrow Gate	83
6.3	Simulated Potential of an Infinipix Wide Drain	84
6.4	Simulated Suppression Factors	85
6.5	Build-up of a Simulation	87
6.6	Convolution of Charge Cloud with Readout	88
6.7	Validation of the Python Simulation	89
6.8	Full Parallel Readout	90
6.9	Spectrum of a 1 μ s Measurement and Simulations	91
7.1	Noise of PXD11 Technology Variants	95
7.2	Charge Loss Improvements	96
7.3	Wide Drain and Full Parallel Readout	97
7.4	Simulated 12 μ m Pixel	98
7.5	Inter-Frame Recombination	99
A.1	Die Positions on PXD8	125
D.1	Measures for Simulated Devices	129

List of Tables

1.1	Instrument Performances	2
2.1	X-ray Line Energies	16
2.2	Typical Depletion Zone Widths	26
5.1	Performance of the Layout Variants	67
5.2	Energy Dependent Resolution	76
5.3	Spectral Degradation at High Frame Rates	78
5.4	Advantages and Disadvantages of the Infinipix Layouts	80
A.1	Investigated Devices	125
B.1	Example Sequence	126
C.1	Typical Operation Voltages	128
D.1	Measures of Simulated Devices	129

Appendix A

The active pixel arrays of 32×32 DEPFETs with the three Infinipix layouts were prototype structures on the production run PXD8 at the semiconductor laboratory of the Max Planck Society. The investigated devices are from Wafer 47 (termed #W1 in this thesis) and Wafer 49 (#W2) from the second run PXD8-2.

Table A.1: The five Infinipix devices in three layout variants from two different wafers as well as the non-storage DEPFETs are listed with their nomenclature within this work, their device names on the wafer production as well as the gate shape and its approximated width W and length L considering over-etching effects emerging during their fabrication.

Naming	Production	Wafer	Die	Gate Shape	W (μm)	L (μm)
Wide Gate #W1	PXD8-2	W47	P20	linear	61.5	3.5
Double Clear #W1	PXD8-2	W47	I01	linear	31.5	3.5
Single Clear #W1	PXD8-2	W47	J01	linear	31.5	3.5
Single Clear #W2	PXD8-2	W49	J01	linear	31.5	3.5
Double Clear #W2	PXD8-2	W49	I01	linear	31.5	3.5
Cut Gate	PXD5	W80	H01	circular	41.6	5.0
Linear Gate (halo)	PXD11	W10	C01	linear	21.5	3.5
Linear Gate thin oxide	PXD11	W12	C01	linear	21.5	3.5
Linear Gate thick oxide	PXD11	W04	C01	linear	21.5	3.5

PXD8 was a production of DEPFETs for an instrument at a free-electron laser in the X-ray regime. As prototype structures, the Infinipix layouts were placed near the border of the 6'' wafer besides the actual devices the production was intended for as shown in Fig. A.1.

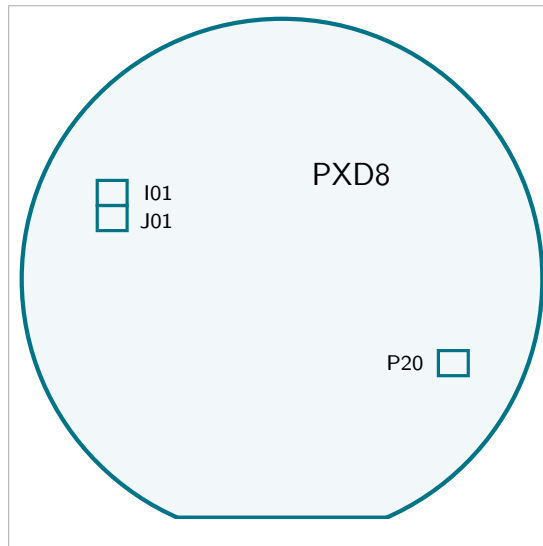


Figure A.1: The positions of the three investigated dies in the PXD8 wafer layout.

Appendix B

The digital control unit provides various commands (*OpCodes*) which are used to shorten a sequence. In the presented excerpt (Table B.1), three different jump commands are used. *JMP* is an absolute jump to the row with the address given in *OpData* while *JMPR* is the counterpart with a relative jump in negative or positive direction by the given number of lines. *JNZR* is also a relative jump which is executed only if the register given in *Operand* is zero. A register is set with *LI* and can be in- or decremented with *ACC*. The *HLT* command extends the execution time in units of the internal clock (12.5 ns) by the number given in *OpData* plus one. Finally *JIOR* is the point where the sequence is stopped if the digital control unit is instructed to do so.

Table B.1: Example of a sequence for the operation of a DEPFET with 32 rows and 32 columns. For an Infinipix, this sequence is required twice with additional two columns for the digital signals that steer the drain switching unit. In a start block before the shown part, the switcher ASIC is reset and the first line is already powered.

Frame Term	Line Term	Gate Term	S_IN	CLK	Load	Gate_pol	ClearGate_pol	Clear_pol	Gate	ClearGate	Clear	MUX_CLK	S_CLK	Address	OpCode	Operand	OpData
0	0	0	0	0	0	1	0	0	1	0	0	0	1	26	JIOR	1	0
0	0	0	0	0	1	1	0	0	1	0	0	0	0	27	0	0	0
0	0	0	0	0	0	1	0	0	1	0	0	0	0	28	HLT	4	0
0	0	0	0	0	0	1	0	0	1	0	0	0	0	29	JMPR	0	3
0	0	0	0	0	1	1	0	0	1	0	0	0	1	30	0	0	0
0	0	0	0	0	0	1	0	0	1	0	0	0	0	31	HLT	0	9
0	0	1	0	0	0	1	0	0	1	0	0	1	1	32	LI	7	2
0	0	0	0	0	0	1	0	0	1	0	0	0	0	33	ACC	7	-1
0	0	0	0	0	0	1	0	0	1	0	0	0	0	34	HLT	0	8
0	0	1	0	0	0	1	0	0	1	0	0	1	0	35	JNZR	7	-2
0	0	0	0	0	0	1	0	0	1	0	0	0	0	36	HLT	0	1
0	0	0	0	0	0	1	0	0	1	0	0	0	1	37	LI	7	12
0	0	0	0	0	0	1	0	0	1	0	0	0	0	38	HLT	0	5
0	0	1	0	0	0	1	0	0	1	0	0	1	0	39	ACC	7	-1
0	0	0	0	0	0	1	0	0	1	0	0	0	0	40	HLT	0	8
0	0	0	0	0	0	1	0	0	1	0	0	0	0	41	JNZR	7	-2
0	0	1	0	0	0	1	0	0	1	0	1	1	1	42	0	0	0
0	0	0	0	0	0	1	0	0	1	0	1	0	0	43	0	0	0
0	0	0	0	0	0	1	0	0	1	1	1	0	0	44	HLT	0	5
0	0	0	0	0	0	1	0	0	1	1	1	0	1	45	0	0	0
0	0	0	0	0	0	1	0	0	1	1	1	0	0	46	HLT	0	0
0	0	1	0	0	0	1	0	0	1	1	1	1	0	47	0	0	0

Frame Term	Line Term	Gate Term	S_IN	CLK	Load	Gate_pol	ClearGate_pol	Clear_pol	Gate	ClearGate	Clear	MUX_CLK	S_CLK	Address	OpCode	Operand	OpData
0	0	0	0	0	0	1	0	0	1	1	1	0	0	48	0	0	0
0	0	0	0	0	0	1	0	0	1	0	1	0	0	49	HLT	0	0
0	0	0	0	0	0	1	0	0	1	0	0	0	1	50	ACC	2	-1
0	0	0	0	0	0	1	0	0	1	0	0	0	0	51	HLT	0	5
0	0	1	0	0	0	1	0	0	1	0	0	1	0	52	LI	7	2
0	0	0	0	0	0	1	0	0	1	0	0	0	0	53	ACC	7	-1
0	0	0	0	0	0	1	0	0	1	0	0	0	0	54	HLT	0	8
0	0	1	0	0	0	1	0	0	1	0	0	1	0	55	JNZR	7	-2
0	0	0	0	0	0	1	0	0	1	0	0	0	0	56	HLT	0	2
0	0	0	1	0	0	1	0	0	1	0	0	0	0	57	JNZR	2	3
0	0	0	1	1	0	1	0	0	1	0	0	0	0	58	LI	2	32
0	0	0	0	0	0	1	0	0	1	0	0	0	0	59	JMPR	0	3
0	0	0	0	1	0	1	0	0	1	0	0	0	0	60	0	0	0
0	0	0	0	0	0	1	0	0	1	0	0	0	0	61	0	0	0
0	0	0	0	0	0	1	0	0	1	0	0	0	1	62	LI	7	11
0	0	0	0	0	0	1	0	0	1	0	0	0	0	63	HLT	0	1
0	0	1	0	0	0	1	0	0	1	0	0	1	0	64	ACC	7	-1
0	0	0	0	0	0	1	0	0	1	0	0	0	0	65	HLT	0	8
0	0	0	0	0	0	1	0	0	1	0	0	0	0	66	JNZR	7	-2
0	0	1	0	0	0	1	0	0	1	0	0	1	0	67	ACC	1	-1
0	0	0	0	0	0	1	0	0	1	0	0	0	0	68	ACC	3	-1
0	0	0	0	0	0	1	0	0	1	0	0	0	0	69	HLT	0	6
0	0	0	0	0	0	1	0	0	1	0	0	0	0	70	JNZR	3	3
0	0	0	0	0	0	1	0	0	1	0	0	0	0	71	LI	3	32
1	0	0	0	0	0	1	0	0	1	0	0	0	0	72	JMPR	0	3
0	0	0	0	0	0	1	0	0	1	0	0	0	0	73	0	0	0
0	1	0	0	0	0	1	0	0	1	0	0	0	0	74	0	0	0
0	0	0	0	0	0	1	0	0	1	0	0	1	0	75	JNZR	1	3
0	0	0	0	0	0	1	0	0	1	0	0	0	0	76	LI	1	32
0	0	0	0	0	0	1	0	0	1	0	0	0	0	77	JMP	0	26
0	0	0	0	0	0	1	0	0	1	0	0	0	0	78	0	0	0
0	0	0	0	0	0	1	0	0	1	0	0	0	0	79	JMP	0	30

The sequence in Table B.1 features a readout time per line of $5\mu\text{s}$ for a clock operated at 80 MHz. For the 32×32 pixels, it results in a total frame time of $160\mu\text{s}$ in the rolling shutter mode. In the starting block before the looped part shown here, the switcher ASIC is reset and the first line is already powered. In addition, the registers 1, 2, 3 and 4 are set to 32, 31, 1 and 0.

Appendix C

Besides the depletion voltage at the back side which strongly depends on the resistivity within the measured wafer die (see Fig. 5.9), the voltages applied to the different Infinipix devices were roughly the same for all five investigated samples. They are listed in Table C.1. The consumed current is not necessarily used up by the detector part, it is assigned to in Table C.1. For example, the current at the gate, clear gate and clear contacts is consumed by the steering ASIC to switch these voltages according to the control sequence shown in Appendix B.

Table C.1: The typical operation voltages for an Infinipix Single Clear with the DEPFET source as point of reference. The consumed currents are given for the measurement shown in Fig. 5.12.

		Voltage (V)	Current (mA)	
Asteroid	VSS	-1.8	-118.8	
	VDD	+1.8	121.4	
	VSSD	-1.7	-9.4	
	VDDD	+1.7	5.8	
	VSST	-1.7	-11.6	
	VDDT	+1.7	8.2	
	Vref	-0.3	-0.3	
	VBST	+1.1	0.2	
Switcher S	VDDA	+3.3	26.0	
	Substrate	-7.0	-20.5	
	Vref	-3.7		
Temperature Diode	high	+7.0	192.8	
	low	-7.0	-0.6	
	Guard	-15.0	0.0	
Drain Driver	high	+6.0	5.1	
	low	-5.9	-1.8	
DEPFET	Ring	-5.8	0.3	
	Inner Substrate	+1.5	0.0	
	Gate	high	+5.8	4.2
		low	+0.8	0.0
	Clear Gate	high	+3.5	3.8
		low	-1.5	-1.8
	Clear	high	+11.0	4.7
		low	+1.3	0.0
	Guard Ring	-2.0	0.0	
	Drain A	high	0.0	0.1
		low	-5.8	-3.5
	Drain B	high	0.0	0.0
		low	-5.8	-3.3
	Back Side Contact	-96.0	0.0	
Drain-Source Current	(per DEPFET)	-0.1		

Appendix D

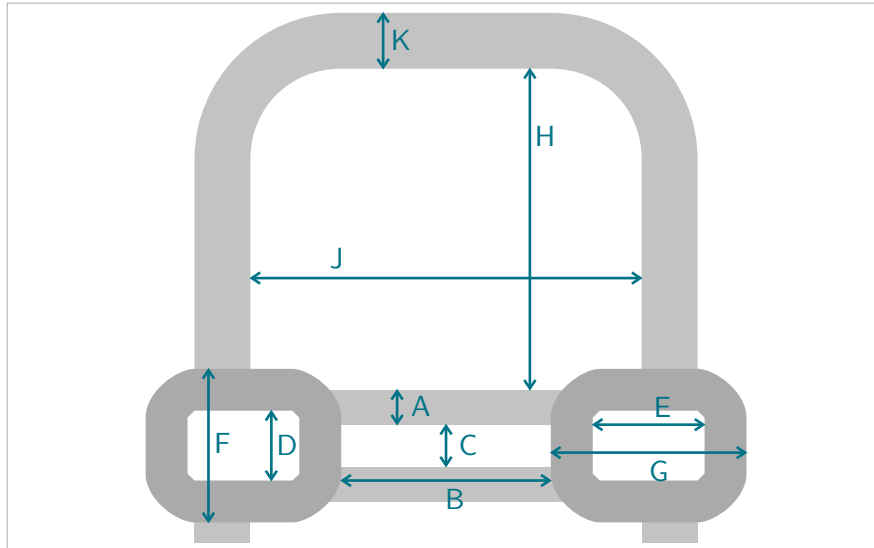


Figure D.1: Nomenclature for the measures given in Table D.1.

The measures for the quantities indicated in Fig. D.1 are presented in Table D.1. The layouts of these four simulated devices are shown in Fig. 6.1 and Fig. 7.4. They are the dimensions of the isolators (silicon oxide and silicon nitride) against the polysilicon structures as they end up after all edging steps in the fabrication at the semiconductor laboratory of the MPG.

Table D.1: Measures of the simulated devices. All values are given for the actual simulated sizes of the structures considering over-etching effects during the fabrication process. The corresponding dimensions are shown in an example in Fig. D.1. The TwinPix is the structure shown in Fig. 7.4.

	Fig. D.1	Wide Drain	Narrow Gate	Unique Clear	TwinPix
Pixel Size		150 μm	150 μm	100 μm	12 μm
Gate length	A	4.0 μm	4.0 μm	3.6 μm	2.0 μm
Gate width	B	31.0 μm	31.0 μm	\sim 14.3 μm	\sim 5.4 μm
Source width	C	7.0 μm	7.0 μm	7.4 μm	2.6 μm
Clear	D	9.0 μm	21.0 μm	21.4 μm	3.0 μm
	E	17.0 μm	8.0 μm	9.4 μm	1.3 μm^*
Clear Gate	F	19.0 μm	31.0 μm	34.6 μm	8.0 μm
	G	27.0 μm	18.0 μm	22.6 μm	3.8 μm^*
Drain	H	47.0 μm	47.0 μm	27.8 μm	2.7 μm^*
	J	57.0 μm	57.0 μm	32.4 μm	6.0 μm
Drain-Ring Separator	K	7.0 μm	7.0 μm	6.6 μm	—

* Only half the size of the actual structure is given, since it is shared with neighbouring pixels

ASSOCIATED PUBLICATIONS

Spectroscopic Performance of DEPFET active Pixel Sensor Prototypes suitable for the high count rate Athena WFI Detector

Johannes Müller-Seidlitz^a, Robert Andritschke^a, Alexander Bähr^a, Norbert Meidinger^a, Sabine Ott^a, Rainer H. Richter^b, Wolfgang Treberspurg^a, and Johannes Treis^b

^aMax-Planck-Institute for extraterrestrial Physics, Giessenbachstr. 1, 85748 Garching,
Germany

^bSemiconductor Laboratory of the Max-Planck-Society, Otto-Hahn-Ring 6, 81739 München,
Germany

ABSTRACT

The focal plane of the WFI of Athena consists of two sensors. One features a large field of view of $40' \times 40'$ and one is foreseen to be used for bright point like sources. Both parts base on DEPFET active pixel sensors. To fulfil the count rate requirement for the smaller sensor of less than 1% pile-up for a one Crab source it has to have a sufficient high frame rate. Since therefore the readout becomes a large fraction of the total photon integration time, the probability of measurements with incomplete signals increases. A shutter would solve the problem of these so called misfits but is not in agreement with the required high throughput of more than 80%. The Infinipix design has implemented a storage in addition to separate the collection and the readout of the charges without discarding them. Its working principle was successfully shown by Bähr et al.¹ on single pixel level. For the further development three layout variants were tested on a 32×32 pixel array scale. The measurements of the spectroscopic performance show very promising results even for the intended readout speed for the Athena WFI of $2.5 \mu s$ per sensor row. Although, there are still layout and technology improvements necessary to ensure the reliability needed for space missions. In this paper we present the measurement results on the comparison of the three prototype layout variants.

Keywords: Athena WFI, DEPFET, Active pixel sensor, Infinipix, High count rate, X-ray astronomy

1. INTRODUCTION

The wide field imager (WFI)² is one of the two focal plane instruments planned for the Advanced Telescope for High-energy Astrophysics (Athena), ESA's second large-class mission of the cosmic vision programme (L2) which will observe the hot and energetic universe³ in the energy range from 0.2 to 15 keV. The large sensor of the WFI⁴ has a field of view of $40' \times 40'$ and is suitable for the observation of the large scale structures in the universe like hot gas tracing the gravitational potential in galaxy clusters. The high count rate capability of the Athena WFI will be provided by a second small sensor. It allows for a short readout time to handle bright point sources of the order of one Crab with a throughput of $>80\%$ and a pile-up of less than 1%. A defocusing of the sensor is necessary to achieve this scientific requirements. A point like source will be spread over the whole sensor consisting of 64×64 pixels with a pixel size of $130 \times 130 \mu m^2$. The sensor is designated to observe bright objects with a time resolution of $80 \mu s$.

Both sensors base on DEpleted P-channel Field Effect Transistors (DEPFET)⁵ processed on wafers with a thickness of $450 \mu m$. In this sensor concept the silicon bulk is depleted from the front and the back side. Signal charges generated by an X-ray photon drift towards and are stored in a so called internal gate that is implemented underneath a transistor gate and influence the transistor current proportional to their number. That allows the collected charge to be measured directly in the pixel without destruction. It is read out row

Further author information: (Send correspondence to Johannes Müller-Seidlitz)

Johannes Müller-Seidlitz: E-mail: jms@mpe.mpg.de, Telephone: +49 (0)89 30 000 3509

wise via the Asteroid⁶ - a readout ASIC that is planned to be replaced by a newer version called Veritas.⁷ It measures either the variation of the source voltage for a constant transistor current or the current itself for up to 64 columns in parallel. After a first measurement the collected charge is removed from the internal gate via the clear transistors of the DEPFET (Fig. 2) and a second measurement is performed to determine the baseline. Charge arriving during the first signal sampling is measured incompletely. Misfits that appear later in the readout sequence add entries to the spectrum that are more negative than the noise peak. Ignoring pile-up, these events can be removed from the spectrum easily.

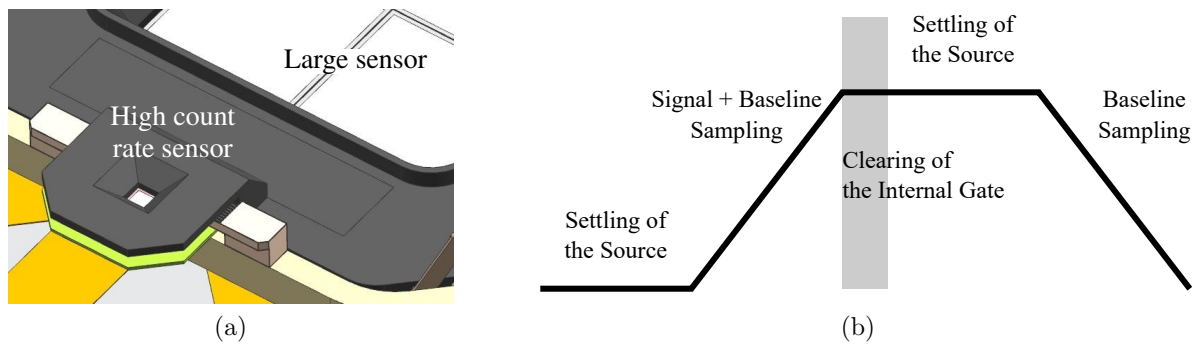


Figure 1. (a) The 64×64 pixel high count rate sensor flanking the large sensor of the WFI² which is built of four wafer scale 512×512 pixel DEPFET arrays. (b) Weighting function of a DEPFET. In the source follower mode the source has to settle after the turning-on of the transistor and after the end of the clear process. The two sampling times are used by the readout ASIC to measure the source voltage before and after the clearing of the internal gate to determine the influence of potentially collected charge on the transistor current.

A higher count rate can be achieved by shortening of the frame length. If the readout time for one row becomes a larger fraction of the total frame time the probability of misfits increases and reduces the quality of the spectral performance. A shutter suppresses these misfits but also reduces the throughput significantly. To omit this disadvantage a storage has to be added into the pixel. By separating the location of the charge collection and the readout, the time for misfits to occur is reduced by two orders of magnitude to a short transfer or switching time.

2. INFINIPIX ARRAYS

To read out charge collected at a spatially separated place, the charge can either be transferred to the readout node or the pixel can be composed of two DEPFETs. The Infinipix, which has its name from its originally ∞ -like shape, is designed according to the second approach.

Fig. 2 shows the layout of an Infinipix structure. The biasing voltage of the drains of the two DEPFETs is, in addition to its function in the transistor, used to suppress charge collection in the read out internal gate. While the voltage level of drain B is on a negative potential for the readout of the hole current, the charge cloud of a detected X-ray photon is forced into the internal gate of transistor A. At the end of the frame, the bias voltages and as a result the tasks of the two drains are interchanged. Since newly arriving charge is now collected in internal gate B, the charge collected under gate A in the previous frame can be read out without any misfit. Only the switching time of the drain voltages allows for the splitting of a charge cloud between two frames.

After the working principle was demonstrated by Bähr et al.¹ with single pixel devices, tests on small arrays with 32×32 pixels with a pixel size of $150 \times 150 \mu\text{m}^2$ were conducted. Exemplary three layout variants were tested. Since all transistors have slightly different biasing conditions, the operation of thousands of them on one sensor requires sufficient large operating windows for the applicable voltages.

Beside a baseline layout called “Double Clear” (clear contacts for both transistors separately) a “Wide Gate” ($60 \mu\text{m}$ gate width) variant was manufactured as a backup in case the dimensions of the baseline layout were too tight for a feasible operation of the device. The “Single Clear” is an option to save control lines and therefore reduce the electronics needed for operation as well as relax the routing on the sensor.

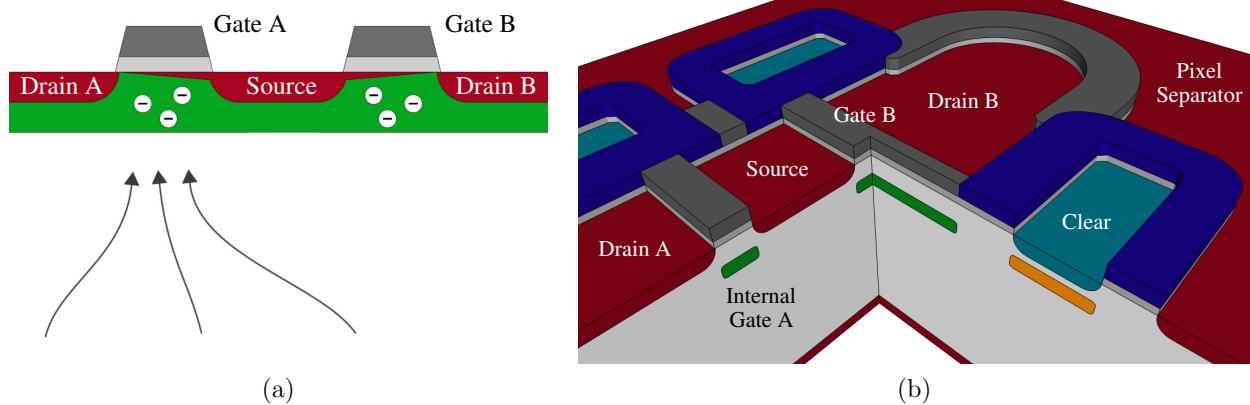


Figure 2. (a) The working principle of an Infinipix. While transistor B is read out, the charge is collected under gate A. By changing the bias voltages for the drains, the tasks of the two DEPFETs are interchanged for the next frame. (b) Cross section of an Infinipix pixel. The source is shared. The drains are separated from the surrounding implantations which separate the individual pixels from each other. The clear transistors (drain in turquoise, gate in blue) remove the charges from the internal gates (green) after they were measured.

The Infinipix arrays were manufactured in the semiconductor laboratory of the Max-Planck-Society (HLL) as test structures on a production run for another DEPFET sensor project. Since the focus of these sensors is on extreme high frame rates, the technology used for the processing was not optimized for spectral performance.

3. MEASUREMENTS AND RESULTS

The three Infinipix arrays were investigated in a vacuum chamber at a sensor temperature of around 220 K. The X-ray photons were provided by an ^{55}Fe source which decays to ^{55}Mn via electron capture with a half-life of 2.7 years.⁸ The ^{55}Mn K- $\alpha_{1,2}$ lines at 5.89 keV and the K- β line at 6.49 keV⁹ are used for the gain calibration of the individual DEPFETs and for the determination of the spectral performance around 6 keV. All devices were illuminated from the back side. The readout of the Infinipix is done in the source follower mode by the Asteroid ASIC.

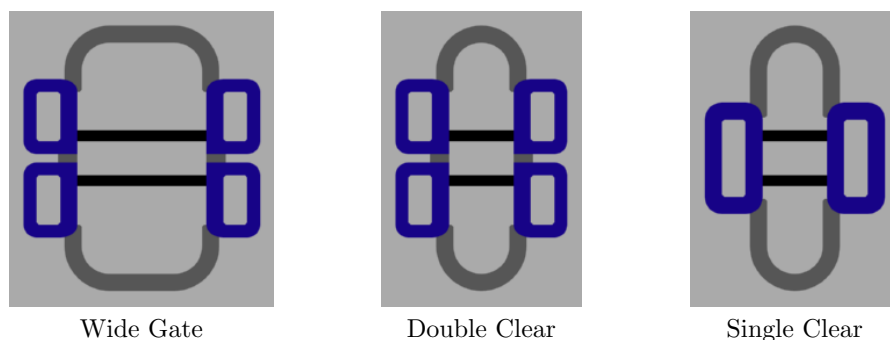


Figure 3. The three layout variants of the Infinipix available for testing. The baseline is the “Double Clear”. The “Wide Gate” is a more relaxed variant to reduce possible influences of the implantations to each other. The more risky “Single Clear” variant saves space within the pixel and control lines for the biasing.

The readout of the devices was performed with a quite moderate timing of $12.25 \mu\text{s}$ per sensor row. $1.5 \mu\text{s}$ were used for each of the both signal sampling times of the readout ASIC. The necessary clear time varies between the different layout variants of the Infinipix. The remaining time in the operation sequence was used for the settling of the source voltage after the turning-on of a sensor row and after the clear process as well as for the data output of the ASIC.

Beside a good set of voltage parameters for the clear contacts, which ensure that the charge is removed from the internal gate after their measurement but no electrons are injected over the clear transistor, the main challenge with the Infinipix is an optimal balance between the back side contact voltage necessary for the bulk depletion and the charge collection, and the drain voltage. A more negative back side voltage leads to a shorter collection time but counteracts the suppression performance of the drain voltages. It turned out that the optimal value for the back side voltage of the present prototypes is the minimum one that fully depletes the silicon bulk. The drain voltage then can be optimized regarding two effects as shown in Fig. 4 (a). On one hand a more negative drain voltage at the transistor of the read out internal gate leads to a better suppression of newly arriving charges. On the other hand the higher voltage difference to the transistor gate causes higher electric fields and therefore the generation of hot carriers that generate additional electron-hole pairs. They increase the noise and degrade the spectral performance. Both voltages, for the back side contact and the drains, do not show a large operational window and only specific values are suitable.

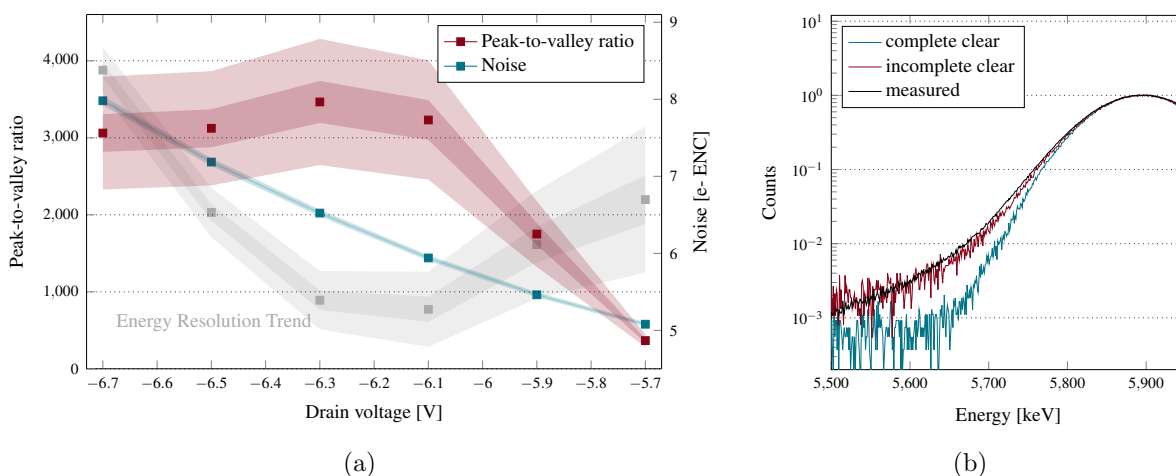


Figure 4. (a) A more negative drain voltage leads to a better suppression of charges from ending up in the wrong internal gate, but also causes generation of noise due to a higher electric field between drain and gate. The peak-to-valley ratio, the ratio of the $^{55}\text{Mn-K}\alpha$ peak height and the mean value in the spectrum between 0.9 and 1.1 keV, is a good tracer for the suppression quality. Considering both key figures gives an optimal value for the drain voltage regarding the optimization of the energy resolution. The error bands represent a 1σ and a 3σ error of the measured data. (b) Simulated data¹⁰ for a 32×32 pixel array with an incomplete clear and a complete clear of the signal charges in the internal gate. Compared with the measurement data from the “Wide Gate” variant the simulation shows the influence of an incomplete clear on the spectral performance.

3.1 Clearing capability

A main issue of DEPFET devices in general is the capability to remove the collected charge from the internal gate. If the clear process is incomplete, the missing charge reduces the quality of the spectrum. The Infinipix layout with its linear gate delivers more promising results regarding the clear performance than the DEPFETs without storage available for testing which have a round gate that limits the minimum gate length. But the width of $60\ \mu\text{m}$ of the “Wide Gate” variant is too large for a complete clear process. Even for high voltages ($>20\ \text{V}$) at the clear contact and for long clear times ($>1\ \mu\text{s}$) about 30% of the pixels of the “Wide Gate” array show an incomplete clear behaviour. The reason may be potential pockets that can not be cleared within one clear cycle. The “Double Clear” does not suffer from an incomplete clear process. The time needed to remove the whole charge from the internal gate is only 100 to 150 ns which would allow for high readout speeds as intended for the Athena WFI.

Nevertheless the “Wide Gate” variant already shows the functionality of the Infinipix for about 1000 pixels respectively 2000 transistors with the same bias voltages. The energy resolution is 147 eV at 5.9 keV for recombined events over up to 4 pixels and the peak-to-valley ratio is 4000 which is already higher than for all

present DEPFETs without storage. This demonstrates the advantage of an DEPFET with storage even for a moderate timing.

The incomplete clear was studied with a programmable real-time emulator that is under development for the WFI.¹⁰ The measurement results were used as input parameters for a first simulation to reproduce the measured spectrum. In a second run, the incomplete clear was neglected to evaluate its influence on the spectral performance (Fig. 4 (b)). The energy resolution for the simulation with a complete clear is 138 eV which proves the assumption that the “Wide Gate” variant suffers mainly from an insufficient clearing capability.

3.2 Bulk doping variations

A result of the narrower gate width of the “Double Clear” (30 μm) is also a smaller drain area. The consequence is an even worse suppression capability of the read out internal gate. If the complete 32×32 pixel array is depleted, parts of sensor already loose about 30% of the charge to the wrong DEPFET. Therefore the sensor can not be operated as a whole with the same back side voltage due to bulk doping variations of about 15% to 20% (peak to peak).¹¹ Using the window mode capability of an active pixel sensor, at least the functionality of that layout could be verified. A 13×16 pixel window ($\sim 20\%$ of the sensor) was selected by using the capability of the readout ASIC to skip columns and a sequence that cycles only through the designated rows. All other pixel rows only have to be cleared to avoid a turning-on of their transistors. The better clear performance and the higher gain results in better spectroscopic performance of these pixels. While the peak-to-valley ratio is roughly the same, the energy resolution increases to 136 eV. The “Wide Gate” variant does not show such good results for selected windows of the same size.

Table 1. Spectral performance of the three layout variants for a moderate timing of 12.25 μs per row. The energy resolution is determined for recombined events over up to 4 pixels. The “CutGate” is the current standard for DEPFETs without storage. Since the pixel size of the available sensors is different, the fraction of single (appear in only one pixel) and multiple events varies and a comparison of the energy resolution of recombined events is not feasible. The 75 μm devices available for measurement also suffer from an incomplete clear.⁴

	Wide Gate	Double Clear	Single Clear	75 μm “CutGate”
Energy resolution @ 5.9 keV	147 eV	136 eV*	134 eV	142 eV
for singles	137 eV	128 eV*	127 eV	132 eV
Peak-to-valley ratio	4000	4200*	4900	1000
Noise	4.6 e^- ENC	3.5 e^- ENC	3.3 e^- ENC	3.6 e^- ENC

* Only a small window ($\sim 20\%$) of the sensor

The “Single Clear” layout saves control lines by using the same clear transistors for both internal gates. The selection of the DEPFET for the clearing is done only by the bias voltage of the readout transistor gate. That restricts the applicable voltages of the clear and the clear gate. Too low voltages prevent a clearing of the read out internal gate. Too high voltages remove charge from the collecting one. These conditions shrink the operational window. Nevertheless this variant is working but 10% of the pixels show a slight incomplete clear due to the lower clear voltages. The voltage applied to the implantation separating the individual pixels can be ~ 3 V more positive than for the other two layouts, which then suffer from a high leakage current on this contact that worsens the spectral performance. As a consequence the “Single Clear” shows the best results of all three layout variants even though it is the most challenging one. The reason for that difference is under investigation by device simulations. But a more positive pixel separator seems to reduce the worse suppression efficiency of the smaller drain areas. With an energy resolution of 134 eV, a peak-to-valley ratio of 4900 and a noise of 3.3 e^- ENC it has an even better spectral performance than the best sub-array of the “Double Clear”, but for the whole 32×32 pixel array. The results for the “Single Clear” were confirmed with a second array manufactured on another wafer of the same production run. Measurements on a second “Double Clear” array are in preparation.

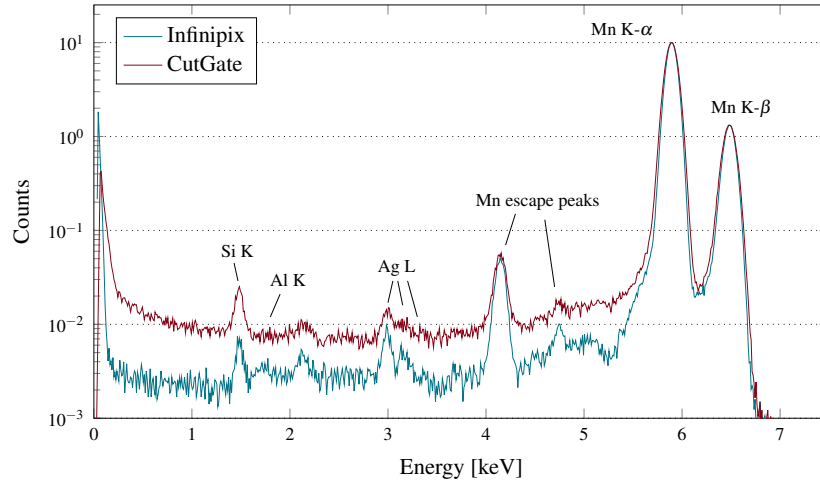


Figure 5. Spectrum of an ^{55}Fe source measured with an Infinipix “Single Clear” and a “CutGate”,⁴ the current standard DEPFET without storage. Both measurements were done with an ASIC sampling time of $1.5 \mu\text{s}$ and a time per row of $12.25 \mu\text{s}$ for the Infinipix and $12.075 \mu\text{s}$ for the “CutGate”. Due to the different sizes of the matrices (64×64 for the “CutGate”) the photon integration time of the Infinipix is as half as long as for the non-storage DEPFET. The difference in the spectral response of the sensor due to less misfits leads to a better resolution of weak spectral features.

3.3 Fast readout

The necessary readout timing to fulfil the requirements for the small sensor, like the high count rate capability and a time resolution of $80 \mu\text{s}$, is $2.5 \mu\text{s}$ per row. The 64×64 pixel high count rate sensor is planned to be read out in two halves.² As a first test the most promising layout, the “Single Clear”, was operated with a corresponding sequence. While the ASIC sampling times were reduced to 500 ns each, the settling of the source that occurs also twice per readout cycle was set to 625 ns each. The remaining 250 ns are used for the clear (150 ns) and for the switching sequence of the clear gate and the clear voltages. The ASIC data output of the row measured before was done in parallel. The shorter signal sampling of the ASIC increases the noise of the measurement while a shorter frame time decreases the amount of noise due to leakage current. As a result the noise increases only slightly from $3.3 e^- \text{ ENC}$ to $3.4 e^- \text{ ENC}$. While the energy resolution degrades also only slightly to 135.5 eV , the peak-to-valley ratio worsens to 3600.

Table 2. Advantages and Disadvantages of the three layout variants.

	Advantages	Disadvantages
Wide Gate	<ul style="list-style-type: none"> • Most robust against backside voltage shifts 	<ul style="list-style-type: none"> • Incomplete clear due to the wide gate
Double Clear	<ul style="list-style-type: none"> • Good results for small detector windows 	<ul style="list-style-type: none"> • Very sensitive to bulk doping variations - no operation of the whole 32×32 pixel array possible
Single Clear	<ul style="list-style-type: none"> • Most promising results • Saving of control lines 	<ul style="list-style-type: none"> • Small operational window for the clear voltages

4. SUMMARY AND OUTLOOK

The Infnipix, a DEPFET with an implemented storage, has been tested as an array of a few thousand transistors biased with the identical voltages and is therefore suitable for imaging detectors. The spectral performance with an energy resolution of 134 eV for events recombined for up to 4 pixels together with a good peak-to-valley ratio is very promising. The width of the gate should not be much larger than $30\ \mu\text{m}$ to avoid incomplete clearing. The high sensitivity of the “Double Clear” to the bulk doping has to be clarified, since the “Single Clear” shows a good performance but has a very limited range in all applied voltages. At the current development status it may be too ambitious to use the Infnipix for the high count rate sensor. In addition, a DEPFET without storage is sufficient for a frame-rate of 12.5 kHz and the proposed science for Crab like targets. With the good results from the Infnipix measurements we are confident that the next generation of non-storage prototypes for the WFI, which also base on narrow linear gate structures, will show similar or even better results in the spectral performance.

Nevertheless for future applications which require an even higher time resolution, an Infnipix or a similar device is necessary to overcome the increasing problem of misfits a DEPFET without storage suffers from. The obvious approach for such an active pixel sensor is the full parallel readout of all pixels. The frame length therefore is reduced to the readout time of one pixel - leading to a spectroscopic imaging sensor with a frame rate in the order of a million frames per second.

ACKNOWLEDGMENTS

Development and production of the DEPFET sensors for the Athena WFI is performed in a collaboration between MPE and the MPG Semiconductor Laboratory (HLL).

We gratefully thank all people who gave aid to make the presented measurements possible. Special thanks go to Danilo Mießner from HLL for his reliable and valuable wire bonding of the sensors and ASICs.

The work was funded by the Max-Planck-Society and the German space agency DLR (FKZ: 50 QR 1501).

REFERENCES

- [1] Baehr, A., Aschauer, S., Bergbauer, B., Lechner, P. H., Majewski, P., Meidinger, N., Ott, S. M., Porro, M., Richter, R. H., Strueder, L., and Treis, J., “Development of depfet active pixel sensors to improve the spectroscopic response for high time resolution applications,” *Proc. of SPIE* **9144** (2014).
- [2] Meidinger, N. et al., “The wide-field imager instrument for athena,” *Proc. of SPIE*(9905-78) (2016). (to be published).
- [3] Nandra, K. et al., “The hot and energetic universe - a white paper presenting the science theme motivating the athena+ mission,” (2013).
- [4] Treberspurg, W. et al., “Studies of prototype depfet sensors for the wide field imager of athena,” *Proc. of SPIE*(9905-80) (2016). (to be published).
- [5] Kemmer, J. and Lutz, G., “New detector concepts,” *Nucl. Instr. and Meth. A* **253**, 365–377 (1987).
- [6] Porro, M. et al., “Asteroid: A 64 channel asic for source follower readout of depfet arrays for x-ray astronomy,” *Nucl. Instr. and Meth. A* **617**, 351–357 (2010).
- [7] Porro, M. et al., “Veritas 2.0 a multi-channel readout asic suitable for the depfet arrays of the wfi for athena,” *Proc. of SPIE* **9144** (2014).
- [8] Audi, G. et al., “The nubase evaluation of nuclear and decay properties,” *Nuclear Physics A* **729**, 3–128 (2003).
- [9] Bearden, J. A., “X-ray wavelengths,” *Rev. Mod. Phys.* **39**, 78 (1967).
- [10] Ott, S. et al., “New evaluation concept of the athena wfi camera system by emulation of x-ray depfet detectors,” *Journal of Instrumentation* **11** (January 2016).
- [11] von Ammon, W. and Herzer, H., “The production and availability of high resistivity silicon for detector application,” *Nucl. Instr. and Meth. A* **226**, 94–102 (1984).

Performance study of spectroscopic DEPFET arrays with a pixel-wise storage functionality

J. Müller-Seidlitz,^{a,1} R. Andritschke,^a A. Baehr,^b N. Meidinger,^a R. H. Richter,^b
W. Treberspurg^a and J. Treis^b

^aMax-Planck-Institute for Extraterrestrial Physics,
Gießenbachstraße 1, 85748 Garching bei München, Germany

^bSemiconductor Laboratory of the Max-Planck-Society,
Otto-Hahn-Ring 6, 81739 München, Germany

E-mail: jms@mpe.mpg.de

ABSTRACT: To maintain a good spectral performance even at high readout speeds, active pixel sensors like the DEPFET need to be equipped with a storage functionality. Enhancing the frame rate to its limit — the readout time per pixel itself — the charge collection and the readout need to be separated spatially to avoid a significant degradation of the spectral performance. One implementation of a storage concept is the Infinipix DEPFET. The most promising Infinipix variant was investigated in greater detail to study the spectral performance for an array of 32×32 pixels. This includes the characterization of the temperature dependence and the contributions of the different noise components. With an optimal set of temperature and timing parameters, a spectrum taken with an iron-55 source was analyzed with high statistics and the energy response for different X-ray photon energies was evaluated.

KEYWORDS: Imaging spectroscopy; X-ray detectors and telescopes; Detector design and construction technologies and materials; Solid state detectors

¹Corresponding author.

Contents

1	Introduction	1
2	Spectral performance	3
2.1	Noise	3
2.2	Energy resolution	5
2.3	Energy response	7
3	Summary	9

1 Introduction

A DEpleted P-channel Field Effect Transistor (DEPFET) is a MOS¹-transistor that is placed on a fully depleted high resistivity n-doped silicon bulk [1]. The majority carriers are removed from the sensitive volume via the principle of sideward depletion [2]. These electrons drift to the electrostatic potential's minimum which is located closer to the front than to the back side. Ring-like structures at the front side enable the sideways drift towards the pixel center (see figure 1) before the electrons are collected under the gate-source region. The volume below the transistor gate is slightly higher n-doped and acts as storage for the electrons.² If the transistor is turned on via the gate, an inversion layer of holes forms below the gate — the transistor channel. The collected electrons induce mirror charges into the channel and its conductivity scales with the number of collected electrons. Due to the steering effect on the channel, the collection region is called internal gate. For an optimum energy resolution, the transistor channel conductivity is measured twice for a fixed current via the floating source³ potential by a readout ASIC⁴ [4]. Electrons collected in the internal gate are removed via an n-channel clear transistor in between.

Incident photons whose charge carriers approach the internal gate during the first signal integration in the readout process are detected with a reduced, incorrect energy (see [5] for more details). Such so-called energy misfits degrade the spectral performance. The extent of degradation depends on the fraction of the signal integration time by the readout ASIC to the exposure time per frame. With a higher frame rate, the degradation increases. To overcome this issue, an additional storage functionality can be implemented into each pixel by separating the charge collection and the readout spatially. One approach is the usage of two sub-pixels with alternating assignments of collection and readout [6]. A charge transfer is avoided. One implementation of the concept is the Infinipix. Two DEPFETs share their source region which is also the common readout node for both sub-pixels. The detector presented in greater detail in this paper was selected in a tradeoff of

¹Metal-Oxide-Semiconductor.

²The charge handling capacity of one pixel is at about 10^5 electrons [3].

³The gain defined as source potential variation per electron in the internal gate is about $4.5 \mu\text{V}/e^-$.

⁴Application-Specific Integrated Circuit.

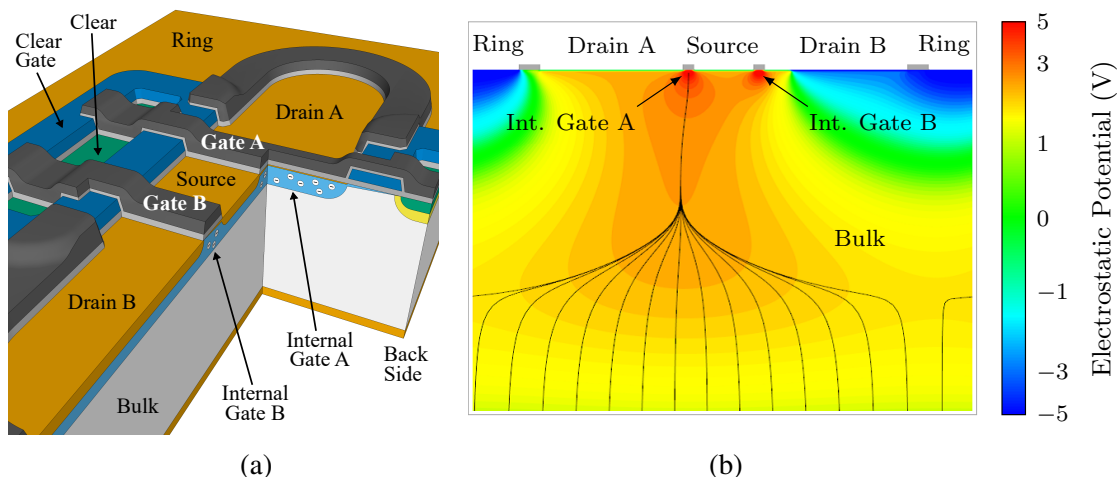


Figure 1. (a) The layout of an Infinipix DEPFET is sketched. Two sub-pixels share their source region which serves as readout node. Electrons generated by an incident photon are collected under the gate of the sensitive sub-pixel — the so-called internal gate. (b) The electrostatic potential demonstrates the selection of the sub-pixel. Internal gate B is shielded by a negative potential applied to Drain B. The voltage level of Drain A and Drain B are interchanged after every frame. The black stream lines represent the paths of electrons generated far from the front side which is the most probable case for a back side illuminated device when detecting low energy X-rays.

different layouts presented in [7]. The clear transistors implemented at both ends of the gates are shared as well in this layout (see figure 1a). The selection of the sub-pixel that needs to be cleared is done via the gate voltage. In the on-state of the transistor (gate-to-source voltage V_{GS} at about -1 V), the internal gate couples to the transistor channel with a potential located between the one of the source and the drain regions. In the off-state ($V_{GS} \approx -6$ V), the internal gate is pulled towards the more positive gate voltage [8]. It becomes attractive enough to hold back collected electrons during a clear pulse for the other sub-pixel.

The assignment of the sub-pixels to be the sensitive or the insensitive one is done with different voltages at the drain regions. A voltage level of -6 V with respect to the source shields the corresponding internal gate against electrons drifting through the silicon bulk. The drain of the charge collecting sub-pixel is roughly at the source potential. Since the readout takes place only at the insensitive sub-pixel, no potential difference is needed. After a complete frame is read out, the drain voltages and, thereby, the assignment to the sub-pixels is interchanged. The electrostatic potential of an Infinipix is shown in figure 1b for one pixel and in figure 2 for three adjacent pixels. Electrons generated in most of the sensitive volume will end up in the internal gate of sub-pixel A. Only electrons of a small area around internal gate B will be attracted by the insensitive sub-pixel. While energy misfits are avoided, a charge cloud can still split between two frames if it arrives at the pixel surface during the switching process of the drain voltages. But such inter-frame split events can be recombined by a subsequent analysis.

The functional principle of the Infinipix was already demonstrated with single pixel devices [9]. Layout comparisons on matrix scale [7] revealed potential for improvement [10]. The most promising layout variant of the three existing and investigated ones was selected for a more detailed study

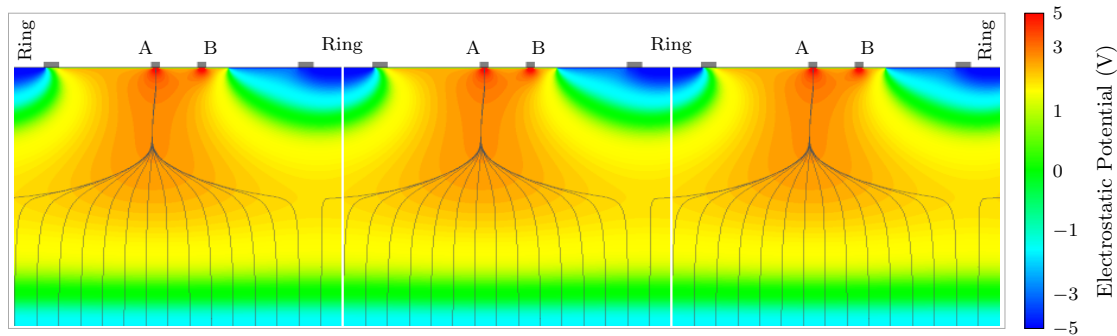


Figure 2. Three adjacent Infinipix pixels. The charge collection area of a pixel does not match the theoretical pixel borders (indicated in white) due to the asymmetric voltage distribution within the pixels. It also changes with the interchange of the drain voltages of the sub-pixels. The shown electrostatic potential flips horizontally. Therefore, the pixel positions of two consecutive frames have a slight offset in one dimension.

of the noise performance and the energy resolution for different temperatures, timing parameters and photon energies. The Infinipix DEPFET array consists of 32×32 pixels with a size of $150 \mu\text{m} \times 150 \mu\text{m}$ each. The thickness of the fully depleted silicon bulk is $450 \mu\text{m}$ to enable a high quantum efficiency also for photons with energies at the order of 10 keV [11].

2 Spectral performance

An important precondition of a good spectral performance is the sensor temperature. As shown in figure 3, an increasing noise worsens the energy resolution above 240 K. The leakage current scales exponentially with temperature and its square root is linearly connected to the shot noise [12]. The whole detector — the Infinipix sensor, the steering and the readout ASICs — are cooled to temperatures between 220 K and 200 K for the measurements presented in this paper. It is done in a vacuum chamber — one option to avoid icing of the detector caused by freezing water contained in the circumambient air. In addition, the lower particle density in the measuring environment reduces the absorption of the X-ray photons emitted by the different sources mounted inside the vacuum tube. The energy resolution does not further improve towards lower temperatures since the reduced thermal energy of the electrons decreases the diffusion which is necessary in low field regions of the internal gate during the clear process. If the drift and the diffusion are slow with respect to the clear pulse, electrons remain in the internal gate. The fluctuation in the number of such electrons — the reset noise — prevents a further improving performance.

2.1 Noise

For a non-illuminated sensor, the different temperature dependent noise contributions can be analyzed in more detail. Beside the exponentially increasing shot noise, a second noise contribution that scales with temperature is the thermal noise. The thermal noise originates from the DEPFET channel and is caused by the thermal movement of electrons in the conduction band. It scales with the square root of the temperature. Therefore, it is not dominant at high temperatures but cooling has a smaller impact on the reduction of the thermal noise. Both temperature dependent noise

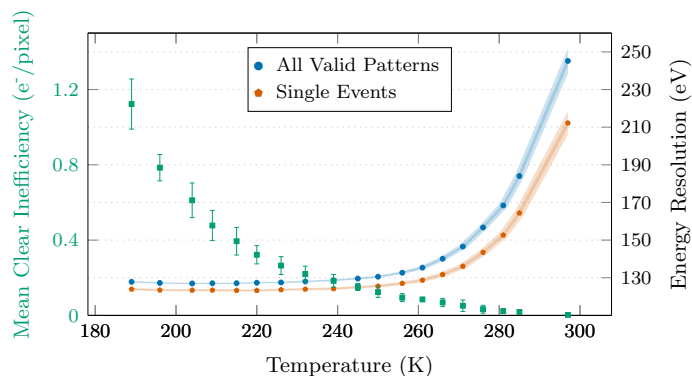


Figure 3. Temperature dependence of the energy resolution at 5.9 keV for all valid patterns (blue) and single events (orange). Below 250 K it is almost stable even though the thermal noise further decreases (see figure 4c). But the influence of reset noise caused by the efficiency of the clear process (green) counteracts the improvement of the thermal noise. The readout was performed within $5 \mu\text{s}$ per row ($160 \mu\text{s}$ per frame) with a signal integration time by the readout ASIC of $1.9 \mu\text{s}$.

components are fitted to the noise determined from non-illuminated frames. The result is shown in figure 4c. The two dashed lines represent the exponential behavior of the shot noise and the square root dependence of the thermal noise. The latter curve also contains a constant offset for further non-thermal noise components. The shot noise is almost not present anymore below temperatures of 220 K.

The weak dependency between the thermal noise and the temperature requires further options to reduce this noise component which is dominant at the measured temperatures and for a signal sampling at the order of one microsecond [4]. By extending this integration time⁵ of the trapezoidal weighting function [13] the thermal noise can be reduced. The effect was investigated with measurements at a constant frame length of $448 \mu\text{s}$. The maximum length of the signal integration time is limited by a combination of the input range of the ADC⁶ and the total detector gain which scales with the integration time τ . The noise dependency and the resulting energy resolution are shown in figure 4a and are proportional to $1/\tau$ [14]. For a continuous rolling shutter readout, the total frame length scales with the chosen signal integration time. By extending the frame length via additional exposure times while the readout time for the measurements is kept constant, the influence of the frame length on the noise can be determined separately. The increasing component is shot noise caused by dark current. Its location in the DEPFET is not yet known and object of further investigation. With a generation rate of $6.10 \text{ e}^-/\text{ms}/\text{pixel}$ the non-thermal shot noise is significant — contributing $2.47 \text{ e}^- \text{ ENC}/\text{ms}/\text{pixel}$ to the overall noise. It is only almost negligible since the frame rates of the small DEPFET devices are high. The combination of the two effects — a decreasing thermal noise for longer signal integrations and an increasing shot noise for large exposure times⁷ — leads to an optimal detector performance for a readout time between five and nine microseconds per row for the 32 row Infinipix DEPFETs as shown in figure 4d. Almost

⁵The signal integration time is the period in which the readout ASIC samples the signal from the sensor.

⁶Analogue-to-Digital Converter.

⁷The exposure time equals one frame period — the time between two drain voltage switching processes.

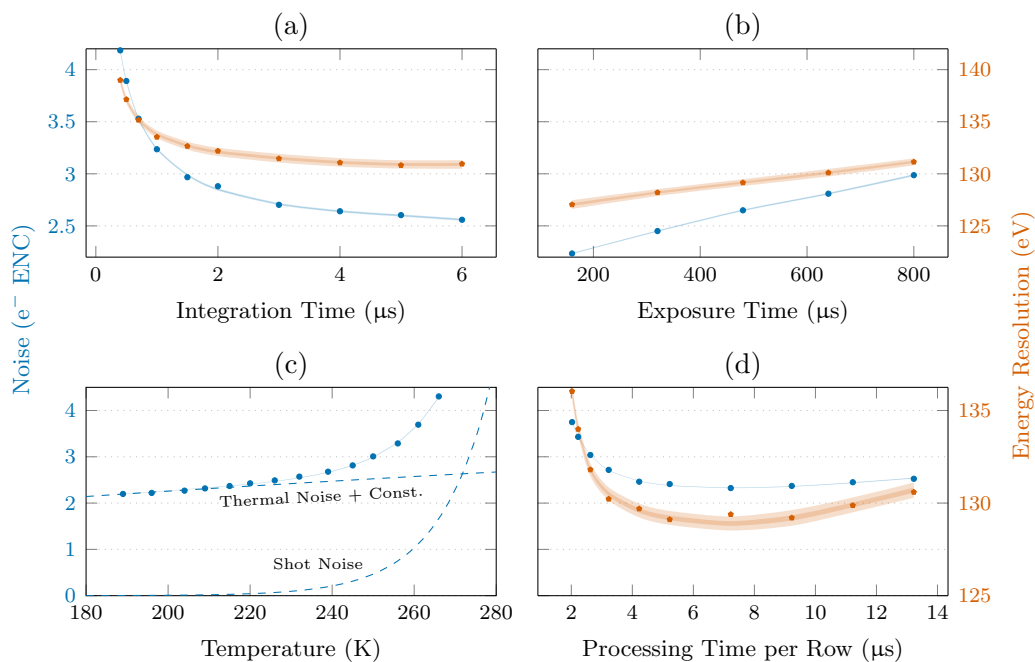


Figure 4. The worsening energy resolution for higher temperatures shown in figure 3 is caused by an increasing shot noise generated by thermal leakage current. This exponential component is fitted to the data shown in (c) and is illustrated together with the other noise components by dashed lines. The remaining temperature dependence is caused by thermal noise. The thermal noise can be reduced by an extension of the integration time in the readout process as shown in (a). An increasing readout processing time also extends the overall exposure time in a continuous rolling shutter readout. Dark current is collected and worsens the noise performance (see (b)). A resulting optimum readout speed for the 32×32 pixel device as result of these counteracting effects is shown in (d). An optimum timing is between $5 \mu\text{s}$ and $9 \mu\text{s}$ per row. Measurements without temperature variation were taken at 220 K.

independent from the timing, crystal defects cause flicker noise. It can be optimized by the shape of the weighting function. The hardware presented in this paper only allows for an optimization towards a triangular weighting function. A flat top that is as short as possible (clear pulse and source settling) is targeted anyway to reduce the readout processing time and to improve the time resolution. The issue of flicker noise can be addressed with specific readout ASICs and DEPFETs like the RNDR⁸ structures [8]. DEPFETs with gate dimensions comparable to the Infinipix operated at the same timing conditions show a flicker noise of about $0.5 e^- \text{ ENC}$ [14] which can be supposed to contribute at the same amount to the constant noise with respect to timing and temperature.

2.2 Energy resolution

The results from the timing variations were used to define a set of parameters to operate the 32×32 Infinipix DEPFETs with an excellent performance. After a row is switched on, the source nodes of the pixels need to settle since they all have different potentials compared to the ones of the previously read-out row. A second settling is needed after the clear process took place because the

⁸Repetitive Non Destructive Readout.

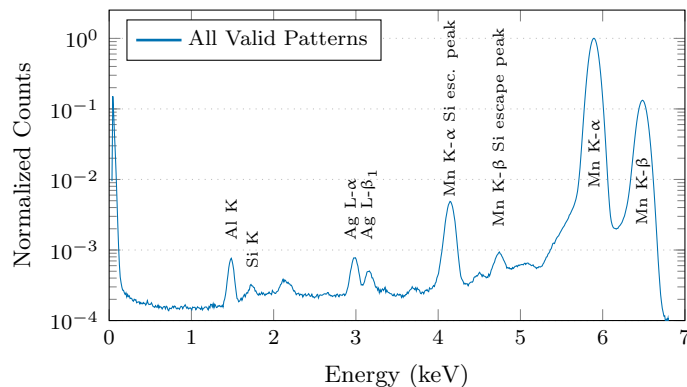


Figure 5. A spectrum taken with a radioactive iron-55 source and the optimized timing parameters at a rate of about 8 photons per second and pixel. Aluminum, silicon, silver and further emission lines generated by fluorescence photons in the mounting of the radioactive source are visible as well as the silicon escape peaks. The energy resolution is 127.4 eV FWHM and 123.6 eV FWHM at 5.9 keV for all valid patterns and single events, respectively. The mean noise per pixel is $2.3 e^-$ ENC at a sensor temperature of 206 K.

positive clear voltage disturbs the source potential. For the present device, they both need a time of 500 ns. The clear process is done within 200 ns. Since the lower limit for an excellent spectral performance for different signal integration times is at about $2 \mu\text{s}$, it was set to $1.9 \mu\text{s}$ to have a resulting total readout processing time per row of $5 \mu\text{s}$.⁹ Those measurements were performed at temperatures of about 200 K.

With these timing parameters a measurement with high statistics was taken to verify the good results that are shown in figure 3 and figure 4 with lower statistics for the temperature and timing sweeps, respectively. Under the optimized conditions, the mean noise per pixel is $2.3 e^-$ ENC.¹⁰ For all valid events — all recombined pattern up to 2×2 pixels — the energy resolution as full width at the half maximum of the peak is 127.4 eV FWHM at 5.9 keV. Compared to non-storage DEPFETs operated at similar conditions, the peak-to-valley ratio is more than three times better and determined to 6900 ± 500 . It is the ratio between the height of the investigated emission line (Mn K- α) and the background taken as mean value between 0.9 keV and 1.1 keV. The lower detector generated background for a storage DEPFET like the Infinipix is a result of the omission of the energy misfits. For recombined events, the noise contribution is higher than for single events since the signal splits over multiple pixels and, thus, the total read noise increases. In addition, a split event tends to lose more likely parts of the signal to neighboring pixels which is not taken into account if it is under the applied pixel-wise threshold of three times the pixel's noise. Therefore, events that occur only in a single pixel give a better indication of the spectral performance of the detector. For such single events, the energy resolution is 123.6 eV FWHM at 5.9 keV. With the spectrum from the high statistics measurement shown in figure 5 small effects can be fitted and quantified. Charge loss on the low energy tail of the investigated Mn K- α emission line or pile-up with noise excesses and the K- β peak on the high energy side can decrease the spectral performance. Extending the

⁹The readout processing time equals the total time a DEPFET is switched on — including the settling processes, the signal integration times and the clear process.

¹⁰Equivalent Noise Charge.

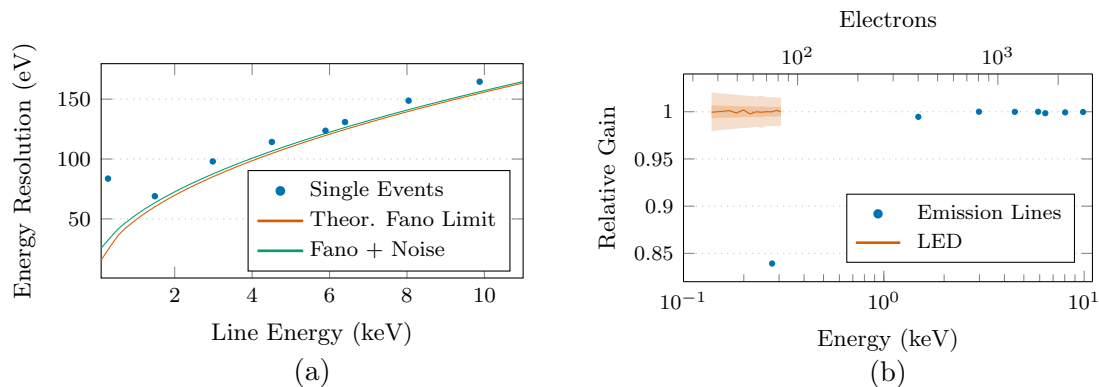


Figure 6. (a) The energy resolutions of various emission lines follow the theoretical Fano limit basing on a Fano factor of 0.118 ± 0.004 according to [15]. Only the carbon K line at 277 eV shows a significant deviation caused by charge loss at the entrance window which increases for low energetic X-ray photons. (b) Missing signal electrons are revealed by a non-linearity at low energies represented by the relative gain normalized to the manganese K- α line. Using a near infrared light emitting diode and a varying number of pulses, the number of collected electrons depends only on the intensity and is, therefore, independent from the attenuation length. Such a measurement demonstrates, that the non-linearity is not an issue of the DEPFET but of the penetration depth of the incident photons.

Gaussian function by additional exponential tails, the influence of charge loss and pile-up on the energy resolution can be evaluated. The resulting energy resolution is 126.7 eV FWHM. It is 0.7 eV below the result using only a Gaussian fit. Therefore, the charge loss and the pile-up and its influence on the spectral performance is very low.

2.3 Energy response

Due to the low noise operation, DEPFETs are mainly limited by Fano noise [16]. The Fano noise limited energy resolution at 5.9 keV is (119 ± 1) eV [15]. Considering the read noise of $2.3 e^-$ ENC, the achievable energy resolution is (121 ± 1) eV for single events and (123 ± 1) eV for all valid events based on the determined pattern statistics which is 27% single events, 43% that show a signal above the threshold (three times the pixel-wise noise) in two neighboring pixels, 10% triples and 17% of the events that split over four pixels. The remaining 3% are flagged as invalid events as they are most likely composed of pile-up of at least two photon events or a photon and a noise excess. The calculation was done for the energy range up to 11 keV for Fano noise only and in combination with the noise determined with non-illuminated frames and its influence on single events shown in figure 6a. With the X-ray tube mounted at the measurement setup, the energy resolution for different energies was determined.

The determined energy resolutions are slightly above the theoretical expectation. The noise measured with non-illuminated frames contains only the components caused by leakage current, thermal processes, fluctuations due to crystal defects and the noise contributions of the electronic components like the power supplies, the ASICs and the ADC. Reset noise, a broadening of the peak by pile-up or due to charge loss at the entrance window and non-perfect gain calibration of the pixel array is not included in the theoretical energy resolution. In addition, the X-ray tube generates a significant bremsstrahlung continuum which distorts the results. Therefore, the Mn-K- α

emission line shows the best relative performance since it is generated with the radioactive iron-source without a bremsstrahlung continuum. The determined numbers are given in table 1. The largest difference between theoretical and measured energy resolution is found with the carbon K- α emission line. The probability that charge is lost at the entrance window depends on the distance of the first interaction of the photon with the sensor material to the entrance window surface [17]. Since the absorption length is a function of photon energy and since for carbon it is the smallest of the used target materials, charge losses are relatively large. This can be verified with an investigation of the relative gain which is the determined signal divided by the expected signal. The relative gain is about 1 for most of the investigated emission lines but drops to 84% for carbon K- α (figure 6).

Table 1. Theoretical Fano limits and the expected energy resolutions in combination with the noise determined in non-illuminated frames. They are compared to the measured energy resolutions for different K- α and L- α emission lines. To show results independent from the pattern statistics that changes with the number of electrons, only single events are evaluated for the measured energy resolution presented in this table. The errors given for the measured energy resolutions are the ones of the fits used to determine the FWHM. The remaining differences in the theoretical and the actual values are caused by charge loss.

Emission Line	Energy [18]	Fano Limit	Fano + Noise	Energy Resolution
C-K	277 eV	(25.9 ± 0.3) eV	(33.0 ± 0.2) eV	(83.7 ± 0.4) eV
Al-K	1486.6 eV	(60.1 ± 0.5) eV	(63.4 ± 0.5) eV	(69.0 ± 0.2) eV
Ag-L	2983.7 eV	(85.1 ± 0.8) eV	(87.5 ± 0.7) eV	(98.0 ± 0.4) eV
Ti-K	4508.8 eV	(104.6 ± 0.9) eV	(106.6 ± 0.9) eV	(114.3 ± 0.2) eV
Mn-K	5895.1 eV	(119 ± 1) eV	(121 ± 1) eV	(123.6 ± 0.2) eV
Fe-K	6399.5 eV	(125 ± 1) eV	(126 ± 1) eV	(130.9 ± 0.2) eV
Cu-K	8041.0 eV	(140 ± 2) eV	(141 ± 2) eV	(148.7 ± 0.5) eV
Ge-K	9875.9 eV	(155 ± 2) eV	(156 ± 2) eV	(164.6 ± 0.6) eV

To exclude a non-linearity effect of the DEPFET, a sweep with low electron numbers was performed. A near infrared LED¹¹ [19] was used to achieve such measurements and the number of electrons was varied by changing the number of LED pulses. It allows for different intensities that enable a varying number of electrons generated with photons of the same energy and, therefore, penetration depths. The constant relative gain (figure 6) excludes the DEPFET as origin for the non-linearity. Nevertheless, the low energy response is worse than expected from previous results obtained with pnCCDs¹² [20]. The prototype Infinipix DEPFETs were fabricated as test structures on a production that was not optimized for spectroscopic measurements at a few keV. But first measurements with non-storage linear gate DEPFETs also showed an excellent low energy response [21]. They indicate that an improvement of the already good spectral response of these first Infinipix prototypes is possible. Nevertheless, the low energy response is still under investigation. Recent results indicate, that the aluminum on-chip optical blocking filter deposited on the silicon nitride and silicon oxide that protect the back side has an influence on the configuration of the electric field at the entrance window which causes larger charge loss.

¹¹Light Emitting Diode.

¹²Charge-Coupled Device.

3 Summary

The Infinipix DEPFET shows an excellent spectroscopic performance demonstrated by measurements with an array of 32×32 DEPFET pixels. In a continuous rolling shutter readout with a readout processing time per row of $5 \mu\text{s}$ ($160 \mu\text{s}$ per frame) a mean noise per pixel of $(2.333 \pm 0.004) e^-$ ENC and an energy resolution of $(127.40 \pm 0.07) e\text{V}$ FWHM for all valid events ($[123.61 \pm 0.07] e\text{V}$ FWHM for single pixel events) at 5.9 keV was determined. Operation temperatures below 250 K are required to suppress shot noise generated by thermal leakage current in each pixel. It was verified that the functional principle of the separation of charge collection and readout is working also on matrix scale with about $1,000$ pixels. The spectral performance improves compared to non-storage DEPFETs due to the suppression of the energy misfits.

Acknowledgments

We gratefully thank all people who gave aid to make the presented measurements possible. The work was funded by the Max-Planck-Society and the German space agency DLR (FKZ: 50 QR 1501).

References

- [1] J. Kemmer and G. Lutz, *New detector concepts*, *Nucl. Instrum. Meth. Phys. A* **253** (1987) 365.
- [2] E. Gatti and P. Rehak, *Semiconductor drift chamber — An application of a novel charge transport scheme*, *Nucl. Instrum. Meth.* **225** (1984) 608.
- [3] J. Treis et al., *Pixel detectors for x-ray imaging spectroscopy in space*, *2009 JINST* **4** P03012.
- [4] M. Porro et al., *ASTEROID: A 64 channel ASIC for source follower readout of DEPFET arrays for X-ray astronomy*, *Nucl. Instrum. Meth. A* **617** (2010) 351.
- [5] J. Müller-Seidlitz et al., *Spectroscopic DEPFETs at high frame rates using window mode*, to appear in *JINST* (2018).
- [6] R. Richter, J. Treis, F. Schopper and A. Baehr, *Detector arrangement and corresponding operating method wherein the detector is a semi-conductor detector which is switchable between collection states with selected subpixel sensitivity*, United States Patent 9812475 (2017).
- [7] J. Müller-Seidlitz et al., *Spectroscopic performance of DEPFET active pixel sensor prototypes suitable for the high count rate Athena WFI detector*, *Proc. SPIE* **9905** (2016) 990567.
- [8] S. Wölfel et al., *A novel way of single optical photon detection: Beating the $1/f$ noise limit with ultra high resolution depfet-rndr devices*, *IEEE Trans. Nucl. Sci.* **54** (2007) 1311.
- [9] A. Bähr et al., *Development of depfet active pixel sensors to improve the spectroscopic response for high time resolution applications*, *Proc. SPIE* **9144** (2014) 914411.
- [10] J. Müller-Seidlitz et al., *Recent improvements on high-speed DEPFET detectors for X-ray astronomy*, *Proc. SPIE* **10709** (2018) 107090F.
- [11] N. Meidinger et al., *Development of the wide field imager for Athena*, *Proc. SPIE* **9601** (2015) 96010H.
- [12] G. Lutz, *Semiconductor Radiation Detectors*, first edition, Springer, Berlin Germany (1999).

- [13] E. Gatti and P. F. Manfredi, *Processing the signals from solid-state detectors in elementary-particle physics*, *Riv. Nuovo Cim.* **9** (1986) 1.
- [14] W. Treberspurg et al., *Achievable noise performance of spectroscopic prototype DEPFET detectors*, to appear in *JINST* (2018).
- [15] B. G. Lowe and R. A. Sareen, *A measurement of the electron–hole pair creation energy and the Fano factor in silicon for 5.9 keV X-rays and their temperature dependence in the range 80–270 K*, *Nucl. Instrum. Meth. A* **576** (2007) 367.
- [16] U. Fano, *Ionization yield of radiations. II. The fluctuations of the number of ions*, *Phys. Rev.* **72** (1947) 26.
- [17] F. Scholze and M. Procop, *Modelling the response function of energy dispersive x-ray spectrometers with silicon detectors*, *X Ray Spectrom.* **38** (2009) 312.
- [18] A. Thompson et al., *X-ray data booklet*, Lawrence Berkeley National Laboratory, Berkeley U.S.A. (2009).
- [19] H. Halbritter et al., *High-speed LED driver for ns-pulse switching of high-current LEDs*, *IEEE Photon. Technol. Lett.* **26** (2014) 1871.
- [20] N. Meidinger et al., *First measurements with DUO/ROSITA pnCCDs*, *Proc. SPIE* **5898** (2005) 58980W.
- [21] W. Treberspurg et al., *Energy response of Athena WFI prototype detectors*, *Proc. SPIE* **10699** (2018) 106994F.

RECEIVED: September 21, 2018

REVISED: November 18, 2018

ACCEPTED: November 29, 2018

PUBLISHED: December 14, 2018

Spectroscopic DEPFETs at high frame rates using window mode

J. Müller-Seidlitz,^{a,1} P. Lechner,^b N. Meidinger^a and W. Treberspurg^a

^aMax-Planck-Institute for Extraterrestrial Physics,
Gießenbachstraße 1, 85748 Garching bei München, Germany

^bSemiconductor Laboratory of the Max-Planck-Society,
Otto-Hahn-Ring 6, 81739 München, Germany

E-mail: jms@mpe.mpg.de

ABSTRACT: An active pixel sensor like an array of DEPFET (DEpleted P-channel Field Effect Transistor) pixels allows for very flexible operation modes and an adaptability of the sensor design to the specific needs of the scientific instrument objectives. For a very high time resolution at the order of one microsecond, a full parallel readout of all pixels is required. Every readout node needs to be connected to readout electronics separately. Furthermore, to preserve a good spectroscopic performance, the integration of a storage functionality into each pixel prevents the influence of events occurring during the readout process and provoking an incorrect energy information. The energy of such events is detected incorrectly and is not falsifiable with a subsequent analysis. An active pixel sensor based on a DEPFET with internal storage and wired for full parallel readout is in production and will be available for testing in the future. Alternatively, the ability of an active pixel sensor to be read out in window (region-of-interest readout) mode allows for the investigation of the behavior at high frame rates at the order of 100 kHz for DEPFET devices with and without storage functionality.

KEYWORDS: Imaging spectroscopy; X-ray detectors and telescopes; Solid state detectors

¹Corresponding author.

Contents

1	Introduction	1
1.1	Readout of spectroscopic DEPFETs and energy misfits	2
1.2	The Infinipix — a DEPFET with integrated storage	4
2	Window mode	5
3	High frame rate measurements	6
4	Future prospects	8
5	Summary	9

1 Introduction

X-ray spectroscopy with imaging cameras requires single photon counting. For bright sources, either filters in front of the sensor or a sufficient high frame rate are necessary to ensure only single events per pixel and frame for most of the time. While there is a choice of methods for bright sources, compact astronomical objects and their direct vicinities may feature high temporal variability and a high frame rate is essential to achieve an excellent time resolution. Such compact objects are black holes and neutron stars as well as potential accretion disks, coronae and nebulae in their surrounding. They feature sizes of a few kilometers which allow for temporal changes in their electromagnetic emission of the order of microseconds. A sensor with a time resolution of that order can be used to study the virulent environments of black holes using X-ray reverberation [1], to investigate accretion disks by observing quasi-periodic oscillations [2], or even to navigate in space with future spacecrafts using the pulsed signals from rotating neutron stars [3]. X-ray emission from these objects is caused by thermal emission from heated material in the deep gravitation potentials and from synchrotron radiation emitted by charged particles accelerated in the strong magnetic fields of the stellar endpoints.

CCDs¹ are widely used for astronomical imaging cameras. One of their disadvantages is the presence of so-called out-of-time events. Charge carriers generated by incident photons that reach a pixel during the charge transfer towards the readout node are associated with the wrong position on the sensor. The signal of an observed object is smeared over the whole channel parallel to the direction of transfer. Out-of-time events of bright sources may cover weaker objects. For a continuous readout, the information on one spatial dimension is completely lost. It limits the frame rate of CCD imaging detectors. This issue is overcome with the usage of active pixel sensors. An amplifier circuit is used to read out the signal directly in each pixel. The equivalent to the clocked operation of a CCD with readout nodes at every row is the rolling shutter readout of an active pixel sensor. The individual rows of the sensor are addressed one after the other while the columns are

¹Charge-Coupled Devices.

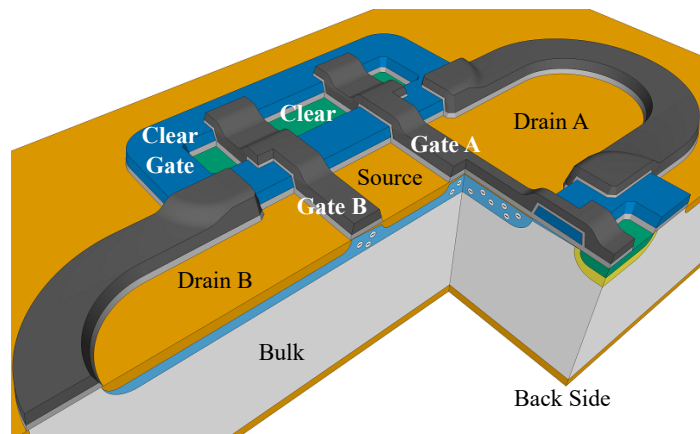


Figure 1. The layout of an Infinipix DEPFET with its two sub-pixels. Electrons are collected in the internal gate either under Gate A or under Gate B, depending on the applied voltages at the Drain regions.

read out fully parallel. Such a row-wise readout has slight offsets in the corresponding timestamp for each row. The time resolution is limited by the readout processing time per row — typically of the order of microseconds — and the total number of rows — the size of the sensor. If even higher frame rates are desired, the complexity of the readout chain can be increased. In principle, an active pixel sensor allows for a full parallel readout of each pixel. The frame period is reduced to the readout time of one pixel. Such a scenario sets additional demands to the pixel design as long as an excellent spectroscopic performance is required.

The DEPFET (DEpleted P-channel Field Effect Transistor) is one implementation of an active pixel. It is a p-channel MOS² field effect transistor integrated on a fully depleted high resistivity n-type silicon bulk [4]. The sensor is depleted asymmetrically from the front side and the back side with a potential minimum generated closer to the front side. A lateral drift within this minimum can be ensured by ring-like structures on the front side. Finally, electrons inside the sensitive volume of the detector are collected beneath the transistor channel of the DEPFET (see figure 1). This volume is most attractive since it is slightly higher n-doped than the rest of the silicon bulk. Electrons inside this volume generate mirror charges in the transistor channel that change its conductivity. Due to its steering effect on the transistor channel conductivity, this volume is called internal gate corresponding to the transistor gate (external gate). The amount of signal charges can be determined via a direct current measurement at the drain contact for fixed transistor voltages (drain current readout) or as voltage variation at the source node for a fixed transistor current (source follower readout). Both quantities are proportional to the number of collected electrons. Unless otherwise indicated, all measurements in this paper are taken in the source follower readout mode.

1.1 Readout of spectroscopic DEPFETs and energy misfits

For an optimal spectroscopic performance, the signal of a DEPFET pixel is sampled twice (see figure 2) — with and without potentially collected signal electrons. Pixels are activated for the readout by a switch-on via the external gate. Then, in the source follower readout, the floating

²Metal-Oxide-Semiconductor.

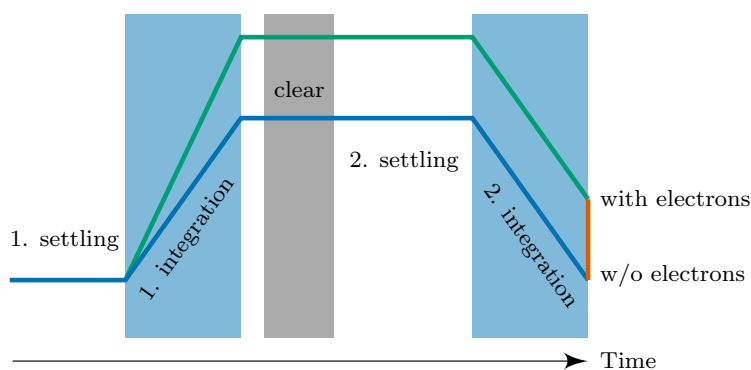


Figure 2. The readout scheme of a spectroscopic DEPFET pixel. The trapezoidal weighting function [8] is the optimum one to reduce the dominating thermal noise. The difference between the two signal integrations (indicated in orange) is the actual signal caused by collected electrons which have been removed from the internal gate during the clear process. The blue and the green line represent the weighting function and the signal in the readout ASIC for electrons that arrived in the internal gate before the readout takes place, respectively. Typical readout processes are of the order of microseconds.

source node needs to settle. In a first integration of the source level using the readout ASIC³ [5–7], the baseline signal together with the influence of potentially collected charge carriers (electrons) is determined. Subsequently, the electrons are removed over clear transistors which are located in every pixel. Due to the positive voltage applied to the clear contact, which influences the source potential, a second settling is needed. Then, the baseline signal of the pixel is measured again via a second signal integration. The readout ASIC takes the difference of the two integrated signals. The result quantifies the amount of collected charge carriers. The trapezoidal weighting function [8] that forms inside the readout ASIC is the optimum to reduce the thermal noise which is the dominant noise contribution at the applied conditions at the order of 1 μ s signal integration and a temperature below 220 K [5]. A typical clear pulse needed to empty the linear internal gates of the devices used for the results in this paper requires about hundred nanoseconds. The settling times in the source follower readout depend on the sensor size. For the prototype sensors of several millimeters the settling time is of the order of a few hundred nanoseconds. Typical integration times vary between several hundred nanoseconds and a few microseconds.

The DEPFET is always collecting signal electrons. Since in astronomy photons can hit the detector at any time, it cannot be avoided that the charge generation and collection overlap with the readout process. Electrons that arrive in the internal gate during the first integration are detected only with a reduced signal (see figure 3). In the subsequent analysis, the signal cannot be distinguished from one generated by a lower number of electrons residing in the internal gate during the whole integration time. Such energy misfits degrade the spectrum. A second origin for such unidentifiable misfits are events that occur at the end of the clear process and which are moved partly into the clear region. Events arriving earlier during the clear process are completely lost. They reduce the detective quantum efficiency but do not reduce the spectral performance. Charge clouds that approach the DEPFET between the end of the clear process and the end of the second signal integration are detected as signals with apparent negative energy. As long as pile-up is negligible, these misfits can easily be marked and skipped.

³Application-Specific Integrated Circuit.

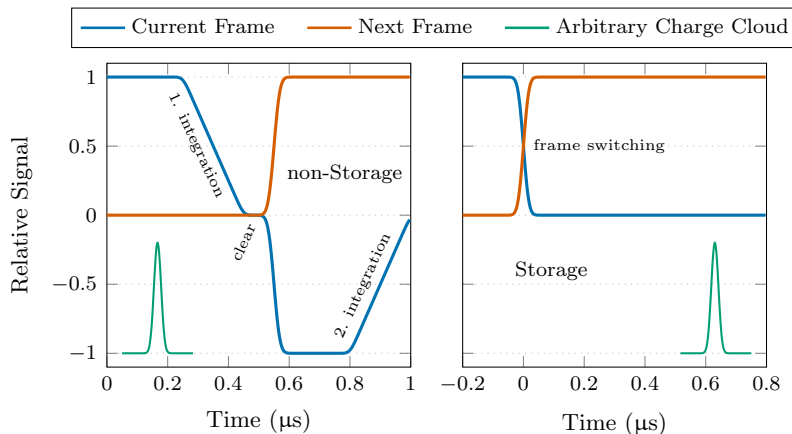


Figure 3. Time-dependence of the signal detected by the readout ASIC. An arbitrary charge cloud convolved with the trapezoidal weighting function of the readout process (figure 2) and the switching process between two frames for a non-storage and a storage DEPFET, respectively, are shown. While the signal that splits over two frames of a storage DEPFET can be recombined, the energy misfits that occur during the first integration and at the end of the clear process degrade the spectral performance of a non-storage device.

1.2 The Infinipix — a DEPFET with integrated storage

The influence on the spectrum by energy misfits becomes relevant only for large fractions of the ASIC’s signal integration time to the total frame period. A temporary blinding of the DEPFET by dumping arriving electrons in an extra contact without charge storage and readout would result in a significant drop of the detective quantum efficiency. In addition, the switching to such a blinding contact is also a potential source for partial charge loss like at the end of the clear process that results in energy misfits. Therefore, the readout and the charge collection have to be separated spatially. One implementation of such a DEPFET with integrated storage functionality is the Infinipix DEPFET [9]. It consists of two sub-pixels with a shared source node and — in the investigated layout variant — shared clear contacts (see figure 1). The spectroscopic performance of 32×32 Infinipix pixels and the layout is described in more detail in [10]. By switching the voltages at the drain regions of the two sub-pixels, the collection and the readout functionality are switched after each frame. Charge carriers that are potentially collected in the sensitive sub-pixel will be read out during the next frame while the sub-pixel is insensitive. The negative voltage at the drain regions of the read-out sub-pixel shields the corresponding internal gate against electrons generated in the sensitive detector volume. The readout process itself is the same as for the non-storage DEPFETs described in section 1.1. Charge clouds arriving at the front side of the sensor while the drain voltages are switched globally are split between two sub-pixels and, thereby, frames. These events are referred to as inter-frame splits. They can be recombined in a subsequent analysis. The resulting signal that splits between the two sub-pixels is shown in figure 3 as theoretical model and in figure 4 as actual measurement using a light emitting diode. Its pulse was temporally shifted over the switching process between two frames.

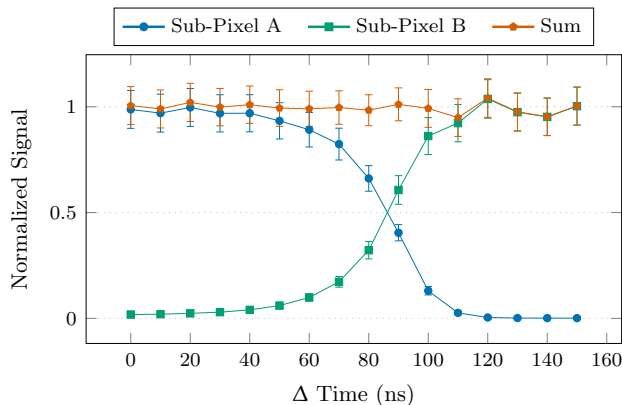


Figure 4. Inter-frame splits in an Infinipix DEPFET. The pulse of a high-speed light emitting diode in the near infrared [11] was temporally shifted over the switching process. According to this measurement, no charge carriers seem to be lost. The asymmetric shape of the single curves is caused by an afterglow of the light emitting diode.

2 Window mode

The effect of misfit events is maximized for a full parallel readout of all pixels. Devices with individual readout connections that would enable this readout mode are still in production for X-ray astrophysics applications. The existing Infinipix DEPFET arrays are designed to be read out in the rolling shutter mode. To increase the fraction between the ASIC’s signal integration and frame time, the latter is reduced by using the capability of active pixel sensors to be read out in window mode. Also known as region-of-interest readout [12], such a concept considers only a part of the rows and columns of the full sensor. In principle, the window mode allows for the readout of arbitrary clusters of pixels. But since the readout already takes place column parallel, there is no further benefit in time from skipping columns. Therefore, a window consists of a number of contiguous sensor rows, which are read out one after the other. The reduction of the number of read-out rows scales nearly with a reduction of the frame period. Additional time is needed to clear all pixels that are not read out regularly. Collected electrons in the internal gates could switch on these pixels otherwise. Since all pixels of a column are connected to one channel of a readout ASIC for the present devices, the switched-on pixels would disturb the results of all read-out pixels in the corresponding columns. This additional clear processes consume an increasing fraction of time the smaller the selected window is. To simplify the steering algorithm for the sensor, this clear process is applied in every frame even though it would not be necessary.

To operate a DEPFET array in the window mode, the flexibility of the steering ASIC is utilized [13]. Its shift register can be programmed with arbitrary patterns to select the sensor rows that need to be activated for the readout or the clear process. While the window is read out row-wise, the clear process is applied to blocks of five contiguous rows to reduce the required time.

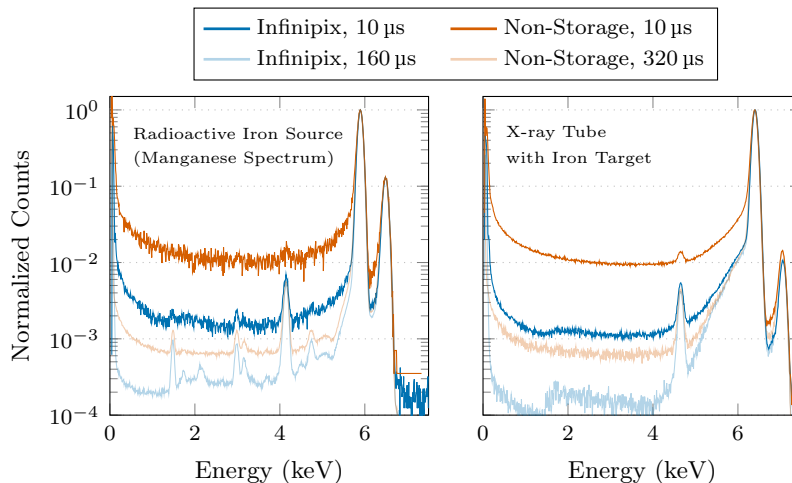


Figure 5. Spectral performance at high frame rates of 100 kHz. With increasing frame rates the sensor generated background dominates the spectral features. Weak emission lines disappear in the increasing number of energy misfits and inter-frame splits. The manganese spectrum shows more spectral features caused by fluorescence photons from elements of the radioactive source’s mounting whereas the X-ray tube allows for higher intensities at the high readout speed to obtain a good statistic with a reasonable number of frames. The measurements were taken at a sensor temperature of about 205 K. Numbers for the spectral performance are given in table 1.

3 High frame rate measurements

To maximize the frame rate, a window of three rows was selected. It is the minimum window that is sensible. All pixels at the borders are only used to ensure that there exists no split partner of an event in adjacent pixels. All events that are at least partly within the border pixels are discarded since there may be charge loss to pixels outside the read-out window. Therefore, only events of the central row are considered for the spectrum. That includes events that occur in a single pixel or that split over two pixels in this row. The three rows were processed within $2.5 \mu\text{s}$ each. 650 ns were used per signal integration. Each settling time was 500 ns . The remaining 200 ns were needed for the clear between the two integrations (150 ns) and for a delay in the switching processes of the clear and the clear gate to avoid back injection of charge carriers into the internal gate as they are turned off. The block-wise clear process of the remaining rows and the time that is needed to program the steering ASIC takes $2.3125 \mu\text{s}$ per frame. This results in a total frame time of $9.8 \mu\text{s}$ and, thus, a frame rate of 102 kHz. The Infinipix DEPFET arrays have 32×32 pixels with a pixel size of $150 \mu\text{m}$. The comparison with a non-storage DEPFET was taken with prototype sensors fabricated for layout and technology tests for the Wide Field Imager of Athena⁴ [14]. They consist of 64×64 DEPFET pixels with a pixel size of $130 \mu\text{m}$. The selected variant also features a linear gate design to gain results that are as comparable as possible. Due to the larger size of 64×64 pixels, the frame time for the full frame mode for the non-storage device is twice as long. In case of the window mode operation with three rows the number of columns was reduced to 32 to have the same dimension as for the Infinipix device.

⁴Advanced Telescope for High ENergy Astrophysics.

From measurements with a NIR LED⁵ [11] the total time spread of the charge cloud was roughly estimated to 80 ns. For a signal integration time of 650 ns about 730 ns of the time are affected for energy misfits during the first integration. Convolved with the fall time of the switching process of the clear pulse, additional 100 ns have to be considered as time of partial charge loss due to the readout process. For a frame time of 9.8 μ s about 8.5% of all events suffer from seeming charge loss and add up to the sensor generated background. It is shown in figure 5 measured with a radioactive ⁵⁵Fe source emitting the characteristic Mn emission lines and with an X-ray tube using an iron target. The mounting of the ⁵⁵Fe source generates some further emission lines caused by fluorescence photons from its materials like aluminum or silver. Their visibility in the spectrum is a good tracer for the spectral quality. With increasing background generated by energy misfits they cannot be detected anymore. It implies for astronomical applications that stronger emission lines can cover weaker, less energetic ones at high frame rates for standard DEPFET detectors. At the high frame rates of 102 kHz taken in the window mode of only 30 pixels that enter into the spectrum, the photon rate per frame is extremely low. The X-ray tube with a tunable intensity was used to obtain better statistics for the high frame rates in a reasonable time and a reasonable amount of data.

Table 1. Energy resolution FWHM_E and peak-to-valley ratio. The results comprise all single events as well as doubles that split within one sensor row. Since other events do not exist in the window mode measurements, they are also skipped in the full frame results for a better comparison. The numbers correspond to the spectra shown in figure 5.

		⁵⁵ Fe Source 5895.1 eV		X-Ray Tube, Iron Target 6399.5 eV	
		FWHM _E	Peak/Valley	FWHM _E	Peak/Valley
non-storage	Full Frame	131.4 eV	1400	138.6 eV	1300
DEPFET	Window	144.4 eV	70	149.0 eV	70
Infinipix	Full Frame	125.6 eV	5400	134.8 eV	9600
DEPFET	Window	131.2 eV	700	138.9 eV	800

The spectrum taken with a storage DEPFET like the Infinipix also degrades as long as the inter-frame split events are not recombined. Such a recombination needs to be implemented in the complex step of the pattern recognition in the offline analysis tools. It will be done in a revision of the software but is not yet implemented. Therefore, the full advantage of a DEPFET array with pixel-wise integrated storage capability cannot yet be demonstrated with measurements. Nevertheless, the inter-frame splits contribute less to the sensor generated background than the energy misfits. The temporal charge cloud size convolved with the switching time of the voltages applied to the drain regions is only about 100 ns. It is only 1% of the overall frame time for the window mode operation. The sensor generated background is about one order of magnitude lower than for a non-storage DEPFET operated at the same timing conditions. The difference decreases for an increasing number of rows that are read out. The ratio between the peak height of the most prominent emission line and the mean value between 0.9 and 1.1 keV — the peak-to-valley ratio —

⁵Near InfraRed Light Emitting Diode.

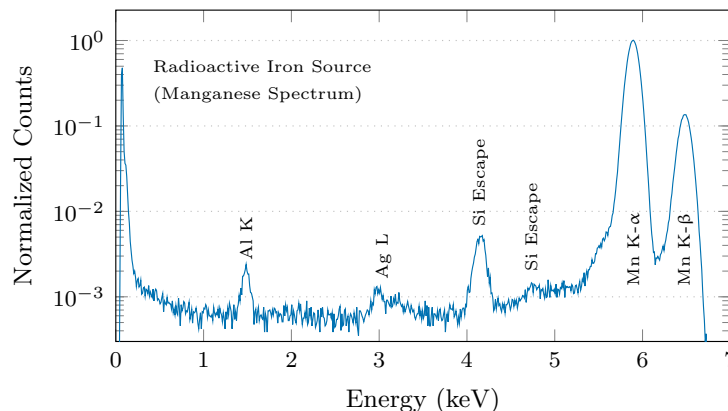


Figure 6. Spectrum for a readout time per row of $1 \mu\text{s}$. The measurement was taken with an Athena prototype sensor in full frame mode (64 rows) using the drain current readout. It demonstrates that with full parallel readout devices, X-ray detectors with a frame rate of 1 MHz are feasible conserving a good spectral performance.

is given in table 1 for a non-storage DEPFET and an Infinipix for a small window with a frame rate of 102 kHz and a full frame readout with a readout time per row of $5 \mu\text{s}$ ($1.9 \mu\text{s}$ integration time). The factor of the peak-to-valley ratio between non-storage DEPFET and Infinipix increases from roughly four to ten from the full frame mode to the window mode.

A significant degradation of the spectrum by energy misfits or inter-frame splits not only affects the sensor generated background and, thereby, low-intensity spectral features, but also the achievable energy resolution. Energy misfits and inter-frame splits broaden the low energetic side of the peak generated by photons from an emission line. For a large sensor-generated background, the energy resolution decreases significantly. The full width at half maximum (FWHM_E) worsens by more than 10 eV for the non-storage DEPFET, but only about 4 eV for the Infinipix. This difference will further reduce with an inter-frame split recombination.

4 Future prospects

The window mode measurements are only a first demonstration of the advantage a DEPFET with storage capability offers at high frame rates of about 0.1 MHz. With future devices that enable a full parallel readout (see figure 7), the frame rate can be further increased by one order of magnitude. A readout time per row of $1 \mu\text{s}$ was already demonstrated with Athena prototype sensors [15]. The linear gate design that was chosen for the Infinipix layout and the sensor of the Wide Field Imager of Athena only enables such short readout processing times due to the short necessary clear process. The higher gain of the linear gate devices compared to previous circular gate layouts [16] further reduces the necessity of long integration times. In addition, the drain current readout significantly improves the time needed to settle the electronic components in the detector [17]. Especially for large detectors with large capacities connected to the readout ASIC, it enables a faster settling and, thereby, longer integration times for a fixed total processing time per row. This advantage in the timing overcompensates the slightly worse noise performance of the drain current readout compared to the source follower one. The bottleneck in the subsequent serial signal chain is reduced by calibrating and subtracting the crosstalk appearing in the analog data that is serialized with high

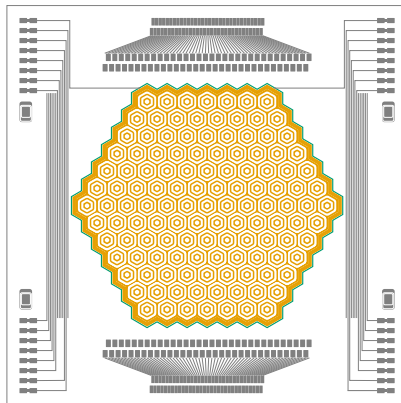


Figure 7. Full parallel readout Infinipix array. The 127 hexagonal pixels are prepared for a full parallel readout on a $16 \times 16 \text{ mm}^2$ chip. Each pixel is a drift detector with six rings and an incircle diameter of $800 \mu\text{m}$. The sensitive area has a width of about 10 mm. The device is in fabrication at the semiconductor laboratory of the Max Planck Society.

frequencies [15]. The resulting energy resolution for all valid events is 146.8 eV at 5.9 keV (135.9 eV for single pixel events). The spectrum is shown in figure 6. The sensor generated background is low since it is measured in a full frame rolling shutter readout. Therefore, the misfit fraction is low. The existing hardware does not allow for a drain readout of an Infinipix DEPFET. The Veritas 2.1 readout ASIC [6] pulls the drain region to a fixed potential. But the functional principle of the Infinipix needs drain regions that have to be switched by at least six volts. It needs either an adaption of the storage DEPFET concept or a new readout ASIC. But the disadvantage of the source follower is dominant only for large devices in rolling shutter readout mode. For full parallel enabled DEPFET arrays, there is no need of a first settling since the pixel are always switched on in a continuous readout.

On the software side, an inter-frame split recombination will be implemented. At the current status, only split events over several pixels within one frame are recognized and recombined [18]. At higher frame rates, not only the number of energy misfits in non-storage DEPFETs increases, but also the number of inter-frame splits — for both kinds of DEPFETs. For storage devices, it is the only reason for a spectral degradation. Therefore, the inter-frame split recombination is necessary to be able to fully utilize the advantage on a DEPFET with storage capability.

5 Summary

We demonstrated the advantage of a DEPFET with pixel-wise integrated storage functionality at high frame rates. The high flexibility of an active pixel sensor in combination with flexible steering and readout ASICs allows for the usage of only a small window of the sensor to be read out. It enables short frame length even though the investigated devices are designed for a row-wise readout. At frame rates of about 100 kHz the difference in the degradation of the spectral performance compared to a slow full frame readout is clearly visible. Even though inter-frame splits are not recombined yet, the difference between a DEPFET with and without storage is already remarkable. Using the internal storage device, the sensor-generated background is reduced by one order of magnitude at a frame rate of 100 kHz . The degradation of the energy resolution compared to a standard full

frame readout is more than two times higher for a non-storage device than for the storage DEPFET. With even higher frame rates enabled by full parallel readout devices and the implementation of inter-frame split recombination, the difference between DEPFETs with and without internal storage will further increase. To enable high frame rates at the order of 1 MHz with the conservation of an excellent spectroscopic performance, a storage functionality is, therefore, indispensable.

Acknowledgments

We gratefully thank all people who gave aid to make the presented measurements possible.

Development and production of the DEPFET sensors for the Athena WFI is performed in a collaboration between MPE and the MPG Semiconductor Laboratory (HLL).

The work was funded by the Max-Planck-Society and the German space agency DLR (FKZ: 50 QR 1501).

References

- [1] D.R. Wilkins, E.M. Cackett, A.C. Fabian and C.S. Reynolds, *Towards modelling X-ray reverberation in AGN: piecing together the extended corona*, *Mon. Not. Roy. Astron. Soc.* **458** (2016) 200 [[arXiv:1602.00022](#)].
- [2] L. Titarchuk, I. Lapidus and A. Muslimov, *Mechanisms for high-frequency qpos in neutron star and black hole binaries*, *Astrophys. J.* **499** (1998) 315 [[astro-ph/9712348](#)].
- [3] W. Becker, M.G. Bernhardt and A. Jessner, *Autonomous spacecraft navigation with pulsars*, *Acta Futura* **7** (2013) 11.
- [4] J. Kemmer and G. Lutz, *New detector concepts*, *Nucl. Instrum. Meth. A* **253** (1987) 365.
- [5] M. Porro et al., *ASTEROID: a 64 channel ASIC for source follower readout of DEPFET arrays for X-ray astronomy*, *Nucl. Instrum. Meth. A* **617** (2010) 351.
- [6] M. Porro et al., *VERITAS 2.0 a multi-channel readout ASIC suitable for the DEPFET arrays of the WFI for Athena*, *Proc. SPIE* **9144** (2014) 91445N.
- [7] S. Herrmann et al., *VERITAS 2.2: a low noise source follower and drain current readout integrated circuit for the wide field imager on the Athena X-ray satellite*, *Proc. SPIE* **10709** (2018) 1070935.
- [8] E. Gatti and P.F. Manfredi, *Processing the signals from solid-state detectors in elementary-particle physics*, *Riv. Nuovo Cim.* **9** (1986) 1.
- [9] R. Richter, J. Treis, F. Schopper and A. Baehr, *Detector arrangement and corresponding operating method wherein the detector is a semi-conductor detector which is switchable between collection states with selected subpixel sensitivity*, Patent, November 2017.
- [10] J. Müller-Seidlitz et al., *Performance study of spectroscopic DEPFET arrays with a pixel-wise storage functionality*, *2018 JINST* **13** P11018.
- [11] H. Halbritter et al., *High-speed LED driver for ns-pulse switching of high-current LEDs*, *IEEE Photon. Technol. Lett.* **26** (2014) 1871.
- [12] R. Blair et al., *The ATLAS high level trigger region of interest builder*, *2008 JINST* **3** P04001 [[arXiv:0711.3217](#)].

- [13] P. Fischer, W. Neeser, M. Trimpl, J. Ulrici and N. Wermes, *Readout concepts for DEPFET pixel arrays*, *Nucl. Instrum. Meth. A* **512** (2003) 318 [[hep-ex/0209074](#)].
- [14] W. Treberspurg et al., *Studies of prototype DEPFET sensors for the wide field imager of Athena*, *Proc. SPIE* **10397** (2017) 103970U.
- [15] W. Treberspurg et al., *Achievable time resolution of spectroscopic prototype DEPFET detectors*, to appear in *JINST* (2019).
- [16] J. Treis et al., *DEPMOSFET active pixel sensor prototypes for the XEUS wide field imager*, *IEEE Trans. Nucl. Sci.* **52** (2005) 1083.
- [17] W. Treberspurg et al., *Studies of prototype DEPFET sensors for the wide field imager of Athena*, *Proc. SPIE* **9905** (2016) 99052C.
- [18] T. Lauf and R. Andritschke, *ROOT based offline and online analysis (ROAn): an analysis framework for X-ray detector data*, *Nucl. Instrum. Meth. A* **762** (2014) 142.

Recent improvements on high-speed DEPFET detectors for X-ray astronomy

J. Müller-Seidlitz^a, A. Bähr^b, N. Meidinger^a, and W. Treberspurg^a

^aMax-Planck-Institute for Extraterrestrial Physics, Gießenbachstraße 1, 85748 Garching bei München, Germany

^bSemiconductor Laboratory of the Max-Planck-Society, Otto-Hahn-Ring 6, 81739 München, Germany

ABSTRACT

Sensors that are based on active pixels enable a flexible adaption to the needs of a scientific instrument. The DEPFET,^{*} a p-channel field effect transistor implemented on a fully depleted silicon bulk, contains a so-called internal gate that serves as potential minimum for collected charge carriers generated by incident photons.¹ The potentially collected electrons induce mirror charges in the FET channel and change its conductivity. It changes the current through the DEPFET or – for a fixed current – the source potential proportionally to the collected charge carriers and, therefore, to the energy of the incident photon. By the integration of a storage into each pixel, the accuracy of the energy measurement can be improved, especially for high frame rates in the order of the readout time of one pixel. One implementation of such a concept is the so-called Infinipix.² It is composed of two sub-pixels that share their source node in the center. The functional principle was already demonstrated on single pixel³ and matrix scale⁴ but enhancements are still necessary to improve the robustness of the devices. In this paper we present variations in the processing technology and the layout that enhance the reliability of the DEPFETs with integrated storage. Adaptions in the technology help to increase the operation voltages for the charge suppression at the insensitive sub-pixel which is demonstrated with measurements. A layout variation combines the advantages of existing layout variants. It was tested with 3D TCAD[†] simulations and is in fabrication to be available for measurements.

Keywords: X-ray detector, high frame rates, DEPFET with storage, layout simulation

1. INTRODUCTION

With BepiColombos MIXS instrument⁵ and the WFI on board of the X-ray telescope Athena,⁶ the first instruments that base on DEPFET pixels are about to be launched into space and in development, respectively. A DEpleted P-channel Field-Effect Transistor (DEPFET) is a FET[‡] implemented on a fully depleted, high resistive n-doped silicon bulk. In the transistor region, a weak n-implant builds the basis for the DEPFET. Strong p-implants that form the source and the drain regions partially compensate the n-implant which only remains completely under the transistor gate. It forms a potential minimum for electrons. Electron-hole pairs that are generated in the sensitive volume of the silicon sensor are separated by the applied voltages at the front and the back side. Holes are removed over the back side while electrons drift into a potential minimum in z-direction before they move sideways driven by ring-like structures at the front side. Finally, they are collected in the potential minimum underneath the transistor gate. These electrons induce mirror charges in the p-channel of the DEPFET that change its conductivity. Depending on the readout mode, the resulting change in the transistor current or the changing voltage level at the source node for a fixed current can be determined. This signal is proportional to the number of collected electrons. Due to the influence of this collection region on the transistor

Further author information:

J. Müller-Seidlitz: E-mail: jms@mpe.mpg.de, Telephone: +49 89 30 000 3509

^{*}DEpleted P-channel Field-Effect Transistor

[†]Technology Computer Aided Design

[‡]Field-Effect Transistor

High Energy, Optical, and Infrared Detectors for Astronomy VIII, edited by Andrew D. Holland,
James Beletic, Proc. of SPIE Vol. 10709, 107090F · © 2018 SPIE
CCC code: 0277-786X/18/\$18 · doi: 10.1117/12.2313203

channel, it is called internal gate in analogy to the original transistor gate that is often called external gate for differentiation purposes.

To reduce the noise contribution to the measurement and, thereby, to increase the energy resolution of spectroscopic measurements, the signal is sampled twice by the readout ASIC^{§,7}. After a first signal integration, the potentially collected electrons are removed from the internal gate via clear transistors that are implemented in each pixel. The second signal integration is used to identify the baseline signal. The difference of the two determined values presents the actual measurement. It requires an almost complete clear process to measure the full number of collected electrons. Due to the form of the signal at the integration stage of the readout ASIC, it is called trapezoidal weighting function.⁸

Charge clouds generated by incident photons that arrive at the internal gate during the readout process may be detected with a wrong energy or are even lost. If a photon hits the detector during the first signal integration by the readout ASIC or at the end of the clear process in the pixel, the amount of detected charge carriers is reduced. It is not possible to discriminate between an event with a lower energy or a more high energetic event whose signal is reduced by (apparent) charge loss. Such energy misfits cannot be neglected in the subsequent analysis. They worsen the spectral performance of the detector. The effect increases with the ratio of readout time to total frame length. For a full parallel readout of all pixels, the readout time per pixel equals the frame time. In this extreme case, a large fraction of events is affected by an incorrectly measured energy. For a readout processing time in the order of 1 μ s, that are about 40% of all events. To omit such energy misfits without reducing the throughput of the detector, a storage can be integrated into each pixel.

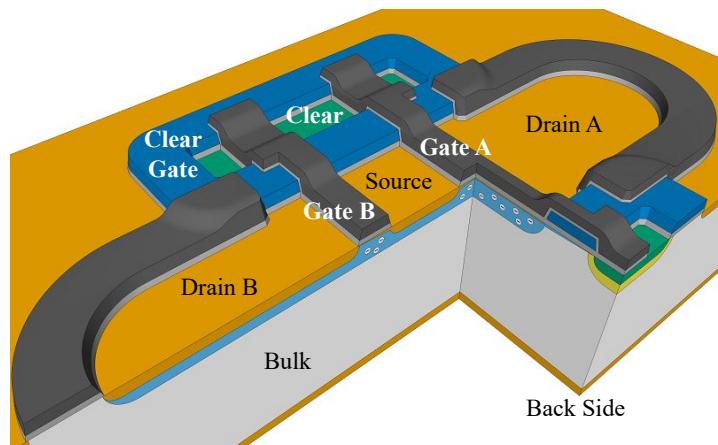


Figure 1. Layout of an Infinipix DEPFET. Two sub-pixels consisting of a DEPFET each share their source region that acts also as readout node. The task of a sub-pixel, being the insensitive, read-out one or the collecting sub-pixel, is assigned via appropriate drain voltages. They are switched globally for all pixels of a DEPFET array and mark the temporal boundary between two frames. A negative voltage at one drain region shields the internal gate while arriving charge carriers are collected in the internal gate of the sensitive sub-pixel defined by a more positive drain voltage.

One implementation of a DEPFET with storage is the Infinipix² as shown in Fig. 1. It consists of two sub-pixels. Alternating, they act as storage or as read-out DEPFET. The readout is performed in the source follower mode.⁷ The readout node is the shared source region of the two DEPFETs that build the sub-pixels. The two drain regions are not only necessary for the DEPFET operation, but are also used to assign the tasks to the sub-pixels. For the readout of one of the p-channel FETs, the drain needs to be on a potential more negative than the source. In addition, the negative voltage level of the drain region shields the associated internal gate. The drain region of the other sub-pixel is roughly at the potential of the shared source region to make its internal gate more attractive compared to the shielded, read-out one. After a complete readout of each pixel, the voltage levels at the drain regions are interchanged globally. It supplies a global shutter even if the readout takes place one row after each other which results in a rolling shutter for a DEPFET without storage.

[§]Application Specific Integrated Circuit

The functional principle was already demonstrated by measurements on single pixel³ and matrix scale.⁴ The spectral performance for a 32×32 pixels Infnipix array was determined to (127.40 ± 0.07) eV FWHM and (123.61 ± 0.07) eV FWHM at 5.9 keV and a readout time per row of 5 μ s for all valid patterns and single events, respectively, with a mean noise per pixel of (2.333 ± 0.004) e⁻ ENC at -70°C .⁹ Valid patterns are defined as all recombined patterns up to two times two pixels that show a signal above the threshold of three times the pixel-wise noise.

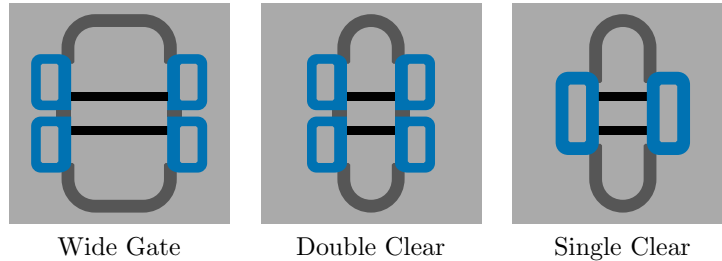


Figure 2. On the basis of previous measurements for a layout comparison,⁴ the layout is adapted to combine the advantages of the existing variants that are shown here. While the two layouts with a narrow gate (Double Clear and Single Clear) show an almost complete clear process within 100 ns, the Wide Gate device is much more robust against resistivity variations in the wafer material (see Fig. 4). The reduction of the clear contacts (Single Clear) reduces the operation voltage window at the clear contacts but shows no impact on the spectral performance of the device.

The spectral performance presented above was measured using an Infnipix Single Clear. It is one of three layout variants that already exist as arrays of 32×32 pixels (130 μm pixelsize). They were developed and layouted at the Semiconductor Laboratory of the Max-Planck-Society to enable a further progress in the production of a DEPFET sensor with integrated storage. In the Single Clear layout, the two sub-pixels not only share the source region but also the clear transistors. To obtain the isolation of the internal gate of the sensitive sub-pixel to the clear contact, a DEPFET in its off-state is sufficient. The positive voltage at the external gate causes an internal gate that is attractive enough not to loose potentially collected electrons into the clear while the clear transistor is in its on-state. The Double Clear variant was fabricated in case the principle of clear-process selection by the state of the external gate is not working efficiently. To relax the layout, also a larger variant – the Infnipix Wide Gate – was fabricated. In case the size of the drains that scales with the width of the gates, is not large enough to supply a reliable operation of the Infnipix principle, the relaxed layout enlarges the operation windows.

2. CHARGE SUPPRESSION EFFICIENCY

Spectroscopic DEPFETs are successfully operated already for more than a decade.¹⁰ The additional key issue for an Infnipix DEPFET is the capability to shield the internal gate against charge carriers that are generated during the time of insensitivity of a sub-pixel. The shielding is only supplied by the voltage at the corresponding drain region. Therefore, a sufficient negative level compared to the source is not only needed to increase the gain of the DEPFET, but also to ensure the functional principle of the storage. The ratio between the peak height of the emission line that is used to illuminate and investigate the sensor, and the sensor-generated background, is the peak-to-valley ratio. It is the height of the Gaussian-shaped, detected peak divided by the mean value of the interval between 0.9 keV and 1.1 keV. If electrons are drained to the shielded, by intention insensitive internal gate, these electrons generate a low energetic signal in the previous or in the next frame depending on its relative temporal position compared to the readout of that sub-pixel. As long as the shielding is only weak, the peak-to-valley is a good indicator as shown in Fig. 3. For small charge losses only the energy resolution or a detailed examination of the spectra can reveal an imperfect shielding. But the drain-source voltage is also limited at even more negative values. If the drain level is shifted to more negative potentials, also the voltage difference between the FET channel and the drain increases. A high field region establishes and causes a nascent avalanche breakdown. The generated charge appears as additional leakage current, increasing the sensor noise and also degrading the spectral performance. . Both effects lead to an optimal drain-source voltage of a few deci-volts around -5.5V (see Fig. 3). A larger operation voltage window would be desirable. Only if such an interval of a

constant spectral performance would exist, a perfect shielding of the insensitive pixel and the absence of leakage current at the boundary between the FET channel and the drain region can be ensured.

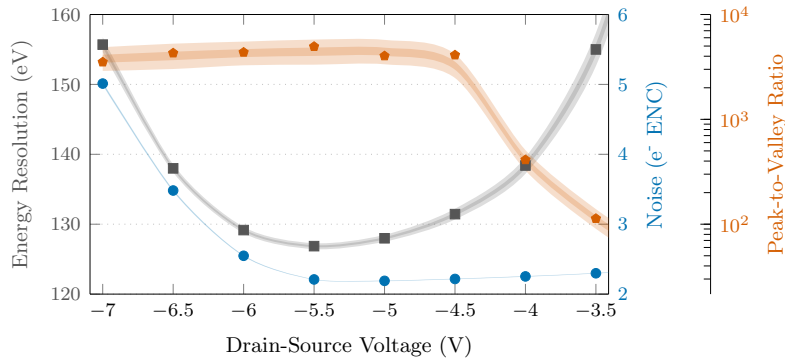


Figure 3. A good indicator for a successful charge suppression at the insensitive sub-pixel is the peak-to-valley ratio. If charge is drained to that internal gate it will be measured as low energy signal in an adjacent frame. Since the quantity for the valley is determined as the mean value between 0.9 keV and 1.1 keV, large charge losses into the insensitive sub-pixel show up as worse peak-to-valley ratio. The functional principle of the Infinipix sets a minimum for the applied drain voltages. On the other hand, a nascent avalanche breakdown at the channel-drain boundary caused by high electric fields limits the applicable drain voltages. The current samples do not show a settled region for the energy resolution for a varied drain-source voltage even though the achieved results are already excellent around the optimal drain-source voltage of -5.5 V. The energy resolution is given for all valid events.

The second crucial voltage is the one at the back side contact. Its minimum value is the depletion voltage that is determined by the dopant concentration of the wafer. This concentration can show strong local variations even on the scale of the small prototype devices.¹¹ For the operation of the whole device, the entire sensor has to be fully depleted. This requires at least the depletion voltage of the area with the lowest resistivity. But more negative voltage levels at the back side also lead to a minimum of the electrostatic potential in the silicon bulk that is shifted towards the front side. It causes a higher probability of charge loss into the insensitive sub-pixel or even into the clear contact. If the operation voltage window at the back side for a single pixel is smaller than the differences in the depletion voltages over the whole sensor, the operability of the detector is very limited with one set of voltages.

To be able to distinguish the operation voltage window at the back side for single pixels and the differences in the depletion voltage over the whole devices, the sensors were illuminated with an LED[¶] and the voltage level at the back side contact was varied. The group of three times three pixels that requires the most positive depletion voltage and the one with the most negative depletion voltage were selected at each device. The normalized signals are shown in Fig. 4. At the depletion voltage, the signal increases rapidly from zero to one – the pixels become sensitive. For even more negative voltages the signal starts to decrease due to charge loss. Therefore, the plateau indicates the operation voltage window at the back side contact while the difference in the depletion voltage is revealed by the selection of pixels that become sensitive at the earliest and at the latest during a back side contact voltage sweep. Fig. 4 shows, therefore, clearly, that the combination of a small operation voltage window at the back side and large resistivity variations can lead to an inoperable sensor. Since the doping variations are an intrinsic property of the wafer material, only the layout can be adapted to enlarge the back side voltage operation window.

3. LAYOUT AND TECHNOLOGY ADAPTIONS

Even though measurements with an excellent spectral performance can be obtained with most of the Infinipix devices, a few limitations still exist as presented in section 2. They have to be overcome to ensure a reliable operation of an array of Infinipix DEPFET pixels. The enlargement of the operation voltage windows at the

[¶]Light Emitting Diode

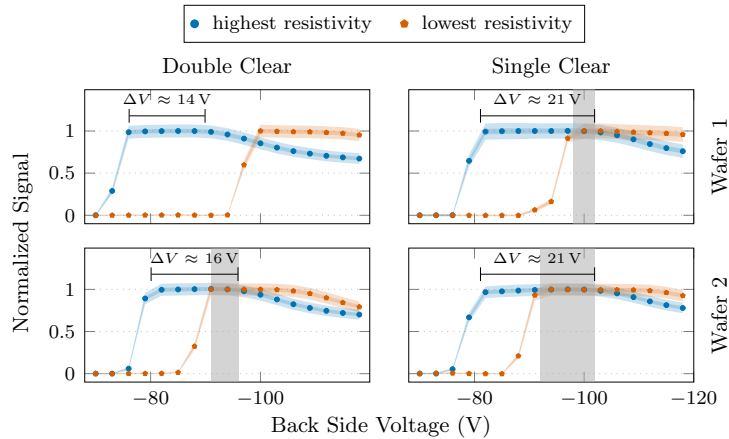


Figure 4. The Infinipix devices with a narrow gate suffer from a limited back side operation voltage window. It is defined by the depletion voltage and the point at which charge is lost into the insensitive sub-pixel and measured to only 15 V to 20 V. Due to local resistivity variations of the wafer material, the depletion voltage differences could even be higher. This can lead to a sensor that is not operable for one set of voltages. The 3×3 pixels with the lowest (orange) and highest (blue) resistivity of four devices are shown. The detected signal from an infra-red LED increases from 0 to 1 at the depletion voltage and starts to decrease as soon as electrons are drained to the insensitive sub-pixel. The black bar indicates the operation voltage window of single pixels while the gray box represents the one of the whole sensor.

drain regions and at the back side contact is addressed with two different approaches. Finally, they both affect the drain voltage. Technology variations investigated in the course of the prototype development for the Athena WFI help to enable more negative voltages at the two drain regions. Layout adaptations that increase the size of the drain regions help to decrease the influence of the back side contact voltage on the charge suppression efficiency of the Infinipix.

For the evaluation of the optimal sensor for the Wide Field Imager of Athena, DEPFETs with two different gate oxide thicknesses were fabricated by the semiconductor laboratory of the Max-Planck-Society – besides other technology variations.¹² The larger capacity of the thinner oxide variant causes a more pronounced vertical electric field component compared to DEPFETs with thicker gate oxides operated with the same external voltages at source, drain and gate. At the boundary between the FET channel and the drain, the field peaks and causes an avalanche breakdown whose intensity depends on the applied voltages and the gate oxide thickness. The effect on the shot noise generated by additional leakage current at that point for a varied drain voltage is shown in Fig. 5. A larger noise not only broadens the measured emission line, but also adds an additional apparent charge loss. It is caused by charge cloud fractions collected in neighboring pixels that are below the threshold which scales with the noise. Using a thick gate oxide, the operation voltage window could be extended by more than one volt. Nevertheless, the thin oxide technology is more resistant against radiation damage and allows also for a self-aligning implantation of the implant that shields the clear contact which increases the homogeneity of the DEPFETs within a sensor array.¹² To benefit from the advantages of the thin gate oxide technology – that was used also for the fabrication of the investigated Infinipix arrays – and to reduce the peak in the electric field anyway, an additional so-called halo implant can reduce the intrinsic electric field by the flattening of the p-n junction between the drain region and the area below the transistor gate. As shown in Fig. 5, a first attempt already shows a step in the right direction even though the thick oxide devices still show the lowest noise contribution.

The resistivity variations of the wafer material that also show strong deviations in the small Infinipix prototype devices allow for an investigation of the influence the resistivity has on the charge suppression efficiency. A lower resistivity caused by a higher dopant concentration requires a higher depletion voltage. The establishment of a steeper electrostatic potential leads to a more well defined potential configuration that improves the charge collection efficiency into the right internal gate. With this knowledge the selection of an adequate wafer material also improves the performance of the Infinipix devices.

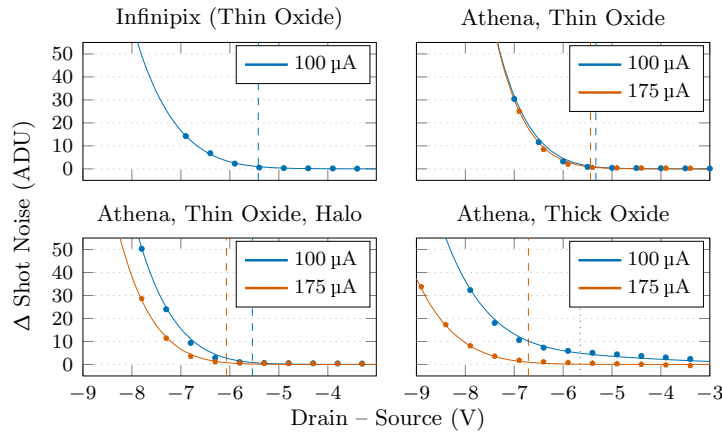


Figure 5. In the course of the prototype development for the Athena wide field imager, various technology variants were tested.¹² It allowed for the investigation of their influence on the operation window of the drain-source voltage. The measurements of the shot noise caused by a nascent avalanche breakdown for two different bias currents show clearly that the operation voltage window can be extended compared to the thin oxide technology used for the investigated Infinipix arrays. For a bias current of $100\ \mu\text{A}$, the gate voltage is set to a more positive value to keep the source on a constant potential with respect to the $175\ \mu\text{A}$ measurements. The resulting enlarged channel layer causes short channel effects that counteract the decreased electric field strength at the channel-drain boundary. Therefore, the improvement of the operation voltage window requires larger bias currents. The vertical, dashed lines indicate the voltage at which the noise increased by 10%.

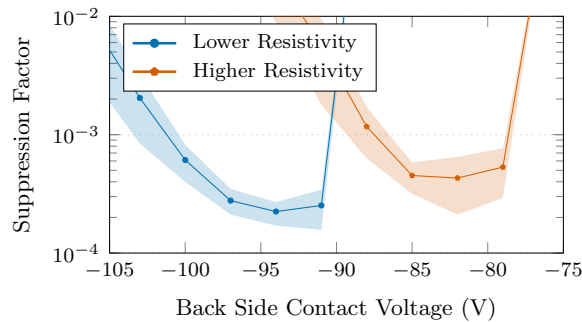


Figure 6. The suppression factor – the fraction of charge that is collected in the insensitive sub-pixel – depends on the resistivity of the wafer material. The resistivity is inversely proportional to the dopant concentration and, therefore, the absolute value of the depletion voltage. The depletion voltage is indicated by the rapid change in the suppression factor on the more positive side. Selected pixels with very high and very low dopant concentrations of the device with the high resistivity variations (see upper left of Fig. 4) show, that a lower resistivity leads to a better shielding of the internal gate of the insensitive sub-pixel.

The extension of the operation voltage window at the back side contact is addressed with the size of the drain region. A more pronounced potential configuration at the front side that defines the sensitive and the insensitive sub-pixels reduces the influence of the depletion voltage necessary for the low-resistivity regions. Since a narrow gate is needed to enable an efficient clear process, the size of the drain region and the width of the gate need to be decoupled. Potential layout variations were tested with 3D TCAD simulations using Sentaurus Device.¹³ As a first step, the existing layout variants were set up to enable a direct comparison with new layouts. The simulation results for the suppression factor for the three existing Infinipix variants are shown in Fig. 7. A new proposal for the layout, the Infinipix Wide Drain, realises the decoupling of the drain and the gate size by the rotation of the clear transistors and the shift of the drain-ring separation towards the outer edge of the clear gate. The reduced distance between the channel under the clear gate and the drain during the clear process

shifts the clear channel slightly towards the pixel center. The negative drain that is needed to shield the internal gate constrains the clear channel but seems not to influence the clear behavior significantly according to the simulation results.

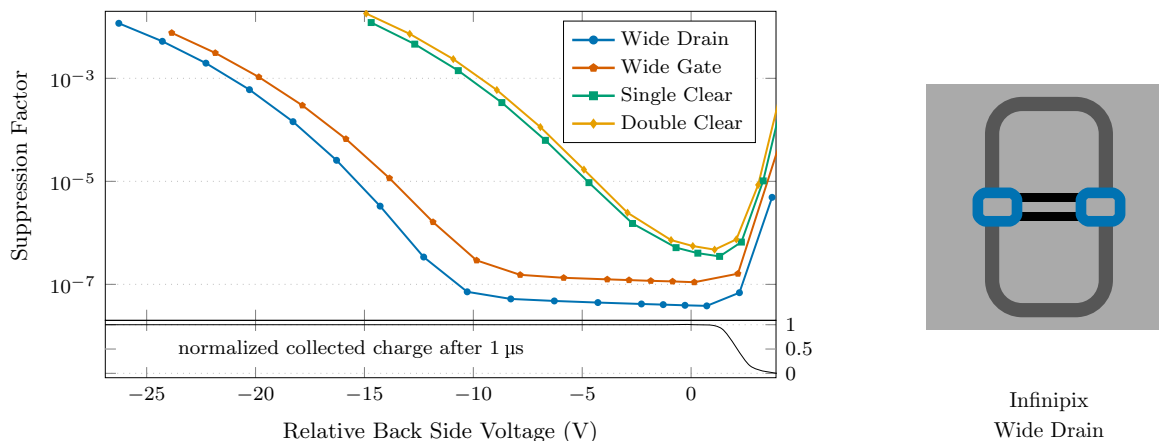


Figure 7. As shown on the right, the rotation of the clear transistors by 90 degree and the shift of the drain-ring separators to the outer end of the clear contact allows for less coupling between the gate width and the drain region size. According to the simulations shown on the left, this adaption of the Infinipix should gain from the reliability of the Wide Gate layout (cf. Fig. 2) without the reduction of the efficient clear process of the narrow gate variants that is necessary to obtain an excellent spectroscopic performance. A smaller distance between the gates also improves the charge suppression efficiency. It is limited by the space needed to place a contact hole from the aluminum readout line to the source region.

Due to the layout adaption, the broadest position of the drain is not directly at the associated internal gate anymore. Therefore, the collection of the electrons in the depth is slightly shifted towards the center of the drain region. The final drift into the internal gate takes place near the surface. Depending on the actual distance to the surface in a real device, the larger number of crystal defects there might influence the charge collection efficiency. To rule out these last concerns by measurements, the proposed layout is in fabrication as 32×32 pixel array.

4. SUMMARY

To reduce so-called energy misfits that appear during the readout of a DEPFET, DEPFETs with a storage functionality implemented into each pixel are in development. One implementation, the so-called Infinipix, already shows an excellent spectroscopic performance of (127.40 ± 0.07) eV FWHM at 5.9 keV and a readout time per row of $5 \mu\text{s}$ for all valid events ($[123.61 \pm 0.07]$ eV FWHM for single events) with a mean noise per pixel of (2.333 ± 0.004) e⁻ ENC at -70°C on matrix scale (32×32 pixels, $130 \mu\text{m}$ pixelsize).⁹ Nevertheless the technology and the layout need to be adapted to ensure a more reliable operation in particular for large-format devices. Adaptions in the technology were investigated with measurements while a layout proposal was studied with 3D TCAD simulations. The modifications show an improvement at the crucial points that may limit the functionality of the Infinipix – the depletion voltage at the back side and the drain voltage that also acts as a shielding for the readout process. Using different technology options, the drain voltage can be extended by at least one volt while it is limited to a few deci-volts at the moment as long as an excellent spectroscopic performance is required. The proposed layout variant is in fabrication and will – according to the simulations – result in a significantly extended operation voltage window at the back side. It needs to be larger than the depletion voltage differences caused by resistivity variations of the wafer material. This intrinsic property of the silicon material would lead to inoperable devices otherwise. If the simulation results can be verified by experimental measurements, DEPFET active pixel sensors with storage will allow a time resolution in the order of one microsecond – still maintaining the excellent spectral performance of DEPFET detectors.

ACKNOWLEDGMENTS

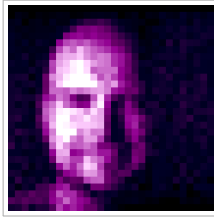
We gratefully thank all people who gave aid to make the presented measurements and simulations possible.

Development and production of the DEPFET sensors for the Athena WFI is performed in a collaboration between MPE and the MPG Semiconductor Laboratory (HLL).

The work was funded by the Max-Planck-Society and the German space agency DLR (FKZ: 50 QR 1501).

REFERENCES

- [1] Kemmer, J. and Lutz, G., “New detector concepts,” *Nucl. Instr. Meth. Phys. Res. A* **253**, 365–377 (1987).
- [2] Richter, R., Treis, J., Schopper, F., and Baehr, A., “Detector arrangement and corresponding operating method wherein the detector is a semi-conductor detector which is switchable between collection states with selected subpixel sensitivity.” Patent (11 2017). US 9812475.
- [3] Bähr, A. et al., “Development of DEPFET active pixel sensors to improve the spectroscopic response for high time resolution applications,” in [*Proc. of SPIE*], **9144** (2014).
- [4] Müller-Seidlitz, J. et al., “Spectroscopic performance of DEPFET active pixel sensor prototypes suitable for the high count rate Athena WFI detector,” in [*Proc. of SPIE*], **9905**, 9905 – 9905 – 7 (2016).
- [5] Treis, J. et al., “MIXS on BepiColombo and its DEPFET based focal plane instrumentation,” *Nucl. Instr. Meth. Phys. Res. A* **624**(2), 540 – 547 (2010). New Developments in Radiation Detectors.
- [6] Meidinger, N. et al., “Development of the wide field imager instrument for ATHENA,” in [*Proc. of SPIE*], **10699**, 10699–50 (2018).
- [7] Porro, M. et al., “ASTEROID: A 64 channel ASIC for source follower readout of DEPFET arrays for X-ray astronomy,” *Nucl. Instr. Meth. Phys. Res. A* **617**(1), 351 – 357 (2010). 11th Pisa Meeting on Advanced Detectors.
- [8] Gatti, E. and Manfredi, P. F., “Processing the signals from solid-state detectors in elementary-particle physics,” *La Rivista del Nuovo Cimento (1978-1999)* **9**(1), 1–146 (1986).
- [9] Müller-Seidlitz, J. et al., “Performance study of spectroscopic depfet arrays with a pixel-wise storage functionality,” *in preparation* (2018).
- [10] Treis, J. et al., “First results of DEPFET-based active-pixel-sensor prototypes for the XEUS wide-field imager,” in [*Proc. of SPIE*], **5501**, 89–100 (2004).
- [11] Majewski, P. et al., “DEPFET macropixel detectors for MIXS: Integration and qualification of the flight detectors,” *IEEE Transactions on Nuclear Science* **59**(5, 3), 2479–2486 (2012).
- [12] Treberspurg, W. et al., “Characterization of different options for spectroscopic X-ray DEPFETs,” *in preparation* (2018).
- [13] Synopsys, Inc., Mountain View, California, United States, “Sentaurus Device,” (version J-2014.09).



SELFIE TAKEN WITH
AN INFINIPIX ARRAY
AND A PINHOLE.

Acknowledgements

I would like to thank Prof. Dr. Werner Becker for accepting me as his PhD candidate even though the topic of my thesis is in a research field he is not specialised in.

Furthermore I would like to address my sincere acknowledgement to Dr. Norbert Meidinger who made the work in the detector group of the High-Energy Astrophysics directorate at the Max Planck Institute for Extraterrestrial Physics possible and to Prof. Dr. Christian Kiesling for agreeing to undertake the second review.

I want to express my great gratitude to my colleagues in the detector development: Dr.-Ing. Bettina Bergbauer for her introduction into the measurement setup; Dr. Alexander Bähr as my predecessor for his work on the Infinipix single pixel structures and the introduction into the 3D simulations as basis for my thesis; Dr. Wolfgang Treberspurg for the deeper discussion of measurement results and his ideas for sophisticated measurement methods; and Dr. Robert Andritschke for his expertise in the interpretation of spectral features, the support for the analysis tools and all his help with any software and hardware problem.

Sincere thanks are given to the people working at the semiconductor laboratory of the Max Planck Society, especially: Rainer Richter and Dr. Johannes Treis for the idea and the implementation of the Infinipix layout; Danilo Mießner for his reliable integration and wire bonding of the detector components, including all special wishes necessary for the complex devices; Dr. Peter Lechner for the implementation of the new layout resulting from my thesis; and everyone else who is involved in the fabrication of the cutting-edge semiconductor sensors.

It was a pleasure to work with the engineers of the electronic and mechanical development divisions at the MPE. They are in particular Dr.-Ing. Sabine Ott who designed the electrical setup, Anna Koch who was helpful with all special wishes for additive electronic components, Rafael Strecker who supported me with the mechanical setup, Olaf Hälker for the advanced electrical components, Jonas Reiffers who designed the new modular setup used for the Athena detector development, and all others who supported me and my work.

I would like to address that my heart felt thanks to Dr. Wolfgang Treberspurg, Dr. Alexander Bähr, Dr.-Ing. Sabine Ott, Dr. Norbert Meidinger and Anna Kemper for their extensive proofreading.

Finally, I would like to thank cordially all my friends, family and acquaintances for supporting me and cheering me up as well as all the great colleagues that made the work at the MPE a memorable experience.

